

ISSN 2667-4211

ESKİŞEHİR TECHNICAL UNIVERSITY
JOURNAL OF SCIENCE AND TECHNOLOGY
A – Applied Sciences and Engineering

Volume 24 Number 4 - December - 2023

**Volume: 24 / Number: 4 / December - 2023**

Eskiőehir Technical University Journal of Science and Technology A - Applied Sciences and Engineering (ESTUJST-A) is a peer-reviewed and refereed international journal published by Eskiőehir Technical University. Since 2000, it has been regularly published and distributed biannually and it has been published quarterly and only electronically since 2016.

The journal accepts only manuscripts written in English.

The journal issues are published electronically in **March, June, September, and December**.

Eskiőehir Technical University Journal of Science and Technology A - Applied Sciences and Engineering is an international peer-reviewed and refereed journal published by Eskiőehir Technical University.

The journal is dedicated to the dissemination of knowledge in applied sciences and engineering disciplines.

The journal aims to publish high quality, original international scientific research articles with specific contributions to the literature in the field of engineering and applied sciences. The journal publishes research papers in the fields of applied science and technology such as Physics, Biology, Mathematics, Statistics, Chemistry and Chemical Engineering, Environmental Sciences and Engineering, Civil Engineering, Earth and Atmospheric Sciences, Electrical and Electronical Engineering, Computer Science and Informatics, Materials Sciences and Engineering, Mechanical Engineering, Mining Engineering, Industrial Engineering, Aeronautics and Astronautics, Pharmaceutical Sciences.

The journal publishes original research articles and special issue articles. All articles are peer-reviewed and the articles that have been evaluated are ensured to meet with researchers as soon as possible.

Eskiőehir Technical University holds the copyright of all published material that appear in Eskiőehir Technical University Journal of Science and Technology A - Applied Sciences and Engineering.

"Anadolu Üniversitesi Bilim ve Teknoloji Dergisi A - Uygulamalı Bilimler ve Mühendislik (Anadolu University Journal of Science and Technology A - Applied Sciences and Engineering)" published within Anadolu University started to be published within Eskiőehir Technical University which was established due to statute law 7141, in 2018. Hence, the name of the journal is changed to " Eskiőehir Technical University Journal of Science and Technology A - Applied Sciences and Engineering (Eskiőehir Teknik Üniversitesi Bilim ve Teknoloji Dergisi A - Uygulamalı Bilimler ve Mühendislik)".



Volume: 24 / Number: 4 / December– 2023

Owner / Publisher: Prof. Dr. Adnan ÖZCAN for Eskiőehir Technical University

EDITOR-IN-CHIEF

Prof. Dr. Semra KURAMA

Eskiőehir Technical University, Institute of Graduate Programs, 26470 Eskiőehir, TURKEY

Phone: +90 222 213 7470

e-mail: skurama@eskisehir.edu.tr

CO-EDITOR IN CHIEF

Assit. Prof. Dr. Hüseyin Ersin EROL

Eskiőehir Technical University, Institute of Graduate Programs, 26470 Eskiőehir, TURKEY

Phone: +90 222-213 7473

e-mail: heerol@eskisehir.edu.tr

CONTACT INFORMATION

Eskiőehir Technical University Journal of Science and Technology

Eskiőehir Technical University, Institute of Graduate Programs, 26470 Eskiőehir, TURKEY

Phone: +90 222 213 7485

e-mail : btada@eskisehir.edu.tr



Volume: 24 / Number: 4 / December - 2023

OWNER

Adnan ÖZCAN, **The Rector of Eskişehir Technical University**

EDITORIAL BOARD

Semra KURAMA, **Editor in Chief**

Hüseyin Ersin EROL, **Co-Editor in Chief**

LANGUAGE EDITOR-ENGLISH

Burcu ERDOĞAN

İlker DEMİROĞLU

SECTION EDITORS

Sibel AKAR (Eskişehir Osmangazi University, Turkey)
Ziya AKÇA (Eskişehir Osmangazi University, Turkey)
İpek AKIN (İstanbul Teknik University, Turkey)
Sema AKYALÇIN (ESTU, Turkey)
Mehmet ALEGÖZ (ESTU, Turkey)
Suna AVCIOĞLU (Yıldız Teknik University, Turkey)
Uğur AVDAN (ESTU, Turkey)
Zehra YİĞİT AVDAN (ESTU, Turkey)
Ayşe H. BİLGE (Kadir Has University, Turkey)
Müjdat ÇAĞLAR (ESTU, Turkey)
Çağatay DENGİZ (Ortadoğu Teknik University, Turkey)
Rasime DEMİREL (ESTU, Turkey)
Elif Begüm ELÇİOĞLU (ESTU, Turkey)
Barış ERBAŞ (ESTU, Turkey)
Metin GENÇTEN (Yıldız Teknik University, Turkey)
Ömer Nezih GEREK (ESTU, Turkey)
Özer GÖK (ESTU, Turkey)
Cihan KALELİ (ESTU, Turkey)
Gordona KAPLAN (ESTU, Turkey)

T. Hikmet KARAKOÇ (ESTU, Turkey)
Elif KORUYUCU (ESTU, Turkey)
Semra KURAMA (ESTU, Turkey)
Hakan Ahmet NEFESLİOĞLU (ESTU, Turkey)
Anatoly NĪKANOV (Saratov State Technical University, Slovenia)
Murad OMAROV (Kharkiv National University of Radio Electronics, Ukraine)
Mehmet İnanç ONUR (ESTU, Turkey)
Seyhan ÖNDER (Eskişehir Osmangazi University, Turkey)
Zahide BAYER ÖZTÜRK (Nevşehir Hacı Bektaş Veli Univ., Turkey)
Emrah PEKKAN (ESTU, Turkey)
Najeeb REHMAN (Comsat University, Pakistan)
İsmail Hakkı SARPÜN (Akdeniz University, Turkey)
Aydn SİPAHİOĞLU (Eskişehir Osmangazi University, Turkey)
İlkin YÜCEL ŞENGÜN (Ege University, Turkey)
Sevil ŞENTÜRK (ESTU, Turkey)
Gülsüm TOPATEŞ (Ankara Yıldırım Beyazıt University Turkey)
Önder TURAN (ESTU, Turkey)
Muammer TÜN (ESTU, Turkey)
Fatma TÜMSEK (Eskişehir Osmangazi University, Turkey)
Berna ÜSTÜN (ESTU, Turkey)

Secretary/Typeset

Handan YİĞİT



ABOUT

Eskişehir Technical University Journal of Science and Technology A - Applied Sciences and Engineering (ESTUJST-A) is a peer-reviewed and refereed international journal published by Eskişehir Technical University. Since 2000, it has been regularly published and distributed biannually and it has been published quarterly and only electronically since 2016.

The journal accepts only manuscripts written in English.

The journal issues are published electronically in **MARCH, JUNE, SEPTEMBER, and DECEMBER.**

AIM AND SCOPE

Eskişehir Technical University Journal of Science and Technology A - Applied Sciences and Engineering is an international peer-reviewed and refereed journal published by Eskişehir Technical University.

The journal is dedicated to the dissemination of knowledge in applied sciences and engineering disciplines.

The journal aims to publish high quality, original international scientific research articles with specific contributions to the literature in the field of engineering and applied sciences. The journal publishes research papers in the fields of applied science and technology such as Physics, Biology, Mathematics, Statistics, Chemistry and Chemical Engineering, Environmental Sciences and Engineering, Civil Engineering, Earth and Atmospheric Sciences, Electrical and Electronical Engineering, Computer Science and Informatics, Materials Sciences and Engineering, Mechanical Engineering, Mining Engineering, Industrial Engineering, Aeronautics and Astronautics, Pharmaceutical Sciences.

The journal publishes original research articles and special issue articles. All articles are peer-reviewed and the articles that have been evaluated are ensured to meet with researchers as soon as possible.

PEER REVIEW PROCESS

Manuscripts are first reviewed by the editorial board in terms of its its journal's style rules scientific content, ethics and methodological approach. If found appropriate, the manuscript is then send to at least two renown referees by editor. The decision in line with the referees may be an acceptance, a rejection or an invitation to revise and resubmit. Confidential review reports from the referees will be kept in archive. All submission process manage through the online submission systems.

OPEN ACCESS POLICY

This journal provides immediate open access to its content on the principle that making research freely available to the public supports a greater global exchange of knowledge. Copyright notice and type of licence : **CC BY-NC-ND.**

PRICE POLICY

Eskişehir Technical University Journal of Science and Technology A - Journal of Applied Sciences and Engineering is an English, peer-reviewed, scientific, free of charge open-access-based journal. The author is not required to pay any publication fees or article processing charges (APCs) for peer-review administration and management, typesetting, and open-access. Articles also receive Digital Object Identifiers (DOIs) from the CrossRef organization to ensure they are always available.

ETHICAL RULES

You can reach the Ethical Rules in our journal in full detail from the link below:

<https://dergipark.org.tr/en/pub/estubtda/policy>

Ethical Principles and Publication Policy

Policy & Ethics

Assessment and Publication

As a peer-reviewed journal, it is our goal to advance scientific knowledge and understanding. We adhere to the guideline and ethical standards from the Committee on Publication Ethics (COPE) and the recommendations of ICMJE (International Committee of Medical Journal Editors) regarding all aspects of publication ethics and cases of research and publication misconduct to ensure that all publications represent accurate and original work and that our peer review process is structured without bias. We have outlined a set of ethical principles that must be followed by all authors, reviewers, and editors.

All manuscripts submitted to our journals are pre-evaluated in terms of their relevance to the scope of the journal, language, compliance with writing instructions, suitability for science, and originality, by taking into account the current legal requirements regarding copyright infringement and plagiarism. Manuscripts that are evaluated as insufficient or non-compliant with the instructions for authors may be rejected without peer review.

Editors and referees who are expert researchers in their fields assess scientific manuscripts submitted to our journals. A blind peer review policy is applied to the evaluation process. The Editor-in-Chief, if he/she sees necessary, may assign an Editor for the manuscript or may conduct the scientific assessment of the manuscript himself/herself. Editors may also assign referees for the scientific assessment of the manuscript and make their decisions based on reports by the referees. The Editor-in-Chief makes the final decision regarding the publishing of the manuscript.

Articles are accepted for publication by the Editor-in-Chief in accordance with the COPE (Committee on Publication Ethics). Authors can access this information online via the journals' websites (<https://publicationethics.org/>). Articles are accepted for publication on the understanding that they have not been published and are not going to be considered for publication elsewhere. Authors should certify that neither the manuscript nor its main contents have already been published or submitted for publication in another journal.

The journal adapts the COPE guidelines to satisfy the high-quality standards of ethics for authors, editors, and reviewers:

Duties of Editors-in-Chief and co-Editors

The crucial role of the journal Editor-in-Chief and co-Editors is to monitor and ensure the fairness, timeliness, thoroughness, and civility of the peer-review editorial process. The main responsibilities of Editors-in-Chief are as follows:

- Selecting manuscripts suitable for publication while rejecting unsuitable manuscripts,
- Ensuring a supply of high-quality manuscripts to the journal by identifying important,
- Increasing the journal's impact factor and maintaining the publishing schedule,
- Providing strategic input for the journal's development,

Duties of Editors

The main responsibilities of editors are as follows:

- An editor must evaluate the manuscript objectively for publication, judging each on its quality without considering the nationality, ethnicity, political beliefs, race, religion, gender, seniority, or institutional affiliation of the author(s). Editors should decline any assignment when there is a potential for conflict of interest.
- Editors must ensure the document(s) sent to the reviewers does not contain information of the author(s) and vice versa.
- Editors' decisions should be provided to the author(s) accompanied by the reviewers' comments and recommendations unless they contain offensive or libelous remarks.
- Editors should respect requests (if well reasoned and practicable) from author(s) that an individual should not review the submission.
- Editors and all staff members should guarantee the confidentiality of the submitted manuscript.
- Editors should have no conflict of interest with respect to articles they reject/accept. They must not have a conflict of interest with the author(s), funder(s), or reviewer(s) of the manuscript.
- Editors should strive to meet the needs of readers and authors and to constantly improve the journal.

Duties of Reviewers/Referees

The main responsibilities of reviewers/referees are as follows:

- Reviewers should keep all information regarding papers confidential and treat them as privileged information.
- Reviews should be conducted objectively, with no personal criticism of the author.
- Reviewers assist in the editorial decision process and as such should express their views clearly with supporting arguments.
- Reviewers should complete their reviews within a specified timeframe (maximum thirty-five (35) days). In the event that a reviewer feels it is not possible for him/her to complete the review of the manuscript within a stipulated time, then this information must be communicated to the editor so that the manuscript could be sent to another reviewer.
- Unpublished materials disclosed in a submitted manuscript must not be used in a reviewer's personal research without the written permission of the author. Information contained in an unpublished manuscript will remain confidential and must not be used by the reviewer for personal gain.
- Reviewers should not review manuscripts in which they have conflicts of interest resulting from competitive, collaborative, or other relationships or connections with any of the authors, companies, or institutions connected to the papers.

- Reviewers should identify similar work in published manuscripts that has not been cited by the author. Reviewers should also notify the Editors of significant similarities and/or overlaps between the manuscript and any other published or unpublished material.

Duties of Authors

The main responsibilities of authors are as follows:

- The author(s) should affirm that the material has not been previously published and that they have not transferred elsewhere any rights to the article.
- The author(s) should ensure the originality of the work and that they have properly cited others' work in accordance with the reference format.
- The author(s) should not engage in plagiarism or in self-plagiarism.
- On clinical and experimental humans and animals, which require an ethical committee decision for research in all branches of science;

All kinds of research carried out with qualitative or quantitative approaches that require data collection from the participants by using survey, interview, focus group work, observation, experiment, interview techniques,

Use of humans and animals (including material/data) for experimental or other scientific purposes,

- Clinical studies on humans,
- Studies on animals,
- Retrospective studies in accordance with the law on the protection of personal data, (Ethics committee approval should have been obtained for each individual application, and this approval should be stated and documented in the article.)

Information about the permission (board name, date, and number) should be included in the "Method" section of the article and also on the first/last page.

During manuscript upload, the "Ethics Committee Approval" file should be uploaded to the system in addition to the manuscript file.

In addition, in case reports, it is necessary to include information on the signing of the informed consent/ informed consent form in the manuscript.

- The author(s) should suggest no personal information that might make the identity of the patient recognizable in any form of description, photograph, or pedigree. When photographs of the patient were essential and indispensable as scientific information, the author(s) have received consent in written form and have clearly stated as much.
- The author(s) should provide the editor with the data and details of the work if there are suspicions of data falsification or fabrication. Fraudulent data shall not be tolerated. Any manuscript with suspected fabricated or falsified data will not be accepted. A retraction will be made for any publication which is found to have included fabricated or falsified data.
- The author(s) should clarify everything that may cause a conflict of interests such as work, research expenses, consultant expenses, and intellectual property.
- The author(s) must follow the submission guidelines of the journal.
- The author(s) discover(s) a significant error and/or inaccuracy in the submitted manuscript at any time, then the error and/or inaccuracy must be reported to the editor.
- The author(s) should disclose in their manuscript any financial or other substantive conflicts of interest that might be construed to influence the results or interpretation of their manuscript. All sources of financial support should be disclosed under the heading of "Acknowledgment" or "Contribution".
- The corresponding author should ensure that all appropriate co-authors and no inappropriate co-authors are included in the paper and that all co-authors have seen and approved the final version of the paper and have agreed to its submission for publication. All those who have made

significant contributions should be listed as co-authors. Others who have participated in certain substantive aspects of the research should be acknowledged or listed under the heading of “Author Contributions”.

Cancellations>Returns

Articles/manuscripts may be returned to the authors in order to increase the authenticity and/or reliability and to prevent ethical breaches, and even if articles have been accepted and/or published, they can be withdrawn from publication if necessary. The Editor-in-Chief of the journal has the right to return or withdraw an article/manuscript in the following situations:

- When the manuscript is not within the scope of the journal,
- When the scientific quality and/or content of the manuscript do not meet the standards of the journal and a referee review is not necessary,
- When there is proof of ruling out the findings obtained by the research, (When the article/manuscript is undergoing an assessment or publication process by another journal, congress, conference, etc.,)
- When the article/manuscript was not prepared in compliance with scientific publication ethics,
- When any other plagiarism is detected in the article/manuscript,
- When the authors do not perform the requested corrections within the requested time (maximum twenty-one (21) days),
- When the author does not submit the requested documents/materials/data etc. within the requested time,
- When the requested documents/materials/data etc. submitted by the author are missing for the second time,
- When the study includes outdated data,
- When the authors make changes that are not approved by the editor after the manuscript was submitted,
- When an author is added/removed, the order of the authors is changed, the corresponding author is changed, or the addresses of the authors are changed without the consent of the Editor-in-Chief,
- When a statement is not submitted indicating that approval of the ethics committee permission was obtained for the following (including retrospective studies):
- When human rights or animal rights are violated,

ETHICAL ISSUES

Plagiarism

The use of someone else’s ideas or words without a proper citation is considered plagiarism and will not be tolerated. Even if a citation is given, if quotation marks are not placed around words taken directly from other authors’ work, the author is still guilty of plagiarism. Reuse of the author’s own previously published words, with or without a citation, is regarded as self-plagiarism.

All manuscripts received are submitted to iThenticate®, which compares the content of the manuscript with a database of web pages and academic publications. Manuscripts are judged to be plagiarized or self-plagiarized, based on the iThenticate® report or any other source of information, will be rejected. Corrective actions are proposed when plagiarism and/or self-plagiarism is detected after publication. Editors should analyze the article and decide whether a corrected article or retraction needs to be published.

Open-access theses are considered as published works and they are included in the similarity checks.

iThenticate® report should have a maximum of 11% from a single source, and a maximum of 25% in total.

Conflicts of Interest

Eskişehir Technical University Journal of Science and Technology A - Applied Sciences and Engineering should be informed of any significant conflict of interest of editors, authors, or reviewers to determine whether any action would be appropriate (e.g. an author's statement of conflict of interest for a published work, or disqualifying a referee).

Financial

The authors and reviewers of the article should inform the journal about the financial information that will bring financial gain or loss to any organization from the publication of the article.

*Research funds; funds, consulting fees for a staff member; If you have an interest, such as patent interests, you may have a conflict of interest that needs to be declared.

Other areas of interest

The editor or reviewer may disclose a conflict of interest that, if known, would be embarrassing (for example, an academic affiliation or rivalry, a close relationship or dislike, or a person who may be affected by the publication of the article).

Conflict of interest statement

Please note that a conflict of interest statement is required for all submitted manuscripts. If there is no conflict of interest, please state “There are no conflicts of interest to declare” in your manuscript under the heading “Conflicts of Interest” as the last section before your Acknowledgments.

AUTHOR GUIDELINES

All manuscripts must be submitted electronically.

You will be guided stepwise through the creation and uploading of the various files. There are no page charges. Papers are accepted for publication on the understanding that they have not been published and are not going to be considered for publication elsewhere. Authors should certify that neither the manuscript nor its main contents have already been published or submitted for publication in another journal. We ask a signed copyright to start the evaluation process. After a manuscript has been submitted, it is not possible for authors to be added or removed or for the order of authors to be changed. If authors do so, their submission will be cancelled.

Manuscripts may be rejected without peer review by the editor-in-chief if they do not comply with the instructions to authors or if they are beyond the scope of the journal. After a manuscript has been accepted for publication, i.e. after referee-recommended revisions are complete, the author will not be permitted to make any changes that constitute departures from the manuscript that was accepted by the editor. Before publication, the galley proofs are always sent to the authors for corrections. Mistakes or omissions that occur due to some negligence on our part during final printing will be rectified in an errata section in a later issue.

This does not include those errors left uncorrected by the author in the galley proof. The use of someone else's ideas or words in their original form or slightly changed without a proper citation is considered plagiarism and will not be tolerated. Even if a citation is given, if quotation marks are not placed around words taken directly from another author's work, the author is still guilty of plagiarism. All manuscripts received are submitted to iThenticateR, a plagiarism checking system, which compares the content of the manuscript with a vast database of web pages and academic publications. In the received iThenticateR report; The similarity rate is expected to be below 25%. Articles higher than this rate will be rejected.

Uploading Articles to the Journal

Authors should prepare and upload 2 separate files while uploading articles to the journal. First, the Author names and institution information should be uploaded so that they can be seen, and then (using the additional file options) a separate file should be uploaded with the Author names and institution information completely closed. When uploading their files with closed author names, they will select the "Show to Referee" option, so that the file whose names are closed can be opened to the referees.

Preparation of Manuscript

Style and Format

Manuscripts should be **single column** by giving one-spaced with 2.5-cm margins on all sides of the page, in Times New Roman font (font size 11). Every page of the manuscript, including the title page, references, tables, etc., should be numbered. All copies of the manuscript should also have line numbers starting with 1 on each consecutive page.

Manuscripts must be upload as word document (*.doc, *.docx vb.). **Please avoid uploading texts in *.pdf format.**

Symbols, Units and Abbreviations

Standard abbreviations and units should be used; SI units are recommended. Abbreviations should be defined at first appearance, and their use in the title and abstract should be avoided. Generic names of chemicals should be used. Genus and species names should be typed in italic or, if this is not available, underlined.

Please refer to equations with capitalisation and unabbreviated (e.g., as given in Equation (1)).

Manuscript Content

Articles should be divided into logically ordered and numbered sections. Principal sections should be numbered consecutively with Arabic numerals (1. Introduction, 2. Formulation of problem, etc.) and subsections should be numbered 1.1., 1.2., etc. Do not number the Acknowledgements or References sections. The text of articles should be, if possible, divided into the following sections: Introduction, Materials and Methods (or Experimental), Results, Discussion, and Conclusion.

Title and contact information

The first page should contain the full title in sentence case (e.g., Hybrid feature selection for text classification), the full names (last names fully capitalised) and affiliations (in English) of all authors (Department, Faculty, University, City, Country, E-mail), and the contact e-mail address for the clearly identified corresponding author. The first page should contain the full title, abstract and keywords (both English and Turkish).

Abstract

The abstract should provide clear information about the research and the results obtained, and should not exceed 300 words. The abstract should not contain citations and must be written in Times New Roman font with font size 9.

Keywords

Please provide 3 to 5 keywords which can be used for indexing purposes.

Introduction

The motivation or purpose of your research should appear in the “Introduction”, where you state the questions you sought to answer, and then provide some of the historical basis for those questions.

Methods

Provide sufficient information to allow someone to repeat your work. A clear description of your experimental design, sampling procedures, and statistical procedures is especially important in papers describing field studies, simulations, or experiments. If you list a product (e.g., animal food, analytical device), supply the name and location of the manufacturer. Give the model number for equipment used.

Results

Results should be stated concisely and without interpretation.

Discussion

Focus on the rigorously supported aspects of your study. Carefully differentiate the results of your study from data obtained from other sources. Interpret your results, relate them to the results of previous research, and discuss the implications of your results or interpretations.

Conclusion

This should state clearly the main conclusions of the research and give a clear explanation of their importance and relevance. Summary illustrations may be included.

Acknowledgments

Acknowledgments of people, grants, funds, etc. should be placed in a separate section before the reference list. The names of funding organizations should be written in full.

Conflict of Interest Statement

The authors are obliged to present the conflict of interest statement at the end of the article after the acknowledgments section.

Author Contributions

All authors, author contributions and contribution rates should be clearly stated.

References

Writing Style; **AMA; References Writing format** should be used in the reference writing of our journal. If necessary, at this point, the reference writings of the articles published in our article can be examined.

Citations in the text should be identified by numbers in square brackets. The list of references at the end of the paper should be given in order of their first appearance in the text. All authors should be included in reference lists unless there are 10 or more, in which case only the first 10 should be given, followed by ‘et al.’. Do not use individual sets of square brackets for citation numbers that appear together, e.g., [2,3,5–9], not [2], [3], [5]–[9]. Do not include personal communications, unpublished data, websites, or other unpublished materials as references, although such material may be inserted (in parentheses) in the text. In the case of publications in languages other than English, the published English title should be provided if one exists, with an annotation such as “(article in Turkish with an abstract in English)”. If the publication was not

published with an English title, cite the original title only; do not provide a self-translation. References should be formatted as follows (please note the punctuation and capitalisation):

Journal articles

Journal titles should be abbreviated according to ISI Web of Science abbreviations.

Guyon I, Elisseeff A. An introduction to variable and feature selection. *J Mach Learn Res* 2003; 3: 1157-1182.

Izadpanahi S, Ozcinar C, Anbarjafari G, Demirel H. Resolution enhancement of video sequences by using discrete wavelet transform and illumination compensation. *Turk J Elec Eng & Comp Sci* 2012; 20: 1268-1276.

Books

Haupt RL, Haupt SE. *Practical Genetic Algorithms*. 2nd ed. New York, NY, USA: Wiley, 2004.

Kennedy J, Eberhart R. *Swarm Intelligence*. San Diego, CA, USA: Academic Press, 2001.

Chapters in books

Poore JH, Lin L, Eschbach R, Bauer T. Automated statistical testing for embedded systems. In: Zander J, Schieferdecker I, Mosterman PJ, editors. *Model-Based Testing for Embedded Systems*. Boca Raton, FL, USA: CRC Press, 2012. pp. 111-146.

Conference proceedings

Li RTH, Chung SH. Digital boundary controller for single-phase grid-connected CSI. In: *IEEE 2008 Power Electronics Specialists Conference*; 15–19 June 2008; Rhodes, Greece. New York, NY, USA: IEEE. pp. 4562-4568.

Theses

Boynukalin Z. *Emotion analysis of Turkish texts by using machine learning methods*. MSc, Middle East Technical University, Ankara, Turkey, 2012.

Tables and Figures

All illustrations (photographs, drawings, graphs, etc.), not including tables, must be labelled “Figure.” Figures must be submitted in the manuscript.

All tables and figures must have a caption and/or legend and be numbered (e.g., Table 1, Figure 2), unless there is only one table or figure, in which case it should be labelled “Table” or “Figure” with no numbering. Captions must be written in sentence case (e.g., Macroscopic appearance of the samples.). The font used in the figures should be Times New Roman. If symbols such as \times , μ , η , or ν are used, they should be added using the Symbols menu of Word.

All tables and figures must be numbered consecutively as they are referred to in the text. Please refer to tables and figures with capitalisation and unabbreviated (e.g., “As shown in Figure 2...”, and not “Fig. 2” or “figure 2”).

The resolution of images should not be less than 118 pixels/cm when width is set to 16 cm. Images must be scanned at 1200 dpi resolution and submitted in jpeg or tiff format. Graphs and diagrams must be drawn with a line weight between 0.5 and 1 point. Graphs and diagrams with a line weight of less than 0.5 point or more than 1 point are not accepted. Scanned or photocopied graphs and diagrams are not accepted.

Figures that are charts, diagrams, or drawings must be submitted in a modifiable format, i.e. our graphics personnel should be able to modify them. Therefore, if the program with which the figure is drawn has a “save as” option, it must be saved as *.ai or *.pdf. If the “save as” option does not include these extensions, the figure must be copied and pasted into a blank Microsoft Word document as an editable object. It must not be pasted as an image file (tiff, jpeg, or eps) unless it is a photograph.

Tables and figures, including caption, title, column heads, and footnotes, must not exceed 16 × 20 cm and should be no smaller than 8 cm in width. For all tables, please use Word’s “Create Table” feature, with no tabbed text or tables created with spaces and drawn lines. Please do not duplicate information that is already presented in the figures.

Article Corrections and Uploading to the System

Authors should upload the desired edits for their articles without destroying or changing the Template file of the article, by selecting and specifying the relevant edits as Colored, and also submit the Clean version of the article in 2 separate files (using the Additional file option if necessary). * In case of submitting a corrected article, a separate File in Reply to the Referees must be prepared and the "Reply to the Referees" option in the Add additional file option should be checked and uploaded. If a separate file is not prepared in response to the referees, the Author will definitely be asked to upload the relevant file again and the evaluation will be in the pending phase.

CONTENTS

RESEARCH ARTICLE

SYNTHESIS, CHARACTERIZATION OF CYANIDE COMPLEXES WITH 2-(HYDROXYMETHYL)PYRIDINE BY VIBRATIONAL SPECTROSCOPIC, THERMAL STUDIES AND ELECTRICAL PROPERTIES

E. Sayın, G. S. Kürkçüoğlu216

SYNTHESIS OF POLYMER ELECTROLYTE MEMBRANES BASED ON IONIC LIQUID DOPED SPEEK

Ş. Karadirek, M. Yılmazoğlu230

DETECTION OF RHODAMINE VIA SURFACE ENHANCED RAMAN SPECTROSCOPY UTILISING AG NANOWIRES

K. O. Ay240

A NEW BIO-INSPIRED WING DESIGN WITH 3D ADDITIVE MANUFACTURING SCANNING AND PRINTING METHOD: MJF TECHNOLOGY

N. Aydın250

INVERTED BRAYTON CYCLE ENGINE OPTIMIZATION FOR HYPERSONIC FLIGHT

M. Karabacak, Ö. Turan257

A GIS-SUPPORTED ANALYSIS ON ACCESSIBILITY IN WOMEN-FRIENDLY SOCIETIES: EVALUATION OF WALKING ROUTES AT NIGHT HOURS

E. Tükel, K. M. Çubukçu, S. N. Çabuk, G. Öztürk275

CONJUGATED LINOLEIC ACID AND FATTY ACID ISOMERS IN SELECTED COLD PRESSED OILS: ANALYSIS BY GC/FID TECHNIQUE

F. N. Arslan289

HARNESSING GOLD NANORODS FOR NON-ENZYMATIC GLUCOSE SENSING

Z. C. Canbek Özdil300

THE EFFECT OF GRINDING ON OPTICAL BAND GAP AND URBACH ENERGY OF POLYPYRROLE/GRAPHENE COMPOSITES

M. Okutan309

ON THE MAXIMUM CIRCULAR INVERSES OF MAXIMUM CIRCLES

S. Ekmekçi.....324



RESEARCH ARTICLE

SYNTHESIS, CHARACTERIZATION OF CYANIDE COMPLEXES WITH 2-(HYDROXYMETHYL)PYRIDINE BY VIBRATIONAL SPECTROSCOPIC, THERMAL STUDIES AND ELECTRICAL PROPERTIES

Elvan SAYIN^{1,*} , Güneş Süheyla KÜRKCÜOĞLU² 

¹ Turkish Standards Institution, Eskişehir Certification Directorate, Eskişehir, Turkey

² Eskişehir Osmangazi University, Faculty of Sciences, Department of Physics, TR-26040 Eskişehir, Turkey

ABSTRACT

In this investigation, we present synthesis and characterized of three new heteropolynuclear cyanide complexes with 2-(Hydroxymethyl)pyridine (hmpH) of $[M(H_2O)(hmpH)Ni(CN)_4]_2 \cdot nH_2O$, (M(II) = Fe, Co and Ni); n = 12 for Fe, 2 for Co and Ni). The obtained complexes have been studied by elemental, thermal analysis, FT-IR, and Raman spectroscopic measurement techniques. Considering the alterations in characteristic peaks of cyanide, aqua, and hmpH ligands, general knowledge about the structural features of the complexes was detected from the vibrational spectra. The Ni(II) ion is coordinated by four cyanide-carbon atoms forming a square planar geometry. In addition, thermal analyses and electrical features of the complexes were investigated.

Keywords: Cyanide complex; Tetracyanonickelate(II) complex; 2-(Hydroxymethyl)pyridine complex; FT-IR and Raman spectra; Thermal analyses

1. INTRODUCTION

Since Diesbach discovered Prussian blue in the 18th century, metal cyanide complexes containing cyanometallate building blocks have attracted significant interest in recent years. Due to the role of cyanide ion as a bridging ligand to connect transition metal ions, cyanometallate building blocks, $[M(CN)_x]^{n-}$, were employed to create different dimensional molecular structures in these complexes [1-3]. Short bridging ligands like cyanides, azides and nitrile donors ensure a suitable way of linking transition metals in the solid state [1]. The cyanide ligand is rigid and adopts a linear coordination mode, supplying a presumable structure owing to rational design [1]. Therefore, cyanide ligands use as a ligand in the synthesis of coordination complexes has led to a wide area of research such as conductivity [2, 3], catalysts [4], ion conductors [5], spin crossover [6], porosity [7], sensors [8] and magnetic materials [9, 10].

Cyanide ligand can function as either a monodentate ligand or a bridging ligand resulting from the reactivity of a mononuclear complex with another metal ion via the nitrogen atom, thanks to its ambidentate nature [11]. Through the utilization of this particular attribute, the cyanide ligand has the capacity to generate different polymeric species [12-19]. Building blocks such as $[M(CN)_6]^{3-}$ (M(III) = Fe, Co, Cr or Mn) [20, 21], $[M(CN)_4]^{2-}$ (M(II) = Ni, Pd or Pt) [20-23], $[M(CN)_4]^{2-}$ (M = Zn, Cd or Hg) [24, 25], $[M(CN)_2]^-$ (M = Au or Ag) [26, 27] and auxiliary ligands such as pyridine, imidazole, and their derivatives with coordination bonds comprise the multi-dimensional cyanide complexes. In the design of metal complexes, ligands with cyanide groups and neutral molecules can be chosen as useful building blocks. In literature, ligands containing nitrogen, oxygen and sulfur atoms have been widely used to form cyanide complexes [28-30]. The architectures and topologies of metal-cyanide systems are

*Corresponding Author: elvansayin@hotmail.com

Received: 05.01.2023 Published: 27.12.2023

strongly affected by the nature of the auxiliary ligand (density, volume, rigidity, etc.). As an auxiliary ligand, 2-(hydroxymethyl)pyridine in this work functions as a bidentate or chelate ligand via its -N and -O donor sites which is rare in the literature. Particularly important, because of their spectroscopic and electrochemical properties, are the discrete heteropolynuclear cyanide-bridged complexes. The heteropolynuclear cyanide complexes with 2-(hydroxymethyl)pyridine as chelate ligand have been limited [31, 32]. Therefore, we preferred the 2-(hydroxymethyl)pyridine as chelate ligand in this study.

In our previous studies, we have used hmpH for preparation of $[\text{Cu}(\text{hmp})_2][\text{Cu}(\text{hmpH})_2\text{Ni}(\mu\text{-CN})_2(\text{CN})_2]_2 \cdot 4\text{H}_2\text{O}$, $[\text{Zn}_3(\text{hmp})_2(\text{hmpH})_4\text{Ni}_2(\mu\text{-N})_6(\text{CN})_2] \cdot 2\text{H}_2\text{O}$, $[\text{Cd}_2(\text{H}_2\text{O})_2(\text{hmpH})_2\text{Ni}(\mu\text{-CN})_4\text{Ni}(\mu\text{-CN})_2(\text{CN})_2]$, $[\text{Cu}(\text{hmpH})_2\text{Pd}(\mu\text{-CN})_2(\text{CN})_2]_n$ and $[\text{Cu}(\text{hmpH})_2\text{Pt}(\mu\text{-CN})_2(\text{CN})_2]_n$ and the structural studies have been shown to act as a chelate ligand of hmpH [31, 32]. As part of our ongoing research, we report the syntheses, structural and physical characterizations of three cyanide-bridged heteronuclear complexes, $[\text{Fe}(\text{H}_2\text{O})(\text{hmpH})\text{Ni}(\text{CN})_4]_2 \cdot 12\text{H}_2\text{O}$, $[\text{Co}(\text{H}_2\text{O})(\text{hmpH})\text{Ni}(\text{CN})_4]_2 \cdot 2\text{H}_2\text{O}$ and $[\text{Ni}(\text{H}_2\text{O})(\text{hmpH})\text{Ni}(\text{CN})_4]_2 \cdot 2\text{H}_2\text{O}$ (where hmpH = 2-(Hydroxymethyl)pyridine, abbreviated hereafter as **M-Ni-hmpH**).

2. EXPERIMENTAL

2.1. Materials and Instrumentation

The study utilized essential chemical substances including iron(II) chloride tetrahydrate ($\text{FeCl}_2 \cdot 4\text{H}_2\text{O}$, 99%), cobalt(II) chloride (CoCl_2 , 99%), nickel(II) chloride hexahydrate ($\text{NiCl}_2 \cdot 6\text{H}_2\text{O}$, 97%), potassium cyanide (KCN, 96%) and 2-(Hydroxymethyl)pyridine ($\text{C}_6\text{H}_7\text{NO}$, 98%). These chemicals were of reagent grade and were employed without undergoing additional purification.

Elemental analysis of the percentage of hydrogen, carbon and nitrogen atoms was performed on a LECO, CHNS-932 analyzer. The FT-IR and Raman spectra of the complexes were recorded at room temperature as pure solids by using a Perkin Elmer 100 FT-IR spectrometer with ATR (Attenuated Total Reflection) and Bruker Senterra Dispersive Raman instrument using 785 nm laser excitation in the range of $4000\text{-}250\text{ cm}^{-1}$, respectively. Thermal analyzes of the complexes were recorded simultaneously in a static air atmosphere at a heating rate of 10 K min^{-1} in the temperature range of $30\text{-}1000\text{ }^\circ\text{C}$ using platinum crucibles on a Perkin Elmer Diamond TG/DTA thermal analyzer. The electrical conductivity values were determined using the four-probe technique at room temperature. This was done by applying a programmable direct current (dc) using the Keithley 2601 A System Sourcemeter to the sample pellets. The pellets were specifically designed to be 1 mm thick and 1.0 cm in diameter, and were subjected to a hydraulic pressure of 10 tons.

2.2 Preparation of the Complexes

The synthesis of the complexes was prepared in a mention similar to that described method in cited literature [33], but hepH ligand was replaced by hmpH ligand (0.218 g; 2 mmol). As a mention [33] reference, the synthesis of the complexes in three stages; in the first stage $\text{K}_2[\text{Ni}(\text{CN})_4] \cdot \text{H}_2\text{O}$, in the second stage $\text{M}[\text{Ni}(\text{CN})_4] \cdot \text{H}_2\text{O}$ [$\text{M}(\text{II}) = \text{Fe, Co or Ni}$] and in the final stage $[\text{M}(\text{H}_2\text{O})(\text{hmpH})\text{Ni}(\text{CN})_4]_2 \cdot n\text{H}_2\text{O}$ [$\text{M}(\text{II}) = \text{Fe, Co and Ni; hmpH} = 2\text{-}(\text{Hydroxymethyl})\text{pyridine}$]. The powder forms of the complexes were all produced.

3. RESULTS AND DISCUSSION

3.1. Elemental Analyses

In Table 1, the analytical data, elemental analyses (C, H and N), molar ratio and color of the **M-Ni-hmpH** ($\text{M}(\text{II}) = \text{Fe, Co or Ni}$) complexes are detailed. There is agreement between the calculated and

measured elemental analysis values. Based on the obtained data, the prepared complexes are formulated and composition has been determined by elemental analyses.

Table 1. Results of elemental analysis of the complexes.

Complex	Molecular formula	M _{wt.} (g/mol)	Elemental analyses						Color
			C%		H%		N%		
			Calc.	Found	Calc.	Found	Calc.	Found	
[Fe(H ₂ O)(hmpH)Ni(CN) ₄] ₂ ·12H ₂ O	C ₂₀ H ₄₂ N ₁₀ O ₁₆ Ni ₂ Fe ₂	907.68	26.46	25.65	4.66	4.26	15.43	15.08	Brown
[Co(H ₂ O)(hmpH)Ni(CN) ₄] ₂ ·2H ₂ O	C ₂₀ H ₂₂ N ₁₀ O ₆ Ni ₂ Co ₂	733.71	32.74	34.87	3.02	3.63	19.09	18.35	Pink
[Ni(H ₂ O)(hmpH)Ni(CN) ₄] ₂ ·2H ₂ O	C ₂₀ H ₂₂ N ₁₀ O ₆ Ni ₄	733.23	32.76	34.57	3.02	3.31	19.10	18.77	Pale Blue

3.2 Vibrational Spectra of the Complexes

The FT-IR and Raman spectra of the ligands (aqua and hmpH) and obtained complexes are presented in Figures 1 and 2. The characteristic peaks hmpH observed with shifts their positions in the spectra of the complexes studied are listed in Table 2, together with free hmpH wavenumbers for comparison [34]. The fact that the vibrational spectral properties of the complexes are very close to each other indicates that they have similar structures [31, 32].

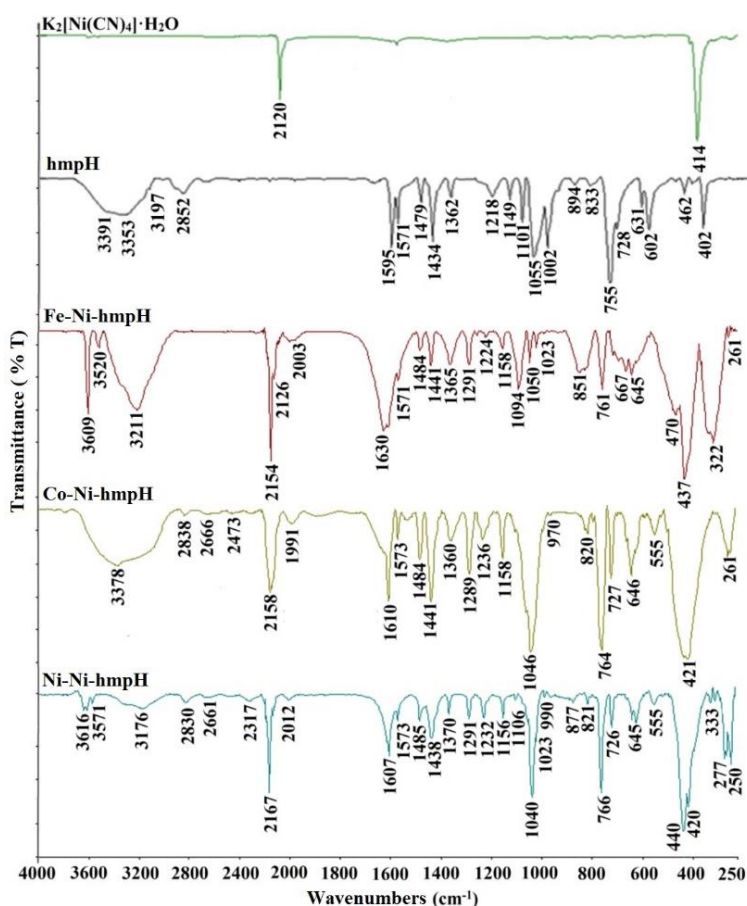


Figure 1. The FT-IR spectra of $K_2[Ni(CN)_4] \cdot H_2O$, hmpH and the complexes

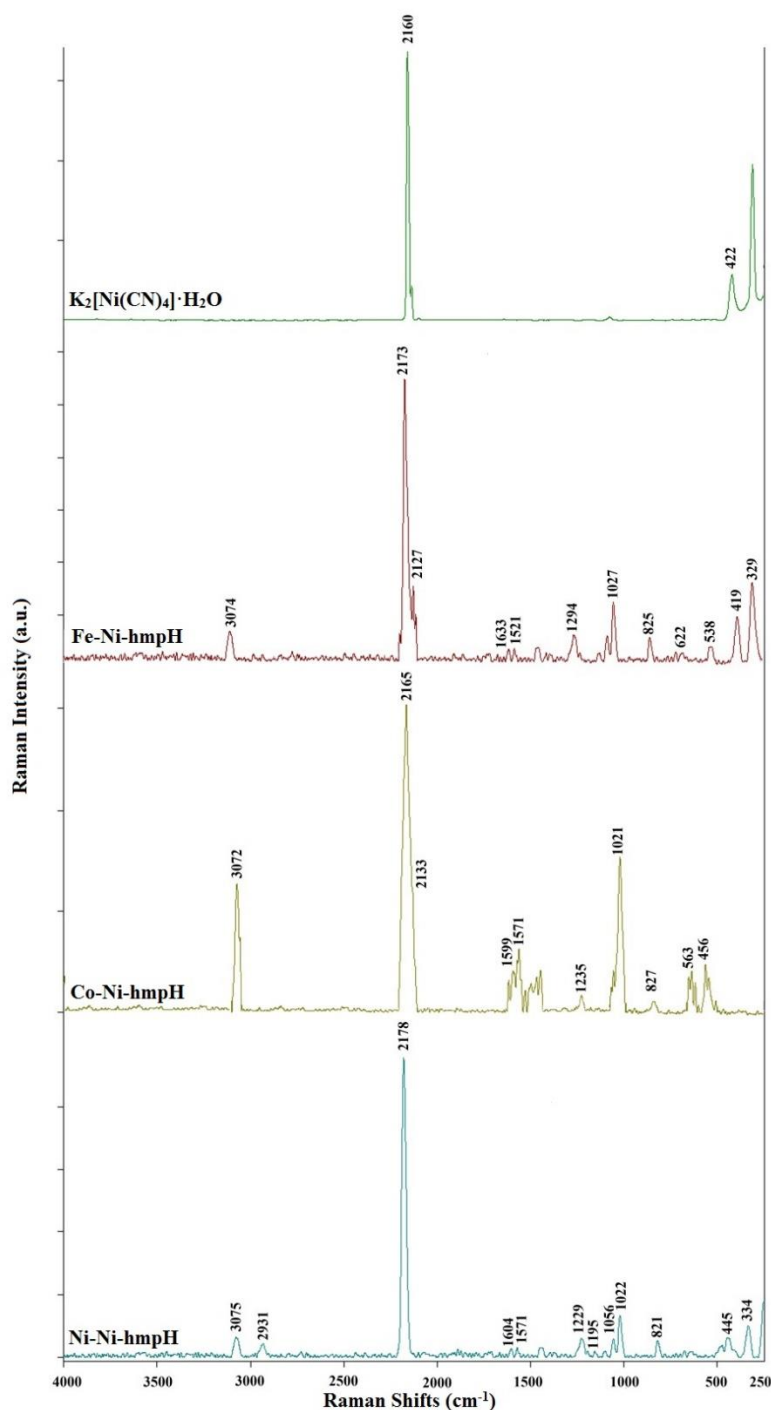


Figure 2. Raman spectra of $K_2[Ni(CN)_4] \cdot H_2O$ and the complexes.

3.2.1. Aqua vibrations

The aqua molecule has vibrations as asymmetrical OH stretching bands, symmetrical OH stretching bands, and OH bending bands. The $\nu(OH)$ stretching vibration bands of the coordinated aqua molecules, both symmetric and asymmetric, are detected in the region 3700 cm^{-1} - 3300 cm^{-1} [35]. Furthermore, the entity of aqua molecules shows up as two shoulders at 1690 cm^{-1} and 1620 cm^{-1} owing to $\delta(OH)$ deformation vibrations. In our former study, the presence of water molecules in the structures of the complexes was determined by vibration analysis and supported by X-ray diffraction of the complexes

such as $[\text{Cd}(\text{H}_2\text{O})(2\text{mpz})\text{Ni}(\mu\text{-CN})_4]_n$ [36]. The $\nu(\text{OH})$ stretching vibrations of the aqua molecules have been experimentally detected at 3609 and 3520 cm^{-1} in **Fe-Ni-hmpH**, 3784 cm^{-1} and 3690 cm^{-1} in **Co-Ni-hmpH** and 3616 and 3571 cm^{-1} in **Ni-Ni-hmpH** (see Figure 3). The $\nu(\text{OH})$ deformation vibration in complexes is found to be 1630 cm^{-1} in **Fe-Ni-hmpH**, 1641 cm^{-1} in **Co-Ni-hmpH** and 1651 cm^{-1} in **Ni-Ni-hmpH**.

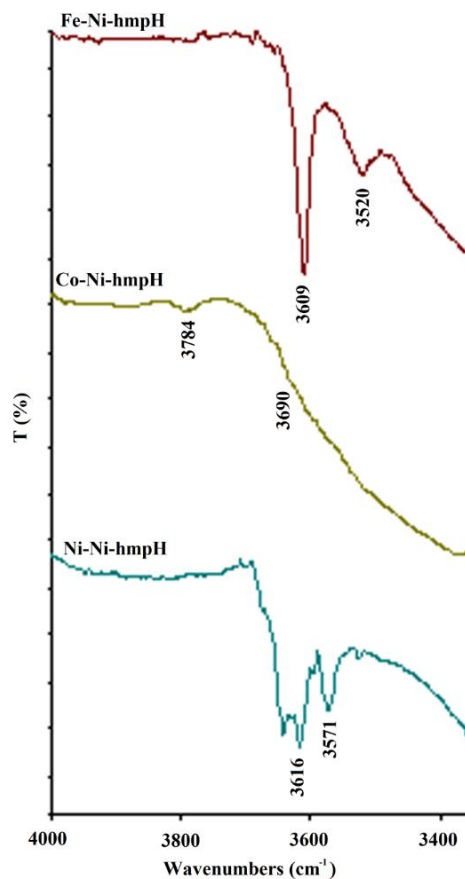


Figure 3. FT-IR spectra of water molecules in obtained complexes.

3.2.2. 2-(Hydroxymethyl)pyridine vibrations

In the literature, there are various studies conducted with hmpH by many researchers. The $\nu(\text{OH})$ vibrations of hmpH are shown the strong and broad absorption bands in the range $3500 - 3200$ cm^{-1} [37]. The $\nu(\text{OH})$ stretching band is detected at frequency of 3211 cm^{-1} for **Fe-Ni-hmpH**, 3378 cm^{-1} for **Co-Ni-hmpH**, 3374 cm^{-1} for **Ni-Ni-hmpH** in the FT-IR spectra but this band is absent from the Raman spectrum.

As stated in the literature, most aromatic complexes in the region $3100 - 3000$ cm^{-1} in FT-IR spectra have their own bands [38-42]. $\nu(\text{CH})$ stretching vibrations in the complexes are detected in the region of $3136 - 3010$ cm^{-1} in FT-IR spectra and $3075 - 3031$ cm^{-1} in Raman spectra. The asymmetric $\nu(\text{CH}_2)$ stretching vibration are detected at 2913 cm^{-1} in **Fe-Ni-hmpH**, 2915 cm^{-1} in **Co-Ni-hmpH** and 2917 cm^{-1} in **Ni-Ni-hmpH**. In the complexes; the symmetric $\nu(\text{CH}_2)$ stretching vibrations are detected at 2838 cm^{-1} in **Fe-Ni-hmpH** and in **Co-Ni-hmpH**, 2830 cm^{-1} in **Ni-Ni-hmpH** in the FT-IR spectra and are determined at 2848 cm^{-1} in **Fe-Ni-hmpH** and at 2825 cm^{-1} in **Co-Ni-hmpH**, 2839 cm^{-1} in **Ni-Ni-hmpH** in the Raman spectra. The $\gamma(\text{CH})$ out of plane deformation is detected in the region of $1000 - 700$ cm^{-1} [43]. In the complexes; these vibrations are found at 992 and 822 cm^{-1} in **Fe-Ni-hmpH**, at 970 and 820 cm^{-1} in **Co-Ni-hmpH** and 990 , 908 and 818 cm^{-1} in **Ni-Ni-hmpH** in the FT-IR spectra.

Table 2. The FT-IR and Raman wavenumbers of the hmpH in complexes (cm⁻¹).

Assignments [34]	hmpH	hmpH [33]		Fe-Ni-hmpH		Co-Ni-hmpH		Ni-Ni-hmpH	
		Experimental	Calculated	FT-IR	Raman	FT-IR	Raman	FT-IR	Raman
v(OH)	3391 s	3400 s	3398	3211 m	3286 m	3378 m	-	3374 m	-
v(CH)	3101 vw	3103 s	3102	3132 sh	-	3100 w	-	3136 vw	-
v(CH)	3066 w	3075 s	3079	3067 sh	3075 m	3070 m	3072 vw	3072 sh	3075 m
v(CH)	3050 sh	-	3059	-	3031 w	-	3042 vw	-	-
v(CH)	3014 vw	3022 m	3037	3012 sh	-	3015 w	-	3010 sh	-
v _a (CH ₂)	2903 vw	2914 m	2919	2913 w	2900 w	2915 w	2933 vw	2917 w	2935 w
v _s (CH ₂)	2853 m	2856 s	2890	2838 w	2848 m	2838 w	2825 m	2830 w	2839 vw
v(C=C)	1595 s	1595 vs	1599	1610 s	1631 m	1610 s	1621 w	1607 s	1628 vw
v(C=C)	1570 m	1575 vs	1582	1571 m	1570 w	1573 m	1571 m	1573 s	1572 m
v(C=N)	1477 m	1482 s	1478	1484 m	-	1488 m	-	1485 m	-
v(CC)	1454 sh	-	1467	1441 m	1435 w	1441 m	1457 m	1439 m	1450 s
δ(CH ₂)	1434 s	1437 vs	1436	-	-	-	1445 s	1438 m	1439 m
v(CC)	1360 m	1386 m	1407	1365 m	1395 vw	1360 m	1403 vw	1370 m	1397 vw
v(CC)	1320 vw	1329 m	1300	-	1335 w	-	1316 vw	-	1320 w
v(CN)	1280 vw	1268 w	1277	1291 m	1294 vw	1289 m	1286 w	1291 m	1291 m
β(OH)	1217 m	1228 m	1229	1224 m	1261 vw	1236 m	1235 m	1232 w	1228 w
β(CH)	-	-	1224	-	-	-	-	-	-
β(CH)	1148 m	1160 m	1164	1158 m	1189 vw	1158 m	1163 vw	1156 m	1157 m
β(CH)	1100 m	-	1147	-	1126 w	1107 w	1123 vw	1106 vw	1128 vw
v(CO)	1057 s	1110 s	1096	1094 m	1096 m	1066 s	1061 w	1058 m	1056 m
β(CH)	1052 sh	1068 vs	1048	1050 vs	1027 m	1046 vs	1023 m	1040 s	1022 m
γ(CH)	-	-	1042	-	-	-	-	-	-
ω(CH ₂)	1002 m	1019 vs	1011	1023 w	-	1023 m	-	1023 m	-
γ(CH)	993 m	1007 s	992	992 w	-	970 m	981 vw	990 w	987 w
ρ(CH ₂)	960 v	974 w	991	933 vw	966 vw	935 vw	977 vw	947 vw	968 vw
τ(CH ₂)	957 v	-	955	921 vw	919 vw	927 vw	939 w	932 vw	940 w
γ(CH)	909 vw	910 w	891	-	889 vw	-	-	908 vw	905 vw
γ(CH)	893 w	818 w	797	822 m	846 vw	820 w	827 m	818 m	820 m
γ(OH)	755 vs	777 vw	753	761 s	773 vw	764 vs	768 m	766 s	760 w
β(CCC)	727 m	746 m	729	720 m	737 vw	727 s	739 w	726 m	736 w
β(CCC)	632 m	622 m	627	645 m	653 vw	646 m	659 m	645 m	646 w
β(CC)	570 sh	-	582	-	560 vw	-	563 m	555 w	567 m
β(CNC)	464 m	469 w	461	470 w	476 vw	458 sh	475 w	461 w	480 w
β(CO)	422 w	426 m	431	437 w	429 vw	439 s	445 w	440 s	442 m
γ(CCC)	402 s	389 w	406	338 m	340 vw	-	334 m	333 k	336 m
γ(CCC)	281 vw	228 m	222	261 vw	-	261 w	287 vw	250 m	252 m

Abbreviations used: v-stretching; β - in-plane bending; δ - deformation; ρ - rocking; γ - out of plane bending; ω - wagging and τ - twisting/torsion; s, strong; m, medium; w, weak; sh, shoulder; v, very.

It is very difficult to define C=N, C-N vibrations as it is possible to mix more than one band in this region [34]. The v(CC) stretching bands of the pyridine ring in the free hmpH yields a vibration peak at 1595, 1570, 1360 and 1320 cm⁻¹ wavenumbers in its FT-IR and Raman spectra, respectively, while this vibration peak occurs at 1630, 1571 and 1365 cm⁻¹ in **Fe-Ni-hmpH**, at 1610, 1573 and 1360 cm⁻¹ in **Co-Ni-hmpH** and 1607, 1573 and 1370 cm⁻¹ in **Ni-Ni-hmpH** in the FT-IR spectra and at 1631, 1570 and 1395 cm⁻¹ in **Fe-Ni-hmpH**, at 1621, 1571 and 1403 cm⁻¹ in **Co-Ni-hmpH** and are shown 1628, 1572 and 1397 cm⁻¹ in **Ni-Ni-hmpH** in the Raman spectra. The v(C=N) stretching skeletal bands are observed in the range 1627 - 1566 cm⁻¹ [44-47]. These bands shown at 1484 cm⁻¹ in **Fe-Ni-hmpH**, 1484 cm⁻¹ in **Co-Ni-hmpH** and 1485 cm⁻¹ in **Ni-Ni-hmpH** are assigned to the v(C=N) stretching vibration in the FT-IR spectra of the complexes. When the nitrogen atom of the pyridine aromatic ring participates in complex formation, specific vibration bands shows higher values due to the coupling with M-N_{hmpH} bond vibrations [48-50]. v(CO) stretching vibration bands are observed at 1057 cm⁻¹ for free hmpH in the FT-IR spectrum. This band is observed at 1094 cm⁻¹ in **Fe-Ni-hmpH**, 1066 cm⁻¹ in **Co-Ni-hmpH** and 1058 cm⁻¹ in **Ni-Ni-hmpH** in the FT-IR spectra of the complexes. Additionally, v(CO) stretching vibration band are observed at 1096 cm⁻¹ in **Fe-Ni-hmpH**, 1061 cm⁻¹ in **Co-Ni-hmpH** and 1056 cm⁻¹ in **Ni-Ni-hmpH** in the Raman spectra. This vibration bands in the vibrational spectra of the complexes support each other. The other vibration wavenumbers of hmpH and the complexes are observed in Table 2.

3.2.3 [Ni(CN)₄]²⁻ anion vibrations

Because of its negative charge, the CN⁻ ion may function as both an electron donor (by giving up an electron to the metal) and an electron acceptor (by taking one from the metal). The σ -donation ability also increases when electrons are removed from the weakly antibonding molecular orbital, which results in an increase in the value of $\nu(\text{CN})$. On the other hand, its π -accepting properties decrease when electrons are added to the π bonding orbital, which results in a decrease in the value of $\nu(\text{CN})$. The $\nu(\text{CN})$ stretching vibration bands are considered to be one of the principal vibrational characteristics exhibited by cyanide complexes. $\nu(\text{CN})$ stretching vibrations are dependent to the surroundings of the cyanide ligands. Strong and distinct absorption bands that can be clearly identified in the region of 2200 - 2000 cm^{-1} are defined by the $\nu(\text{CN})$ stretching vibrations originating from the cyanide groups [11]. Due to a reduction in the π -acceptance of the CN⁻ ligand, these bands shift to higher frequencies between 2100 and 2200 cm^{-1} during oxidation of the metal center. Since the electronegativity of Ni(II) is less than that of Pd(II) and Pt(II), the σ -donation will be the least, and it is anticipated that the $\nu(\text{CN})$ will be the lowest [11].

Table 3. Vibrational wavenumbers of the polymeric sheet and metal-ligand vibrations in the complexes (cm^{-1}).

Assignments	K ₂ [Ni(CN) ₄]·H ₂ O [50]	Fe-Ni-hmpH	Co-Ni-hmpH	Ni-Ni-hmpH
A _{1g} , $\nu(\text{C}\equiv\text{N})$	(2160) vs	(2173) vs	(2165) vs	(2178) vs
B _{1g} , $\nu(\text{C}\equiv\text{N})$	(2137) m	(2127) m	(2133) m	-
E _u , $\nu(\text{C}\equiv\text{N})$	2122 vs	2154 vs, 2126 m	2158 vs, 2139 s	2167 vs, 2136 m
$\nu(^{13}\text{CN})$	2084 w	2003 w	2091 w	2012 vw
E _u , $\nu(\text{Ni}-\text{C})$	540 w	558 vw	555 w	555 w
A _{2u} , $\pi(\text{Ni}-\text{CN})$	443 w	458 w	437 m	440 m
E _u , $\delta(\text{Ni}-\text{CN})$	417 s	437 vs	421vw	420 s

Abbreviations used; s strong, m medium, w weak, sh shoulder, v very. The symbols ν , δ and π refer to valence, in-plane and out-of-plane vibrations, respectively.

Raman bands are given in parentheses.

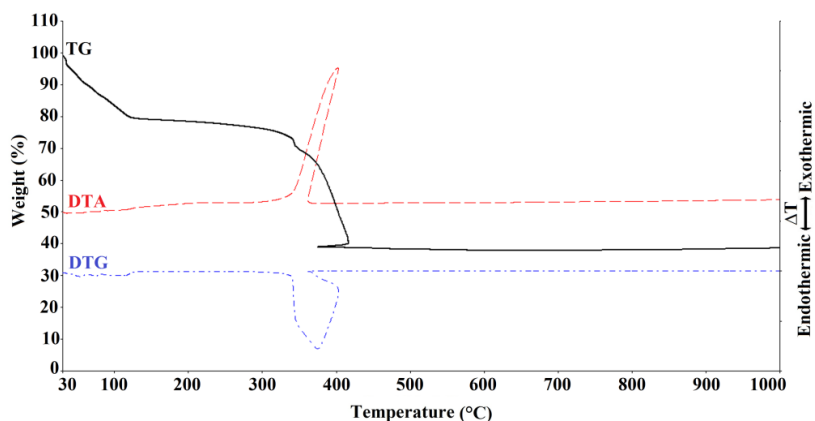
The vibrational wavenumbers for [Ni(CN)₄]²⁻ group in K₂[Ni(CN)₄]·H₂O and in complexes **Fe-Ni-hmpH**, **Co-Ni-hmpH** and **Ni-Ni-hmpH** are presented in Table 3. Based on the work of Mc Cullough et al., who provided vibrational data for the [Ni(CN)₄]²⁻ in Na₂[Ni(CN)₄], the bands of the [Ni(CN)₄]²⁻ in the complexes were assigned [51]. Because the tetracyanometallate(II) anion in this salt was not coordinated to the Na cation, it is possible to regard it as an isolated unit with D_{4h} symmetry. Because of this, it may be used as a reference to remark on vibrational shifts that occur when M-NC bonding occurs [52, 53].

The constitution of a cyanide bridge in the complex can be determined by the $\nu(\text{C}\equiv\text{N})$ band shift in the FT-IR spectrum [19, 54-57]. The $\nu(\text{C}\equiv\text{N})$ absorption band recorded at the highest wavenumber in the complexes can be assigned to the vibration of the structurally identical bridged cyanide group. Mononuclear compound K₂[Ni(CN)₄]·H₂O exhibited a band at 2122 cm^{-1} which can be assigned to the $\nu(\text{CN})$ stretching band, while complexes **Fe-Ni-hmpH**, **Co-Ni-hmpH** and **Ni-Ni-hmpH** exhibited strong absorptions at 2154 and 2126 cm^{-1} ; 2158 and 2139 cm^{-1} and 2167 and 2136 cm^{-1} in the FT-IR spectra, respectively. This stretching band of K₂[Ni(CN)₄]·H₂O complex shows spectra between 2160 cm^{-1} and 2137 cm^{-1} in the Raman spectra. The A_{1g} and B_{1g} cyanide stretching modes in the Raman spectra of the complexes are shown in spectra 2173 and 2127 cm^{-1} for **Fe-Ni-hmpH**, 2165 and 2133 cm^{-1} for **Co-Ni-hmpH** and 2178 cm^{-1} for **Ni-Ni-hmpH**.

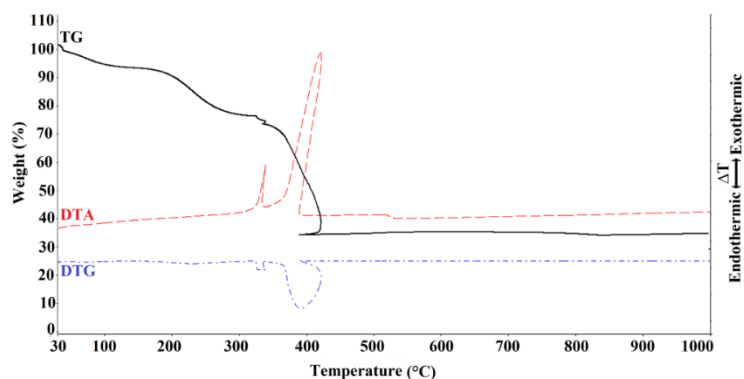
On the other hand, the $\nu(\text{Ni}-\text{CN})$ stretching and $\delta(\text{Ni}-\text{CN})$ in-plane bending vibration bands of K₂[Ni(CN)₄]·H₂O in the low frequency region of the FT-IR spectra is found as 556 cm^{-1} and 441 cm^{-1} , respectively [58]. These bands observed at 558 cm^{-1} and 417 cm^{-1} in **Fe-Ni-hmpH**, 555 cm^{-1} and 437 cm^{-1} in **Co-Ni-hmpH**, 555 cm^{-1} and 440 cm^{-1} in **Ni-Ni-hmpH** in the FT-IR spectra of the complexes, respectively.

3.3 Thermal Behaviors of the Complexes

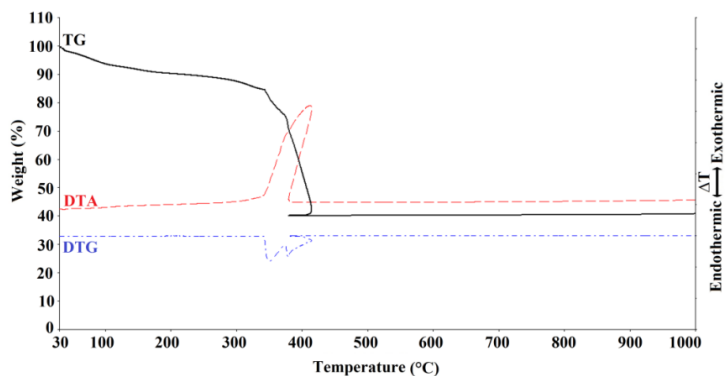
The thermal behaviors of complexes are performed by TG, DTA and TGA methods in the temperature range of 30 - 1000 °C. The TG, DTA and TGA curves are present in Figure 4. The thermal behaviors of the **M-Ni-hmpH** (M(II) = Fe, Co or Ni) complexes are similar and decomposition takes place in three stages.



(a)



(b)



(c)

Figure 4. The TG, DTG and DTA curves of **Fe-Ni-hmpH** (a), **Co-Ni-hmpH** (b) and **Ni-Ni-hmpH** (c)

Firstly, aqua ligands are cleaved from the structure in the temperature range of 31-37 °C for **Fe-Ni-hmpH**, 31-140 °C for **Co-Ni-hmpH** and 34-128°C for **Ni-Ni-hmpH** [found (calcd.): 2.91% (2.77%) in **Fe-Ni-hmpH**, 8.53% (9.82%) in **Co-Ni-hmpH** and 7.24% (9.82%) in **Ni-Ni-hmpH**]. The second stages of the complexes lose hmpH ligands in the temperature range of 36-340 °C for **Fe-Ni-hmpH**, 140-384 °C for **Co-Ni-hmpH** and 128-356°C for **Ni-Ni-hmpH** [found (calcd.): 26.83% (24.08%) in **Fe-Ni-hmpH**, 30.26% (29.74%) in **Co-Ni-hmpH** and 12.47% (14.88%) in **Ni-Ni-hmpH**]. The following stage for the complexes is related with the exothermic removal of -CN groups in the temperature range of 340-410 °C [DTA_{max} = 402 °C; found: 22.97%, calcd.: 24.76% for **Fe-Ni-hmpH**], 384-846 °C [DTA_{max} = 421 °C; found: 27.91%, calcd.: 228.36% for **Co-Ni-hmpH**] and -CN groups and one hmpH at 356-418 °C [DTA_{max} = 413°C; found: 40.95%, calcd.: 43.27% for **Ni-Ni-hmpH**]. The final degradation products are identified as MO and NiO (M = Fe, Co and Ni, found: 34.60%, calcd.: 32.34% in **Fe-Ni-hmpH**, found: 40.78 %, calcd.: 38.96% in **Co-Ni-hmpH** and found: 40.02%, calcd.: 40.74% in **Ni-Ni-hmpH**).

3.4 Electrical Conductivity

The electrical conductivity values of the polymeric complexes were measured with four probe techniques. Sample pellets obtained from the complexes were designed with a thickness of 1 mm and a diameter of 1.0 cm under 10 tons of hydraulic pressure. The electrical conductivity is achieved owing to intra-molecular and inter-molecular interactions. The similar electrical conductivity measurements were observed for cyanide complexes [33, 59]. Experimental electrical conductivities values of the complexes are $2.94 \times 10^{-8} \Omega^{-1} \text{cm}^{-1}$ for **Fe-Ni-hmpH**, $8 \times 10^{-8} \Omega^{-1} \text{cm}^{-1}$ for **Co-Ni-hmpH** and at $7.0 \times 10^{-8} \Omega^{-1} \text{cm}^{-1}$ for **Ni-Ni-hmpH**. As can be seen from here, the complexes at room temperature show a weak semiconductive behavior.

4. CONCLUSIONS

In our study, a new series of three tetracyanonickelate(II) complexes have been synthesized by using hmpH ligand and characterized by vibration spectroscopic techniques (FT-IR and Raman), elemental analysis, thermal characterization and electrical conductivity. The Ni(II) ion exhibit a square planar coordination geometry by four carbon atoms from the cyanide ligands. Infrared and Raman spectra show the presence of vibrational bands of functional groups of hmpH ligand and $[\text{Ni}(\text{CN})_4]^{2-}$ anion. In addition, the FT-IR spectra of the complexes indicated the entity of terminal and bridged cyanide ligands in the complexes. Thermal analysis demonstrates that all the complexes have similar nature and decomposed in three steps resulting in MO and NiO as the eventual product of the thermal decomposition process. Also, elemental, spectroscopic, and thermal data support the identity in structural features of the complexes. Solid-state electrical conductivity of the complexes shows their semiconducting behavior.

ACKNOWLEDGMENT

This paper is dedicated to Prof. Dr. Ziya KANTARCI, who died in January, 2012.

CONFLICT OF INTEREST

The authors stated that there are no conflicts of interest regarding the publication of this article.

AUTHORSHIP CONTRIBUTIONS

Elvan Sayın: Writing – review & editing, Investigation. **Güneş Süheyla Kürkçüoğlu:** Supervision, Data curation, Methodology.

REFERENCES

- [1] Batten SR, Neville SM, Turner DR. Coordination polymers: design, analysis and application. Royal Society of Chemistry, 2009.
- [2] Tadokoro M, Yasuzukara S, Nakamura M, Shinoda T, Tatenuma T, Mitsumi M, Ozawa Y, Toriumi K, Yoshino H, Shiomi D, Sato K, Takui T, Mori T, Murata K. A High Conductivity Crystal Containing a Copper(I) Coordination Polymer Bridged by the Organic Acceptor TANC. *Angew Chem* 2006; 118: 5268-5271.
- [3] Gapud AA, Weber AP, Alexander JA, Pham L, Khan A, Leatherbury RI, Reyes AP, Lumata LL, Kuhns PL, Valente EJ, Sykora RE. New quasi-one-dimensional tetracyanidoplatinate, Cs₄[Pt(CN)₄](CF₃SO₃)₂: Synthesis, structure, and physical characterization. *J Phys Chem Solids* 2014; 75: 447-452.
- [4] Janiak C. Engineering coordination polymers towards applications. *Dalton Trans* 2003; 14: 2781-2804.
- [5] Di Noto V, Vittadello M, Greenbaum SG, Soares S, Kano K, Furukawa T. A new class of lithium hybrid gel electrolyte systems. *J Phys Chem B* 2004; 108: 18832-18844.
- [6] Real JA, Gaspar AB, Munoz MC. Thermal, pressure and light switchable spin-crossover materials. *Dalton Trans* 2005; 12: 2062-2079.
- [7] Ohtani R, Yoneda K, Furukawa S, Horike N, Kitagawa S, Gaspar AB, Munoz MC, Real JA, Ohba M. Precise control and consecutive modulation of spin transition temperature using chemical migration in porous coordination polymers. *J Am Chem Soc* 2011; 133: 8600-8605.
- [8] Wu CD, Lin W. Highly Porous, Homochiral Metal-Organic Frameworks: Solvent Exchange Induced Single Crystal to Single Crystal Transformations. *Angew Chem Int Ed* 2005; 44: 1958-1961.
- [9] Gu, JZ, Kou HZ, Jiang L, Lu TB, Tan MY. Synthesis, structures and magnetic properties of pentanuclear and trinuclear heterometallic complexes with bended and linear cyano-bridges (tren= tris(2-aminoethyl)amine). *Inorg Chim Acta* 2006; 359: 2015-2022.
- [10] Tanase S, Andruh M, Stanica N, Mathoniere C, Rombaut G, Golhen S, Ouahab L. A novel cyano-bridged pentanuclear complex: [{Mn₃(MAC)₃(H₂O)₂}{Fe(CN)₆}₂]·6H₂O·2CH₃OH-synthesis, crystal structure and magnetic properties (MAC= pentaaza macrocyclic ligand). *Polyhedron* 2003; 22: 1315-1320.
- [11] Nakamoto K. Infrared and Raman spectra of inorganic and coordination compounds. Part B., Applications in coordination, organometallic, and bioinorganic chemistry. John Wiley, 2009.
- [12] Şenocak A, Karadağ A, Soylu MS, Andaç Ö. Two novel cyanido-bridged polymeric complexes with suspension bridge type connections and a series of related complex salts: crystallographic and thermal characterizations. *New J Chem* 2015; 39: 3675-3686.
- [13] Lescouëzec R, Lloret F, Julve M, Vaissermann J, Verdaguer M. [Fe(bipy)(CN)₄]⁻ as a Versatile Building Block for the Design of Heterometallic Systems: Synthesis, Crystal Structure, and Magnetic Properties of PPh₄[Fe^{III}(bipy)(CN)₄]·H₂O, [Fe^{III}(bipy)(CN)₄]₂M^{II}(H₂O)₄·4H₂O, and

- $[\{\text{Fe}^{\text{III}}(\text{bipy})(\text{CN})_4\}_2\text{Zn}^{\text{II}}]\cdot 2\text{H}_2\text{O}$ [bipy= 2, 2'-Bipyridine; M= Mn and Zn]. *Inorg chem* 2002; 41: 818-826.
- [14] Černák J, Lipkowski J, Potočňák I, Hudák A. Bis-(bis-(1,3-diaminopropane)-copper(II) Tetracyanonickellate(II)) Tetrahydrate: Preparation, Characterization, and Crystal Structure of a Novel Molecular Tetracyanonickellate. *Monatsh Chem* 2001; 132: 193-202.
- [15] Cernak J, Abboud KA. $\text{Ni}(\text{bipy})_2\text{Ni}(\text{CN})_4$, a new type of one-dimensional square tetracyano complex. *Acta Crystallogr C* 2000; 56: 783-785.
- [16] Yakuphanoglu F, Karadağ A, Şekerci M. Investigation of the thermal properties of $[\text{Cd}(\text{hydet-en})_2\text{Pd}(\text{CN})_4]$ and $[\text{Zn}(\text{hydet-en})_2\text{Pd}(\text{CN})_4]$ single crystals. *J Therm Anal Calorim* 2006; 86: 727-731.
- [17] Potočňák I, Vavra M, Čižmár E, Tibenská K, Orendáčová A, Steinborn D, Wagner C, Dušek M, Fejfarová K, Schmidt H, Müller T, Orendáč M, Feher A. Low-dimensional compounds containing cyano groups. XIV. Crystal structure, spectroscopic, thermal and magnetic properties of $[\text{CuL}_2][\text{Pt}(\text{CN})_4]$ complexes (L=ethylenediamine or N,N-dimethylethylenediamine). *J Solid State Chem* 2006; 179: 1965-1976.
- [18] Cernak J, Orendáč M, Potočňák I, Chomič J, Orendáčová A, Skoršepa J, Feher A. Cyano complexes with one-dimensional structures: preparations, crystal structures and magnetic properties. *Coord Chem Rev* 2002; 224: 51-66.
- [19] Vavra M, Potočňák I, Marhefková M, Boča R, Dlháň L. Low-dimensional compounds containing cyanido groups. XXII. Crystal structure, spectroscopic, thermal and magnetic properties of four Cu(II) tetracyanidoplatinates with a typical chain-like structures. *Polyhedron* 2012; 48: 227-236
- [20] Eriksen J, Hazell A, Jensen A, Jepsen J, Poulsen RD. Bimetallic assemblies, $[\text{Ni}(\text{en})_2]_3[\text{M}(\text{CN})_6]_2\cdot 3\text{H}_2\text{O}$ (en= $\text{H}_2\text{NCH}_2\text{CH}_2\text{NH}_2$; M = Fe, Co). *Acta Crystallogr C* 2000; 56: 551-553.
- [21] Miyasaka H, Matsumoto N, Okawa H, Re N, Gallo E, Floriani C. Complexes derived from the reaction of manganese(III) Schiff base complexes and hexacyanoferrate(III): syntheses, multidimensional network structures, and magnetic properties. *J Am Chem Soc* 1996; 118: 981-994.
- [22] Černák J, Kuchár J, Stolárová M, Kajňáková M, Vavra M, Potočňák I, Falvello LR, Tomás M. Preparation, spectroscopic and magnetic characterization of $\text{Cu}(\text{cyclam})\text{M}(\text{CN})_4$ complexes exhibiting one-dimensional crystal structures (cyclam= 1, 4, 8, 11-tetraazacyclotetradecane, M= Ni, Pd, Pt). *Transit Met Chem* 2010; 35: 737-744.
- [23] Muga I, Gutiérrez-Zorrilla JM, Vitoria P, Román P, Lezama L, Beitia JL. Unusual Two Dimensional Nickel(II) Complexes Based on $[\text{Ni}(\text{dien})]^{2+}$ and $[\text{M}(\text{CN})_4]^{2-}$ Building Blocks (M = Ni, Pd and Pt)- Synthesis, Structural Diversity and Magnetic Properties. *European J Inorg Chem* 2004; 2004: 1886-1893.
- [24] Pickardt J, Staub B. Kristallstruktur des cyanoverbrückten polymeren Zinkcyanid-Pyridin-Komplexes $[\text{Zn}(\text{py})_2][\text{Zn}(\text{CN})_4]$. *Z für Naturforsch - B J Chem Sci* 1995; 50: 1517-1520.

- [25] Iwamoto T. Past, present and future of the clathrate inclusion compounds built of cyanometallate hosts. *J Incl Phenom Macrocycl Chem* 1996; 24: 61-132.
- [26] Marinescu G, Madalan AM, Tiseanu C, Andruh M. New d¹⁰ heterometallic coordination polymers based on compartmental Schiff-base ligands. Synthesis, structure and luminescence. *Polyhedron* 2011; 30: 1070-1075.
- [27] Lefebvre J, Batchelor RJ, Leznoff DB. Cu[Au(CN)₂]₂(DMSO)₂: Golden polymorphs that exhibit vapochromic behavior. *J Am Chem Soc* 2004; 126: 16117-16125.
- [28] Molnár G, Kitazawa T, Dubrovinsky L, McGarvey JJ, Bousseksou A. Pressure tuning Raman spectroscopy of the spin crossover coordination polymer Fe(C₅H₅N)₂Ni(CN)₄. *J Phys: Condens Matter* 2004; 16: S1129.
- [29] Rigo P, Bressan M. Cyanide complexes of nickel(II) with hybrid bidentate ligands containing phosphorus and nitrogen or sulfur donor atoms. *Inorg Chem* 1975; 14: 1491-1494.
- [30] Stocker FB, Troester M, Britton, D. Crystal Structures of a Family of New Copper(I) Cyanide Complexes of Thiourea and Substituted Thioureas. *Inorg Chem* 1996; 35: 3145-3153.
- [31] Sayın E, Kürkçüoğlu GS, Yeşilel OZ, Hökelek T, Büyükgüngör O. One- and two-dimensional heteropolynuclear complexes with tetracyanonickelate(II) and 2-pyridinemethanol. *Z Kristallogr Cryst Mater* 2014; 229: 563-572.
- [32] Sayın E, Kürkçüoğlu GS, Yeşilel OZ, Hökelek T. 1D cyanide complexes with 2-pyridinemethanol: Synthesis, crystal structures and spectroscopic properties. *J Mol Struct* 2015; 1101: 73-81.
- [33] E. Sayın, G.S. Kürkçüoğlu, Syntheses, structures and physical properties of cyanide-bridged M(II)-Ni(II) bimetallic complexes with 2-pyridineethanol (M(II)= Fe, Co and Ni). *Anadolu University Journal of Science and Technology A-Applied Sciences and Engineering* 17; 2016: 37-49.
- [34] Arjunan V, Balamourougane PS, Govindaraja ST, Mohan S. A comparative study on vibrational, conformational and electronic structure of 2-(hydroxymethyl)pyridine and 3-(hydroxymethyl)pyridine. *J Mol Struct* 2012; 1018: 156-170.
- [35] Karaağaç D, Kürkçüoğlu GS. Syntheses, spectroscopic and thermal analyses of the hofmann-type metal(II) tetra-cyanonickelate(II) pyridazine complexes: {[M(pdz)Ni(CN)₄]·H₂O}_n (M= Zn(II) or Cd(II)). *Bull Chem Soc Ethiop* 2015; 29: 415-422.
- [36] Kürkçüoğlu GS, Yeşilel OZ, Büyükgüngör O. Syntheses, spectral and thermal analyses of heteronuclear aqua(2-methylpyrazine)metal(II) complexes with tetracyanonickelate ion and crystal structure of supramolecular [Cd(H₂O)(2mpz)Ni(μ-CN)₄]_n complex. *Struct Chem* 2008; 19: 879-888.
- [37] Yılmaz VT, Güney S, Andaç Ö, Harrison WTA. Different coordination modes of saccharin in the metal complexes with 2-pyridylmethanol: synthesis, spectroscopic, thermal and structural characterization. *Polyhedron* 2002; 21: 2393-2402.
- [38] Anderson, RJ, Bendell DJ, Groundwater PW. *Organic spectroscopic analysis (Vol. 22)*. Royal Society of Chemistry 2004.

- [39] Socrates, G., Infrared and Raman characteristic group frequencies: tables and charts. John Wiley & Sons 2004.
- [40] Ciajolo A, Apicella B, Barbella R, Tregross, A. Correlations of the spectroscopic properties with the chemical composition of flame-formed aromatic mixtures. *Combust Sci Technol* 2000; 153: 19-32.
- [41] Guchhait N, Ebata T, Mikami N. Structures of hydrogen-bonded clusters of benzyl alcohol with water investigated by infrared-ultraviolet double resonance spectroscopy in supersonic jet. *J Chem Phys* 1999; 111: 8438-8447.
- [42] Puviarasan N, Arjunan V. Mohan S. FT-IR and FT-Raman studies on 3-aminophthalhydrazide and N-aminophthalimide. *Turk J Chem* 2002; 26: 323-334.
- [43] Roeges NP. A guide to the complete interpretation of infrared spectra of organic structures. Wiley 1994.
- [44] Xiao-Hong L, Hong-Ling C, Rui-Zhou Z, Xian-Zhou Z. Theoretical investigation on the non-linear optical properties, vibrational spectroscopy and frontier molecular orbital of (E)-2-cyano-3-(3-hydroxyphenyl) acrylamide molecule. *Spectrochim Acta A Mol Biomol Spectrosc* 2015; 137: 321-327.
- [45] Silverstein R, Webster F. Spectrometric identification of organic compounds. John Wiley & Sons 2006.
- [46] Saxena R, Kandpal L, Mathur G. Synthesis and characterization of poly(benzobisthiazole)s derived from halogenated phthalic acid and isophthalic acid. *J Polym Sci A Polym Chem* 2002; 40: 3959-3966.
- [47] Prasad M, Sri NU, Veeraiah V. A combined experimental and theoretical studies on FT-IR, FT-Raman and UV-vis spectra of 2-chloro-3-quinolinecarboxaldehyde. *Spectrochim Acta A Mol Biomol Spectrosc* 2015; 148: 163-174.
- [48] Parlak C. FT-IR and Raman spectroscopic analysis of some Hofmann type complexes. *Spectrochim Acta A Mol Biomol Spectrosc* 2012; 99: 12-17.
- [49] Suzuki, S. Orville-TW. Molecular force field of pyridine and its application to pyridine-metal complexes. *J Mol Struct* 1977; 37: 321-327.
- [50] Gör K, Kürkçüoğlu GS, Yeşilel OZ, Büyükgüngör O. Syntheses, crystal structures and spectroscopic properties of cyano-bridged two-dimensional coordination polymers with 3-methylpyridazine. *Inorg Chim Acta* 2014; 414: 15-20.
- [51] McCullough RL. Jones LH, Crosby, GA. An analysis of the vibrational spectrum of the tetracyanonickelate(II) ion in a crystal lattice. *SpectrochimActa*, 1960; 16: 929-944.
- [52] Kürkçüoğlu GS, Sayın E, Şahin O. Cyanide bridged hetero-metallic polymeric complexes: Syntheses, vibrational spectra, thermal analyses and crystal structures of complexes $[M(1,2-dmi)_2Ni(\mu-CN)_4]_n$ (M= Zn (II) and Cd (II)). *J Mol Struct* 2015; 1101: 82-90.

- [53] Kubas GJ, Jones LH. Potential constants of the tetracyanide ions of nickel, palladium, and platinum. *Inorg Chem* 1974; 13: 2816-2819.
- [54] Kuchar J, Cernak J, Abboud KA. The one-dimensional structure of $\text{Cu}(\text{dmen})_2\text{Pd}(\text{CN})_4$ (dmen is N,N-dimethylethylenediamine). *Acta Crystallogr C* 2004; 60: M492-M494.
- [55] Karaağaç D, Kürkçüoğlu GS, Yeşilel OZ, Hökelek T, Dal H. Synthesis and crystal structure of cyano-bridged three dimensional polyheteronuclear complex. *Z Kristallogr* 2012; 227: 639-645.
- [56] Karadağ A, Şenocak A, Önal İ, Yerli Y, Şahin E, Başaran AC, Preparation, structural, magnetic and thermal properties of two heterobimetallic cyano-bridged nickel(II)-copper (II)/platinum(II) coordination polymers. *Inorg Chim Acta* 2009; 362: 2299-2304.
- [57] Nakamoto K. *Infrared and Raman spectra of coordination compounds*. Wiley, New York 1997.
- [58] Molnár G, Niel V, Gaspar AB, Real JA, Zwick A, Bousseksou A, McGarvey JJ. Vibrational spectroscopy of cyanide-bridged, iron(II) spin-crossover coordination polymers: Estimation of vibrational contributions to the entropy change associated with the spin transition. *J Phys Chem B* 2002; 106: 9701-9707.
- [59] Kürkçüoğlu GS, Kiraz FÇ, Sayın E. Vibrational spectra, powder X-ray diffractions and physical properties of cyanide complexes with 1-ethylimidazole. *Spectrochim Acta A Mol Biomol Spectrosc* 2015; 149: 8-16.



RESEARCH ARTICLE

SYNTHESIS OF POLYMER ELECTROLYTE MEMBRANES BASED ON IONIC LIQUID
DOPED SPEEK

Şeyda KARADİREK^{1,*} , Mesut YILMAZOĞLU¹ 

¹ Chemical Engineering Department, Engineering Faculty, Yalova University, Yalova, Türkiye

ABSTRACT

The sustainable and environmentally benign energy demand of the world has been increasing. Among the various options, proton exchange membrane fuel cell is an attractive choice for energy supply due to its high efficiency and application conditions without waste. In this research, triazole-based ionic liquid doped sulfonated polyether ether ketone (SPEEK) composite membranes were presented for proton exchange membrane fuel cell (PEMFC) applications. Composite membranes were prepared by incorporating 1,2,3-triazole-based ionic liquids (TIL 1-2-3) into poly(ether ether ketone) (PEEK) matrices. The mechanical, structural, and thermal properties of both composite membranes and the triazole-based ionic liquids were thoroughly characterized using dynamic mechanical analysis (DMA), Fourier transform infrared spectroscopy (FTIR), and thermogravimetric analysis (TGA). The performance and viability of composites for PEMFC applications that involve elevated temperatures were conducted by proton conductivity test across a broad range of temperatures (30-180 °C). High-temperature proton conductivity was measured as 1.73×10^{-2} S/cm for SPEEK/TIL-3(1.0). According to the proton conductivity test results, it was concluded that the composite membranes may exhibit improved performance in PEMFC applications due to increased proton conductivity values.

Keywords: Proton conductivity, Proton exchange membrane, Triazole, Ionic liquid, Polyether ether ketone

1. INTRODUCTION

The high dependence of traditional energy sources on fossil fuels has led to the emergence of energy demand and environmental pollution problems [1-3]. The ecological and economic issues resulting from the consumption of fossil fuels have increased the need for new technologies for energy production based on alternative energy sources. Polymer electrolyte fuel cells are a promising new technology for generating clean, efficient, and sustainable electricity. Due to these characteristics, the polymer electrolyte fuel cell is presented as an efficient and environmentally friendly energy source that eliminates the CO₂ emission problem of traditional internal combustion engines.

The membrane fuel cell contains a solid polymeric electrolyte that provides proton conductivity and separates the cathode and anode from each other [4]. The efficiency of a polymer electrolyte membrane fuel cell is mainly determined by its proton exchange capacity. PEM is a critical part of the fuel cell module designed for improved proton conduction performance. PEM should resist the harsh environment inside the fuel cell to provide efficient proton conduction. The good thermal, mechanical, and oxidation properties of PEM depend on its hydrophilicity [5]. Among widely used PEM for PEMFC, Nafion is the most preferred due to its high stability and proton conductivity. However, due to reasons such as high production costs and low proton transmission capacity at high temperatures, the need to evaluate alternative materials for PEM has arisen [6].

*Corresponding Author: seyda.karadirek@yalova.edu.tr

Received: 16.01.2023 Published: 27.12.2023

Alternatively, aromatic thermoplastics such as polyether-ether-ketone (PEEK) are suitable for application as polymer electrolyte membranes owing to their thermal resistance, oxidation resistance, easy processing, and low cost. The sulfonation process could increase the conductivity of aromatic thermoplastics exhibited by protons. The sulfonated polyether-ether-ketones have superior structural properties than Nafion due to their hydrophilic structure and wide separation between $-SO_3H$ groups. Although their hydrophilic capacity determines the proton conductivity of sulfonated polymeric membranes, they have high conductivity values for their aromatic structure in low humidity and high-temperature conditions [7]. The high sulfonation degree of aromatic thermoplastics provides high proton conductivity values (at $\approx 10^2$ S/cm, 25 °C in fully hydrated media). On the other hand, the high sulfonation degree of aromatic membranes results in low structural stability and solubility [8].

In recent years, ionic liquids have drawn significant attention for their superior thermal, physical, and electrochemical characteristics, environmental safety, and low vapor pressure [9–11]. Ionic liquids are preferred in many application areas because they have adjustable cationic and anionic functions [12]. Combining anion-cation pairs with a wide variety of physicochemical and electrochemical properties increases the diversity of synthesized ionic liquids. The most preferred anion groups for ionic liquid synthesis are tetrafluoroborate (BF_4^-), hexafluorophosphate (PF_6^-), trifluoromethane sulfonate ($CF_3SO_3^-$), and cation groups are imidazole and pyridine [13, 14].

The application of imidazole-based ionic liquids as electrolytic material in PEMFCs has been investigated owing to its enhanced conductivity and cell performance. Triazole-based ionic liquids are believed to be an alternative to imidazole since they have high thermal stability because of intense hydrogen bonding in their structures. 1,2,3 triazole-based ionic liquids have high stability, variety, and versatility of polymer design. Triazole-based ionic liquids obtained from appropriate anion-cation combinations, demonstrate a significant potential for utilization in proton exchange membrane (PEM) applications [15, 16].

In the present study, ionic liquid-based polymer composite membranes with high thermal resistance were produced for use in PEMFC systems. PEEK polymer matrix was sulfonated to have SPEEK structure as an alternative polymer electrolyte membrane. The proton exchange membrane was prepared by doping 1,2,3 triazole-based ionic liquids at varying mole rates. The structure of synthesized ionic liquids was analyzed. The proton conductivity of composites was measured between 30-180 °C, and their conformations in thermal-resistant fuel cell systems were evaluated.

To the best of our knowledge, there is limited research on producing composite materials comprising triazole-based polymer electrolyte membranes. This current investigation introduces a novel composite material with the potential for application as a proton exchange membrane in thermally resilient fuel cell systems.

2. MATERIALS and METHOD

2.1 Materials

Polyether ether ketone (PEEK) polymer matrix, copper sulfate, silver tetrafluoroborate, sodium ascorbate, butyl alkyne, and n-butylazide were obtained from Merck. Methyl trifluoromethane sulfonate, trimethylsilyl chlorosulfonate, diethyl ether, and ethyl acetate were obtained from Merck-Millipore. All reagents were used as reagent grade.

2.2 Synthesis of Ionic Liquids

Briefly, the synthesis method of ionic liquids involved combining n-butylated, sodium ascorbate, copper sulfate, and butyl alkyne in methanol, followed by the addition of water and extraction with ethyl acetate.

The organic phase was subjected to purification steps, including brine washing and reduction of water content. The resulting oily phase containing 1,4-di(n-butyl)-1H-1,2,3-triazole was further reacted with methyl trifluoromethanesulfonate to yield 3,5-dibutyl-1-methyl-3H-1,2,3-triazolium trifluoromethanesulfonate (TIL-1) [17].

The subsequent synthesis procedures for TIL-2 and TIL-3 were described in our previous study [18].

2.3 Synthesis of SPEEK/TIL-(1-3) Composites

Sulfonated polyether ether ketone was produced by the sulfonation process to be used in the synthesis of SPEEK/TIL-(1-3) composite membranes. Initially, a specific quantity of anhydrous pure polyether ether ketone was solubilized in H₂SO₄. The red-colored viscous solution resulting from the sulfonation process was carefully added drop by drop into a mixture of 1 L of distilled water and ice to ensure the completion of the reaction while effectively dissipating the heat released during the process. The sulfonated polyether ether ketone was produced in the form of small droplets. Then, any excess sulfuric acid on the surface of the synthesized SPEEK polymer droplets was rinsed off using distilled water. The polymer matrices were dried in an oven at 65°C for a certain time. An appropriate amount of SPEEK was measured and dissolved in a suitable solvent (NMP) to prepare composite membranes with added triazole-based ionic liquid. The mixture was then stirred for 2 hours. Equimolar (n: 1.0) ionic liquids to the sulfonic acid groups in the structure were added to the resulting solution and agitated for 3 hours. The mixtures were transferred to glass petri dishes for solvent removal, and composites were obtained after 48 hours at 40°C.

The SPEEK matrix composite membranes prepared in the study are labeled with the notation SPEEK/TIL-'X'(n); where 'X' corresponds to the ionic liquid type and 'n' corresponds to the ionic liquid/HSO₃ mole ratio.

2.4 Characterizations

The structure determination of the ionic liquids and proton exchange membranes synthesized in the study was performed with the Fourier Transform Infrared Spectroscopy characterization method through wavelengths between 500-4000 cm⁻¹. The degradation temperatures of the polymer electrolyte membranes were determined with the Thermogravimetric Analysis (TGA, SEIKO TG/DTA 6300) method between the range of 25°C to 800°C. Mechanical features were determined by Dynamic Mechanical Analysis over a wide temperature range. Proton conductivity (σ) assessments were conducted using an Agilent 4284A LCR Meter system. These measurements were conducted over a frequency spectrum spanning from 40 Hz to 1 MHz and within a temperature range spanning from 30 °C to 180°C. In preparation for these measurements, membrane samples were appropriately dimensioned and then coated with silver paste to establish electrodes on their surfaces.

3. RESULTS and DISCUSSION

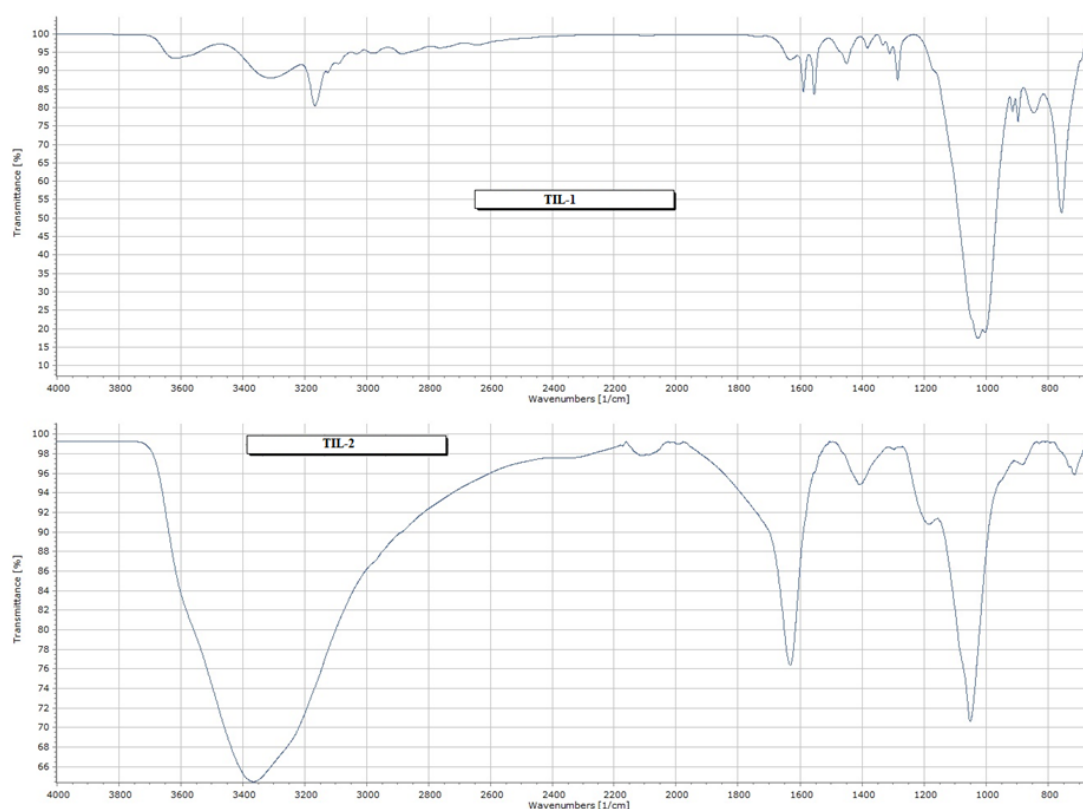
3.1. Elemental Analysis and Fourier Transformed Infrared Spectroscopy (FTIR)

FT-IR analysis was performed as a preliminary characterization to determine the molecular structure of materials and the structural interactions of these materials with each other. Firstly, prepared ionic liquids were characterized with elemental analysis and FTIR spectroscopy. C, H, and N ratios of TIL-1, TIL-2, and TIL-3 were presented in Table 1.

Table 1. Theoretical and experimental C, H, N ratios of ionic liquids

Ionic liquid	Theoretical			Elemental Analysis			Yield (%)	Molecular Weight (g mol^{-1})
	C (%)	H (%)	N (%)	C (%)	H (%)	N (%)		
TIL-1	41.74	6.38	12.17	41.87	6.34	12.21	99.1	345
TIL-2	48.85	7.46	14.25	47.94	7.46	14.34	97.9	294.8
TIL-3	57.94	7.38	11.93	53.16	7.19	14.23	92.8	352.1

The bands observed at 1048 cm^{-1} and 1192 cm^{-1} in the FTIR spectrum of TIL-2 ionic liquid are attributed to BF_4^- anion and C-N & C-H bonds, respectively (Figure 1). Characteristic broad bands of NH stretching vibrations of ionic liquid structures were observed at 3360 cm^{-1} . The absorption peaks at 720 cm^{-1} and 1633 cm^{-1} denote the bending in the C-H bonds and C=N tensions. The peak observed at 1400 cm^{-1} ascribed to C=C to aromatic stretching vibrations [19, 20].

**Figure 1.** FT-IR spectra of TIL-1 and TIL-2 ionic liquids.

The broad spectral peak of sulfonated polyetheretherketone (SPEEK), derived from polyetheretherketone (PEEK) through sulfonation, is observed at 3400 cm^{-1} (Figure 2). The presence of this distinctive peak can be attributed to the vibrations of hydroxyl (OH) groups within the sulfonic acid groups. The vibration bands of all composite samples and sulfonated polymer matrix at 1023 cm^{-1} are due to S-O tensions. Also, the bands at 1080 and 1223 cm^{-1} confirmed S=O and O=S=O stretching forces formed, respectively [20]. Observations revealed that the broad peaks associated with the hydroxyl (OH) groups of TIL molecules exhibited partial narrowing. The observed phenomenon can be defined by the interaction between TIL structure and sulfonic acid molecules in the polymer matrices, leading to a reduction in the concentration of hydroxyl (OH) groups. The presence of peaks detected at

3066 cm^{-1} approved the tension of C-H bonds originating from the aromatic rings. The absorption bands observed at 1595 cm^{-1} were associated with the presence of the triazolium cation within the composite membrane structures. Fourier Transform Infrared Spectroscopy characterization confirmed the successful production of all the samples in the present work [20, 21].

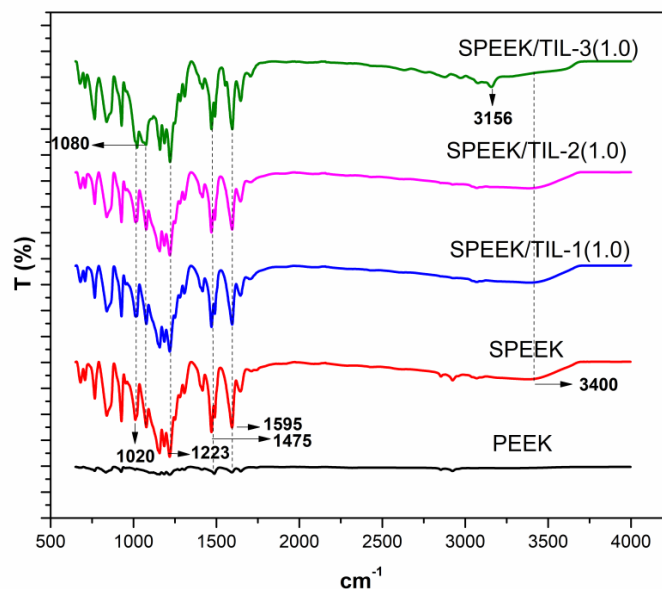


Figure 2. FT-IR spectra of SPSU, SPSU/TIL-1, and SPSU/TIL-2 composite polymer electrolyte membranes.

3.2 Thermogravimetric Analysis

The temperature resistance of the composite polymer membranes synthesized in the present work was characterized by TGA. Since polymer electrolyte membranes were synthesized for high-temperature fuel cell applications, they should have elevated temperature resistance. The TGA curve shows that the type of TIL structure has a significant effect on the degradation temperature of the final PEEK polymer.

In the Figure 3, the pristine polyether ether ketone structure has a single-step thermal degradation above 600°C. On the other hand, sulfonated polyether ether ketone structure and polymer electrolytes obtained by sulfonation indicated multiple degradation stages. The primary thermal degradation behavior under 100 °C is attributed to the evaporation of water attached to the membrane structures. The first degradation step of composite membranes and SPEEK polymer matrix at 150-200°C is on account of the degradation of the sulfonic acid group in the polymer structures [20, 22].

As observed in Figure 3, the thermal stability of the composite membranes is close to the thermal stability of the neat SPEEK polymer matrix. While SPEEK/TIL-1(1.0) and SPEEK/TIL-2(1.0) composite membranes exhibited poor performance due to both the removal of water at low temperatures and earlier degradation, the first degradation step of the SPEEK/TIL-3(1.0) membrane after the removal of water occurred at higher temperatures than the SPEEK membrane. Thermal resistance was slightly increased by the incorporation of TIL-3. While all composite membranes are effective at low temperatures, SPEEK/TIL-3(1.0) composite membrane is quite suitable for electrochemical processes at high temperatures (>200°C).

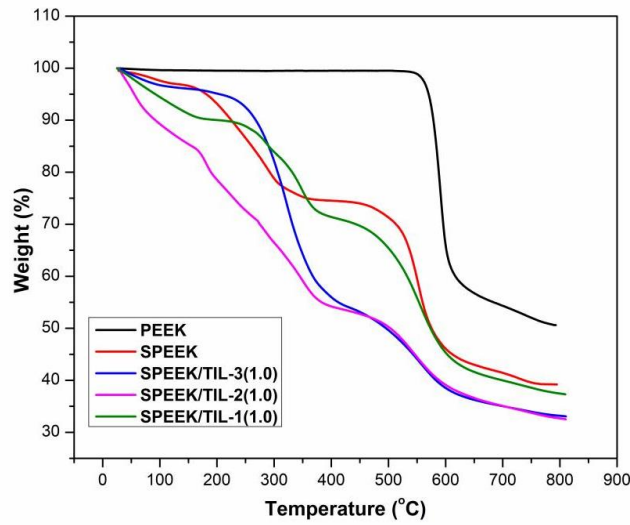


Figure 3. TGA curves of PEEK, SPEEK, SPEEK/TIL-1, SPEEK/TIL-2 SPEEK/TIL-3 composite membranes.

3.3 Proton Conductivity

Proton conductivity of SPEEK/TIL composite synthesized in this work was performed and the analysis results were determined by Equation 1.

$$\sigma = \frac{L}{RA} \tag{1}$$

The conductivity (σ) of the membrane is determined by its thickness (L) and the cross-sectional area (A) of the membrane. In Figure 4, The temperature variation is used as a parameter to present the proton conductivities of composite membranes fabricated using SPEEK.

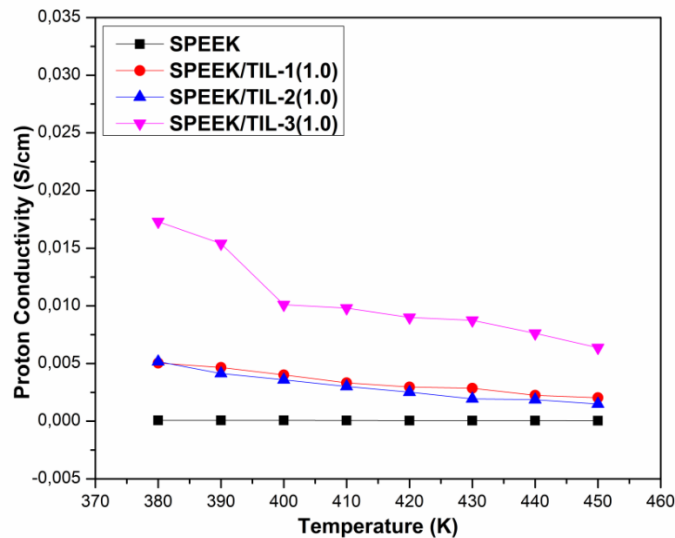


Figure 4. Temperature-dependent proton conductivity values of SPSU/TIL-(1-3) composite membranes.

It has been noted that the proton conductivity of composites doped with SPEEK and TIL decreases as the temperature increases in the absence of water, and this result is consistent with previous studies [20, 23, 24]. It is known that the conductivity of SPEEK matrix may decrease due to the crosslinking of -SO₃H groups at high temperatures. Furthermore, the decrease in conductivity can be attributed to the evaporation of the water in the polymer matrix and the TIL structure. The sulfonic acid groups of the sulfonated polyether ether ketone matrix exhibit insufficient conductivity and even become virtually inert under anhydrous conditions. Compared to the pure sulfonated polyether ether ketone polymer matrix, the proton conductivity of the composites increased with the contribution of TIL (1-3) under anhydrous conditions. The conductivity values for the SPEEK polymer matrix were measured in the range of 4.05×10^{-5} - 7.41×10^{-5} S/cm and within the determined temperature range. The incorporation of TIL into the matrix, contributed to the improvement of ionic mobility and thus facilitation of proton transfer across polymeric membranes [25]. Additionally, it is anticipated that TIL will create pathways for proton conduction within the composites, resembling the role of water in hydrated proton exchange membranes. [26]. The conductivity values for TIL-1 and TIL-2 doped composites were very close, and the maximum measured proton conductivity rate of composites was approximately 5×10^{-3} S/cm. The highest proton conductivity value was observed as 1.73×10^{-2} S/cm for SPEEK/TIL-3(1.0). The result demonstrated that TIL-3 doped membranes exhibited higher conductivity values, indicating their potential as a viable substitute for electrochemical applications.

3.4 Dynamic mechanical analysis (DMA)

The DMA method was employed to evaluate the mechanical behavior of sulfonated polyether ether ketone composites in the conducted study. The peak values of the graph produced by dynamic mechanical analysis exhibited the glass transition temperature (T_g) of the composites. Figure 5 presents the temperature-dependent changes in tanδ values for both the SPEEK polymer matrix and the SPEEK/TIL-3(1.0) composite membrane. The increase in chain mobility of the polymer matrix creates electrostatic interactions between TIL and SPEEK structures, improving proton conductivity. The figure shows that T_g of the pure SPEEK membrane was measured as 172°C. However, the incorporation of TIL-3 ionic liquid resulted in a reduction in the glass transition temperature (T_g) of the membrane, which was measured to be 190°C. This change in T_g trends of pure SPEEK and TIL-doped composite membranes is consistent with the literature [20, 27, 28]. This decreasing trend is explained by the molecular Brownian motion that starts in the polymer structure due to T_g value [29, 30]. The decrease in the glass transition temperature (T_g) of the composite membrane, induced by different additives or treatments, leads to enhanced versatility and conductivity of molecules. This effect is attributed to the transformation of the crystalline structure into an amorphous structure. The electrostatic interactions between the TIL and SPEEK chains increase due to the mobility of the polymer matrix, and thus, the proton conductivity is further improved [31]. The storage (E') and loss (E'') modulus of SPEEK-2 and SPEEK/TIL-3(1.0) electrolytes were presented with DMA plots in Figure 5b. As illustrated in the figure, the storage modulus (E') and loss modulus (E'') values of the pure SPEEK membrane exceeded those of SPEEK/TIL3-(1.0). This result can be attributed to the plasticizing influence exerted by the presence of the ionic liquid (TIL3) within the composite membrane. The TIL3 ionic liquid has the capacity to enhance the mobility of polymer chain segments by reducing the viscosity of the composite membrane. Specifically, the storage moduli for the SPEEK and SPEEK1.0-2 composite membranes were determined to be 1.7 GPa and 1.3 GPa, respectively. In the context of sulfonated polymers and ionic liquid-doped sulfonated polymers reported in previous studies, it is evident that the SPEEK and SPEEK/TIL3-(1.3) electrolytes exhibit reasonable maximum stress levels at elevated temperatures.

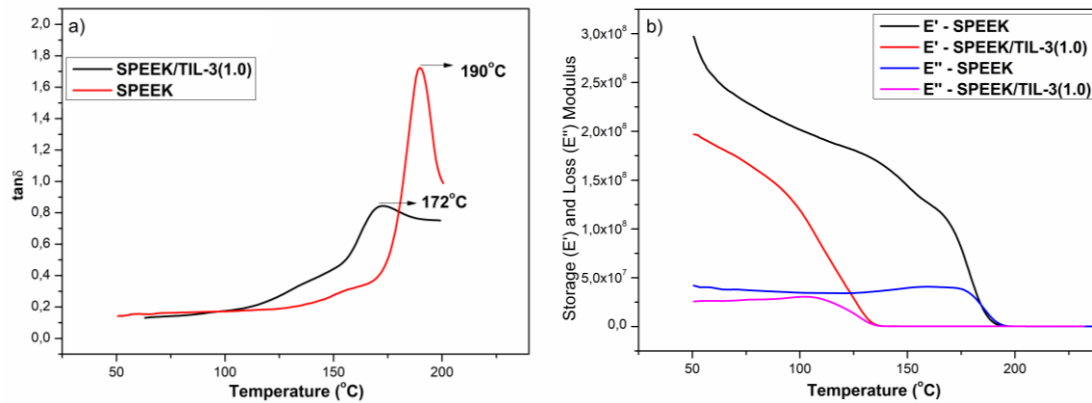


Figure 5. a) $\tan\delta$ curves of SPEEK and SPEEK/TIL-3(1.0). **b)** The storage (E') and loss (E'') modulus of SPEEK and SPEEK/TIL-3(1.0) electrolytes

4. CONCLUSION

This study carried out three different ionic liquid syntheses based on triazole and ionic liquid doped sulfone polyether ether ketone synthesis. Composite electrolytes were prepared, including different ratios of ionic liquids to the SPEEK matrix obtained by the sulfonation process of PEEK polymer. Proton conductivity of sulfonated polymer matrices is greatly improved by ionic liquid doping. The proton conductivity of the SPEEK/TIL-3(1.0) composite electrolyte was determined as 1.73×10^{-2} S/cm). The polymer composites produced in this study have demonstrated their potential as alternative materials suitable for high-temperature PEM fuel cells. The thermal stability of the composite membranes was evaluated through TGA analysis. The results showed that all membrane composites exhibited satisfactory ionic conductivity and temperature resistance under cell conditions ($>200^\circ\text{C}$).

ACKNOWLEDGMENT

This study was supported by the Yalova University Scientific Research Foundation (Project number: 2019/AP/0006).

CONFLICT OF INTEREST

The authors stated that there are no conflicts of interest regarding the publication of this article.

AUTHORSHIP CONTRIBUTIONS

Şeyda Karadirek: Formal analysis, Investigation, Writing - original draft, Visualization, Conceptualization. **Mesut Yilmazoğlu:** Formal analysis, Investigation, Writing - original draft, Visualization, Conceptualization.

REFERENCES

- [1] Adabi H, Shakouri A, Hassan N Ul, Varcoe J R, Zulevi B, Serov A, Regalbuto J R, Mustain W E. High-performing commercial Fe–N–C cathode electrocatalyst for anion-exchange membrane fuel cells, *Nat Energy* 2021; 6: 834–843.
- [2] Jamil A, et al. Development of an extended model for the permeation of environmentally hazardous CO₂ gas across asymmetric hollow fiber composite membranes. *J Hazard Mater* 2021; 417: 126000.

- [3] Zaidi J, Matsuura T. Polymer Membranes for Fuel Cells. Springer 2008.
- [4] Atanasov V, Lee A S, Park J F, Sandip M, Baca E D, Fujimoto C, Hibbs M, Matanovic I, Kerres J, Kim Y S. Synergistically integrated phosphonated poly (pentafluorostyrene) for fuel cells, *Nat Mater* 2021; 20: 370–377.
- [5] Shen G, Liu J, Wu H B, Xu P, Liu F, Tongsh C, Jiao K, Li J, Liu M, Cai M, Lemmon J P, Soloveichik G, Li H, Zhu J, Lu Y. Multi-functional anodes boost the transient power and durability of proton exchange membrane fuel cells. *Nat Commun* 2020; 1191.
- [6] Ahmad H, Kamarudin S K, Hasran U A, Daud W R W. Overview of hybrid membranes for direct-methanol fuel-cell applications. *Int J Hydrogen Energy* 2010; 35: 2160–2175.
- [7] Jannasch P. Recent developments in high-temperature proton conducting polymer electrolyte membranes 2003; 8 (1): 96-102.
- [8] Yang J, Gao L, Wang J, Xu Y, Liu C, He R. Strengthening phosphoric acid oped polybenzimidazole membranes with siloxane networks for using as high temperature proton exchange membranes. *Macromolecular Chemistry and Physics* 2017; 218 (10): 1700009.
- [9] Sergio C, Martha R, Francisco J S, Olga L T, Militza M P, Margarita C. Optofluidic compound lenses made with ionic liquid. *Applications of ionic liquids in polymer science and technology* 2015; 5: 662-44903-5.
- [10] Armand M, Endres F, MacFarlane D R, Ohno H, Scrosati B., Ionic-liquidmaterials for the electrochemical challenges of the future. *Nat Mater* 2009; 621–629.
- [11] Welton T. Room-temperature ionic liquids. *Solvents for Synthesis and Catalysis*, *Chem Rev* 1999; 99: 2071–2084.
- [12] Liu Y, Guo L, Zhu L, Sun X, Chen J. Removal of Cr(III, VI) by quaternary ammonium and quaternary phosphonium ionic liquids functionalized silica materials. *Chem Eng J* 2010; 158: 108–114.
- [13] Liu H, Yu H. Ionic Liquids for Electrochemical Energy Storage Devices Applications. *Journal of Materials Science & Technology* 2019; 35 (4): 674- 686.
- [14] Fernandes A M, Rocha M A A, Freire M G, Marrucho I M, Coutinho J A P, Santos L M N B F. Evaluation of cation–anion interaction strength in ionic liquids. *The Journal of Physical Chemistry B* 2011; 115 (14): 4033- 4041.
- [15] Sun Y, Shi L. Basic ionic liquids with imidazole anion: New Reagents to Remove Naphthenic Acids From Crude Oil With High Total Acid Number. *Fuel* 2012; 99: 83-87.
- [16] Luo J, Hu J, Saak W, Beckhaus R, Wittstock G, Vankelecom I F J, Agert C, Conrad O. Protic ionic liquid and ionic melts prepared from methanesulfonic acid and 1H-1,2,4- triazole as high temperature PEMFC electrolytes. 2011; 21 (28): 0426-10436.
- [17] Kim K, Jung B K, Ko T, Kim T H, Lee J C. Comb-shaped polysulfones containing sulfonated polytriazole side chains for proton exchange membranes. *Journal of Membrane Science* 2018; 554: 232-243.

- [18] Yilmazoğlu M, Korkmaz Ş. Development of 1,2,3-Triazole based ionic liquid doped sulfonated polysulfone (SPSU) electrolytes for anhydrous proton exchange membrane applications. *El-Cezerî Journal of Science and Engineering* 2022; 9(2): 584-597.
- [19] Kantheti S, Narayan R, Raju K V S N. Development of moisture cure polyurethane–urea coatings using 1,2,3-triazole core hyperbranched polyesters. *Journal of Coatings Technology and Research* 2013; 10 (5): 609- 619.
- [20] Yilmazoğlu M, Bayıroğlu F, Erdemi H, Abaci U, Guney H Y. Dielectric properties of sulfonated poly(ether ether ketone) (SPEEK) electrolytes with 1-ethyl-3-methylimidazolium tetrafluoroborate salt: Ionic liquid-based conduction pathways. *Colloids and Surfaces A: Physicochemical and Engineering Aspects*. 2021; 611: 125825.
- [21] Xu T, Hou W, Wu X S H, Li X, Wang J, Jiang Z. Sulfonated titania submicrospheres-doped sulfonated poly(ether ether ketone) hybrid membranes with enhanced proton conductivity and reduced methanol permeability. *Journal of Power Sources* 2011; 196: 4934–4942.
- [22] Qu S, Li M, Zhang C, Sun Y, Duan J, Wang W, Li J, Li X. Sulfonated poly(ether ether ketone) doped with ammonium ionic liquids and nano-silicon dioxide for polymer electrolyte membranes. *Polymers* 2019; 11 (7): 1-14.
- [23] Shashidhara G M, Kumar K N. Proton conductivity of SPEEK membranes. *Polymer-Plastics Technology and Engineering*. 2010; 49 (8): 796-80.
- [24] Malik R S, Verma P, Choudhary V. A study of new anhydrous, conducting membranes based on composites of aprotic ionic liquid and cross-linked SPEEK for fuel cell application. *Electrochimica Acta* 2015; 152: 352-359.
- [25] Yi S, Zhang F, Li W, Huang C, Zhang H, Pan M. Anhydrous elevated-temperature polymer electrolyte membranes based on ionic liquids. *Journal of Membrane Science* 2011; 366 (1-2); 349–355.
- [26] Mistry M K, Subianto S, Choudhury N R, Dut N K. Interfacial interactions in aprotic ionic liquid based protonic membrane and its correlation with high temperature conductivity and thermal properties. *Langmuir* 2009; 25: 9240-9251.
- [27] Wang X, Jin M, Li Y, Zhao L. The influence of various ionic liquids on the properties of SPEEK membrane doped with mesoporous silica. *Electrochimica Acta* 2017; 257: 290-300.
- [28] Khan S S, Hanelt S, Liebscher J. Versatile synthesis of 1, 2, 3-triazolium-based ionic liquids. *Arkivoc* 2009; 12: 193-208.
- [29] Zaidi S M J. Preparation and characterization of composite membranes using blends of SPEEK/PBI with boron phosphate. *Electrochimica Acta* 2005; 50 (24): 4771-4777.
- [30] Nakabayashi K, Umeda A, Sato Y, Mori H. Synthesis of 1,2,4-triazolium salt-based polymers and block copolymers by RAFT polymerization: ion conductivity and assembled structures. *Polymer* 2016; 96: 81–93.
- [31] Mondal A N, Tripathi B P, Shahi V K. Highly stable aprotic ionic-liquid doped anhydrous proton-conducting polymer electrolyte membrane for high-temperature applications. *Journal of Material Chemistry* 2011; 21: 4117-4124.



RESEARCH ARTICLE

DETECTION OF RHODAMINE VIA SURFACE ENHANCED RAMAN SPECTROSCOPY
UTILISING AG NANOWIRES

Kürşad Osman AY¹ 

¹Eskisehir Osmangazi University, Central Research Laboratory Application and Research Center (ARUM), Eskisehir, 26040, Turkey

ABSTRACT

Rhodamine, which is extensively used as a synthetic dye in food industry, is regarded as an illegal additive by European Food Safety Authority because of its carcinogenic and toxicological properties. Since it's a colourless material at low concentrations such as 10^{-7} M, its detection via spectroscopical methods is very challenging and crucial in terms of food safety issues. In this study Ag nanowires were synthesized, their crystal structure is characterized via XRD analysis, their surface morphology and radius are determined via SEM images and their chemical composition was determined by EDS analysis. Afterwards, rhodamine solutions which were prepared at 10^{-4} – 10^{-7} M were dropcasted onto Ag nanowire solutions. After selecting three characteristic Raman peaks belonging to the Rhodamine molecule, which are located at 612, 1189 and 1362 cm^{-1} , detection of Rhodamine was performed at these ultra low concentrations. As a result, one can conclude that Ag nanowires can be utilized as possible SERS substrates for detection of Rhodamine at low concentrations by exhibiting significant reproducibility, stability and recyclability features.

Keywords: Rhodamine, SERS, Detection, Ag nanowires

1. INTRODUCTION

Raman spectroscopy has gained a significant importance by the discovery of utilising surface enhancement to boost Raman signals in order to detect molecules even at ultra low concentrations [1]. This phenomenon, which is referred as Surface Enhanced Raman Spectroscopy (SERS), provides a fast and cheap method for detection of such molecules at ultra-low concentrations. It is based on the principle of boosting Raman signals, which have low intensity by nature, by utilising metal nanoparticles in order to enhance Raman signals by creating hot-spots. At this point, the signal enhancement primarily depends on the distribution, shape, size, morphology and density of the nanoparticles implented on the substrate [2, 3]. To obtain uniform and reproducible SERS substrates, various nanomaterials utilised, while most preferred ones are Ag, Au, ZnO and ZnO/Ag [4].

The signal enhancement in Raman spectrum depends on two components, namely, electromagnetical enhancement and chemical enhancement. The electromagnetical component, being the main contribution to the signal enhancement, arises due to the surface plasmons on the metallic nanomaterials. Basically, free electrons of the nanomaterial substrate (generally Ag or Au) oscillate at the same frequency, when these plasmons resonate at the identical frequency with the laser light. Thus, analyte molecules adsorbed on the metal surface are stimulated in a more effective way, with the existence of the enhanced electromagnetic field [5]. The second contribution is of chemical nature and has a shorter range compared to the electromagnetic contribution. It simply depends on molecular polarization, where charge-transfer complexes occur between the metal nanomaterial substrate and the analyte molecule. This type of contribution needs so-called active-sites where analyte molecules should adsorb directly on the nanomaterial substrate [6].

Rhodamine B, with the chemical formula $C_{28}H_{31}ClN_2O_3$, extensively used as a synthetic dye in food industry, is accepted as an illegal additive by European Food Safety Authority because of its carcinogenic and toxicological properties for human beings and as well as animals [7]. In this sense, detection of Rhodamine at even low concentrations is an important issue, in terms of human and animal health. Up to present, various methods have been utilised in order to determine Rhodamine presence in condiments and peanuts[8]. Among them, one can mention High Performance Liquid Chromatography (HPLC) [7], Spectrofluorimetry [8], Liquid Chromatography - Mass Spectrometry (LC-MS) [9]. However, these methods have several situation-specific disadvantages, such as long preparation times, expensive equipment necessities and complex and long pre-treatments. Moreover, these methods are not suitable for on-site analysis [10]. At this point, SERS emerges as a useful alternative, for rapid and precise detection of Rhodamine at even low concentrations.

In this study, SERS method was utilised in order to detect Rhodamine molecule at varying concentrations from 10^{-4} M to 10^{-7} M, where Ag Nanowires were employed as the substrate in order to form hotspots on rhodamine solution.

2. EXPERIMENTAL SECTION

2.1. Reagents

Ethylene glycol (EG) (99.8 %), ethanol (99.9 %), polyvinylpyrrolidone (PVP, Mw 55.000) and silver nitrate ($AgNO_3$) (99 %) were purchased from Sigma Aldrich. During all experimental procedures, ultrapure water was utilized.

2.2. Synthesis of Ag Nanowires

5 ml EG was poured into a three necked balloon and was stirred for 20 minutes at 600 rpm, $160^{\circ}C$. Afterwards, it was flashed via Ar gas for one minute. A solution of 0.25 mg $AgNO_3$, which was prepared in 5 ml EG was slowly added into the first EG solution at $160^{\circ}C$. Afterwards, 1.56 g PVP was prepared in 10 ml EG and was added into the first EG solution after the $AgNO_3$ solution. This mixture was left to stir for 2 hours at $160^{\circ}C$. At the end of this process, the mixture was put into ice bath in order to terminate the reaction and was left to cool down at ambient temperature for 20 minutes. Then, the centrifugation procedure was performed in order to purify ag-nanowires. The first centrifugation was performed via acetone at 2000 rpm for 30 minutes, while the next two cycles were performed via distilled water with the same rpm and time settings [11].

2.3. Characterization

For the visual verification of the $AgNO_3$ nanowire synthesis, Hitachi Regulus 8230 FEG-SEM instrument was utilized and the elemental analysis was carried out via the Oxford EDS detector attached to this electron microscope. For determining the $AgNO_3$ nanowires' crystal structure, X-Ray Diffraction (XRD) method was utilized. The instrument was a Panalytical Empyrian diffractometer which operates with 45-kV anode voltage and 40-mA filament current settings. Nickel-filtered $Cu K\alpha$ radiation had a wavelength of 0.1542 nm, the goniometer of the diffractometer had a scanning speed of $0.133^{\circ}/s$ with a step size of 0.01° and it diffracted X-rays in the 2θ of 30° – 90° . For obtaining the Raman spectra, Renishaw Invia Raman instrument was utilized. For all Raman spectrums, the excitation energy was 532 nm and the objective lens was 20x. For measurements, a silicon wafer was preferred as the standart material, while the raman peak for this material is observed at 520 cm^{-1} and all spectra were acquired between 400 cm^{-1} – 2000 cm^{-1} .

2.4. Preparation of SERS Substrate

As a first step, glass was disinfected via ethanol and acetone. Then, 10 μl AgNO_3 nanowire solution was dropped onto glass. Rhodamine solutions in distilled water were prepared with concentrations varying from 10^{-3} M to 10^{-7} M. Afterwards, Rhodamine solutions were dropped onto AgNO_3 nanowire deposited glasses. Later, glasses were left to dry at room temperature for 20 minutes, following this procedure the SERS measurements were performed.

3. RESULTS AND DISCUSSION

3.1. Raman spectrum of Rhodamine Molecule

As the first step of the Raman experiments, Raman spectrum of Rhodamine was obtained from the powder form of the sample directly and the resulting spectrum is presented in Figure 1. As seen from the figure, the peak observed at 612 cm^{-1} belongs to the C-C-C in-plane vibration mode, while the peak observed at 774 cm^{-1} belongs to the C-H out-of plane bending vibration mode. The peaks observed at 1189 cm^{-1} and 1509 cm^{-1} belong to C-H in-plane bending, C-H bending and C-C stretching vibration modes, respectively, while the peaks at 1362 cm^{-1} and 1650 cm^{-1} are attributed to aromatic C-C stretching modes. The obtained Raman spectra of powder sample are in agreement with the literature findings [12-16].

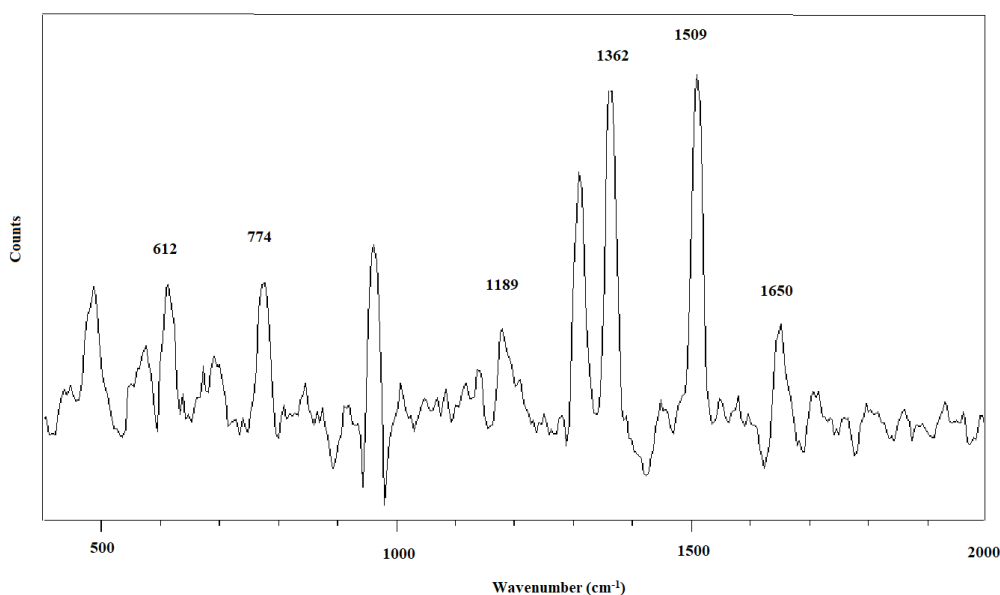


Figure 1. Raman spectrum of powder Rhodamine.

3.2. Characterization of Ag Nanowires as SERS Substrate

Ag nanowires' XRD pattern is presented in Figure 2. The crystalline peaks belonging to Ag nanoparticles are located at 38.192 , 44.391 , 64.585 , 77.578 and 81.735 , which is in accordance with the library values. The Miller index values belonging to these peaks are [111], [200], [220], [311] and [222], respectively. When Figure 2 is examined, one can clearly see that the intensity of the peak located at 38.192 with [hkl] value [111] is greater than the other Ag peaks, revealing that the development of the structure is towards silver nanoparticles [17,18]. Thus, one can conclude that XRD pattern of the structure reveals that the Ag nanoparticle synthesis is successful. The rest of the peaks located at 27.732 , 32.130 , 46.077 , 54.632 , 57.280 and 62.206 , which are labeled with Asterix (*) are residues of the NaCl solution which was utilized during the synthesis.

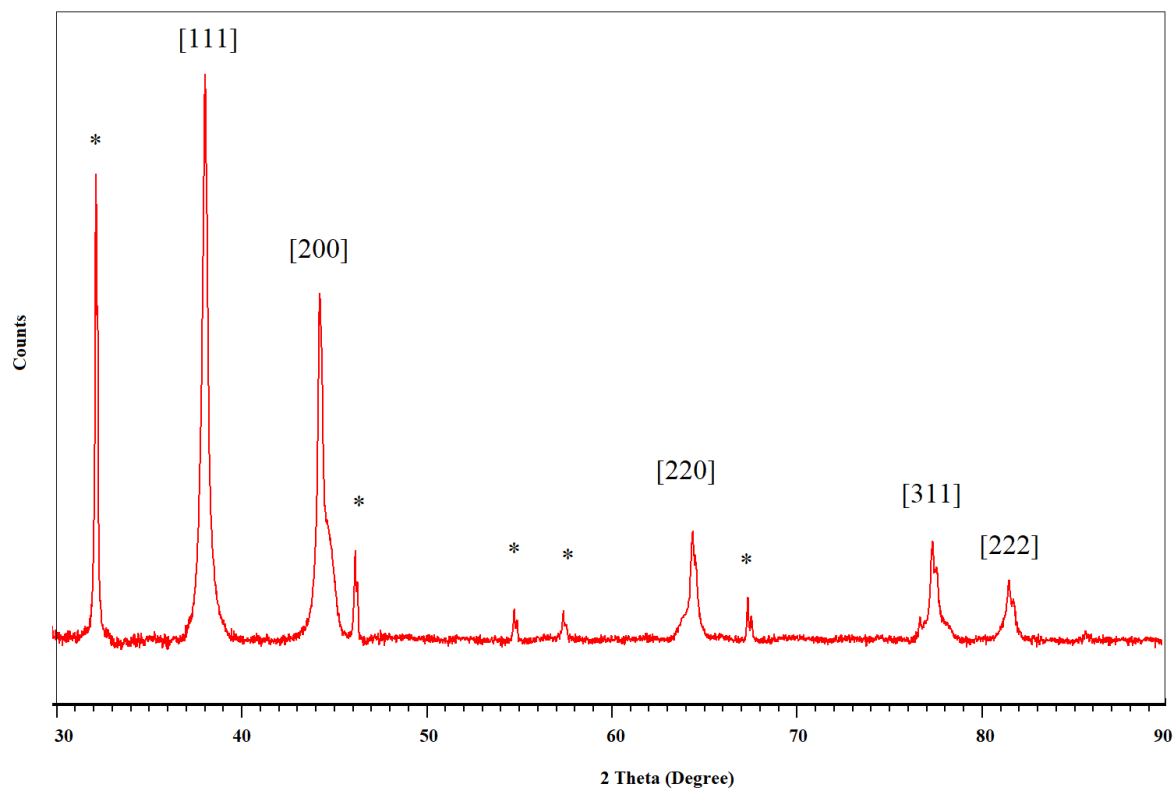


Figure 2. XRD Pattern of Ag Nanowires

SEM was utilized in order to examine the morphology of the Ag nanoparticles. Figure 3 exhibits the SEM image belonging to the nanoparticles. As the image reveals, nanoparticles have an average diameter of 90-100 nanometers. Furthermore, EDS analysis was performed via an Oxford Ultima EDS detector, which shows that the selected area in the SEM image consists of 96.50 % Ag, 2.28 % C and 1.22 % O in percentage.

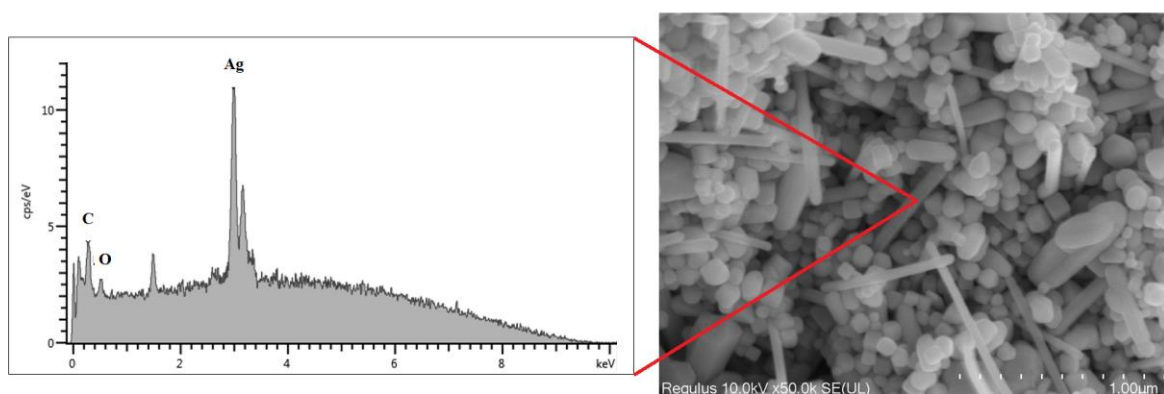


Figure 3. EDS Spectrum and SEM image of Ag Nanowires

3.3. SERS Studies of Rhodamine

In order to verify the SERS performance of Ag nanowires, various experiments were conducted for several concentrations of Rhodamine solutions. In these experiments, Rhodamine and Ag nanowires were utilized as the analyte molecule and the SERS substrate, respectively.

In Figure 4, SERS spectrum of Rhodamine molecule is presented at concentrations from 1×10^{-4} M to 1×10^{-7} M. As seen from Figure 4, Rhodamine's characteristic peak intensities decrease as the Rhodamine concentration decreases. In this study, three distinct peaks were selected for SERS studies. These peaks, which were selected because of their discrete locations, were observed at 612 , 1189 and 1362 cm^{-1} . Another reason for their selection is their visibility at even ultra-low concentrations. For the selected 3 peaks, concentration versus intensity graphics were obtained in order to demonstrate the relation between Rhodamine concentration and peak intensity. These graphs are presented in Figure 4. The correlation coefficients (R^2), which were calculated for the peaks located at 612 , 1189 and 1362 cm^{-1} were calculated as 0.9691 , 0.9572 and 0.9628 , respectively. These (R^2) values clearly demonstrate that Ag nanowires can be used for detection of Rhodamine at even low concentrations.

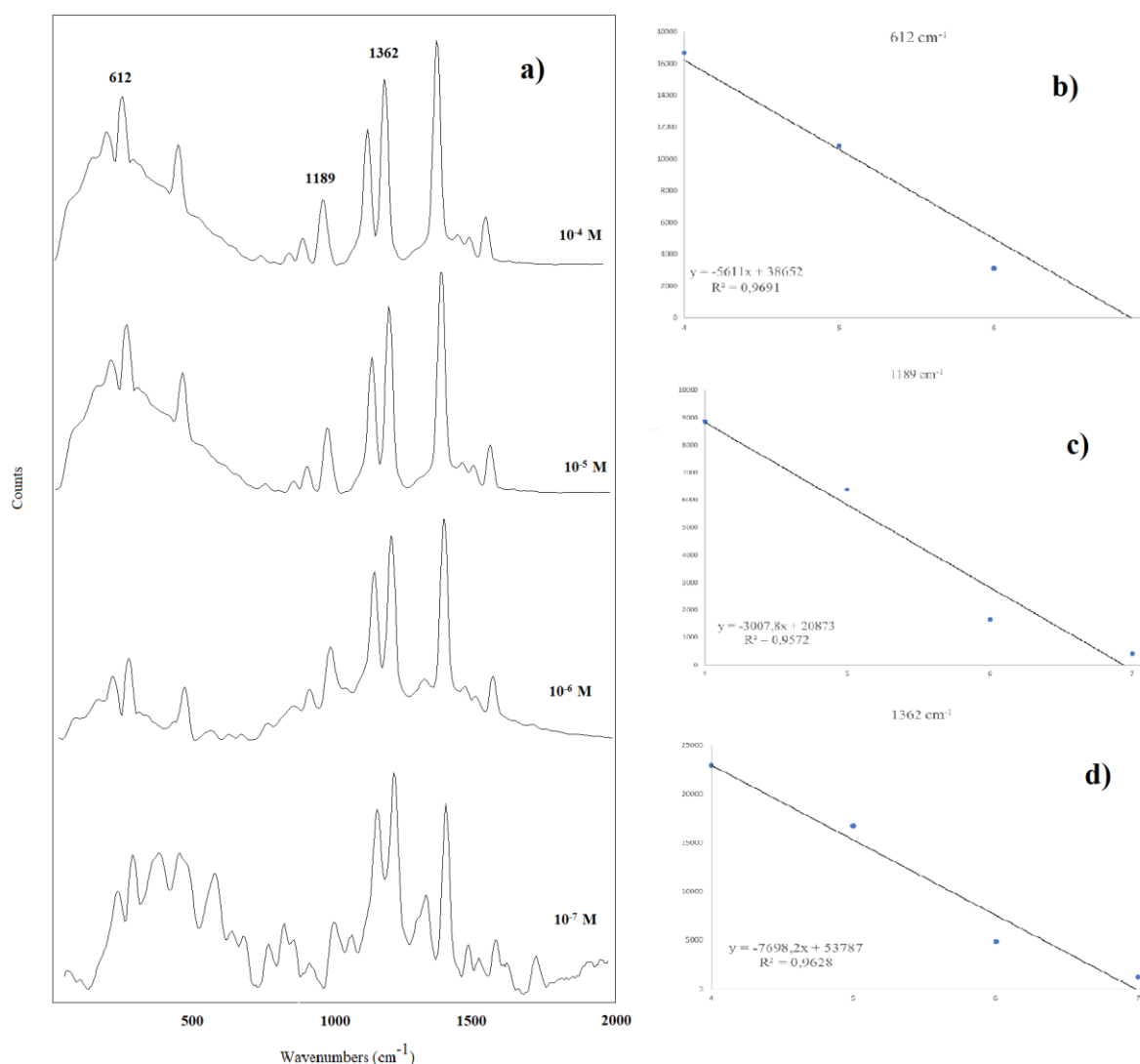


Figure 4. a) Raman spectrum of Rhodamine at concentrations from 10^{-4} to 10^{-7} and b,c,d) R^2 values for the selected peaks.

The next step is to calculate the enhancement factor (EF) which is another feature demonstrating the Ag nanowires' SERS capability. In order to calculate EF, the following formula was utilized [19]:

$$EF = \frac{I_{SERS} \times C_0}{I_0 \times C_{SERS}}$$

Here, I_{SERS} is Rhodamine's SERS intensity, I_0 is Rhodamine's normal Raman intensity, C_{SERS} (10^{-4} M) is Rhodamine concentration adsorbed on Ag Nanowires and C_0 is only Rhodamine concentration. Using the peak located at 612 cm^{-1} , Rhodamine's EF was computed as 1.39×10^6 .

In the literature, various studies discussed EF of several nano-scaled systems with different sizes and geometries. For example, Dikmen calculated the enhancement factor of the silver nanocubes as 3.13×10^8 for the characteristic peak observed at 1456 cm^{-1} of the amoxicillin molecule [20]. In another study, Francis et.al. calculated the enhancement factor for the characteristic peak of Rhodamine located at 1648 cm^{-1} as 6.93×10^{13} [21].

Additionally, the limit of detection (LOD) was determined using the following formula [22]:

$$LOD = \frac{3.3\delta}{k}$$

where, δ is the peak intensities' standard deviation and k is the calibration curve's slope.

In this study, LOD was calculated as 1.8×10^{-8} M, concluding that, depending on the SERS experiments conducted, Ag Nanowires can be utilized for detection of Rhodamine as SERS substrates at low concentrations.

3.2 Reproducibility and Stability of Ag Nanowires

Reproducibility is another important feature when utilizing specific detection applications. Two samples which were prepared under equal conditions were used in order to test the reproducibility of Ag nanowires. Four random points were selected on each sample and Raman spectrums were obtained from a total of eight points. The spectra belonging to these eight points are demonstrated in Figure 5. As seen from this figure, there are no discrepancies between the shapes of the peaks. For the selected peaks located at 612 , 1189 and 1362 cm^{-1} , relative standard deviation (RSD) values were calculated as well. These values were 10.285% , 9.887% and 4.815% for 612 , 1189 and 1362 cm^{-1} respectively, which clearly exhibits that Ag nanowires can be utilized for detection of Rhodamine in terms of their reproducibility features.

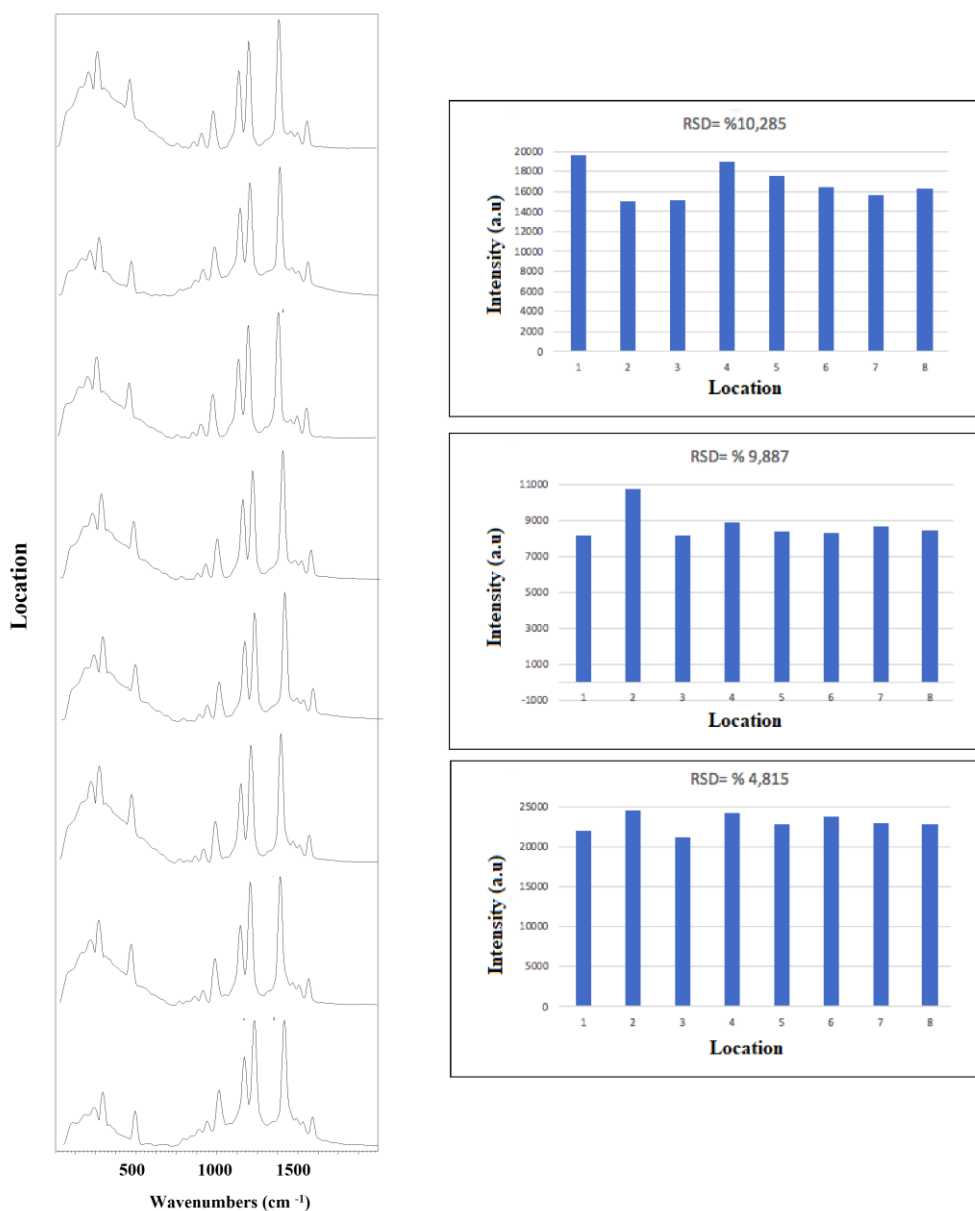


Figure 5. 8 random points' Raman intensities for Rhodamine adsorbed Ag NWs (left), RSD % values at 612, 1189 and 1362 cm⁻¹(right).

Reproducibility is a characteristic property which is easily affected by the stability of the substrate. For this reason, the substrate's stability should be checked when concluding about their convenience to be used as SERS substrates. In this study, Ag nanowires were left to ambient environment for 40 days and at the end of 40 days, their Raman spectra were collected again and the spectra were examined in order to check characteristic peak intensities at 612, 1189 and 1362 cm⁻¹. Figure 6 exhibits the spectrum obtained within 40 days of storage at ambient environment. The spectra demonstrate that there is no significant change in the intensities of the characteristic peaks, indicating that Ag nanowires are chemically stable substrates for Rhodamine detection via SERS method.

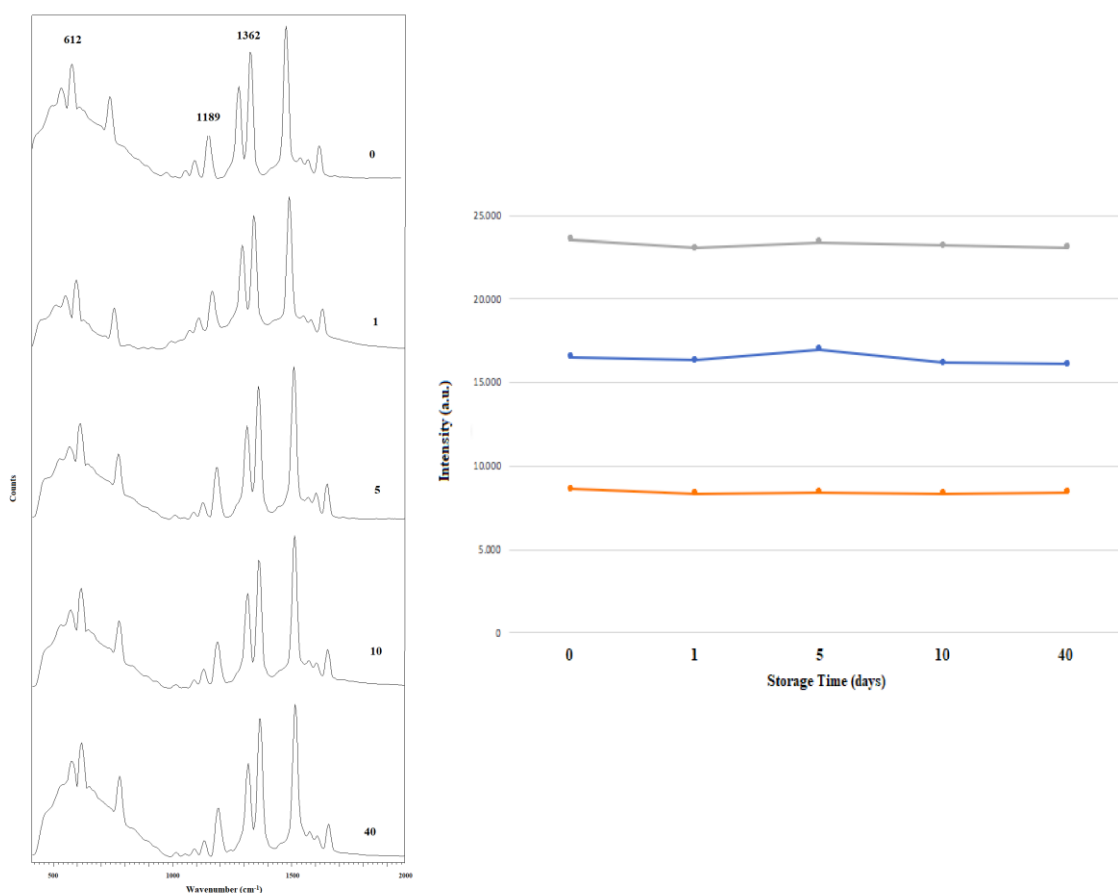


Figure 6. SERS spectra of Rhodamine on Ag NWs substrate stored within 40 days (a) and peak intensities of characteristic peaks of Rhodamine and storage times.

4. CONCLUSION

In this study, Ag nanowires were synthesized and this nanostructure was utilized as a SERS substrate in order to detect Rhodamine molecule. Rhodamine concentrations varying from 10^{-4} to 10^{-7} were prepared for SERS experiments. Afterwards, SERS experiments were conducted and three of Rhodamine's characteristic peaks, which are 612, 1189 and 1362 cm^{-1} were selected for SERS studies. LOD and EF values for Ag nanowires were calculated as $1.8 \times 10^{-8}\text{ M}$ and 1.39×10^6 respectively. In the study, Ag nanowire substrates made the Rhodamine detection possible at even low concentrations such as 10^{-7} M , by boosting up the Raman signals via electromagnetic and chemical enhancements. Moreover, this nanostructure exhibited high sensitivity, chemical stability and reproducibility for detection of Rhodamine molecule. Finally, it can be concluded that, Ag nanowires can be used for detection of Rhodamine at ultra low concentrations via SERS method as a reliable and sensitive substrate.

ACKNOWLEDGEMENT

The author would like to acknowledge Eskişehir Osmangazi University Central Research Laboratory Application and Research Center (ARUM) for their support.

CONFLICT OF INTEREST

The author stated that there are no conflicts of interest regarding the publication of this article.

REFERENCES

- [1] Fleischmann M, Hendra PJ, McQuillan AJ. Raman spectra of pyridine adsorbed at a silver electrode, *Chem. Phys. Lett.* 1974; 26 (2): 163-166.
- [2] Feldheim DL, Foss CA. *Metal nanoparticles: Synthesis, Characterization and Applications*. New York, USA: Marcel Dekker Inc., 2002.
- [3] Kneipp K, Moskovits MH. *Surface Enhanced Raman Scattering*. Berlin, Germany: Springer-Verlag, 2006.
- [4] Sun CH, Wang ML, Feng Q. Surface-enhanced Raman scattering (SERS) study on Rhodamine B adsorbed on different substrates. *Russ. J. Phys. Chem.* 2014; 89: 291–296.
- [5] Lombardi JR, Birke RL. A unified view of surface-enhanced Raman scattering. *Acc Chem Res.* 2009; 42(6): 734-742.
- [6] Valley N, Greeneltch N, Van Duyne RP, Schatz GC. A look at the origin and magnitude of the chemical contribution to the enhancement mechanism of surface-enhanced Raman spectroscopy (SERS): Theory and experiment. *J. Phys. Chem. Lett.* 2013; 4(16): 2599-2604.
- [7] Li X, Li M, Li J, Lei F, Su X, Liu M, Tan X. Synthesis and characterization of molecularly imprinted polymers with modified rosin as a cross-linker and selective SPE-HPLC detection of basic orange II in foods. *Analytical Methods* 2014; 6(16): 6397–6406.
- [8] Xu D, Li J, Zhang S, Zhang Y, Yang W, Wang Z, Chen J. A novel and controllable SERS system for crystal violet and Rhodamine B detection based on copper nanonoodle substrates. *Spectrochim Acta A Mol Biomol Spectrosc.* 2022; 5 (275): 121165.
- [9] Fang G, Wu YU, Dong X, Liu C, He S, Wang S. Simultaneous determination of banned acid orange dyes and basic orange dyes in foodstuffs by liquid chromatography–tandem electrospray ionization mass spectrometry via negative/positive ion switching mode. *Journal of Agricultural and Food Chemistry.* 2013; 61(16): 3834–3841.
- [10] Botek P, Poustka J, Hajšlová J. Determination of banned dyes in spices by liquid chromatography-mass spectrometry. *Czech J. Food Sci.* 2007; 25(1):17-24.
- [11] Sun Y. Silver nanowires – unique templates for functional nanostructures. *Nanoscale.* 2010; 2: 1626-1642.
- [12] Barveen NR, Wang TJ, Chang YH, Yuan-Liu Z. Ultrasensitive and reusable SERS probe for the detection of synthetic dyes in food industry through hybrid flower-shaped ZnO@Ag nanostructures. *Journal of Alloys and Compounds.* 2021; 861: 157952.
- [13] Shao J, Tong L, Tang S, Guo Z, Zhang H, Li P, Wang H, Du C, Yu XF. PLLA nanofibrous paper-based plasmonic substrate with tailored hydrophilicity for focusing SERS detection, *ACS Appl. Mater. Interfaces.* 2015; 7(9): 5391-5399.
- [14] Pal AK, Pagal S, Prashanth K, Chandra GK, Umopathy S, Bharathi Mohan D. Ag/ZnO/Au 3D hybrid structured reusable SERS substrate as highly sensitive platform for DNA detection. *Sensors and Actuators B: Chemical.* 2019; 279: 157-169.

- [15] Zhao K, Lin J, Guo L. ZnO/Ag porous nanosheets used as substrate for surface-enhanced Raman scattering to detect organic pollutant, *RSC Advances*. 2015; 5: 53524 – 53528.
- [16] Pal AK, Bharathi Mohan D. SERS enhancement, sensitivity and homogeneity studies on bi-metallic Ag-Cu films through tuning of broad band SPR towards red region. *Journal of Alloys and Compounds*. 2017; 698: 460-468.
- [17] Chen Z, Balankura T, Fichthorn KA, Rioux RM. Revisiting the polyol synthesis of silver nanostructures: role of chloride in nanocube formation. *ACS Nano*. 2019; 13: 1849-1860.
- [18] Wiley B, Sun Y, Mayers B, Xia Y. Shape-controlled synthesis of metal nanostructures: The case of silver. *Chem. - A Eur. J.* 2005; 11(2): 454-463.
- [19] Bell SEJ, Charron G, Cortés E, Kneipp J, Chapelle ML, Langer J, Procházka M, Tran VI, Schlücker S. Towards reliable and quantitative surface enhanced Raman scattering (SERS): from key parameters to good analytical practice, *Angew. Chemie Int. Ed.* 2020; 59(14): 5454-5462.
- [20] Dikmen G. Ultrasensitive detection of amoxicillin using the plasmonic silver nanocube as SERS active substrate. *Spectrochim. Acta A Mol. Biomol. Spectrosc.* 2022; 278: 121308.
- [21] Francis MK, Sahu BK, Bhargav PB, Balaji C, Ahmed N, Das A, Dhara S. Ag nanowires based SERS substrates with very high enhancement factor, *Physica E: Low-dimensional Systems and Nanostructures*. 2022; 137: 115080.
- [22] Kamal S, Chowdhury A, Yang TCK. Ultrasensitive SERS detection of Rhodamine 6G using a silver enriched MOF-derived CuFe₂O₄ microcubes substrate. *Spectrochim. Acta A Mol. Biomol. Spectrosc.* 2020; 235: 118262.



RESEARCH ARTICLE

A NEW BIO-INSPIRED WING DESIGN WITH 3D ADDITIVE MANUFACTURING
SCANNING AND PRINTING METHOD: MJF TECHNOLOGY

Neslihan AYDIN ^{1,*} 

^{1,*} Department of Machinery and Metal Technologies, Machinery Program, Bursa Uludağ University, Bursa, Turkey

ABSTRACT

In this study, unlike many wing profiles currently available, a new wing design has been carried out with bio-inspiration, which has attracted the attention of many scientists. There are many traditional methods in 3d additive manufacturing technologies. There are several types of 3D printing method. The four most preferred 3d printing methods are as follows. Fused Deposition Modeling (FDM), Stereolithography (SLA), Selective Laser Sintering (SLS), Multi Jet Fusion (MJF). MJF technology, one-to-one prototype production of wings with very small dimensions and aerodynamic structure has been achieved. In contrast to FDM and other additive printing technologies, it is possible to eliminate highly sensitive and high surface quality products.

Keywords: Bio-inspired wings, 3D additive manufacturing technologies, Multi Jet Fusion (MJF) technology

1. INTRODUCTION

Until the industrial revolution, different working styles were not adopted, except for handmade production and design. With the industrial revolution, the increase of mechanization and the introduction of new technologies into our lives has paved the way for achieving low material prices and fast delivery times. Despite all this forward-looking movement, the basic design and manufacturing process has not changed fundamentally over the past 100 years. Celebi et al. produced a damaged skull with a three-dimensional printer made of PLA material and performed prosthesis production with Ti-6Al-4V, a biocompatible material on the damaged area, and concluded that using three-dimensional printers used in the medical field will safely reduce the time of operation to be applied to the patient [1]. Karaman et al. conducted a study on the furniture sector; 8 mm diameter brackets were manufactured using ABS and PLA materials and used in furniture corner joints. As a result, it was noted that PLA material gives better results and three-dimensional production technology will also be used as an alternative in the furniture sector [2]. Ozgöl et al. in 2021, 3D printer design and production was carried out using FDM technology. Tensile and bending tests of 5 different geometrical hourglass were performed and their mechanical properties were examined. They emphasized that FDM technology is the most popular, most preferred production method and the cheapest method on the market[3].

With MJF (Multi Jet Fusion) technology, a different perspective has come to production and design. Today, many leading companies are taking advantage of MJF technology by using 3D printing method. In this way, it can produce products for final use or prototyping. The flexibility offered to the designer, the fact that the raw material is reusable for the next production, high surface quality, low cost per part and the ability to produce 10 times faster than competitors have allowed HP MJF technology to lead the industry.

1.1.Raw Materials used in 3D Printers

A lot of work is being done on new materials that eliminate some of the traditional obstacles to the non-choice of 3D printing, such as cost, quality and variety. When we look at the areas where MJF

*Corresponding Author : neslihanaydin@uludag.edu.tr

Received: 22.03.2023 Published: 27.12.2023

technology is used and the raw materials that can be used with this technology, we can examine the raw materials that can be used with the systems in two main categories respectively; Polyamides and Polyurethanes. The raw materials belonging to the Polyamide family that can be used in the HP MJF 4200 and HP MJF 5200 systems are PA12, PA12 Glass Beads and PA11. With the HP PA12, it is possible to produce powerful, functional and finely detailed parts. Due to its ability to ensure dimensional accuracy, provide fine details in complex designs, and be waterproof, it is used in the industry for the production of functional final parts/prototypes. PA12 is a thermoplastic that has excellent chemical resistance to oils, greases, aliphatic hydrocarbons and alkalis. In addition, thanks to the US FDA biocompatibility certificate, it is also possible to use it in the medical / medical field.

Since the HP PA12 Glass Beads are 40% glass bead filled thermoplastic material, it is possible to produce hard, functional and cost-effective parts with the product. For example, it is suitable to be used in the production of fixtures, models, body and housing parts. It is a material that has both favorable mechanical properties and high reusability.

It is possible to produce powerful, soft and functional parts with the HP PA11. PA11 is a thermoplastic with a low environmental impact, since it is a renewable raw material derived from vegetable castor oil. It has high impact resistance and flexibility, so it is suitable for use in areas such as prostheses, insoles, sports equipment, snap-in parts, movable hinges.

1.2. Polyurethane Raw Material

The raw materials belonging to the Polyurethane family that can be used in the HP MJF 4200 and HP MJF 5200 systems are ESTANE 3D TPU M95A1 and BASF Ultrasint TPU01. ESTANE 3D TPU M95A1 is a thermoplastic polyurethane (TPU) material developed by Lubrizol specifically for use in HP's Multi Jet Fusion 4200 3D printing solution. Its use is recommended for a wide range of applications that require high elasticity, good wear resistance and high impact absorption. BASF Ultrasint TPU01 is a multi-purpose thermoplastic polyurethane (TPU) material developed by BASF specifically for use in HP's Multi Jet Fusion 5200 Series 3D printing solution. TPU01 is an easy-to-print material with good UV and hydrolysis resistance and can only be used on HP Multi Jet Fusion 3D printing machines. This material can be used in the production of parts that are flexible, have high shock absorption, and whose thin structures require printing with high detail.

Today, due to the reasons mentioned above, this technology appears in many areas due to the point we have come to. With MJF technology, products with high strength and surface solubility, the ability to produce very detailed models without support, products with sealing and high strength can be obtained.

2.MATERIALS AND METHODS

Aerodynamics is the study of phenomena around objects moving in air, or a constant an event that occurs due to the movement of air around an object or one of these two in the form of a combination. In order to design and produce maple seed in the form of turbine blades in the form of first of all, there are about a hundred different lengths and sizes of various parks and gardens in Bursa. Dried maple seeds were collected on the expanses. Maple seeds were collected from different places and scanned as shown in Figure 1 so that they could be processed in 3D printers.

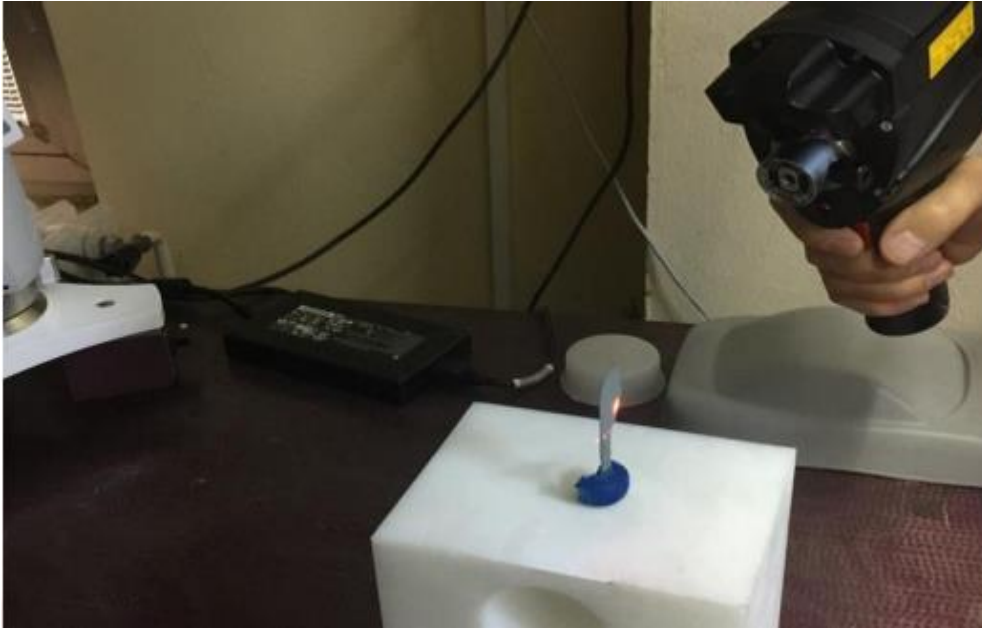


Figure 1. 3D laser scanning of maple seed

Maple seeds collected from parks and gardens from various places are processed by optical scanning and laser scanning the measurement. They will be scanned with scanners and transferred to a computer and will be 12-14-16 cm the model created in the figure has 3 prototype models of different lengths for experimental study. CAD files have been created.

3.RESEARCH FINDINGS AND DISCUSSION

3.1.Fused Deposition Modeling (FDM)

FDM (Fused Deposition Modeling) or FFF (Fused Filament Fabrication) is a technology used in three-dimensional printing technologies to create strong, durable and dimensionally stable parts with its dimensional accuracy and repeatability. It is an additive manufacturing technology that works with thermoplastics. It is based on the principle of melting thermoplastic parts made into filaments and applying them to the production table layer by layer. Fused Deposition Modeling, also known as FFF (Fused Filament Fabrication), can create any geometry you have in mind. For this reason, you can use the parts produced with this technology as end-use components in the aircraft industry, to meet all your prototype needs, such as production vehicles in the military industry or automotive factory. Tagliaferri in 2019 compared 4 different 3D production technologies in terms of production techniques and cost. They have suggested that FDM technology is the most preferred production technique in the Italian manufacturing and industrial sector for economic and mass production [4].

3.2.Stereolithography (SLA)

SLA (Stereolithography) technology is a 3D printer technology that works by curing the resin with light. Light solidifies a liquid resin through a process called photopolymerization, layering on the part to be produced. Currently, Stereolithography Technology is one of the most stable forms of dimensionality of 3D printing. There are two main types of SLA technologies: laser-based (typically abbreviated as SLA) or projection-based (DLP abbreviated for Digital Light Projection). Stereolithography was the world's first 3D printing technology, invented in the 1980s, and is still one of the most popular

technologies for professionals. Material manufacturers have created innovative SLA photopolymer resin formulations with a wide range of optical, mechanical, and thermal properties to match those of standard, engineering, and industrial thermoplastics.

3.3. Selective Laser Sintering (SLS)

Selective laser sintering is the most common additive manufacturing technology for industrial applications, trusted by engineers and manufacturers across different industries for its ability to produce strong, functional parts. Rosso et. al have experimented with the mechanical properties of materials produced by MJF and SLS 3d printers. They have observed that there is less porosity and ductility for MJF technology [5].

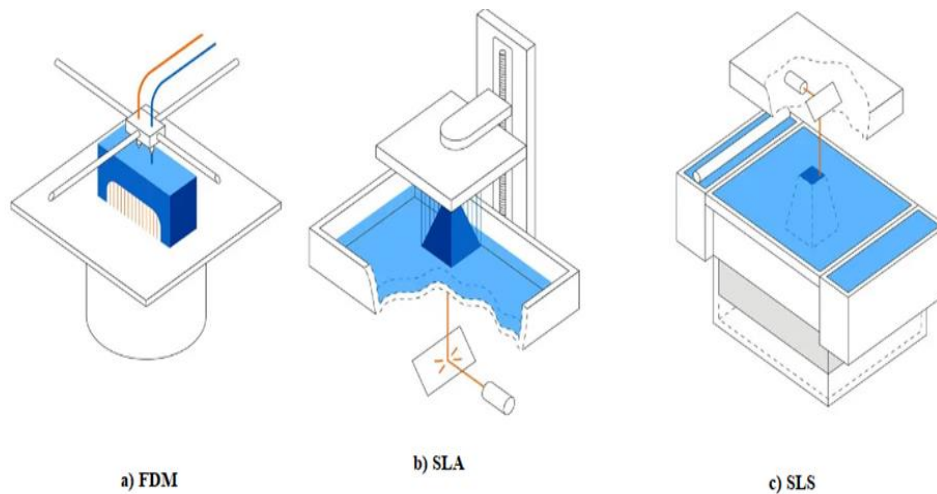


Figure 2. 3D Printer Technologies in used traditional methods. respectively; a)FDM, b) SLA, c)SLS

3.4. Multi Jet Fusion (MJF)

Multi Jet Fusion; as it is known, SLS is the 3D production technology used since the 1980s and is the most frequently preferred after FDM in the industry. After a long break, a new ambitious manufacturer has joined this production area. The differences between the HP Multi Jet Fusion MJF from the same family are as follows the differences between the Multijet Fusion (MJF) and Selective Laser Sintering (SLS) are as follows. In a study conducted by Mele et al. in 2019, they examined the capillary effects on the upper surface of 3d printed parts using MJF production technology [6].

Both technologies use PA material. But they diverge here on the issue of production. SLS sinters each section separately using a laser, while MJF produces a layer at each transition of the table [7]. The biggest difference when performing this operation is that it uses additives called “fusing agent” and “detail agent”. Thanks to the infrared heat source, the agent and PA material are cured to form a high-quality part, and the whole process takes 9 seconds, it takes. Obviously, MJF is much faster than SLS. Studies have shown that MJF is approximately 10 times faster [8].



Figure 3. Hp Jet Fusion 3D, used for scanning the prototype Maple seed 4200 Printer.

Our Maple prototype model has been scanned with the Breuckmann Smart Scan optical scanning device. After that, a scaling study was carried out at 12-14-16 cm. The prototype wing made of Polyamid12 material with HP 4200 3D Printer is manufactured using MJF(Multi jet fusion) technology.



Figure 4. Prototype aerodynamic bionic wing manufactured with 3D MJF Technology

Since the maple seed part is quite small in size and detailed in structure, MJF has been proven by experimenting as the most tolerant, precise manufacturing method when creating prototype aerodynamic wings. Other scanning methods have also been tried. However, it has been observed that the other FDM method is more suitable for larger car parts and engine components. In addition, the characteristics of the aerodynamic wing are such that such precise scans could not be obtained with other 3d printers.

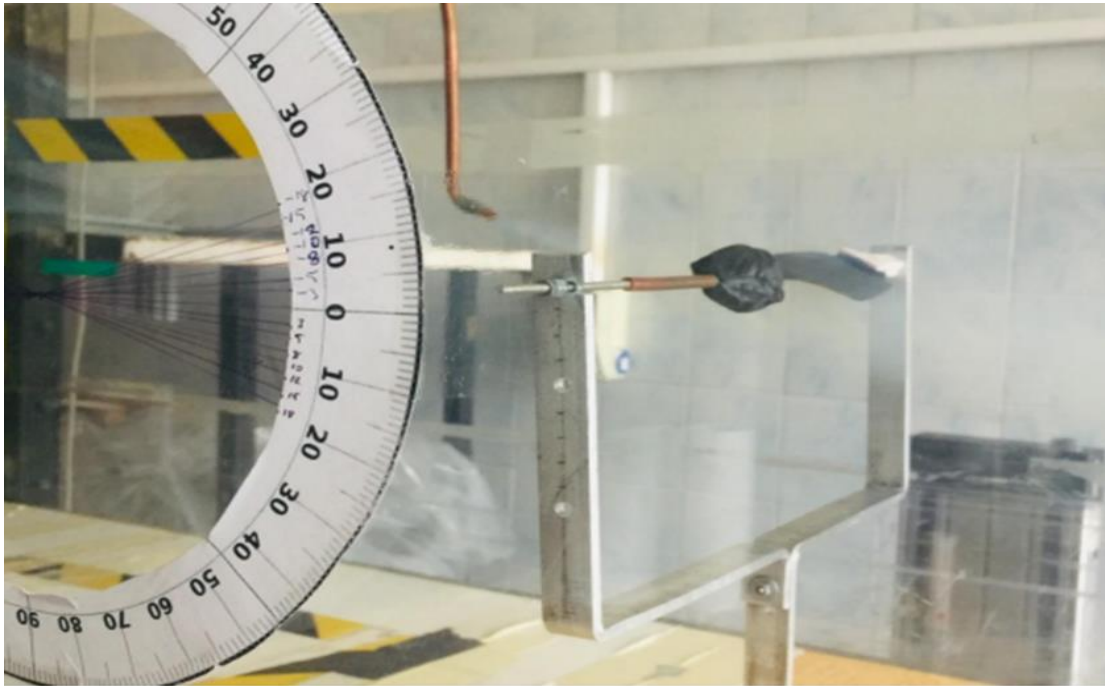


Figure 5. The use of a bionic wing in experimental equipment for the calculation of aerodynamic forces.

This bionic wing, scanned with a 3D printer MJF Technology, was mounted in a wind tunnel on an experimental set and aerodynamic forces were measured. Detailed one-to-one prototype production has been provided so that the dimensions of the aerodynamic wing are tested in the wind tunnel and optimal performance is ensured at the design point.

4.CONCLUSION

In this study, 3-D scanning of maple seed with 3-D printers and aerodynamic testing in a wind tunnel were studied to produce it. As a result of the studies carried out, it has been seen that MJF Technology from 3D printers provides faster and more detailed one-to-one prototyping than other SLA, FDM, SLS techniques. Finally, the achievements of MJF technology are as follows;

1. To provide isotropy in the produced models,
2. It has the lowest unit volume cost compared to competing technologies,
3. It can produce the desired number of products in the shortest time compared to other technologies.

ACKNOWLEDGEMENTS

The author would like to thank Hexagon 3D Scanning Materials Company and Poligon R&D staff for their help in scanning the three-dimensional wing. The author has done scientific writing and scientific contribution processes alone.

CONFLICT OF INTEREST

The author declares that she has no known competing financial interests or personal relationships that could have appeared to influence the work reported in this paper. In addition, all materials are available in the study. In addition, the author would like to state that there was no support or funding from any institution in the preparation of this study.



REFERENCES

- [1] Celebi A, Tosun H, Oncag AÇ. Manufacturing A Damaged Skull with 3D Printer and Implant A Design, *international Journal of 3d Printing Technologies And Digital Industry*, 2017; 1(1): 27-35.
- [2] Karaman A, Yıldırım MN, Yaşar ŞŞ. Determination of Bending Moment Capacity on “L” Type Furniture Corner Assembly Elements Produced by 3D Printers, *Gümüşhane Üniversitesi Fen Bilimleri Dergisi*, 2020; 10(4): 1057-1065.
- [3] Özgül HG, Tatlı O. 3d Printer Design, Manufacturing And Effect of Infill Patterns On Mechanical Properties. *Icontech International Journal*, 2020; 4(1), 13-24.
- [4] Tagliaferri V, Trovalusci F, Guarino S, Venettacci, S. Environmental and Economic Analysis of FDM, SLS and MJF Additive Manufacturing Technologies. *Materials*, 2019;12(24), 4161.
- [5] Rosso S, Meneghello R, Biasetto L, Grigolato L, Concheri G, Savio G. In-depth comparison of polyamide 12 parts manufactured by Multi Jet Fusion and Selective Laser Sintering. *Additive Manufacturing*. 2020;36. 1-13.
- [6] Mele M, Campana G, Monti GL. Modelling of The Capillarity Effect in Multi Jet Fusion Technology, *Additive Manufacturing*, 2019;30, 100879.
- [7] Habib FN, Iovenitti P, Masood SH, Nikzad M, Fabrication of Polymeric Lattice Structures for Optimum Energy Absorption Using Multi Jet Fusion Technology, *Materials and Design*, 2018;155. 86-98.
- [8] Aydın N, Caliskan ME, Sabirli MU, Karagoz I. An experimental study of the aerodynamic performance of a maple wing model at low Reynolds numbers, *Mechanics Research Communications*, 2023;130. 104104.



RESEARCH ARTICLE

INVERTED BRAYTON CYCLE ENGINE OPTIMIZATION FOR HYPERSONIC FLIGHT

Mustafa KARABACAK^{1,*} , Önder TURAN² 

¹ Department of Aeronautical Engineering, Faculty of Aeronautics and Astronautics, Necmettin Erbakan University, Konya, TR- 42140, Turkey

² Department of Airframe and Powerplant Maintenance, Faculty of Aeronautics and Astronautics, Eskişehir Technical University, Eskişehir, TR-26470, Turkey

ABSTRACT

The objectives of this study are to determine the optimum design parameters of a IBCE for hypersonic flight and to investigate the relationship between engine performance and design parameters. The investigation of these objectives is made first in the literature in this study. The optimization of inverted Brayton cycle engine ,IBCE, is performed using the particle swarm optimization method in this study. The optimum specific thrust, sT , value is reached by staying within the optimization constraints. When the total temperature of the cooling section is examined, a temperature above the freezing temperature of the air is obtained. A very high sT value, 451 N.s/kg is obtained at the hypersonic flight Mach Number (5 Mach) as a result of optimization. By the investigation, it is concluded that specific fuel consumption, SFC, reduces % 5.3 and sT increases % 5.6 dependent on preburner exit total temperature, PETT, change from 2100 K to 1400 K. Based on total temperature decrease at cooling section, $T_{cooling}$, change from 100 K to 500 K, it is seen that by the investigation, SFC increases %23.7 and sT increases % 13.1. It is seen that SFC reduces by % 6.3 and sT increases by % 35.9 depending on afterburner exit total temperature, AETT, change from 2000 K to 2300 K. It is observed that SFC reduces % 10.5 and sT increases % 11.7 dependent on total pressure ratio of turbine, π_t , change from 0.9 to 0.1.

Keywords: Jet engine, Optimization, Hypersonic flight, Inverted Brayton cycle, Engine performance

NOMENCLATURE

Abbreviations

AETT	Afterburner Exit Total Temperature
IBCE	Inverted Brayton Cycle Engine
PETT	Preburner Exit Total Temperature
SFC	Specific Fuel consumption (unit: g/(kN.s))

Greek Letters

τ	Total temperature ratio
π	Total pressure ratio

Latin Symbols

a	Sound speed (unit m/s)
c	Specific heat (unit: J/(kg.K))
K	Kelvin
m	Mass flow rate (unit: kg/s)
M	Flight Mach Number
$M_{flightlimit}$	Maximum Flight Mach Number thrust can be generated
N	Newton (unit: kg.m/s ²)
P	Pressure (unit: N/m ²)
R	Molar gas constant (unit: J/(K.kg))
s	Second
sT	Specific Thrust (unit: (m/s))

*Corresponding Author: karabacak7@itu.edu.tr

Received: 25.03.2023

Published: 27.12.2023

T	Temperature (unit: K)
$T_{cooling}$	Total temperature decrease at cooling section
$T_{c\,limit}$	Total temperature limit of engine gas flow at compressor exit
$T_{flow\,limit}$	Total temperature limit of engine gas flow at specific engine section
$T_{material\,limit}$	Material temperature limit
$T_{n\,limit}$	Total temperature limit of engine gas flow at nozzle inlet
$T_{t\,combuster\,exit\,limit}$	Combustors exit total temperature limit of gas flow
$T_{t\,limit}$	Total temperature limit of engine gas flow at burner exit
$T_{t\,flow\,limit}$	Allowable total temperature limit of engine gas flow
$T_{t\,cooling}$	Engine gas flow total temperature decrease at cooling section
V_{flight}	Flight velocity
γ	Specific heat ratio

Subscripts

a	Ambient
p	Constant pressure

Superscripts

afterburner	Afterburner
c	Compressor
preburner	Preburner
t	Total, Turbine
total	Total
1,2,3...	Engine section that expressed in nomenclature

1. INTRODUCTION

Engineering design concepts are created with the expectation of meeting the requirements of the engineering discipline [1,2]. While some engineering design concepts achieve success during the design period, many engineering design concepts have to wait until they are used in the engineering world related to their discipline [3,4]. However, whether engineering design concepts succeed on time or wait for the time when they will be applied to current practice, the maturation process of engineering design must begin in order to achieve success [5]. However, concepts with a waiting period requirement for applicability usually require a longer and more challenging maturity process.

IBCE is a concept that is categorized as a concept that requires a waiting period before it can be implemented [6]. During the maturity process of engineering design, the concept needs to be optimized to more adequately meet the design requirements depending on the design conditions [7,8]. Aviation design concepts are unexceptional with respect to maturity process requirements. To ensure a feasible design, aeronautical design concepts, such as jet engine concepts, should be optimized [9-11].

The design conditions are flight conditions for aero engines and the ICCE is expected to be used for hypersonic flight propulsion. Therefore, the ICCE should be optimized to meet the hypersonic flight requirements. To meet the hypersonic flight requirement, the IBCE concept is expected to provide sufficient thrust to overcome the enormous drag caused by hypersonic flight. Conventional engines cannot produce thrust or sufficient thrust in hypersonic flight, so engines used to propel hypersonic vehicles can produce sufficient thrust in hypersonic flight, and IBCE is a suitable candidate for these conditions.

It is expected that with the intercooled turbofan concept, the SFC is reduced and the thermal efficiency is increased [12,13]. Precooled cycles, such as the ATREX [14], the SABRE [15] and Scimitar [16] have been developed for the vision of next-generation low-cost transportation [17]. The state-of-the-art heat exchanger and manufacturing technology were investigated by Murray et al [18], and it was

concluded that heat exchangers based on current technology level are not sufficient for the aviation industry [17]. Using an inverted Brayton cycle to recover thermal energy from exhaust gas is a novel technological option that has not been widely discussed [19]. In the investigation of Kennedy et al [20], inverted Brayton cycle-based application on a reciprocating internal combustion engine was studied on a preliminary experimental setup for a gasoline engine; nevertheless, this is the only experimental conduct developed for this concept [19]. Besides, this concept expressed is also used to generate supersonic and hypersonic propulsion. The use of ramjet engine and scramjet engines to generate thrust for supersonic and hypersonic propulsion has been widely investigated. Generation of sufficient thrust through heat addition at supersonic speeds is still a challenging task due to the residence time of the supersonic speed in scramjet combustors is only a few milliseconds [21,22] Shock waves and fuel entrainment's coupled effect phenomena are required to perform plenty of situations efficiently [23,24,25] and to discover more [26]. Few of these coupled effect phenomenon transitions have been analyzed by researchers of supersonic flow engines. Although it has been working in the field of scramjet for a long time, the lack of required maturity in this field still shows that new engine concepts required to be investigated on. IBCE for higher speed aero vehicle which is a novel technological option that has not been investigated enough in the literature for reaching required maturity, is investigated in this study. Zhang et al. [27] studied exergy analysis and optimization of an inverted Brayton cycle and indicated that exergy loss of combustion in the cycle is the largest and followed by heat exchanger.

1.1. The Novelty of the Study

This study focuses on the optimization of IBCE to provide hypersonic flight. IBCE optimization is the first step in this study. First, in the literature, IBCE performance investigation dependent on design parameters is made in this study. Equations for IBCE are derived and demonstrations of these equations are made firstly in this study. Performance analysis depends on design parameters and design conditions are discussed in detail in this study firstly. The conventional particle swarm optimization algorithm firstly applied IBCE optimization in this study and the application of the particle swarm optimization algorithm on IBCE optimization is the novelty of this study.

The main novelties of this study are expressed as follows,

- IBCE performance investigation based on the design parameters of engine firstly made in this study.
- IBCE optimization for hypersonic flight is made in this study firstly.
- The particle swarm algorithm is applied to engine optimization for hypersonic flight subject firstly in this study.

2. SYSTEM DESCRIPTION

The IBCE components are illustrated in Figure 1 [28].

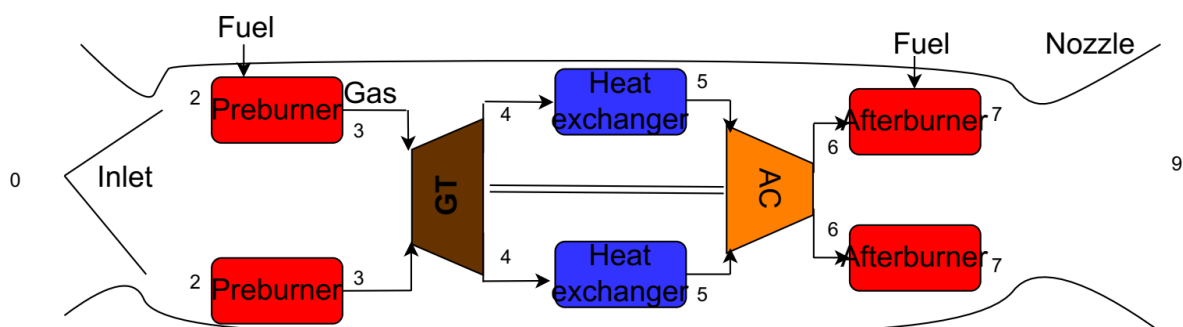


Figure 1. IBCE scheme and nomenclature [28]

Assumed that IBCE is ideal as expressed in Table 1 in more detail in this study.

Diffuser section reduces air flow velocity to the value that is suitable for preburner and later engine sections; preburner section increase total temperature of flow by using combustion energy; turbine section uses energy of flow to work compressor and so flow total temperature and flow total pressure reduce; heat exchanger or cooling section reduce total temperature of flow at constant flow total pressure to increase compressor exit total pressure; compressor increases total pressure and total temperature of flow and works by turbine power; afterburner increases total temperature of flow at constant flow total pressure; nozzle increases velocity of flow with reduce static pressure of flow and nozzle reduces static pressure of flow to value that is equal atmosphere pressure to obtain maximum thrust and minimum SFC on ideal conditions.

The assumptions for the engine system used in this study are expressed as,

- Isentropic compressor and turbine
- Constant pressure combustion and cooling
- No energy losses in the system
- No losses in the nozzle and diffuser
- % 100 combustion efficiency
- Constant flow characteristics
- The fuel mass flow rate is neglected.
- Optimum expansion in the nozzle

2.1. The Mathematical Model of the IBCE

The components of the IBCE concept and the nomenclature of the engine concept are shown in Figure 1.

The equations used to determine sT and SFC of the ideal IBCE dependent on the nomenclature shown in Figure 1 are expressed in Equations. (1) – (33).

It is assumed that the inlet flow Mach Number is equal to the flight Mach Number and by applying the isentropic relations of total temperature and total pressure at the inlet expressed as follows:

$$P_{t_0} = P_a \times \left(1 + \frac{\gamma - 1}{2} \times M^2 \right)^{\frac{\gamma}{\gamma - 1}} \quad (1)$$

$$T_{t_0} = T_a \times \left(1 + \frac{\gamma - 1}{2} \times M^2 \right) \quad (2)$$

Inlet flow pressure losses occur due to the viscosity of air and friction at the inlet solid layer between air flow and due to the shock generation due to the supersonic and hypersonic flow in this study, it is assumed that the ideal engine that is no losses of the pressure as described equation:

$$P_{t_2} = P_{t_0} \quad (3)$$

In the inlet heat flow between the inlet wall and the atmosphere, so it is expected that total temperature losses occur, but according to the ideal engine assumptions, there are no losses of total temperature at the inlet as shown in equation:

$$T_{t_2} = T_{t_0} \quad (4)$$

Turbulence is the desired state for combustion because of air and fuel mixing requirements. On the other hand, turbulence flow during combustion leads to total pressure losses, but in this study, losses are neglected as expressed in equation:

$$P_{t_3} = P_{t_2} \quad (5)$$

PETT is limited by the turbine section total temperature limit defined as;

$$T_{t_3} = T_{t_{limit}} \quad (6)$$

The turbine total temperature ratio is defined by isentropic relations by applying the isentropic turbine assumption as follows:

$$\zeta_t = \pi_t^{\frac{\gamma-1}{\gamma}} \quad (7)$$

The turbine exit total temperature depends on the total temperature ratio of the turbine, is expressed below:

$$T_{t_4} = T_{t_3} \times \zeta_t \quad (8)$$

It is assumed that the total pressure losses at the cooling section are neglected as determined by the following equation:

$$P_{t_5} = P_{t_4} \quad (9)$$

To reach a higher total pressure at the compressor exit, cooling is applied at the cooling section. Compressor inlet total temperature is dependent on the total temperature decrease at the cooling section as expressed as follows:

$$T_{t_5} = T_{t_4} - T_{t_{cooling}} \quad (10)$$

The energy balance between the turbine and compressor by applying assumption that the fuel flow rate is neglected and the specific heat, c_p , is constant, is defined as the follows:

$$m \times c_p \times (T_{t_3} - T_{t_4}) = m \times c_p \times (T_{t_6} - T_{t_5}) \quad (11)$$

The compressor exit total temperature based on the energy balance between the turbine and compressor is expressed:

$$T_{t_6} = (T_{t_3} - T_{t_4}) + T_{t_5} \quad (12)$$

The compressor total temperature ratio, ζ_c , dependent on compressor exit total temperature, T_{t_6} , and compressor inlet total temperature, T_{t_5} , determined as the following:

$$\zeta_c = \frac{T_{t_6}}{T_{t_5}} \quad (13)$$

Compressor total pressure ratio, π_c , is expressed by applying the isentropic compressor assumption, by isentropic relations as,

$$\pi_c = \zeta_c^{\frac{\gamma}{\gamma-1}} \quad (14)$$

Compressor exit total pressure, P_{t_6} , dependent on compressor total pressure ratio and compressor inlet total pressure, expressed as the following:

$$P_{t_6} = P_{t_5} \times \pi_c \quad (15)$$

$$T_{t_6} < T_{c_{limit}} \quad (16)$$

Similar to the preburner, afterburner exit total pressure equals the afterburner inlet total pressure as shown,

$$P_{t_7} = P_{t_6} \quad (17)$$

Similar to the preburner, the AETT is limited by the nozzle section total temperature limit as defined as,

$$T_{t_7} = T_{n_{limit}} \quad (18)$$

Similar to the inlet, there is heat flow between the nozzle wall and the atmosphere and heat losses due to the shock generation; therefore, it is expected that total temperature losses occur, but according to the ideal engine assumption, there are no losses of total temperature at the inlet as shown in equation:

$$T_{t9} = T_{t7} \quad (19)$$

Similar to the inlet, nozzle flow pressure losses occur, due to the viscosity of air and friction between the nozzle solid layer and air flow and due to the shock generation because of the supersonic and hypersonic flow in the nozzle. However, in this study, it is assumed that the ideal engine has no flow losses of the pressure, as expressed by the equation:

$$P_{t9} = P_{t7} \quad (20)$$

It is assumed that the optimum expansion in the nozzle so that nozzle exit static pressure expands to the ambient pressure, as expressed in equation,

$$P_9 = P_a \quad (21)$$

The nozzle exits flow Mach Number and static temperature, determined by the isentropic relation as expressed,

$$M_9 = \sqrt{\frac{2}{\gamma-1} \times \left(\frac{P_{t9}}{P_9} \frac{\gamma-1}{\gamma} - 1 \right)} \quad (22)$$

$$T_9 = \frac{T_{t9}}{1 + \frac{\gamma-1}{2} \times M_9^2} \quad (23)$$

Sound speed at nozzle exit condition and ambient conditions, and flow velocity of gas at nozzle exit and flow velocity at the engine inlet, which are dependent on sound speed, are calculated as expressed in the following equations,

$$a_9 = \sqrt{\gamma \times R \times T_9} \quad (24)$$

$$V_9 = a_9 \times M_9 \quad (25)$$

$$a_a = \sqrt{\gamma \times R \times T_a} \quad (26)$$

$$V_0 = M_0 \times a_a \quad (27)$$

The sT is determined depending on the flow velocity at the nozzle exit, V_9 , and inlet entrance, V_0 , and by applying the optimum expansion in the nozzle as,

$$sT = V_9 - V_0 \quad (28)$$

Engine flow energy level increasing between the combustor inlet and exit, is caused by the combustion of fuel so by applying this energy balance the fuel mass flow rate is estimated. It is assumed that the specific heat does not change due to the chemical reaction in the combustor. The fuel mass flow rate is at a very low level relative to the engine mass flow rate so it is neglected. All fuel that is mixed with air cannot be burned due to the imperfect mixing, but in this study, it is assumed that all fuel that is sprayed, be burned with air. Preburner, afterburner and total fuel mass flow rate is determined as,

$$m_{f_{preburner}} = \frac{m \times c_p \times (T_{t3} - T_{t2})}{Q_R} \quad (29)$$

$$m_{f_{afterburner}} = \frac{m \times c_p \times (T_{t7} - T_{t6})}{Q_R} \quad (30)$$

$$m_{f_t} = m_{f_{afterburner}} + m_{f_{preburner}} \quad (31)$$

Q_R , is the fuel heat-release rate level per unit fuel mass flow rate. The unit heat release is caused by fuel combustion, and the fuel mass flow rate is determined by the burner entrance and exit flow energy level and the heat of the fuel.

Thrust, T , depends on the sT and mass flow rate. SFC depends on the total fuel-mass flow rate, m_{ft} , and thrust. These are expressed as,

$$T = sT \times m \tag{32}$$

$$sfc = \frac{m_{ft}}{T} \tag{33}$$

3. INVESTIGATION OF THE EFFECT OF DESIGN PARAMETERS ON ENGINE PERFORMANCE

The base engine design parameter values and values of design conditions used to plot graphs that show the effect of design parameters on engine performance, are expressed at Table 1.

Table 1 Base engine design parameters

Design Parameters	Parameter Value
PETT	2050 K
π_t	0.1
$T_{cooling}$	400 K
AETT	2200 K
Flight Mach Number	5 Mach
Flight Altitude	11 km

3.1. PETT Effect on Engine Performance

sT reduces and SFC increases with PETT increases as shown in Figures 2 and 3 and this situation shows that reduce PETT increase performance. To obtain the best performance, PETT can reduce to a value that combustion do not be occurred and this value equals the diffuser exit total temperature that is expressed in Equation 34.

$$T_{t_0} = T_a \times \left(1 + \frac{\gamma - 1}{2} \times M^2 \right) \tag{34}$$

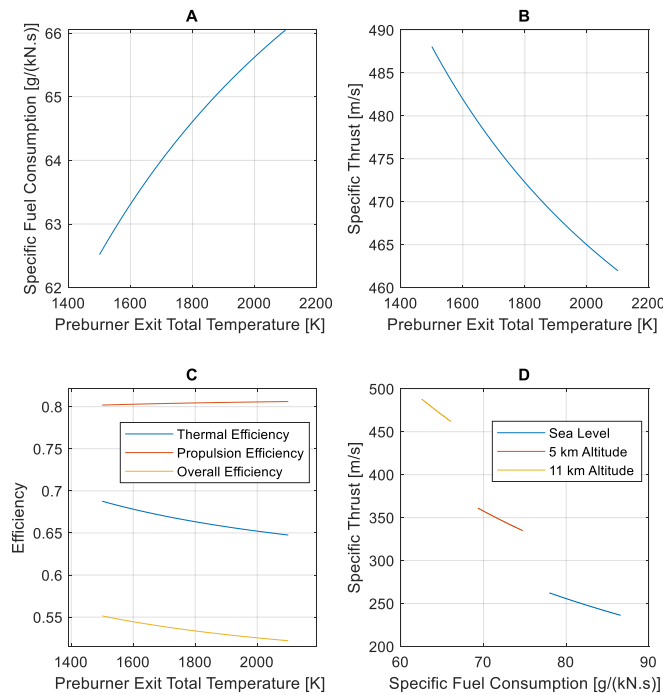


Figure 2. (A) SFC changes with PETT change (B) sT changes with PETT change (C) Engine efficiencies change with PETT (D) sT -SFC change with PETT at different altitudes

As can be observed in Figure 2 (A), the SFC decrease from 66.050 [g/(kN.s)] at 2100 K PETT to 62.518 [g/(kN.s)] at 1400 K PETT. The sT increase from 462.0 [m/s] at 2100 K PETT to 488.1 [m/s] at 1400 K PETT as shown in Figure 2 (B).

As seen in Figure 2 (C), the propulsion efficiency is 0.8019 at 1400 K PETT and 0.8061 at 2100 K PETT. Thus, the PETT has no significant effect on the thrust efficiency. The thermal efficiency is 0.6877 at 1400 K PETT and decreases to 0.6475 at 2100 K PETT. The overall efficiency decreases from 0.5515 at 1400 K PETT to 0.5220 at 2100 K PETT.

As seen in Figure 2 (C) propulsion efficiency increases slightly with PETT and on the other hand thermal efficiency and so overall efficiency reduce with PETT.

As shown in Figure 2 (D), sT is 262.4 [m/s] and SFC is 77.970 [g/(kN.s)] at 1500 K PETT and at 2100 K PETT, performance reduce to 236.3 [m/s] for sT and 86.583 [g/(kN.s)] for SFC at sea level. ST is 361.0 [m/s] and SFC is 69.326 [g/(kN.s)] at 1500 K PETT and at 2100 K PETT, performance reduce to 334.9 [m/s] for sT and 74.728 [g/(kN.s)] for SFC at 5 km altitude.

Two design objectives (sT-SFC) change compatible with each other depending on PETT as shown in Figure 2 (D). Although low PETT values are desirable in terms of performance, it is possible to reduce the PETT to the point where there is no fuel flow.

3.2. Turbine Total Pressure Ratio Effect on Engine Performance

sT increase and SFC reduce with π_t reduce as shown in Figures 3 (A) and 3 (B) this situation shows that reduce π_t increase performance. However, to reduce π_t , it is required that turbomachinery that has more stage and therefore engine have more weight and more complex design and this situation is not desirable for engine design.

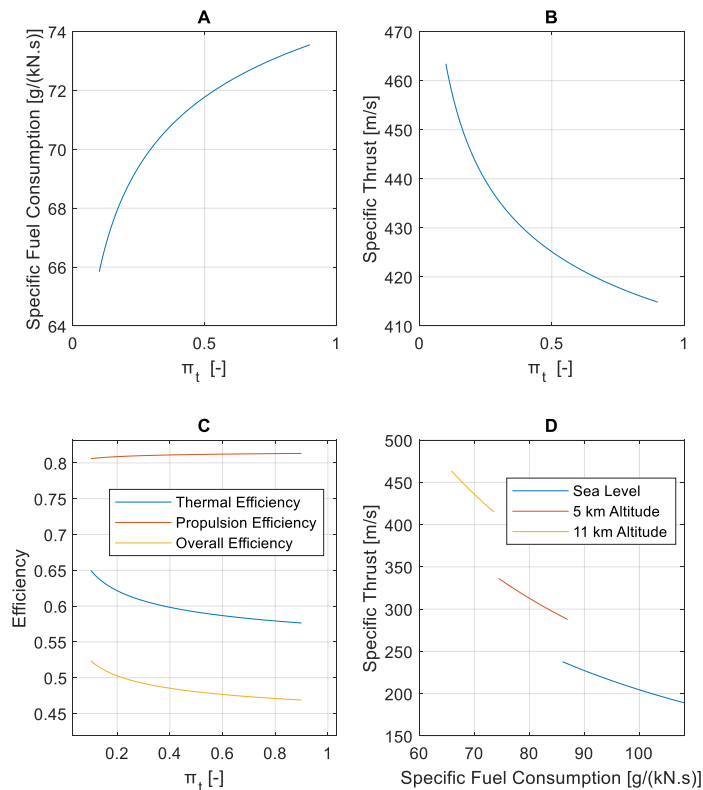


Figure 3. (A) SFC changes with π_t change (B) sT change with π_t change (C) Engine efficiencies change with π_t change (D) sT-SFC change with π_t change at different altitudes

As can be observed in Figure 3 (A), the SFC increase from 65.842 [g/(kN.s)] at 0.1 π_t to 73.551 [g/(kN.s)] at 0.9 π_t . The sT decrease from 463.4 [m/s] at 0.1 π_t to 414.9 [m/s] at 0.9 π_t as shown in Figure 3 (B).

As seen in Figure 3 (C), the propulsion efficiency slightly increase from 0.8059 at 0.1 π_t to 0.8132 at 0.9 π_t . Thermal efficiency is 0.6498 at 0.1 π_t and decreases to 0.5764 at 0.9 π_t . The overall efficiency decreases from 0.5236 at 0.1 π_t to 0.4637 at 0.9 turbine total pressure ratio.

As seen in Figure 3 (C) propulsion efficiency increases slightly with π_t and on the other hand thermal efficiency and so overall efficiency reduce with π_t similar PETT effect on efficiency.

As seen in Figure 3 (D), sT is 237.7 [m/s] and SFC is 86.051 [g/(kN.s)] at 0.1 π_t and performance reduce to 189.1 [m/s] for sT and 108.15 [g/(kN.s)] for SFC 0.9 π_t at sea level. ST is 336.4 [m/s] and SFC is 74.404 [g/(kN.s)] at 0.1 π_t and at 0.9 π_t , performance reduce to 287.8 [m/s] for sT and 86.961 [g/(kN.s)] for SFC at 5 km altitude.

As observed in Figure 3 (D), the two design objectives (ST-SFC) change compatible with each other dependent on π_t . Although low π_t are desirable, this parameter is limited by the requirement that the temperature at the exit the cooling section must not drop below a certain value.

3. 3. $T_{cooling}$ Effect on Engine Performance

ST and SFC increase with $T_{cooling}$ increase as shown in Figures 4 (A) and 4 (B) and this situation shows that lower values of $T_{cooling}$ is advantage for SFC objective and higher values $T_{cooling}$ has advantage for sT objective. Therefore, the tradeoff between the two design objectives, SFC and sT, should be made based on $T_{cooling}$.

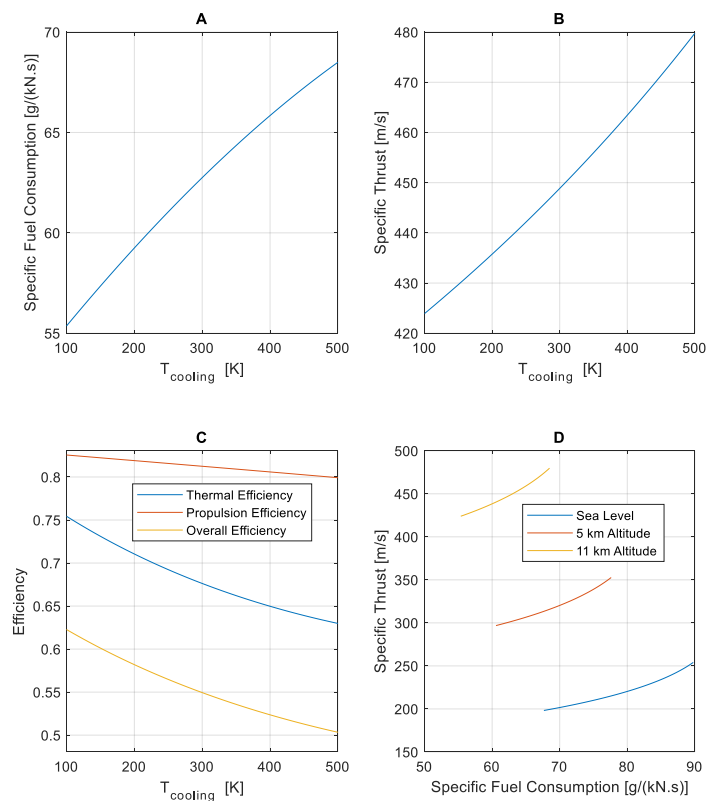


Figure 4. (A) SFC changes with $T_{cooling}$ change (B) sT change with $T_{cooling}$ change (C) Engine efficiencies change with $T_{cooling}$ change (D) sT-SFC change with $T_{cooling}$

As observed in Figure 4 (A) SFC increase from 55.360 [g/(kN.s)] at 100 K $T_{cooling}$ to 68.495 [g/(kN.s)] at 500 K $T_{cooling}$. It is observed that sT increases from 423.9 [m/s] at 100 $T_{cooling}$ to 479.8 [m/s] at 500 K $T_{cooling}$ (as seen in Figure 4 (B)).

Overall engine efficiency change from 0.6228 to 0.5033, propulsion efficiency change from 0.8255 to 0.7992, and thermal efficiency change from 0.7544 to 0.6298 as $T_{cooling}$ change from 100 K to 500 K as seen in Figure 4 (C).

As seen in Figure 4 (D), sT is 198.2 [m/s] and SFC is 67.672 [g/(kN.s)] at 100 K $T_{cooling}$ and performance change to 254.1 [m/s] for sT and 89.763 [g/(kN.s)] for SFC 500 K $T_{cooling}$ at sea level. sT is 269.9 [m/s] and SFC is 60.756 [g/(kN.s)] at 100 K $T_{cooling}$, and at 500 K $T_{cooling}$, performance change to 352.7 [m/s] for sT and 77.617 [g/(kN.s)] for SFC at 5 km altitude.

The two design objectives are in conflict with $T_{cooling}$ as can be seen in Figure 4 (D). This is because as the SFC increases, the sT value also increases. $T_{cooling}$ is limited not only by the capacity of the heat exchanger but also by the Pareto optimum of the design objectives.

Propulsion efficiency reduce slightly and thermal efficiency and so the overall pressure ratio decrease strongly with increase $T_{cooling}$ as observed in Figure 4 (C).

3.4. AETT Effect on Engine Performance

ST increase and SFC reduce with AETT increase as shown in Figures 5 (A) and 5 (B) and this situation shows that increases in AETT increases performance. However, increase in AETT is limited by the material resistance limit to temperature.

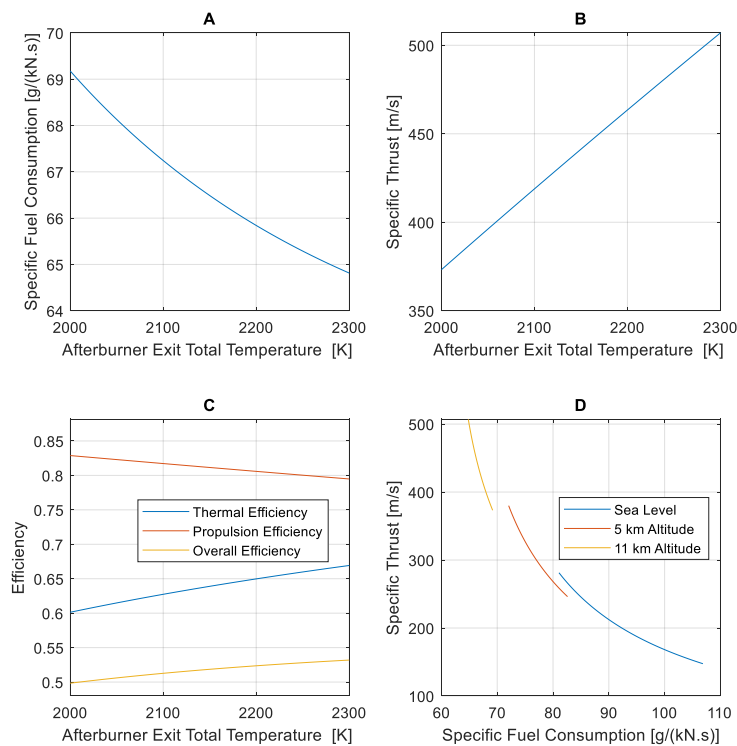


Figure 5. (A) SFC changes with AETT change (B) sT change with AETT change (C) Engine efficiencies change with AETT section (D) sT-SFC change with AETT at different altitudes

As can be seen in Figure 5 (A) the SFC reduces from 69.178 [g/(kN.s)] at 2000 K AETT to 64.814 [g/(kN.s)] at 2300 K AETT . It is observed in Figure 5 (B) that sT increases from 373.2 [m/s] at 2000 K AETT to 507.0 [m/s] at 2300 K AETT.

Overall engine efficiency increases from 0.4984 to 0.5319, propulsion efficiency reduces from 0.8288 to 0.7948 and thermal efficiency increases from 0.6013 to 0.6692 as AETT increase from 2000 K to 2300 K as seen in Figure 5 (C).

As observed in Figure 5 (D), sT is 147.5 [m/s] and SFC is 106.86 [g/(kN.s)] at 2000 K AETT and the performance changes to 281.3 [m/s] for sT and 81.068 [g/(kN.s)] for SFC at 2300 K AETT at sea level. Performance change from ST is 246.1 [m/s] and SFC is 82.601 [g/(kN.s)] at 2000 K AETT, to 380.0 [m/s] for sT and 72.050 [g/(kN.s)] for SFC at 2300 K AETT ,at 5 km altitude

Figure 5 (D) shows that SFC decreases with increasing sT. Although high AETT values are desired, it is known that this parameter is limited by the material temperature resistance.

3. 5. Coupled Parameters Effects on Engine Performance

The changes of sT and SFC depending on the turbine total pressure ratio and the total temperature decrease in the cooling section are illustrated in Figures 6 and 7, respectively. The high total temperature decrease in the cooling section and low turbine total pressure ratio values are advantageous in terms of sT. The high total temperature decrease value in the cooling section and the low turbine total pressure ratio values are advantageous in terms of SFC.

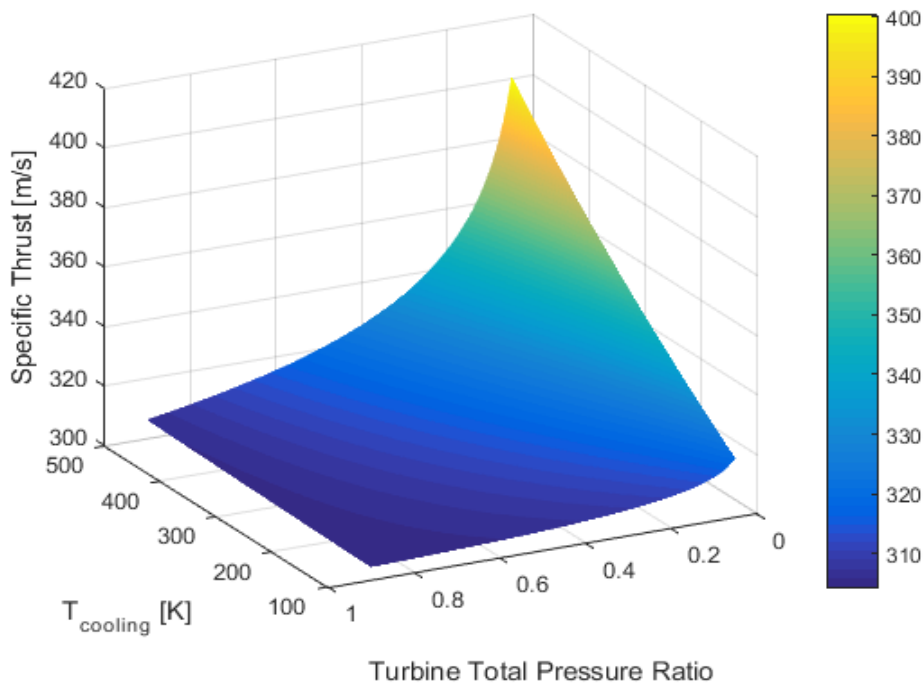


Figure 6. Change of sT dependent on turbine total pressure ratio and total temperature decrease at cooling section

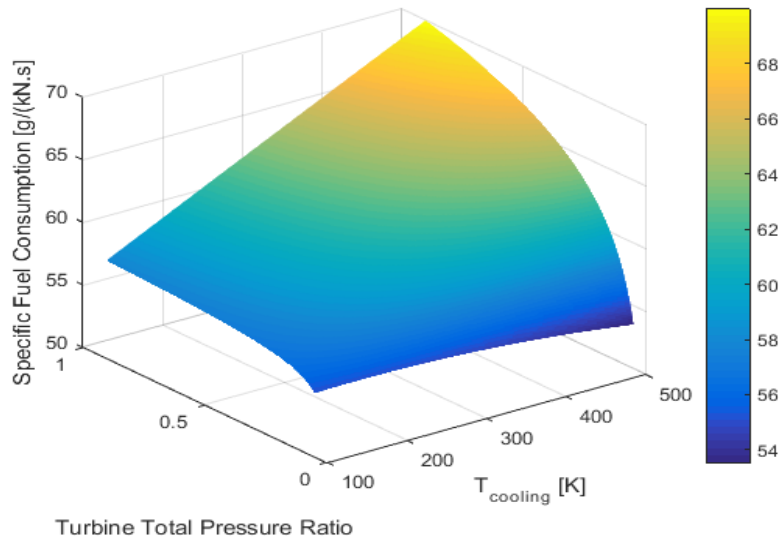


Figure 7. Change of SFC dependent on turbine total pressure ratio and total temperature decrease at cooling section π_t

4. OPTIMIZATION METHOD

Optimization is performed using the design parameters that are expressed in Table 2, based on the design conditions that are expressed in Table 2.

Table 2. Design specifications

Specifications	Parameters
Design Parameters	PETT
	π_t
	$T_{cooling}$ AETT
Design Conditions	Flight Mach Number
	Atmosphere Pressure
	Atmosphere Temperature
Parameters Dependent on Design Parameters	sT
	SFC
	Compressor Pressure Ratio
Design Objectives	sT
	SFC
Constraints	SFC < 55 g/kN. s
	Compressor Exit Total Temperature < 1000 K

Parameters dependent on the design parameters are expressed at Table 2. Parameters are dependent on design parameters and two of parameters dependent on design parameters are selected as design objectives as expressed in Table 2. One parameter dependent on the design parameters, compressor exit total temperature, is used as a constraint, as expressed in Table 2. Two design objectives are ranked based on design objective priority and based on this rank, one of them that is more important, sT, is used as design objective and the other one that is assumed to be less important, SFC, is used as the design constraint expressed in Table 2. The optimization parameters ranges are expressed in Table 3.

Table 3. Range of optimization parameters

Optimization Parameters	Parameter Range
PETT	1500 – 2200 K
π_t	0.1 - 0.9
$T_{coolina}$	100 - 500 K
AETT	2000 - 2300 K

The particle swarm optimization method is used in the optimization of the IBCE and the typical range of particle swarm optimization method control parameters is expressed in Table 4 [29-33].

Table 4. Particle swarm optimization algorithm control parameter typical range [33]

Parameter	Meaning	Typical Range
ω	Inertia Weight	0.8 - 1.2
c_1	Cognition Learning Rate	0 - 4
c_2	Social Learning Rate	0 - 4
N	Number of Particles	20 - 40

The optimization parameter values expressed in Table 5 are obtained by using the values in the mean of the typical range of particle swarm optimization method control parameters expressed in Table 4. In the particle swarm optimization of the IBCE, the optimization control parameters expressed in Table 5 are used in this study.

Table 5 Particle swarm optimization algorithm control parameter values

Parameter	Meaning	Value
ω	Inertia Weight	1
c_1	Cognition Learning Rate	2
c_2	Social Learning Rate	2
N	Number of Particles	30

The optimization algorithm is expressed basically in Figure 12 based on information expressed in Tables 5 and 6.

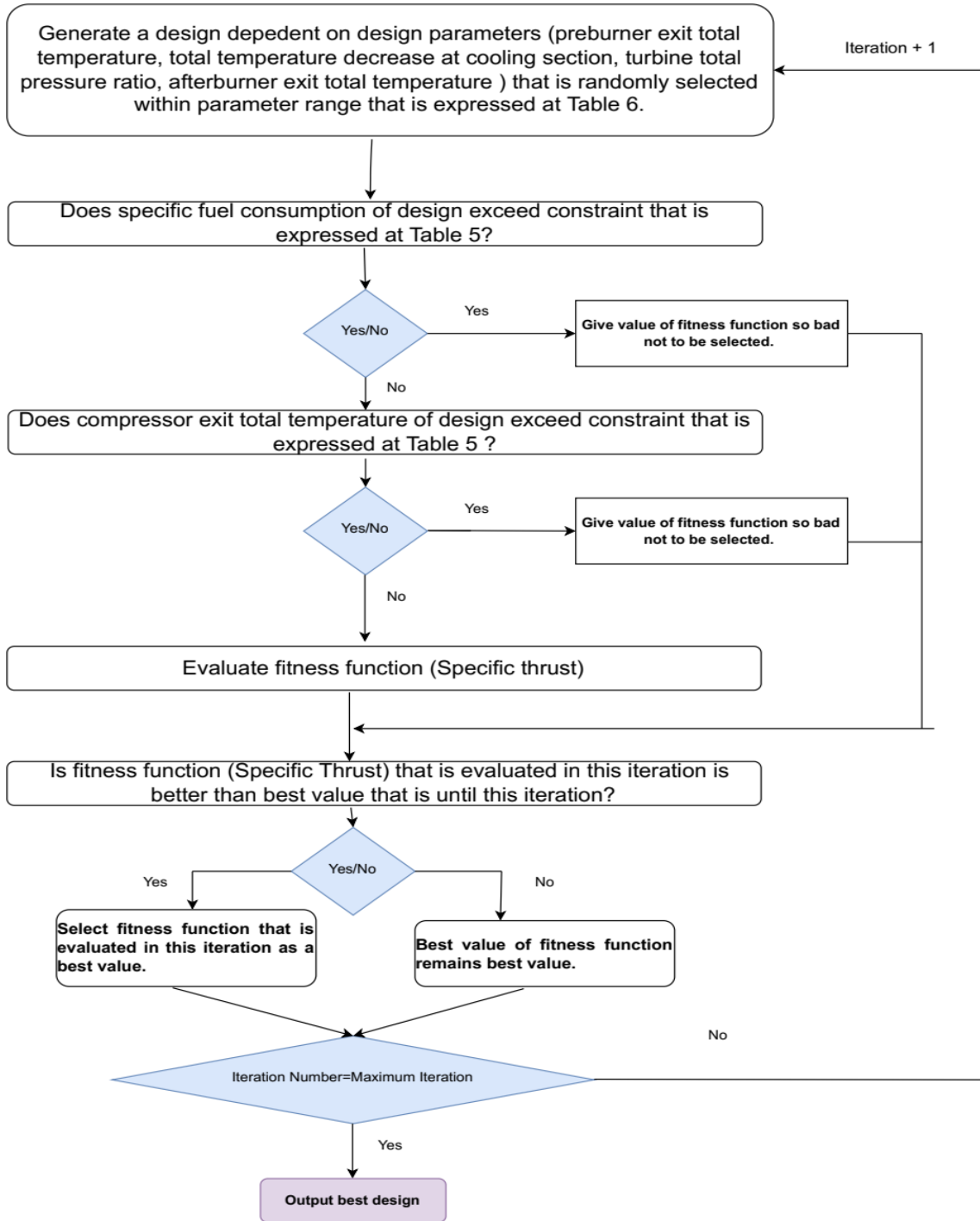


Figure 12. Optimization algorithm flowchart

5. RESULTS

The change of the optimum value of the design objective, sT and the optimum design parameters in optimization with each iteration are expressed Figure 13 and Figure 14, respectively.

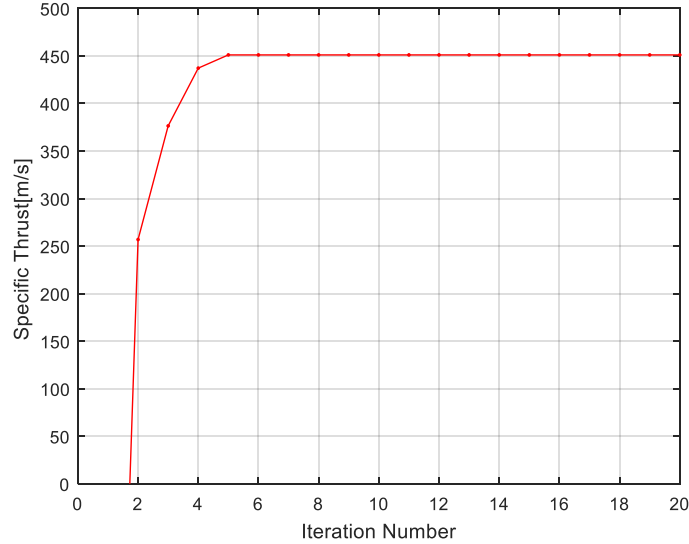


Figure 21. The change of optimum design objective obtained by optimization using genetic algorithms with each iteration

The optimization results of IBCE are given in Table 12. The optimum design parameters obtained as a result of the optimization of the IBCE are given in Table 13.

Table 12. Optimization Results

Optimization Characteristics	Parameter	Value
Optimization Objective	sT [N.s/kg]	451.052
Optimization Constraints	SFC [g/kN.s]	1000
	Compressor Exit Total Temperature [K]	276.9
	Cooling Section Exit Total Temperature [K]	

Table 13. The optimum values of design parameters for sT optimization

Optimization Parameters	Optimum
PETT	1500 K
π_t	0.1
$T_{cooling}$	500 K
AETT	2300 K

6. CONCLUSION

When the total temperature of the cooling section is examined, it is seen that a temperature above the freezing temperature of the air is obtained. A very high sT value is obtained at the hypersonic flight Mach Number (5 Mach) as a result of optimization. Concluded that IBCE is expected to be a candidate for hypersonic flight. There are concluded that:

- SFC reduces % 5.3 and sT increases % 5.6 dependent on PETT change from 2100 K to 1400 K.
- Based on $T_{cooling}$ change from 100 K to 500 K, it is observed that SFC increases %23.7 and sT increases % 13.1.
- It is observed that SFC reduces % 6.3 and sT increases % 35.9 dependent on AETT change from 2000 K to 2300 K.
- SFC reduces % 10.5 and sT increases % 11.7 dependent on π_t change from 0.9 to 0.1.
- Temperature decrease with increasing altitude effect performance dramatically as positive.
- Low PETT values are desirable in terms of performance.
- High AETT values are desired, so increasing material temperature with the development of technology positively effects performance.
- The two design objectives are in conflict with the total temperature decrease at cooling section. Total temperature decrease at cooling section increasing effect sT performance positively and effect SFC negatively.
- Low turbine total temperature ratio values are desirable for two design objectives (sT-SFC) but this parameter is limited by the requirement that the temperature at the exit the cooling section must not drop below a certain value

Heat exchanger efficiency and pressure losses can be determined by conceptual and CFD investigations. After heat exchanger efficiency and pressure losses will be determined real IBCE cycle analysis can be performed. Optimization can be performed based on the real cycle analysis of IBCE. The relationship between the design parameters and the performance of IBCE can be shown based on real cycle analysis.

CONFLICT OF INTEREST

The authors declare that they have no known competing financial interests or personal relationships that could have appeared to influence the work reported in this paper.

AUTHORSHIP CONTRIBUTIONS

Authors contributed equally to the study

Mustafa Karabacak: Software, Methodology, Writing- Reviewing and Editing, Validation; **Onder Turan:** Supervision, Conceptualization, Writing- Reviewing and Editing. The corresponding author **Mustafa Karabacak**, is responsible for ensuring that the descriptions are accurate and agreed by all authors.

REFERENCES

- [1] Cross N, Cross AC. Expertise in engineering design. Research in engineering design 1998; 10(3): 141-149.
- [2] Haik Y, Sivaloganathan S, Shahin, TM. Engineering design process. Cengage Learning 2015.
- [3] Hubka V. Principles of engineering design. Elsevier 2015.
- [4] Buede DM, Miller WD. The engineering design of systems: models and methods 2016.
- [5] Cross N. Engineering design methods: strategies for product design. John Wiley & Sons 2021.
- [6] Bianchi M, Negri di Montenegro G, Peretto A, Spina, PR. A feasibility study of inverted Brayton cycle for gas turbine repowering. J. Eng. Gas Turbines Power 2005; 127(3):599-605.

- [7] Farokhi S. Aircraft propulsion. John Wiley & Sons 2014.
- [8] Kurzke J. GasTurb 13: design and off-design performance of gas turbines. Aachen: GasTurb GmbH 2021.
- [9] Mattingly JD, Heiser WH, Pratt DT. Aircraft engine design. American Institute of Aeronautics and Astronautics 2002.
- [10] Pennington WA. Choice of engines for aircraft. Shell Aviation News. January 1959; 14–19 .
- [11] Raymer D. Aircraft design: A conceptual approach. AIAA 1989; 233–236.
- [12] Kyprianidis KG, Rolt AM, Grönstedt T. Multi-disciplinary analysis of a geared fan intercooled core aero-engine. In Turbo Expo: Power for Land, Sea, and Air, 2013; 55133: V002T07A027.
- [13] Kyprianidis KG, Rolt AM. On the optimisation of a geared fan intercooled core engine design. In Turbo Expo: Power for Land, Sea, and Air. 2014;45653: V03AT07A018.
- [14] Sato T, Tanatsugu N, Naruo Y, Omi J, Tomike JI, Nishino T. Development study on ATREX engine. Acta Astronautica 2000; 47(11): 799-808.
- [15] Webber H, Bond A, Hempzell M. Sensitivity of pre-cooled air-breathing engine performance to heat exchanger design parameters. In 57th International Astronautical Congress, 2006; D2-P.
- [16] Dong P, Tang H, Chen M. Study on multi-cycle coupling mechanism of hypersonic precooled combined cycle engine. Applied Thermal Engineering 2018; 131: 497-506.
- [17] Yu X, Wang C, Yu D. Thermodynamic design and optimization of the multi-branch closed Brayton cycle based precooling-compression system for a novel hypersonic aeroengine. Energy Conversion and Management 2020; 205: 112412.
- [18] Murray JJ, Guha A, Bond A. Overview of the development of heat exchangers for use in air-breathing propulsion pre-coolers. Acta astronautica 1997; 41(11): 723-729.
- [19] Di Battista D, Fatigati F, Carapellucci R, Cipollone R. Inverted Brayton Cycle for waste heat recovery in reciprocating internal combustion engines. Applied Energy 2019; 253(113565).
- [20] Kennedy I, Chen Z, Ceen B, Jones S, Copeland CD. Experimental investigation of an inverted Brayton cycle for exhaust gas energy recovery. Journal of Engineering for Gas Turbines and Power 2019; 141(3).
- [21] Huang W, Du ZB, Yan L, Xia ZX. Supersonic mixing in airbreathing propulsion systems for hypersonic flights. Progress in Aerospace Sciences 2019; 109(100545).
- [22] Huang W, Pourkashanian M, Ma L, Ingham DB, Luo SB, Wang ZG. Investigation on the flame holding mechanisms in supersonic flows: backward-facing step and cavity flameholder. Journal of Visualization 2011; 14: 63-74.
- [23] Khan A, Akram S, Kumar R. Experimental study on enhancement of supersonic twin-jet mixing by vortex generators. Aerospace Science and Technology 2020; 96(105521).

- [24] Verma KA, Pandey KM, Sharma KK. Study of Fuel Injection Systems in Scramjet Engine—A Review. *Recent Advances in Mechanical Engineering: Select Proceedings of ICRAME, 2021; 2020: 931-940.*
- [25] Verma KA, Kapayeva S, Pandey KM, Sharma KK. The recent development of supersonic combustion ramjet engines for augmentation of the mixing performance and improvement in combustion Efficiency: A review. *Materials Today: Proceedings 2021; 45: 7058-7062.*
- [26] Verma KA, Pandey KM, Ray M, Sharma KK. Effect of transverse fuel injection system on combustion efficiency in scramjet combustor. *Energy 2021; 218(119511).*
- [27] Zhang W, Chen L, Sun F, Wu C. Second-law analysis and optimisation for combined Brayton and inverse Brayton cycles. *International Journal of Ambient Energy 2007; 28(1): 15-26.*
- [28] Tsujikawa Y, Kaneko KI, Tokumoto S. Inverted Turbo-Jet Engine for Hypersonic Propulsion. In *Turbo Expo: Power for Land, Sea and Air, 2005; 47284: 343-349.*
- [29] Kennedy J, Eberhart R. Particle swarm optimization. In *Proceedings of ICNN'95-international conference on neural networks IEEE, 1995; 4:1942-1948.*
- [30] Poli R, Kennedy J, Blackwell T. Particle swarm optimization. *Swarm intelligence 2007; 1(1): 33-57.*
- [31] Hu X, Eberhart R. Multiobjective optimization using dynamic neighborhood particle swarm optimization. In *Proceedings of the 2002 Congress on Evolutionary Computation. CEC'02, 2002; 2: 1677-1681.*
- [32] Hu X. Particle Swarm Optimization. <http://www.swarmintelligence.org> [Online: accessed 16-May-2016]
- [33] Beltrán-Prieto JC, Komínková Oplatková Z, Torres Friás R, Escoto Hernández JL. A time performance comparison of particle swarm optimization in mobile devices. In *MATEC Web of Conferences 20th International Conference on Circuits, Systems, Communications and Computers (CSCC 2016). EDP Sciences, 2016.*



RESEARCH ARTICLE

A GIS-SUPPORTED ANALYSIS ON ACCESSIBILITY IN WOMEN-FRIENDLY SOCIETIES: EVALUATION OF WALKING ROUTES AT NIGHT HOURS

Ezgi TÜKEL^{1,*} , K. Mert ÇUBUKÇU² , Saye Nihan ÇABUK³ , Gürkan ÖZTÜRK⁴ 

¹ Department, of Remote Sensing and Geographical Information Science, Eskişehir Technical University, Eskişehir, Türkiye

² Department, of City and Regional Planning, Faculty of Architecture, Dokuz Eylül University, İzmir, Türkiye

³ Department of Geodesy and Geographical Information Technologies, Earth and Space Sciences Institute, Eskişehir Technical University, Eskişehir, Türkiye

⁴ Department of Industrial Engineering, Faculty of Engineering, Eskişehir Technical University, Eskişehir, Türkiye

ABSTRACT

Developing safe cities is one of the Sustainable Development Goals (SDGs) and a vital factor in creating sustainable communities and cities. From this point, ensuring that women use urban spaces accessibly and safely is crucial. This study aims to determine the walking routes between the most used venues in Kadıköy district, Türkiye, open at night hours, and the transportation points using GIS methods. Density analysis was made using Foursquare check-in data collected from 4 different categories in July 2021, and the closest walking routes between the locations and the bus stops were developed using closest facility analysis. The results were classified in a 5-scale suitability range, in which 5 refers to the highest density and more accessible (closest) bus stops. Zone 2 has 266 shortest routes, while zone 5 has 90 shortest routes and there are many eating and drinking places on the shortest routes. Lastly, some sample routes from the densest and least dense routes were observed using Google Street views in terms of safety criteria. The results and the approach used in this study are expected to encourage the local authorities and the decision-makers to improve safe access between the venues and transportation points.

Keywords: Women-friendly societies, Walking routes, Closest facility, Geographic Information Systems (GIS), Night hours

1. INTRODUCTION

Within its 2030 Sustainable Development Agenda, the United Nations outlined a list of sustainable development goals (SDGs). These objectives were introduced on January 1st, 2016, and will be in effect through 2030. There are 169 targets and 17 SDGs on the agenda, and 232 indicators will be used to gauge progress [1]. Sustainable cities and communities are one of the SDGs and besides various issues associated with creating urban and public sustainability, it also focuses on providing fair access to safe and inclusive public spaces for women [1]. However, when considering women's issues, making public places is extremely difficult and requires comprehensive and holistic implementations. Therefore, various dimensions should be considered to provide women-friendly public spaces. For example, urban plans must embrace gender equality principles for developing spatial solutions regarding social life, transportation, housing, and infrastructure services [2,3]. Gender-sensitive applications provide prevention of gender discrimination and work on changing women's status in society because women have a disadvantage in decision-making about urban life [4-6]. Urban buildings and public spaces should be redesigned to become gender-sensitive [7]. Mixed land use and clear street views in the city are essential to support women feel safer in urban places [8].

Many people congregate in public places in cities, especially on walking paths, squares, and public transportation areas [9, 10]. The street is one of the public places in a sustainable environment, and improving walkability is the main issue for people to feel more secure when walking [11-13]. Meetiayagoda [14] investigated pedestrian safety principles in Kandy Heritage City, Sri Lanka in terms

*Corresponding Author: ezgitukel@eskisehir.edu.tr

Received: 14.04.2023

Published: 27.12.2023

of parking vehicles on the street [15, 16]. Street lighting, one of the essential types of city lighting, is also critical in terms of security provided at night [17, 18]. Therefore, cities should be safer for women regarding pedestrian paths, transportation, and street lighting [8].

There are many studies about women in urban life. The research conducted by Umaña-Barrios and Gil [19] shows that women's walking distances are longer than that of men's and the primary public transportation users are women in Latin America. According to different studies, gender equity in transportation should consider design, cost, and safety [20, 21]. Women's issues are also examined from different perspectives and in different urban places such as residential, working, and public spaces. Ceylan [22], for example, implemented a questionnaire for men and women to detect the impacts of women's issues in different urban spaces. The results revealed that the workspaces should be designed considering the needs of the women, and safety and accessibility should be primary issues in the design of urban parks and streets. Lawton and Kallai [23] showed that women felt less safe and had more wayfinding anxiety than men in Hungary and the United States.

Urban spaces and women's safety have also been studied with crime-based viewpoints in the literature. Erkan and Sevin [24] investigated crime fear in Kadıköy, İstanbul, and revealed that people felt more fear at night hours. Another study surveyed in Santiago, Chile, found that women felt unsafe in the darkness in garages, public parks, and underpasses [25, 26]. Women avoid frightening routes, and this situation plays an important role in their travel behavior. Women also notified crime circumstances more than men [27, 28]. The significance and role of street lighting in decreasing crime in the urban environment is another essential emphasis in the literature [29, 30].

In Türkiye, similar studies and research have also been conducted. The Women-Friendly Cities Program is the first project in the country with a sustainable, gender-sensitive, and human rights-based approach. The Women-Friendly Cities United Nations Common Program was introduced in 2006 with the goal of integrating the principle of gender equality into local governments' planning and programming procedures while concurrently fortifying local governments and women's organizations and expanding opportunities [31]. The Women-Friendly Cities United Nations Common Program's second phase began in April 2011, upon the completion of the first phase [31]. Women-Friendly Cities Program suggests well-lighted public places and emergency call point emplacement for public places [32]. Streets can also be equipped with proper lighting and security camera solutions to provide safe walking access to the urban environment [33].

As it is clear from the past studies reviewed, creating safer cities is one of the SDGs of the United Nation's 2030 Agenda [1]. Studies show that urban safety planning is insufficient for women [34]. Public place safety is crucial for creating sustainable communities, and especially providing secure access for women in public spaces both day and night is a significant issue. In crowded cities, creating safe public spaces for women at night hours emerges as a problem that poses crucial risks for creating sustainable communities. Within this scope, it is necessary to support women's participation in social interactions in the city and ensure safe access between the urban spaces and public transportation areas at night hours.

Past studies mainly dealt with the social aspects of women's safety in the city or how safe cities can be created. The number of spatial analysis-based studies within this context is relatively scarce. This study determines the access routes between the popular/densely used urban spaces/uses in the study area open at night hours, as nighttime safety is particularly a critical issue for women. The study focuses on geospatial data-driven analyses to put forward spatial outputs rather than discussing the social aspects of women's participation in nighttime entertainment and views on safety issues. The results are expected to encourage the local authorities and the related parties to improve a wide range of implementations from the planning process to physical measurements in streets to achieve women-friendly and sustainable urban communities.

This study aims to evaluate the walking routes between particular urban spaces and public transportation stops at night hours in Kadıköy district, İstanbul, Türkiye, to provide easy access, especially for women, and an opportunity to evaluate and improve the determined walking routes. The district was chosen as the study area due to the high number of visitors, the existence of diverse socio-cultural facilities, and popular entertainment opportunities. First, the most popular urban destinations (restaurants, pubs, museums, etc.) open at night hours in the district were detected. Then shortest walking routes between the selected places and public transportation stops were determined using geographic information system (GIS) methods. Lastly, the routes were evaluated regarding some basic safety criteria for women. The safety criteria of the routes were based on studies from the literature [32, 33]. Accordingly, the sidewalk, lighting elements, security cameras, and emergency call points were examined to evaluate safe walking routes for women in the city.

2. STUDY AREA

İstanbul is an important historical city, the capital of the Eastern Roman and Ottoman Empires. With this historical background, İstanbul is the most populous city in Türkiye and the twenty-second in the world [35]. Besides, the city is a cosmopolitan urban area, including different communities and cultures [36, 37]. İstanbul connects the Asian and European continents and serves as a vital trade center, resulting in approximately 16 million inhabitants [1].

There are 39 districts in İstanbul. 25 are located on the European and 14 on the Asian side (Figure 1a). The Kadıköy district, located between $41^{\circ}07' 00''$ N and $29^{\circ}54'00''$ E coordinates, has been selected as the study area (Figure 1b). Kadıköy comprises an area of 25.20 km² for its 21 neighborhoods [38]. According to the address-based population registration system, the male population is 218.661, whereas the female population is 266.572. With this rate, the female population corresponds to 54.94% of the overall population of Kadıköy [35]. Kadıköy has critical activity/movement density and hosts various activity opportunities such as shopping, entertainment, art, and culture [39]. The number of people arriving at Kadıköy by public transportation reaches 900.000 people per day [24]. Consequently, the motivation for selecting the Kadıköy district as the study area is the presence of diverse mixed uses (residential, commercial, entertainment, etc.), availability of public services (transport and parks), diversity of transport modes, and the high number of visitors.

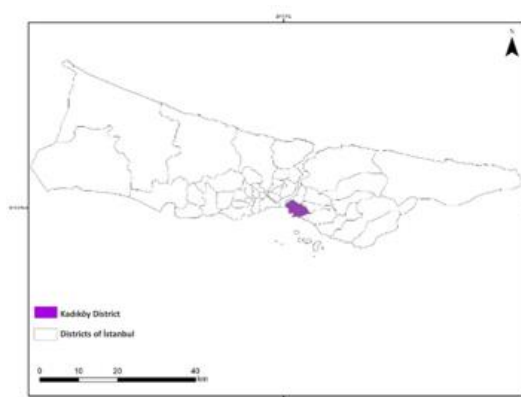


Figure 1a. Districts of Istanbul

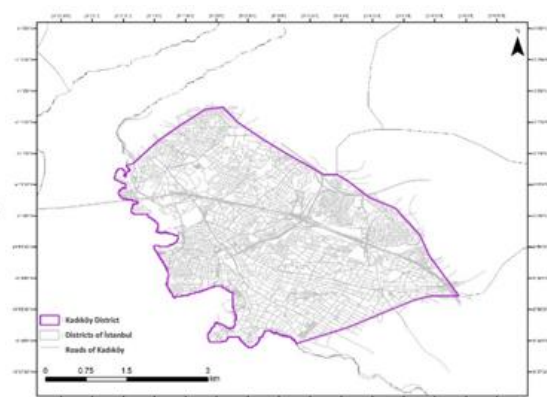


Figure 1b. Kadıköy District

3. MATERIALS AND METHODOLOGY

Foursquare users' check-in data and bus stop locations are the primary data sources of the study. Density analysis was applied to the Foursquare check-in places based on night hours, and buffer zones were created around bus stops. The resulting layers obtained from these two analyses were then overlaid.

The closest facility analysis was carried out from the night venues to the bus stops. Lastly, the sample routes were selected from the most accessible and least accessible zones, and these routes were evaluated from Google Street Views regarding the existence of some basic safety criteria.

Detailed information about the materials and methods of the study is explained in the following sections.

3.1. Materials

The primary material of the study is Foursquare check-in data, road networks, and bus stop locations. Daily Foursquare check-in data was collected using the Python API between June 30 and July 30, 2021, and then saved to the PostgreSQL database. In ArcGIS, Foursquare check-in data was filtered according to user visiting times, and only user check-in data between 10:00 p.m. and 3:00 a.m. were included in this study. The total number of all check-in data is 654, and the number of filtered check-in places is 390. The Foursquare data ignores the gender of the users since gender information for the Foursquare check-in data was unavailable. Table 1 shows the sample content of Foursquare check-in data.

Table 1. Data content of a sample night-time place

ID	5a9a9c0d9de23b77757f0695
Name	Kuba Pasta Cafe & Restaurant
Category	Cafés
Latitude	40.985099
Longitude	29.047953
Address	Feneryolu Sokağı, Feneryolu Mahallesi, Kadıköy, İstanbul (Fahrettin Kerim Gökay Caddesi)
Date	7/9/2021
Check-in Days/Hours	Monday 13:00:00-23:00:00 Wednesday 12:00:00-23:00:00 Friday 10:00:00-0:00:00

The places were divided into four categories (drinking and eating, entertainment, recreation, and shopping) according to their functions/use types. Table 2 shows the four categories of selected places. Drinking and eating places constitute approximately 70% of the overall data, shopping places constitute 8%, and recreation and entertainment comprise 11%.

Table 2. Details of places used in the study

Category of places	Details of place type
Entertainment	Art gallery, museum, theatre, gym, etc.
Drinking and eating	Restaurants, cafes, pubs, etc.
Recreation	Park, stadium, pool, etc.
Shopping	Shop, market, mall, store, etc.

Road networks, bus routes, and bus stop datasets were obtained from Open Street Map (OSM) sources using QGIS. Since the buses also operate at night, bus stop data were used as this study's primary public transportation data. The data of this study is illustrated in Figure 2.

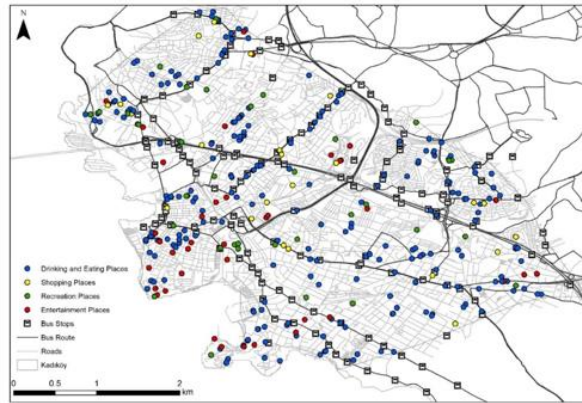


Figure 2. Dataset of the study

3.2. Methods

This study was conducted to determine the closest walking routes between the selected places open between 10:00 p.m. and 03:00 a.m. and the bus stop locations in the Kadıköy district. First, check-in data was obtained from Foursquare places API using Python code, and then data information was automatically saved in the database created in PostgreSQL. The data in the PostgreSQL database was recorded in the grid values of Kadıköy district coordinates created in QGIS and the check-in data was converted into point (vector) data.

The methods of the study include the implementation of some major GIS analyses used to develop density maps, buffer zones, overlaid layers, and the closest paths between the locations. The spatial layers of the study were developed with the application of the below-given methods:

- **Kernel Density Estimation (KDE):** The density estimations of the selected places were determined with the KDE method. KDE is based on a heat map distribution between core areas (kernels) and surrounding neighborhoods to create a cleaner display of break values for quantitative groups [40]. The various density levels in GIS-based KDE are determined using a radius input, and this radius of the circle can be adjusted manually or automatically [41]. The search radius is determined as 50 meters to include the night places located every 50 meters.
- **Buffer Analysis:** Buffer analysis was used to assess the distance to bus stops. A buffer is an area surrounding a geometric geographic feature measured in distance or time and is categorized into vector-based and raster-based techniques [42]. In this study, buffer analysis was applied to identify walking distances to public transportation stops. Past studies suggested walking distances between 300 and 800 meters for public transport [43, 44]. Therefore, 300-meter buffer zones were created around 141 bus stops in the study.
- **Closest Facility Analysis:** Routes were sought by calculating the shortest path between the locations and bus stops in the study area. Within the scope of this study, the shortest routes from the selected places to bus stops were calculated to examine the closest routes. The closest facility analysis finds the closest path for pedestrians or vehicles between incidents and facilities [45]. The closest facility is one of the network analysis techniques in GIS and networks consisting of edges (lines) and junctions (points) [46].
- **Overlay Analysis:** Overlay analysis is one of the multicriteria decision-making methods performed with GIS capabilities. It is widely used in various research fields, such as susceptibility mapping for land use, site selection, and potential zone detection [47-50]. The

densest and least dense zones in the study area were determined according to proximity to the bus stops and the density of places. In other words, the overlay method was used to detect the KDE areas falling into the 300-meter buffer zones around the bus stations. The shortest paths layer produced via closest facility analysis was also overlaid to evaluate all the analysis results in one major map. Analysis of the study was performed in ArcMap 10.3.

After determining the shortest routes, two sample routes were also specified from the study area's densest and least dense zones, and these routes were evaluated depending on the observations made on the Google Street views. The evaluation was simply performed visually focusing on the existence of safety criteria examples along the routes. Therefore no detailed measurements and detections were available. The safety criteria are the sidewalk, lighting elements, security cameras, and emergency call points [32, 33]. Fig 3 shows the methodology of this study.

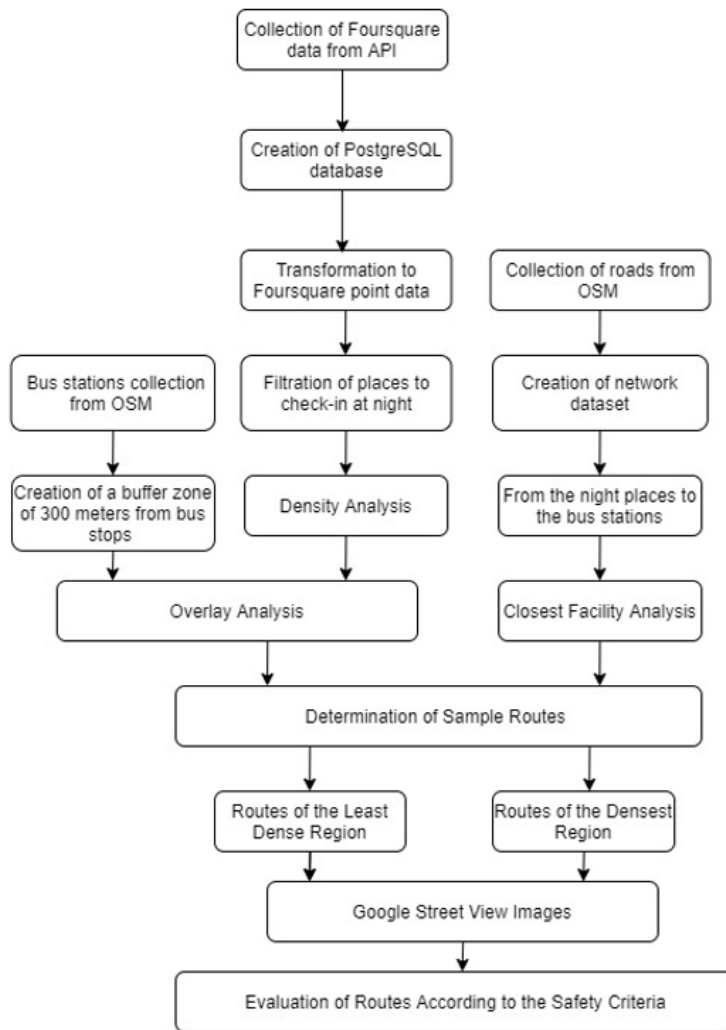


Figure 3. Methodology of the study

4. RESULTS AND DISCUSSION

The results include the spatial layers/outputs obtained concerning the study methodology explained in the relevant sections. As explained, KDE analysis was used to investigate the spatial distribution of places used at night using sample Foursquare check-in data ignoring the gender of the users (Figure 4). The density map was created according to the number of places at night. The analysis revealed that the densest locations are in the southwest Kadıköy district. According to the results, an average of 5 places exist in the least dense area, while the number of venues in the densest zone is around 25. The densest areas are mostly located in the southwest parts of the study area.

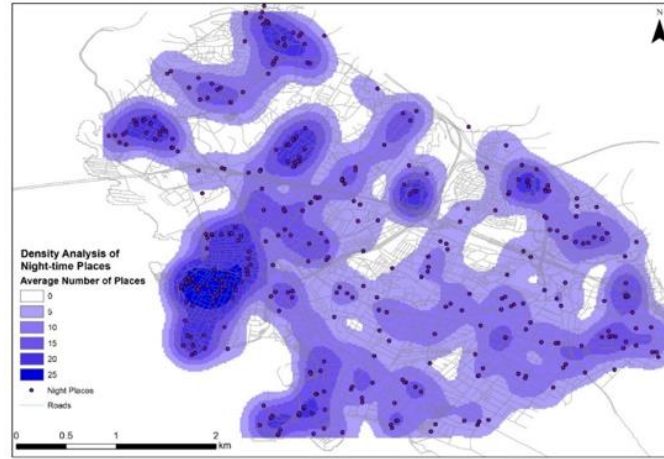


Figure 4. Density analysis of the urban places used at night

Buffer analysis results were made to determine the accessible zones to bus stops, and the dissolving process was applied to combine the buffer areas (Figure 5). According to the overlaid map developed with KDE and buffer analysis layers, the densest and least dense zones in the study area were determined according to proximity to the bus stops and the density of places (Figure 6). The density analysis results and buffer zones were overlaid in a 5-scale suitability range. 1 indicates zones with the least dense places with the furthest access to bus stops, while 5 refers to the highest density and more accessible (closest) bus stops. The closest routes between the locations and the bus stops are given in Figure 6.

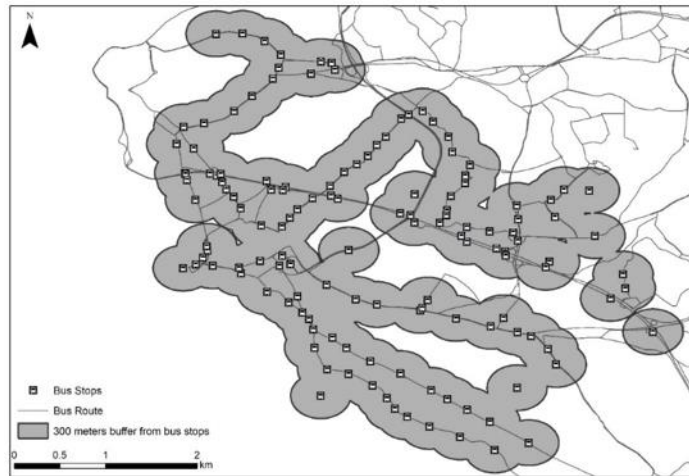


Figure 5. Buffer analysis of bus stops

According to the overlay results, in class 5 eating and drinking venues are the most common. Besides, the number of spaces listed under the recreation and sport category is more than the others in class 1. On the other hand, the closest facility results show there are a total of 780 shortest routes from nighttime venues to bus stops. The overlay result shows that the shortest routes in zone 2 are more than in other zones. Zone 2 has 266 routes, while zone 1 has 83 routes. Moreover, zone 3 has 303 shortest routes while zone 4 has 216 shortest routes. Besides these, zone 5 has the least number of routes and there are 90 shortest routes.

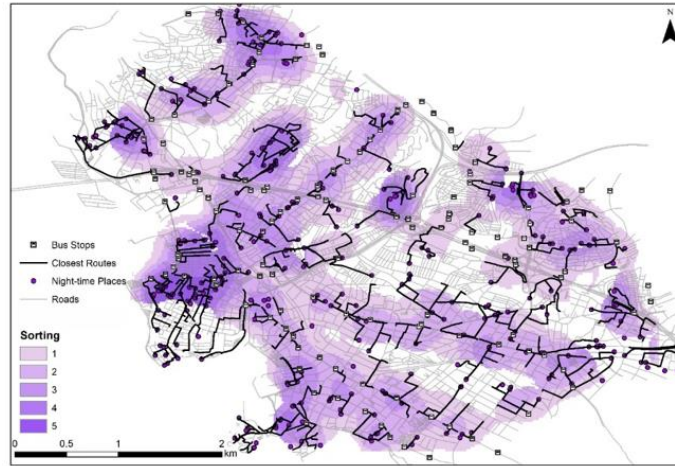


Figure 6. Overlay and closest facility analyses

The final phase of the study includes the observatory evaluations of sample routes. Sample routes were determined from the densest (Figure 7a) and the least dense (Figure 7b) zones according to overlay results. The densest and the least dense zones have more drinking and eating (bars, pubs, restaurants, etc.) places. Google Street views of the selected streets were visually evaluated according to the specified criteria given in Table 3.

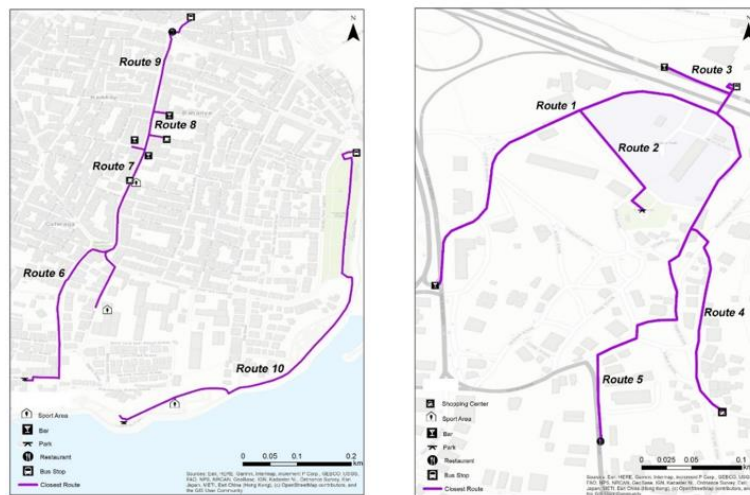


Figure 7. (a) Sample routes of the densest zone; (b) Sample routes of the least dense zone

Routes were evaluated to clarify whether particular safety criteria exist in the selected Google Street photos (Table 3). This is a subjective evaluation based on limited observations of the photos and may fail to reflect necessary details that should be detected comprehensively and quantitatively determined via field surveys or other scientific methods. In other words, the safety evaluation explained here is limited, based on personal observation, and aims to present a sample approach and fast evaluation of the routes.

Table 3. Evaluation of sample routes according to the specified criteria

	Sidewalk	Lighting elements	Security cameras	Emergency call points
Route 1	√	√	×	×
Route 2	√	√	×	×
Route 3	√	√	×	×
Route 4	√	√	×	×
Route 5	√	√	×	×
Route 6	√	√	×	×
Route 7	√	√	√	×
Route 8	√	√	×	×
Route 9	√	√	×	×
Route 10	√	√	×	×

Routes 1,2,3,4, and 5 are in the least dense zone, and 6,7,8,9, and 10 are in the densest zone. There are sidewalks and lighting elements on the routes in both areas, while the security camera (route 7) is available on the routes in the densest area.



Figure 8. Google Street Views of least dense zones' routes



Figure 9. Google Street Views of densest zones' routes

There are more night venues in the densest sample zone, and bus stops are more accessible. The abundance of lighting elements, the sidewalk, and a security camera on a route indicates a safer zone (Figure 8). On the contrary, in the least dense sample zone, safe walking routes meet fewer requirements that may pose risks for women or make them feel unsafe. Access to the bus stop from the overpass on Route 3 can be considered less secure than others. On Route 7, women may feel safer at night because there are security cameras on the street (Figure 9).

In the study, since gender information for the Foursquare check-in data was unavailable, it was impossible to detect the number of female or male users in the study area. However, the safety of walking routes from the venues to bus stops was assessed. The evaluations were made only based on the existence of particular elements along the walking routes. Comprehensive research and field surveys are necessary to determine the safety level of the selected routes exactly.

5. CONCLUSIONS

The main purpose of this study is to determine the walking routes at night between the highly preferred (dense) venues and the bus stops within the Kadıköy region, İstanbul, using GIS techniques. For this aim, various data were obtained from different sources, and spatial GIS analyses were performed. Foursquare, one of the social media datasets, was used in this study to detect the places primarily used at night. Bus stops were selected as public transportation data. In addition, the closest routes from the venues to the bus stops were determined in the case study. Sample routes from two zones were then evaluated according to the selected safety criteria. While determining the security criteria, studies for the safety of women in public spaces were used [32, 33].

Safe cities are among the 16 SDG goals and must be created and organized equally for all residents. This study assessed routes providing access between the locations used at night hours and the transportation points (bus stops), particularly to develop output for the relevant parties and the decision-makers so that women-friendly precautions can be taken to create sustainable urban spaces and communities.

However, the study has some limitations, especially in the data scope/characteristics, safety assessment, and generalizability. The study uses 1-month data from Foursquare, which, as mentioned in the material section, does not differentiate the users' gender. As a result, a gender-neutral approach was adopted, and gender-based specific concerns were ignored in the study. Further detailed analysis based on a more comprehensive and extensive check-in data set is strongly recommended for future research to allow for the possible seasonal changes, the beneficiaries of the target night places, the number of women users, the popularity of the places, and the target period. Utilizing women users' data and a higher number of check-ins within a broader time scope would provide more precious insights and results.

Furthermore, the sample safety assessment practice using Google Street View images is limited in terms of the scope of safety criteria and qualitative assessment methods. Here, the main focus was on the simple and fast detection of particular safety items on the street photos and lead the way for the relevant parties to conduct further and detailed examinations. Therefore, field surveys or other scientific methods to more comprehensively evaluate the safety concerns on the streets are suggested. A similar approach is also essential for future research when considering the data used to determine the routes. This study uses only one mode of public transport, the bus stops. It should be enriched with other modes, such as metro stations, taxis, tram, etc., to provide a comprehensive perspective on accessibility.

ACKNOWLEDGEMENTS

This article was produced within cooperation between Başarsoft Information Technologies and Eskişehir Technical University under the TUBITAK 2244 project numbered 119c200, executed by Prof. Dr. Alper Çabuk/Eskisehir Technical University.

The primary data of this study was provided from research presented as a poster at the ESRI Young Scholars Competition, ESRI Türkiye, 2021.

CONFLICT OF INTEREST

The author(s) stated that there are no conflicts of interest regarding the publication of this article.

AUTHORSHIP CONTRIBUTIONS

Ezgi Tükel: Writing - original draft, Formal analysis, Visualization, Investigation, Conceptualization. K. Mert Cubukcu: Formal analysis, Supervision, Conceptualization. Saye Nihan Cabuk: Writing - original draft, Supervision, Visualization, Conceptualization. Gurkan Ozturk: Supervision, Conceptualization.

REFERENCES

- [1] United Nations. Sustainable Development Goals – Decade of Action. Retrieved from <https://www.un.org/sustainabledevelopment/decade-of-action/>. 2022 (accessed February 22 2022).
- [2] Loukaitou-Sideris A. Fear and safety in transit environments from the 'women's perspective. Security journal. 2014;27(2):242-56.
- [3] Tekinbaş E. Women-friendly cities. TMMOB Şehir Plancıları Odası Haber Bülteni, Kadın Özel Eki 2. 2013; 20-23.
- [4] Demirbilek S. Investigation of gender discrimination sociologically. Finance Politics & Economic Reviews. 2007;44(511):12-27.
- [5] Kaypak Ş. Looking at the city from a gender perspective. Niğde Üniversitesi İktisadi ve İdari Bilimler Fakültesi Dergisi. 2014;7(1):344.
- [6] Yumuş A. Economic, social and political dimensions of the understanding of gender equality within the framework of development plans. PhD diss., Kadının Statüsü Genel Müdürlüğü, 2011.
- [7] Jaeckel M, van Geldermalsen M. Gender sensitive urban planing. Urbanism & Gender. 2006.
- [8] Trench S, Oc T, Tiesdell S. Safer cities for women. In Women and Social Policy. Palgrave, London 1997; 215-223.
- [9] Hildegard LG, Gahr B, Ritz-Timme S. Dealing with victims of domestic violence. In Bundesgesundheitsblatt-Gesundheitsforschung-Gesundheitsschutz. 2016; 59, 1.
- [10] Rivadeneyra A T, Dodero A L, Mehndiratta S R., Alves B, Deakin E. Reducing gender-based violence in public transportation strategy design for Mexico City, Mexico. Transportation Research Record 2015; 2531: 187–194.
- [11] Alfonzo M A. To walk or not to walk. The hierarchy of walking needs. Environment and Behavior 2005; 37: 808.
- [12] Landis B W, Vattikuti V R., Ottenberg R M, McLeod D S, Guttenplan M. Modeling the roadside walking environment: pedestrian level of service. Transportation Research Record 2001; 1773: 82-88.
- [13] Wang Y, Chau C K, Ng W Y, Leung T M. A review on the effects of physical built environment attributes on enhancing walking and cycling activity levels within residential neighbourhoods. Cities 2016; 50: 1–15.

- [14] Meethiyagoda L. Pedestrian safety in Kandy heritage city, Sri Lanka: Lessons from world heritage cities. *Sustainable Cities and Society* 2018; 38: 301-308.
- [15] Pardo-Bosch F, Blanco A, Sesé E, Ezcurra F, Pujadas P. Sustainable strategy for the implementation of energy efficient smart public lighting in urban areas: Case study in San Sebastian. *Sustainable Cities and Society* 2022; 76: 103-454.
- [16] Suk J Y, Walter R J. New nighttime roadway lighting documentation applied to public safety at night: A case study in San Antonio, Texas. *Sustainable Cities and Society* 2019; 46:101-459.
- [17] Boomsma C, Steg L. The effect of information and values on acceptability of educed street lighting. *Journal of Environmental Psychology* 2014; 39: 22-31.
- [18] Kim D, Park S. Improving community street lighting using CPTED: A case study of three communities in Korea. *Sustainable Cities and Society* 2017; 28: 233-241.
- [19] Umaña-Barrios N, Gil A S. How can spatial design promote inclusivity, gender equality and overall sustainability in Costa Rica's urban mobility system? *Procedia Engineering* 2017; 198:1018–1035.
- [20] Campisi T, Nahiduzzaman K M, Akgün N, Ticali D, Tesoriere G. Gender equality on developing transport system in Sicily: A consideration on a regional scale. *AIP Conference Proceedings* 2021; 23-43.
- [21] Tanzam N. Gendered mobilities in developing countries: The case of (urban) Uganda. *Gendered Mobilities* 2012; 159.
- [22] Ceylan S. Gender issues in the built environment: A study on the role of architecture for a sustainable society. *International Journal of Criminology and Sociology* 2020; 9: 748–762.
- [23] Lawton C A, Kallai J. Gender differences in wayfinding strategies and anxiety about wayfinding: A cross-cultural comparison. *Sex Roles* 2002; 47: 389–401.
- [24] Erkan N, Sevin B. An examination of fear of crime: Kadikoy example. *Planlama-Planning* 2018; 28(3).
- [25] Paydar M, Kamani-Fard A, Etminani-Ghasrodashti R. Perceived security of women in relation to their path choice toward sustainable neighbourhood in Santiago, Chile. *Cities* 2017; 60: 289-300.
- [26] Stark J, Meschik M. Women's everyday mobility: Frightening situations and their impacts on travel behaviour. *Transportation Research Part F: Traffic Psychology and Behaviour* 2018; 54: 311-23.
- [27] Reid LW, Konrad M. The gender gap in fear: Assessing the interactive effects of gender and perceived risk on fear of crime. *Sociological Spectrum* 2004; 24: 399–425.
- [28] Stark J, Meschik M. Women's constrained travel behavior: Austrian case study. *TR News* 2019; May(321).
- [29] Farrington D P, Welsh, B. C. Measuring the effects of improved street lighting on crime: A reply to Dr Marchant I. *British Journal of Criminology* 2004; 44: 448-467.

- [30] Tien JM. Street lighting projects. Department of Justice, Law Enforcement Assistance Administration, National Institute of Law Enforcement and Criminal Justice; 1979.
- [31] Şener Ü, Demirdirek H. Gender equality report card for 81 provinces. *Türkiye Ekonomi*. 2014.
- [32] Baykan D. A book of women-friendly urban planning and design principles for local governments. Ankara, Uzerler Matbaacılık. 2015.
- [33] Güney ME, Üstündağ B. Evaluation of urban open green areas within the scope of women-friendly city approach: Bornova example. *Journal of Süleyman Demirel University Institute of Social Sciences Year 2020*; 1: 38-65.
- [34] Reeves D. Putting women and gender in the frame—A consideration of gender in the Global Report on Human Settlement Planning Sustainable Cities 2009. *Habitat International*. 2014; 43: 293-8.
- [35] Statistics Database of TUIK Official Website: <http://www.tuik.gov.tr/>, February 2022.
- [36] Krautheimer R. Three Christian capitals: topography and politics. University of California Press; 1983.
- [37] Toprak Z. La population d'Istanbul dans les premières années de la République. *Travaux et Recherches en Turquie*. Louvain, Peeters 1982; 2: 63-70.
- [38] Murat S. Population and education structure of Kadıköy (Türkiye and Istanbul comparative). In *Journal of Social Policy Conferences 2007*; 52: 1-64.
- [39] Üsküplü T, Çolakoğlu B. The use of social network data and space syntax analysis in developing urban strategies: Kadıköy Example. *Megaron* 2019; 1:14(2).
- [40] Bonnier A, Finné M, Weiberg E. Examining land-use through GIS-Based kernel density estimation: a Re-Evaluation of legacy data from the berbati-limnes survey. *Journal of Field Archaeology*. 2019 Feb 17;44(2):70-83.
- [41] Bintliff J. The complete archaeology of Greece: from hunter-gatherers to the 20th century AD. John Wiley & Sons; 2012 May 21.
- [42] Guo M, Han C, Guan Q, Huang Y, Xie Z. A universal parallel scheduling approach to polyline and polygon vector data buffer analysis on conventional GIS platforms. *Transactions in GIS*. 2020; 24(6):1630-54.
- [43] Canepa B. Bursting the bubble: Determining the transit-oriented development's walkable limits. *Transportation Research Record*. 2007; 1992: 28-34.
- [44] Olszewski P, Wibowo SS. Using equivalent walking distance to assess pedestrian accessibility to transit stations in Singapore. *Transportation research record*. 2005;1927(1):38-45.
- [45] Ahmed S, Ibrahim RF, Hefny HA. GIS-based network analysis for the roads network of the Greater Cairo area. In *Proc. of 2nd International Conference on Applied Research in Computer Science and Engineering*. 2017.
- [46] Das D, Ojha AK, Kramsapi H, Baruah PP, Dutta MK. Road network analysis of Guwahati city using GIS. *SN Applied Sciences*. 2019 Aug;1(8):1-1.

- [47] Basharat M, Shah HR, Hameed N. Landslide susceptibility mapping using GIS and weighted overlay method: a case study from NW Himalayas, Pakistan. *Arabian Journal of Geosciences*. 2016; 9(4): 1-9.
- [48] Halder B, Bandyopadhyay J, Banik P. Assessment of hospital 'sites' suitability by spatial information technologies using AHP and GIS-based multi-criteria approach of Rajpur–Sonarpur Municipality. *Modeling Earth Systems and Environment*. 2020; 6(4): 2581-96.
- [49] Hassan I, Javed MA, Asif M, Luqman M, Ahmad SR, Ahmad A, Akhtar S, Hussain B. Weighted overlay-based land suitability analysis of agriculture land in Azad Jammu and Kashmir using GIS and AHP. *Pakistan Journal of Agricultural Sciences*. 2020;1: 57(6).
- [50] Herbei M, Ular R, Dragomir L. Map overlay in GIS. *Transactions on Hydrotechnics, Politehnica University Timisoara*. 2011; 56: 70.



RESEARCH ARTICLE

CONJUGATED LINOLEIC ACID AND FATTY ACID ISOMERS IN SELECTED COLD
PRESSED OILS: ANALYSIS BY GC/FID TECHNIQUE

Fatma Nur ARSLAN^{1,*}

¹Department of Chemistry, Kamil OZDAG Faculty of Science, University of Karamanoglu Mehmetbey, Karaman, Türkiye

ABSTRACT

The conjugated linoleic acid (CLA) isomers in cold pressed oils [*pomegranate seed oil (PGSO)*, *linseed oil (LSO)*, *black cumin seed oil (BCSO)*, *nettle seed oil (NSO)*, *grape seed oil (GSO)*, *sesame seed oil (SSO)*, *safflower oil (SFO)*, *pumpkin seed oil (PSO)*, *wheat germ oil (WGO)*, *fig seed oil (FSO)*, *coriander oil (CO)*, *walnut oil (WO)* and *coconut oil (CNO)*] extracted with lab-scale screw press machine were further subjected to gas chromatography/flame ionization detection (GC/FID) analysis. The composition of polyunsaturated fatty acids (PUFAs), monounsaturated fatty acids (MUFA) and saturated fatty acids (SFAs) of the samples was also determined. The five different positional and geometric isomers of CLA [*cis-9, cis-11 CLA*, *cis-9, trans-11 CLA*, *trans-9, cis-11 CLA*, *trans-9, trans-11 CLA* and *trans-10, cis-12 CLA*] were also well separated by a highly polar column (100m×0.2µm×0.25mm i.d; HP-88 cyanopropyl) and an applied GC temperature program. It was concluded that the samples were all rich in total CLA (ΣCLA) and they were found between 0.14% for PSO and 2.11% for SSO. The most abundant CLA isomer was in general to be *cis-9, trans-11 CLA* form, which represented the content of isomer between 3.15% and 72.08% of ΣCLA. Besides, the ΣSFA values were detected between 2.43% and 93.14%, ΣMUFA values were between 4.60% and 71.11% and ΣPUFA values were between 1.79% and 87.59%. Therefore, this study might offer valuable information for the introduction of new food sources, as well as incorporation into medicinal purposes and food formulations which have the potential to be commercially valuable.

Keywords: CLA, Cold press oil, Fatty acid, Gas chromatography

1. INTRODUCTION

Conjugated linoleic acid (CLA) is defined as an expression used for a combination of positional and geometric isomers of linoleic acid (*cis*-C18:2, ω-6), including conjugated dual bonds. The *cis*-C18:2 is a polyunsaturated fatty acids (PUFAs) and comprise two dual bonds divided by a -CH₂- group in the Δ^{9,12} positions [1–4]. In the literature, 56 different isomeric structures of CLA including diverse geometric configurations (*cis*-/*cis*-, *trans*-/*cis*-, *trans*-/*trans*- and *cis*-/*trans*-) with 14 different positions present in the chain of C18:2 (Δ^{2,4}, Δ^{3,5}, Δ^{4,6}, Δ^{5,7}, Δ^{6,8}, Δ^{7,9}, Δ^{8,10}, Δ^{9,11}, Δ^{10,12}, Δ^{11,13}, Δ^{12,14}, Δ^{13,15}, Δ^{14,16}, and Δ^{15,17}) were reported [5,6]. These isomers are defined as essential since the body couldn't construct these fatty acids, and they are also described as bioactive compounds have significant roles for health like strengthening the immune system, improving bone and cartilage disease, protecting against heart disease, preventing high cholesterol, obesity, cancer, also it could have many benefits many benefits not be determined yet [7–9].

CLA isomers have an important potential for improving the quality of human health, are produced for the commercial purposes to increase the functions of foods and are used for the enrichment of various foodstuffs. The average intake of CLA by people is 15–400 mg.day⁻¹; however, the beneficial effects of these biologically active isomers could be observed clinically over the dosage of 700–6800 mg.day⁻¹ [10–12]. For this purpose, functional foods rich in linoleic acid and alternative edible oils with enriched CLA content and high nutritive properties obtained from different seeds are recently offered to consumers. In this sense, increased awareness in cold pressed oils has been detected owing to the

demand for natural and healthy edible oils including bioactive compounds. The cold pressed oils are produced by conventional screw pressing technology without any chemical usage or heat treatment.

This technology protects antioxidants, special aromatics, phytochemicals and all other fat-soluble bioactive substances in edible oils. Contrary to the refined edible oils containing relatively large amounts of PUFAs, the cold pressed oils in similar nature often have long shelf-life and higher oxidative stability, due to their antioxidant capacity. In our markets, there are different types of cold pressed oils with different amounts and compositions of PUFAs [13–15]. However; up till now, the literatures focused on cold pressed oils have often reported the contents of their bioactive compounds including antioxidants, polyphenols, phytosterols, and so on, and there is no study on the determination of characteristics of CLA isomers with their fatty acid profile. Thus; in this study, the cold pressed oils greatly pleased by consumers owing to their organoleptic and nutritive characteristics was chosen [pomegranate seed oil (PGSO), linseed oil (LSO), black cumin seed oil (BCSO), nettle seed oil (NSO), grape seed oil (GSO), sesame seed oil (SSO), safflower oil (SFO), pumpkin seed oil (PSO), wheat germ oil (WGO), fig seed oil (FSO), coriander oil (CO), walnut oil (WO) and coconut oil (CNO)] and the characteristics of their CLA isomers [*cis*-9, *cis*-11 CLA, *cis*-9, *trans*-11 CLA, *trans*-9, *cis*-11 CLA, *trans*-9, *trans*-11 CLA and *trans*-10, *cis*-12 CLA] were concluded by GC/FID method. The composition of SFAs, MUFAs and PUFAs of the cold pressed oil samples was also reported under study. This research might offer valuable information for the introduction of new sources of functional edible oil ingredients, as well as incorporation into medicinal purposes and food formulations which could have potential to be commercially developed.

2. EXPERIMENTAL DETAILS

2.1. Chemicals and Instrumentation

High purity chemicals (n-hexane, potassium hydroxide, anhydrous sodium sulphate and methanol) were procured from Sigma-Aldrich Inc. (Zwijndrecht, The Netherlands) and VWR Chemicals BDH Inc. (West Chester, Pennsylvania, US). The reference material of fatty acid methyl esters (FAMES)(C4–C24, wt.%, mixture) was supplied from Sigma-Aldrich Inc. (Zwijndrecht, The Netherlands). A mix of certified methyl ester isomers of CLA [*cis*-9, *cis*-11 CLA (C18:2, $\Delta^{cis-9, cis-11}$), *cis*-9, *trans*-11 CLA (C18:2, $\Delta^{cis-9, trans-11}$), *trans*-9, *cis*-11 CLA (C18:2, $\Delta^{trans-9, cis-11}$), *trans*-9, *trans*-11 CLA (C18:2, $\Delta^{trans-9, trans-11}$) and *trans*-10, *cis*-12 CLA (C18:2, $\Delta^{trans-10, cis-12}$)] reference material was procured from NuChek Prep. Inc. (Elysian, MN, US) and they were prepared in GC grade hexane. An Agilent 7890A GC instrument with a 5975C model FID (Santa Clara, CA, US) and B.03.02–2008 Chemstation software were utilized for the analysis.

2.2. Cold Pressed Oil Samples

The cold pressed oils were extracted with lab-scale machine (single head, 1.5 kw power, 15 kg seed/h capacity, 2hp, screw-press) from pomegranate seed (*Punica granatum L.*), linseed (*Linum usitatissimum L.*), wheat germ (*Triticum aestivum L.*), nettle seed (*Urtica pilulifera L.*), sesame seed (*Sesamum indicum L.*), grape seed (*Vitis vinifera L.*), fig seed (*Ficus carica L.*), coriander (*Coriandrum sativum L.*), black cumin seed (*Nigella sativa L.*), safflower (*Carthamus tinctorius L.*), pumpkin seed (*Cucurbita pepo L.*), walnut (*Juglans regia L.*) and coconut (*Cocos nucifera L.*) samples. The parameters of screw press machine in our laboratory were set as screw rotation of 30 rpm speed and a temperature of 40°C. The obtained samples were stocked up at -18 °C for GC analysis.

2.3. Operating Conditions of GC–FID Analysis

Prior to the GC–FID analysis, the FAME of cold pressed oil samples [PGSO, LSO, WGO, NSO, SSO, GSO, FSO, CO, BCSO, PSO, WO, SFO and CNO] were chemically derivatized using base–catalyzed methanolysis according to our previous studies with some modifications [16–20]. Briefly; n–hexane (10 mL) was mixed with 0.1 g of cold pressed oil; afterwards, 0.1 mL of the base–catalyzation reagent (2N KOH solution in methanol) was poured into the sample and they were mixed for about 2 min. This solution was then centrifugated for 5000 rpm and 10 min, and the upper supernatant was poured into vials for the GC analysis. A highly polar column (100m×0.2µm×0.25mm i.d; Agilent HP–88 cyanopropyl, Santa Clara, CA, US) was used. High purity helium and hydrogen were used as make–up and carrier gases, respectively. The temperature program of GC oven was applied as: begin at 45°C for 4 min, the temperature was then increased to 175°C at a speed of 13 °C/min, detained in this temperature for 27 min, the temperature was then raised to 215°C at a speed of 4°C/min, held at this temperature for 35 min. The FAME of cold pressed oils was injected as 1.0 µL (split; 100:1). The temperatures of detector and injection compartments were set as 250 °C. The findings were reported as percentage of fatty acids by evaluating the values of retention time (t_R) with approved reference materials.

3. RESULTS AND DISCUSSION

The profile of fatty acids in studied oil samples is illustrated in Table 1. The total contents of SFAs, MUFAs and PUFAs are reported as percentage (% , g fatty acid/100 g cold pressed oil). The studied cold pressed oils are mainly characterized by the highest content of PUFAs (1.79%–87.59%), with a predominance of C16:0, C18:0, *cis*–C18:1, *cis*–C18:2 and *cis*–C18:3 fatty acids. As seen in Table 1, the cold pressed SFO, WO, WGO, BCSO, NSO, PSO, SSO and GSO samples have similar types of oils in terms of C18:2 $\Delta^{9,12}$ content (40.57%–73.26%). These oils contain the lowest level of SFAs (9.93%–19.90%) and MUFAs (15.60%–39.08%). The fatty acid composition findings of these samples agreed well with the data in earlier studies [13,14,21–24]. The cold pressed PGSO, FSO and LSO contain the high levels of essential C18:3 $\Delta^{9,12,15}$ fatty acid (41.29%–76.75%), whereas the CO comprise the low content of C18:1 Δ^9 fatty acid (69.71%). Similarly, these findings matched well with the results of previous literatures [15,25,26]. The cold pressed CNO is characterized by the most different composition of fatty acids, with a predominance of SFAs (93.14%), and the obtained result agreed with the literature [27]. Clearly, some discriminations of the fatty acid composition of studied oils from literature is mainly based on the differences in their seed types, geographical region, growing season, cultivar and production parameters. It is also seen that very low values were obtained in all samples in terms of trans fatty acid (0.10–1.02%) content. Therefore; the Σ SFA values were found between 2.43% and 93.14%, Σ MUFA values were between 4.60% and 71.11% and Σ PUFA values were between 1.79% and 87.59% (Table 1) for the cold pressed oils under study.

Table 1. The CLA and fatty acid data for the cold pressed oils (% , g fatty acid/100 g sample)

t_R (min)	CLA and fatty acid data for the cold pressed oils (% , g fatty acid/100 g sample)				
	<i>pomegranate seed oil (PGSO)</i>	<i>linseed oil (LSO)</i>	<i>wheat germ oil (WGO)</i>	<i>nettle seed oil (NSO)</i>	
13.423	butanoic acid (C4:0)	0.1660 ±0.0067	0.0290 ±0.0054	0.0080 ±0.0084	0.0250 ±0.0043
16.861	hexanoic acid (C6:0)	0.2260 ±0.0098	0.0270 ±0.0085	0.0060 ±0.0075	0.0320 ±0.0062
17.72	octanoic acid (C8:0)	0.0660 ±0.0034	0.0280 ±0.0052	0.0080 ±0.0046	0.0280 ±0.0036
20.275	decanoic acid (C10:0)	0.1260 ±0.0057	0.0260 ±0.0048	0.0160 ±0.0062	0.0440 ±0.0037
21.622	dodecanoic acid (C12:0)	0.1660 ±0.0074	0.0260 ±0.0055	0.0080 ±0.0073	0.0300 ±0.0081
23.575	myristic acid (C14:0)	0.1360 ±0.0055	0.0660 ±0.0071	0.0860 ±0.0084	0.0750 ±0.0046
24.459	myristoleic acid, n9(C14:1)	0.0660 ±0.0046	0.0250 ±0.0078	0.0160 ±0.0056	0.0340 ±0.0048
26.188	pentadecanoic acid (C15:0)	0.1160 ±0.0089	0.0280 ±0.0084	0.0060 ±0.0076	0.0240 ±0.0037
27.578	trans-ginkgolic acid (trans-C15:1)	0.0660 ±0.0056	0.0260 ±0.0053	0.0060 ±0.0071	0.0240 ±0.0052
27.81	ginkgolic acid (C15:1)	0.0860 ±0.0044	0.0380 ±0.0061	0.0360 ±0.0055	0.0270 ±0.0042
30.606	palmitic acid (C16:0)	0.7960 ±0.0320	6.3280 ±0.1430	1.2860 ±0.0150	7.4340 ±0.1360
33.043	trans-palmitoleic acid (trans-C16:1)	0.0860 ±0.0074	0.0440 ±0.0041	0.0360 ±0.0082	0.0320 ±0.0064
33.632	palmitoleic acid (C16:1)	0.0960 ±0.0063	0.0960 ±0.0055	0.1560 ±0.0071	0.0820 ±0.0028
35.489	heptadecanoic acid (C17:0)	0.2660 ±0.0110	0.0710 ±0.0130	0.0260 ±0.0170	0.0850 ±0.0150
36.521	heptadecanoleic acid (C17:1)	0.0860 ±0.0051	0.0490 ±0.0042	0.0360 ±0.0057	0.0500 ±0.0066
38.708	stearic acid (C18:0)	2.7060 ±0.1030	5.6280 ±0.1200	0.7160 ±0.1500	3.8020 ±0.1700
40.803	trans-oleic acid (trans-C18:1)	0.4660 ±0.0140	0.0260 ±0.0045	0.0160 ±0.0063	0.0430 ±0.0051
41.805	oleic acid (C18:1, ω9)	5.9760 ±0.2160	20.2980 ±0.9100	7.6560 ±0.1500	19.0460 ±0.1600
42.115	C18:1 izomer	0.5960 ±0.0130	0.6600 ±0.0120	0.5460 ±0.0160	0.7080 ±0.0170
45.302	trans-linoleic acid (trans-C18:2)	0.0560 ±0.0035	0.0960 ±0.0045	0.0460 ±0.0067	0.0650 ±0.0079
46.013	linoleic acid (C18:2, ω6)	4.5560 ±0.1200	13.7380 ±0.2500	8.9960 ±0.1500	67.0830 ±1.2000
46.216	linolenic acid (C18:3, ω6)	76.7560 ±1.300	0.1570 ±0.0093	70.6060 ±1.6000	0.0360 ±0.0027
46.465	arachidic acid (C20:0)	0.2660 ±0.0075	0.4590 ±0.0099	0.1360 ±0.0056	0.3630 ±0.0074
48.052	linolenic acid (C18:3, ω3)	2.4760 ±0.1100	51.7680 ±1.2000	6.8060 ±0.1200	0.5350 ±0.0085
48.728	eicosenoic acid (C20:1)	0.1060 ±0.0054	0.0340 ±0.0025	1.5360 ±0.0850	0.0300 ±0.0074
49.092	CLA isomer, 9 cis, 11 trans	0.0910 ±0.0025	0.1330 ±0.0045	0.1540 ±0.0032	0.3170 ±0.0064
49.755	CLA isomer, 10 trans, 12 cis	0.0110 ±0.0010	0.0250 ±0.0010	0.1030 ±0.0087	0.0240 ±0.0098
49.952	CLA isomer, 9 cis, 11 cis	0.0050 ±0.0001	0.0270 ±0.0075	0.1440 ±0.0079	0.0260 ±0.0010
51.472	CLA isomer, 9 trans, 11 cis	0.0360 ±0.0010	0.0640 ±0.0050	0.0960 ±0.0020	0.0620 ±0.0030
52.703	CLA isomer, 9 trans, 11 trans	0.0070 ±0.0001	0.0280 ±0.0020	0.2650 ±0.0090	0.0240 ±0.0030
54.039	eicosadienoic acid (C20:2)	0.2060 ±0.0055	0.0390 ±0.0025	0.1160 ±0.0070	0.0400 ±0.0090
54.681	erucic acid (C22:1)	0.2960 ±0.0078	0.0310 ±0.0045	0.1160 ±0.0065	0.0520 ±0.0041
55.173	lignoceric acid (C20:4)	0.4860 ±0.0095	0.1960 ±0.0053	0.2660 ±0.0092	0.0950 ±0.0014
55.501	tricosylic acid (C23:0)	0.1460 ±0.0053	0.0310 ±0.0045	0.0060 ±0.0005	0.0260 ±0.0030
56.558	cis-13,16-docosadienoic acid (C22:2)	1.4660 ±0.0150	0.0330 ±0.0010	0.0260 ±0.0006	0.0260 ±0.0024
57.877	eicosapentaenoic acid (C20:5)	0.0560 ±0.0025	0.0380 ±0.0024	0.0160 ±0.0010	0.0380 ±0.0030
59.435	lignoceric acid (C24:0)	0.7460 ±0.0180	0.1270 ±0.0087	0.1260 ±0.0099	0.0770 ±0.0025
61.798	nervonic acid (C24:1)	0.1060 ±0.0076	0.0270 ±0.0041	0.0060 ±0.0010	0.0270 ±0.0032
	∑SFAs	5.9280	12.8740	2.4340	12.0450
	∑MUFAs	7.4140	21.2580	10.1040	20.0560
	∑PUFAs	86.1470	66.2460	87.5940	68.3060
	∑trans FAs	0.6740	0.1920	0.1040	0.1640

FAs; fatty acids, SFAs; saturated fatty acids, MUFAs; monounsaturated fatty acids, PUFAs; polyunsaturated fatty acids, CLA; conjugated linoleic acid

Table 1. Continue

t_R (min)		CLA and fatty acid data for the cold pressed oils (% g fatty acid/100 g sample)			
		sesame seed oil (SSO)	grape seed oil (GSO)	fig seed oil (FSO)	coriander oil (CO)
13.423	butanoic acid (C4:0)	0.0310 ±0.0020	0.1070 ±0.0087	0.0390 ±0.0012	0.1010 ±0.0057
16.861	hexanoic acid (C6:0)	0.0250 ±0.0012	0.0320 ±0.0022	0.0280 ±0.0014	0.7440 ±0.0120
17.72	octanoic acid (C8:0)	0.0380 ±0.0022	0.0580 ±0.0013	0.0520 ±0.0015	0.0260 ±0.0034
20.275	decanoic acid (C10:0)	0.0370 ±0.0015	0.1630 ±0.0085	0.0290 ±0.0021	8.6600 ±0.2400
21.622	dodecanoic acid (C12:0)	0.0330 ±0.0010	0.0330 ±0.0023	0.0310 ±0.0014	0.6750 ±0.0105
23.575	myristic acid (C14:0)	0.0370 ±0.0013	0.0940 ±0.0057	0.0550 ±0.0061	0.0450 ±0.0042
24.459	myristoleic acid, n9(C14:1)	0.0320 ±0.0023	0.1160 ±0.0058	0.0260 ±0.0010	0.0470 ±0.0035
26.188	pentadecanoic acid (C15:0)	0.0300 ±0.0028	0.0940 ±0.0079	0.0340 ±0.0026	0.0610 ±0.0041
27.578	trans-ginkgolic acid (trans-C15:1)	0.0320 ±0.0024	0.0360 ±0.0021	0.0390 ±0.0036	0.0480 ±0.0027
27.81	ginkgolic acid (C15:1)	0.0270 ±0.0025	0.0340 ±0.0023	0.0380 ±0.0027	0.0460 ±0.0035
30.606	palmitic acid (C16:0)	9.5230 ±0.1800	8.8750 ±0.2000	7.3500 ±0.1700	3.1920 ±0.0750
33.043	trans-palmitoleic acid (trans-C16:1)	0.0450 ±0.0032	0.0470 ±0.0037	0.0360 ±0.0031	0.2310 ±0.0096
33.632	palmitoleic acid (C16:1)	0.1440 ±0.0088	0.1880 ±0.0069	0.0860 ±0.0029	0.1660 ±0.0069
35.489	heptadecanoic acid (C17:0)	0.0700 ±0.0085	0.0810 ±0.0065	0.0780 ±0.0081	0.0460 ±0.0027
36.521	heptadecanoleic acid (C17:1)	0.0490 ±0.0026	0.0520 ±0.0033	0.0500 ±0.0028	0.0660 ±0.0046
38.708	stearic acid (C18:0)	5.4210 ±0.1800	4.6780 ±0.1030	2.9870 ±0.0950	0.7290 ±0.0100
40.803	trans-oleic acid (trans-C18:1)	0.1230 ±0.0085	0.1080 ±0.0092	0.0390 ±0.0028	0.1250 ±0.0093
41.805	oleic acid (C18:1, ω9)	37.7390 ±0.9500	17.7440 ±0.7500	16.5030 ±0.8500	69.7160 ±1.3000
42.115	C18:1 izomer	0.8580 ±0.0200	0.7640 ±0.0270	1.0150 ±0.0100	0.7630 ±0.0100
45.302	trans-linoleic acid (trans-C18:2)	0.0790 ±0.0090	0.4860 ±0.0100	0.1010 ±0.0095	0.2470 ±0.0097
46.013	linoleic acid (C18:2, ω6)	42.6020 ±1.2000	64.5750 ±1.1000	29.3460 ±0.9500	13.6980 ±0.1850
46.216	linolenic acid (C18:3, ω6)	0.0350 ±0.0060	0.1580 ±0.0098	0.0630 ±0.0095	0.0300 ±0.0037
46.465	arachidic acid (C20:0)	0.5940 ±0.0150	0.1940 ±0.0095	0.4280 ±0.0096	0.0920 ±0.0066
48.052	linolenic acid (C18:3, ω3)	0.3710 ±0.0088	0.4320 ±0.0092	41.2970 ±1.1000	0.1960 ±0.0082
48.728	eicosenoic acid (C20:1)	0.0310 ±0.0050	0.0400 ±0.0025	0.0450 ±0.0030	0.2500 ±0.0096
49.092	CLA isomer, 9 cis, 11 trans	0.1850 ±0.0025	0.1800 ±0.0039	0.2740 ±0.0024	0.0700 ±0.0010
49.755	CLA isomer, 10 trans, 12 cis	0.2950 ±0.0021	0.1290 ±0.0010	0.0280 ±0.0010	0.0290 ±0.0010
49.952	CLA isomer, 9 cis, 11 cis	0.2810 ±0.0027	0.1700 ±0.0023	0.0310 ±0.0010	0.0280 ±0.0010
51.472	CLA isomer, 9 trans, 11 cis	0.6340 ±0.0054	0.1220 ±0.0032	0.0300 ±0.0010	0.0440 ±0.0015
52.703	CLA isomer, 9 trans, 11 trans	0.7210 ±0.0028	0.2910 ±0.0022	0.0270 ±0.0010	0.0350 ±0.0021
54.039	eicosadienoic acid (C20:2)	0.0420 ±0.0031	0.0540 ±0.0026	0.0460 ±0.0037	0.0850 ±0.0041
54.681	erucic acid (C22:1)	0.0360 ±0.0018	0.0700 ±0.0058	0.0500 ±0.0036	0.0310 ±0.0021
55.173	lignoceric acid (C20:4)	0.1410 ±0.0088	0.0500 ±0.0032	0.1000 ±0.0110	0.0500 ±0.0098
55.501	tricosylic acid (C23:0)	0.0260 ±0.0023	0.0380 ±0.0020	0.0290 ±0.0010	0.0370 ±0.0010
56.558	cis-13,16-docosadienoic acid (C22:2)	0.0330 ±0.0021	0.0360 ±0.0032	0.0290 ±0.0015	0.0260 ±0.0017
57.877	eicosapentaenoic acid (C20:5)	0.0390 ±0.0018	0.0440 ±0.0026	0.0410 ±0.0028	0.0420 ±0.0039
59.435	lignoceric acid (C24:0)	0.1040 ±0.0099	0.1500 ±0.0087	0.0570 ±0.0048	0.0570 ±0.0035
61.798	nervonic acid (C24:1)	0.0260 ±0.0024	0.0450 ±0.0022	0.0340 ±0.0020	0.0340 ±0.0015
	∑SFAs	15.9690	14.5970	11.1970	14.4650
	∑MUFAs	38.9420	19.0530	17.8470	71.1190
	∑PUFAs	45.3790	66.2410	71.3120	14.3330
	∑trans FAs	0.2790	0.6770	0.2150	0.6510

FAs; fatty acids, SFAs; saturated fatty acids, MUFAs; monounsaturated fatty acids, PUFAs; polyunsaturated fatty acids, CLA; conjugated linoleic acid

Table 1. Continue

t_R (min)		CLA and fatty acid data for the cold pressed oils (% g fatty acid/100 g sample)				
		<i>black cumin seed oil (BCSO)</i>	<i>pumpkin seed oil (PSO)</i>	<i>walnut oil (WO)</i>	<i>safflower oil (SFO)</i>	<i>coconut oil (CNO)</i>
13.423	butanoic acid (C4:0)	0.0360 ±0.0024	0.0250 ±0.0010	0.1300 ±0.0095	0.0290 ±0.0031	0.0390 ±0.0022
16.861	hexanoic acid (C6:0)	0.0320 ±0.0017	0.1260 ±0.0084	0.5690 ±0.0120	0.0250 ±0.0030	0.7040 ±0.0087
17.72	octanoic acid (C8:0)	0.0390 ±0.0023	0.0280 ±0.0010	0.0980 ±0.0057	0.0900 ±0.0098	8.6270 ±0.1500
20.275	decanoic acid (C10:0)	0.0280 ±0.0020	0.0820 ±0.0050	1.1400 ±0.0105	0.0300 ±0.0069	6.8370 ±0.1400
21.622	dodecanoic acid (C12:0)	0.0480 ±0.0033	0.0320 ±0.0024	1.5590 ±0.0105	0.0250 ±0.0020	49.5710 ±1.2000
23.575	myristic acid (C14:0)	0.1850 ±0.0088	0.1340 ±0.0093	0.0480 ±0.0020	0.1400 ±0.0089	17.0580 ±1.1000
24.459	myristoleic acid, n9(C14:1)	0.0290 ±0.0025	0.0310 ±0.0030	0.0250 ±0.0010	0.0250 ±0.0015	0.0340 ±0.0020
26.188	pentadecanoic acid (C15:0)	0.0310 ±0.0030	0.0530 ±0.0042	0.0280 ±0.0030	0.0250 ±0.0025	0.0270 ±0.0031
27.578	trans-ginkgolic acid (trans-C15:1)	0.0480 ±0.0020	0.0300 ±0.0030	0.0360 ±0.0025	0.0260 ±0.0021	0.0420 ±0.0030
27.81	ginkgolic acid (C15:1)	0.0360 ±0.0027	0.0440 ±0.0035	0.0380 ±0.0020	0.0340 ±0.0015	0.0280 ±0.0030
30.606	palmitic acid (C16:0)	12.0440 ±0.2500	11.2600 ±0.9700	6.4430 ±0.0850	6.6300 ±0.0750	7.2610 ±0.0680
33.043	trans-palmitoleic acid (trans-C16:1)	0.0360 ±0.0020	0.0350 ±0.0018	0.0730 ±0.0021	0.0430 ±0.0018	0.0410 ±0.0030
33.632	palmitoleic acid (C16:1)	0.2290 ±0.0120	0.1260 ±0.0100	0.0900 ±0.0099	0.1080 ±0.0089	0.0300 ±0.0026
35.489	heptadecanoic acid (C17:0)	0.0900 ±0.0085	0.1040 ±0.0075	0.0680 ±0.0056	0.0540 ±0.0028	0.0250 ±0.0023
36.521	heptadecanoic acid (C17:1)	0.0770 ±0.0036	0.0640 ±0.0040	0.0500 ±0.0035	0.0500 ±0.0039	0.0250 ±0.0030
38.708	stearic acid (C18:0)	3.1380 ±0.0950	7.1630 ±0.0860	2.3890 ±0.0150	2.3140 ±0.0105	2.8340 ±0.0100
40.803	trans-oleic acid (trans-C18:1)	0.1130 ±0.0098	0.1210 ±0.0085	0.0520 ±0.0020	0.1530 ±0.0095	0.1230 ±0.0086
41.805	oleic acid (C18:1, ω9)	22.4240 ±1.2000	38.1060 ±1.0500	16.4770 ±1.3000	14.5680 ±1.0200	4.3520 ±0.0250
42.115	C18:1 izomer	1.0140 ±0.0095	0.6340 ±0.0058	0.7410 ±0.0084	0.7210 ±0.0069	0.0550 ±0.0026
45.302	trans-linoleic acid (trans-C18:2)	0.1150 ±0.0050	0.0690 ±0.0045	0.1820 ±0.0039	0.1120 ±0.0054	0.8230 ±0.0063
46.013	linoleic acid (C18:2, ω6)	56.8640 ±1.4000	40.5760 ±1.2000	58.3950 ±1.3000	73.2610 ±2.0050	0.1460 ±0.0095
46.216	linolenic acid (C18:3, ω6)	0.0340 ±0.0025	0.0270 ±0.0015	0.0310 ±0.0010	0.0440 ±0.0021	1.3380 ±0.0084
46.465	arachidic acid (C20:0)	0.2200 ±0.0095	0.5060 ±0.0105	0.0510 ±0.0050	0.3870 ±0.0100	0.0910 ±0.0057
48.052	linolenic acid (C18:3, ω3)	0.2530 ±0.0084	0.2190 ±0.0063	10.6220 ±0.5200	0.1250 ±0.0085	0.0270 ±0.0015
48.728	eicosenoic acid (C20:1)	0.0330 ±0.0036	0.0250 ±0.0024	0.1440 ±0.0058	0.0290 ±0.0013	0.0240 ±0.0023
49.092	CLA isomer, 9 cis, 11 trans	0.3280 ±0.0105	0.0320 ±0.0022	0.0250 ±0.0030	0.1850 ±0.0095	0.0470 ±0.0037
49.755	CLA isomer, 10 trans, 12 cis	0.0290 ±0.0021	0.1340 ±0.0099	0.1960 ±0.0085	0.0680 ±0.0052	0.0240 ±0.0010
49.952	CLA isomer, 9 cis, 11 cis	0.0380 ±0.0015	0.0270 ±0.0010	0.1050 ±0.0069	0.1790 ±0.0099	0.0250 ±0.0030
51.472	CLA isomer, 9 trans, 11 cis	0.0300 ±0.0020	0.0250 ±0.0015	0.0660 ±0.0020	0.2540 ±0.0105	0.0270 ±0.0010
52.703	CLA isomer, 9 trans, 11 trans	0.0300 ±0.0015	0.0270 ±0.0021	0.4010 ±0.0120	0.2100 ±0.0103	0.0260 ±0.0015
54.039	eicosadienoic acid (C20:2)	0.0440 ±0.0052	0.0390 ±0.0031	0.0480 ±0.0024	0.0400 ±0.0015	0.0290 ±0.0010
54.681	erucic acid (C22:1)	2.6110 ±0.0105	0.0260 ±0.0021	0.0450 ±0.0027	0.0420 ±0.0034	0.0330 ±0.0015
55.173	lignoceric acid (C20:4)	0.0580 ±0.0057	0.1500 ±0.0095	0.0410 ±0.0034	0.2660 ±0.0105	0.0280 ±0.0023
55.501	tricosylic acid (C23:0)	0.0390 ±0.0015	0.2870 ±0.0100	0.0270 ±0.0010	0.0280 ±0.0015	0.0270 ±0.0025
56.558	cis-13,16-docosadienoic acid (C22:2)	0.0330 ±0.0010	0.0300 ±0.0010	0.0340 ±0.0025	0.0310 ±0.0025	0.0400 ±0.0015
57.877	eicosapentaenoic acid (C20:5)	0.0490 ±0.0023	0.0390 ±0.0025	0.0390 ±0.0027	0.0260 ±0.0010	0.0380 ±0.0015
59.435	lignoceric acid (C24:0)	0.0560 ±0.0032	0.1080 ±0.0097	0.0360 ±0.0024	0.1620 ±0.0035	0.0410 ±0.0025
61.798	nervonic acid (C24:1)	0.0280 ±0.0020	0.0260 ±0.0015	0.0290 ±0.0015	0.0300 ±0.0020	0.0250 ±0.0010
	Σ SFAs	15.9860	19.9080	12.5860	9.9390	93.1420
	Σ MUFAs	26.4810	39.0820	17.6390	15.6070	4.6060
	Σ PUFAs	57.7900	41.3250	70.0030	74.6890	1.7950
	Σ trans FAs	0.3120	0.2550	0.3430	0.3340	1.0290

FAs; fatty acids, SFAs; saturated fatty acids, MUFAs; monounsaturated fatty acids, PUFAs; polyunsaturated fatty acids, CLA; conjugated linoleic acid

The GC chromatograms of WGO, GSO and SFO samples are illustrated in Figures 1–3. These oil samples are commonly consumed, and the zoomed chromatograms (upper side) depict the separation of CLA isomers; the main chromatograms show the separation of all fatty acids in *cis*–/*trans*–configurations of the same sample. It can be seen from the representative chromatograms, the fatty acid separations were occurred because of the elution principle of highly polar HP–88 cyanopropyl capillary GC column and the applied temperature program, namely all unsaturated fatty acids which have the chain length of X were eluted between the retention times (t_R) of SFAs ($CX:0$) and ($CX+2:0$). Identification of the other positional and geometric isomers was based on the direct comparison with the target reference fatty acids and our earlier studies [16–20]. The order of retention time (t_R) in GC method was also given in Table 1.

The GC data were gained with a highly polar column (100m×0.2µm×0.25mm i.d; HP–88 cyanopropyl) by a similar temperature program applied for FAME analysis. This column was very practical and currently recommended for the identification of SFAs, *cis*–MUFAs and *cis*–PUFAs based on their chain–lengths, as well the number and position of their dual bonds. Of special interest in this GC column was the identification of five different CLA isomers [*cis*–9, *cis*–11 CLA, *cis*–9, *trans*–11 CLA, *trans*–9, *cis*–11 CLA, *trans*–9, *trans*–11 CLA and *trans*–10, *cis*–12 CLA]. The positional and geometric isomers of CLA were also well separated, and they were eluted as *cis*–/*trans*–, *trans*–/*cis*–, *cis*–/*cis*–, and *trans*–/*trans*–, then relative to the carbon atom where the double bond is located, expressed as Δ for positional isomers within these groups. In positional CLA isomers, the geometric isomers of *cis*–/*trans*– were eluted prior to the *trans*–/*cis*– form. Hence; their t_R was recorded in order: *cis*–9, *trans*–11 CLA ($t_R=49.963$ min), *trans*–10, *cis*–12 CLA ($t_R=50.285$ min), *cis*–9, *cis*–11 CLA ($t_R=50.487$ min), *trans*–9, *cis*–11 CLA ($t_R=50.793$ min) and *trans*–9, *trans*–11 CLA ($t_R=50.963$ min). This elution order obtained under study is in accordance with the literature [1–4,7–12].

It was concluded that the cold pressed oil samples were all rich in total CLA (\sum CLA) contents and they ranged from 0.14% (for PSO) to 2.11% (for SSO). The contents of \sum CLA in cold pressed PGSO (0.14%), LSO (0.27%), WGO (0.76%), NSO (0.45%), SSO (2.11%), GSO (0.89%), FSO (0.3900%), CO (0.20%), BCSO (0.45%), PSO (0.24%), WO (0.79%), SFO (0.89%) and CNO (0.14%) were commonly in similar concentrations. The major CLA isomer in tested cold pressed oils was concluded as *cis*–9, *trans*–11 CLA, which represented the content of isomer between 3.15% and 72.08% of \sum CLA. The contents of *trans*–10, *cis*–12 CLA isomer were between 5.29% and 54.69% of \sum CLA, *cis*–9, *cis*–11 CLA isomer were between 3.33% and 19.97% of \sum CLA, *trans*–9, *cis*–11 CLA isomer were between 6.59% and 29.96% of \sum CLA, *trans*–9, *trans*–11 CLA isomer were between 4.66% and 50.56% of \sum CLA. Thus, the present study contributed valuable information for the introduction of new sources of functional cold pressed oils, as well as incorporation into medicinal purposes and food formulations which could have potential to be commercially developed.

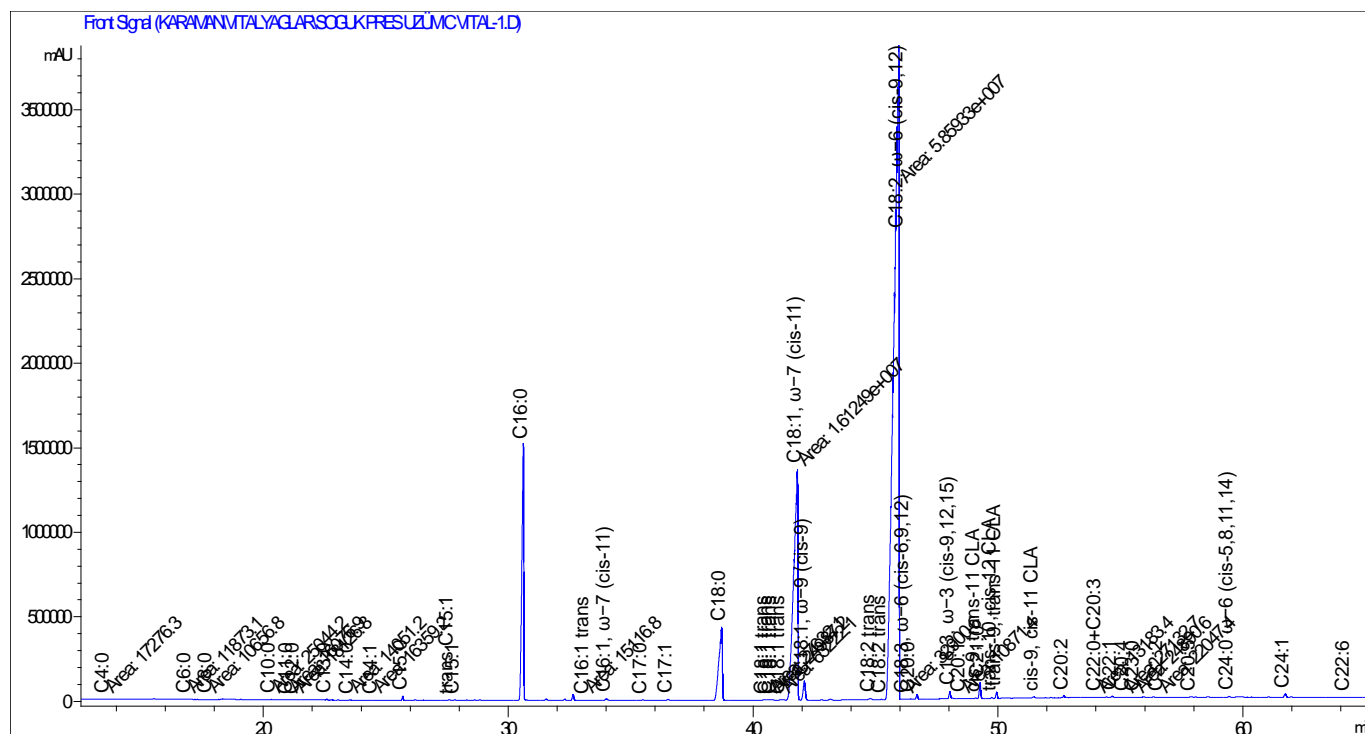


Figure3. GC/FID chromatogram for the CLA and fatty acid analysis of cold pressed grape seed oil (GSO) sample

4. CONCLUSIONS

In conclusion, we aimed to determine the composition and content of CLA isomers, which have been proven to support a health and life quality with many scientific studies, and other valuable fatty acids (SFAs, *cis*-MUFA and *cis*-PUFAs) in some cold pressed oils (*PGSO*, *LSO*, *WGO*, *NSO*, *SSO*, *GSO*, *FSO*, *CO*, *BCSO*, *PSO*, *WO*, *SFO* and *CNO*) extracted with lab-scale screw press machine in our research laboratory. The CLA and fatty acid isomers were profiled by GC/FID method based on the fatty acid composition analysis. The five valuable isomers of CLA [*cis*-9, *cis*-11 CLA, *cis*-9, *trans*-11 CLA, *trans*-9, *cis*-11 CLA, *trans*-9, *trans*-11 CLA and *trans*-10, *cis*-12 CLA] were also well separated according to their geometric and positional structure. The studied samples were all rich in Σ CLA content and they were found between 0.14% and 2.11%. The major isomer was to be *cis*-9, *trans*-11 CLA (ranged from 3.15% to 72.08% of Σ CLA). The Σ SFA values were also detected between 2.43% and 93.14%, Σ MUFA values were between 4.60% and 71.11% and Σ PUFA values were between 1.79% and 87.59%. Therefore, we are of the opinion that the study will be a valuable source for studies that will make it possible to obtain low-cost, high value-added functional food products, and it will also be a guide for the industry of cold press oil.

ACKNOWLEDGEMENT

The study was financed by the project of Karamanoğlu Mehmetbey University (project grant 05-M-20).

CONFLICT OF INTEREST

The researcher declared that she had no conflicts of concern relating to the publication of this research

REFERENCES

- [1] Kramer JKG, Hernandez M, Cruz-herandez C, et al. Combining Results of Two GC Separations Partly Achieves Except CLA Isomers of Milk Fat as Demonstrated Using Ag-Ion SPE Fractionation. *Lipids* 2008;43:259–73.
- [2] Cossignani L, Giua L, Lombardi G, et al. Analysis of CLA Isomer Distribution in Nutritional Supplements by Single Column Silver-Ion HPLC. *J Am Oil Chem Soc* 2013;90:327–35.
- [3] Lehmann L, Yurawecz MP. Synthesis and Isolation of trans -7 , cis -9 Octadecadienoic Acid and Other CLA Isomers by Base Conjugation of Partially Hydrogenated γ -Linolenic Acid. *Lipids* 2003;38:579–83.
- [4] Delmonte P, Roach JAG, Mossoba MM, et al. Synthesis , Isolation , and GC Analysis of All the 6 , 8- to 13 , 15- cis / trans Conjugated Linoleic Acid Isomers. *Lipids* 2004;39:185–91.
- [5] Bertschi I, Collomb M, Rist L, et al. Maternal Dietary Alpine Butter Intake Affects Human Milk : Fatty Acids and Conjugated Linoleic Acid Isomers. *Lipids* 2005;40:581–7.
- [6] Miroslav L, Rumen D, Michal H. Retention behavior of isomeric triacylglycerols in silver-ion HPLC : Effects of mobile phase composition and temperature. *J Sep Sci* 2013;36:2888–900.
- [7] Kuhnt K, Degen C, Jahreis G. 2-Propanol in the mobile phase reduces the time of analysis of CLA isomers by silver ion-HPLC. *J Chromatogr B* 2010;878:88–91.
- [8] Angel M, Fuente D, Luna P, et al. Chromatographic techniques to determine conjugated linoleic acid isomers. *Trends Anal Chem* 2006;25:917–26.
- [9] Rodríguez-Castanedas JL, Pena-Egido MJ, García-Marino M, et al. Quantitative determination of conjugated linoleic acid isomers by silver ion HPLC in ewe milk fat. *J Food Compos Anal* 2011;24:1004–8.
- [10] Katarzyna T, Wszolek M. Comparative study of walnut and *Camelina sativa* oil as a functional components for the unsaturated fatty acids and conjugated linoleic acid enrichment of kefir. *LWT - Food Sci Technol* 2021;147:111681.
- [11] Martín-González MZ, Palacios H, Rodríguez MA, et al. Beneficial Effects of a Low-dose of Conjugated Linoleic Acid on Body Weight Gain and other Cardiometabolic Risk Factors in Cafeteria. *Nutrients* 2020;12:1–20.
- [12] Bruen R, Fitzsimons S, Belton O. Atheroprotective effects of conjugated linoleic acid. *Br J Clin Pharmacol* 2017;83:46–53.
- [13] Ramadan MF. Healthy blends of high linoleic sunflower oil with selected cold pressed oils : Functionality , stability and antioxidative characteristics. *Ind Crop Prod* 2013;43:65–72.
- [14] Lutterodt H, Slavin M, Whent M, et al. Fatty acid composition , oxidative stability , antioxidant and antiproliferative properties of selected cold-pressed grape seed oils and flours. *Food Chem* 2011;128:391–9.

- [15] Michotte D, Rogez H, Chirinos R, et al. Linseed oil stabilisation with pure natural phenolic compounds. *Food Chem* 2011;129:1228–31.
- [16] Emin M, Mustafa S. Recovery of valuable compounds from orange processing wastes using supercritical carbon dioxide extraction. *J Clean Prod* 2022;375:134169.
- [17] Argun ME, Arslan FN, Ates H, et al. A pioneering study on the recovery of valuable functional compounds from olive pomace by using supercritical carbon dioxide extraction : Comparison of perlite addition and drying. *Sep Purif Technol* 2023;306:122593.
- [18] Arslan FN, Çağlar F. Attenuated Total Reflectance – Fourier Transform Infrared (ATR – FTIR) Spectroscopy Combined with Chemometrics for Rapid Determination of Cold-Pressed Wheat Germ Oil Adulteration. *Food Anal Methods* 2019;12:355–70.
- [19] Kenar A, Çiçek B, Arslan FN, et al. Electron Impact – Mass Spectrometry Fingerprinting and Chemometrics for Rapid Assessment of Authenticity of Edible Oils Based on Fatty Acid Profiling. *Food Anal Methods* 2019;12:1369–81.
- [20] Arslan FN. ATR–FTIR spectroscopy combined with chemometrics for rapid classification of extra virgin olive oils and edible oils from different cultivars available on the Turkish markets. *Eskişehir Tech Univ J Sci Technol A- Appl Sci Eng* 2018;19:926–47.
- [21] Dedebas T, Ekici L, Sagdic O. Chemical characteristics and storage stabilities of different cold-pressed seed oils. *J Food Process Preserv* 2021;45.
- [22] Sanja Kostadinovic-Velickovska* SM. Journal of Food Chemistry and Nutrition antioxidant activity of cold pressed and refined edible oils from. *J Food Chemstry Nutr* 2013.
- [23] Arslan FN, Çağlar F. Attenuated Total Reflectance–Fourier Transform Infrared (ATR–FTIR) Spectroscopy Combined with Chemometrics for Rapid Determination of Cold-Pressed Wheat Germ Oil Adulteration. *Food Anal Methods* 2019;12:355–70.
- [24] Gharibzahedi SMT, Mousavi SM, Hamed M, et al. Response surface modeling for optimization of formulation variables and physical stability assessment of walnut oil-in-water beverage emulsions. *Food Hydrocoll* 2012;26:293–301.
- [25] Şirinyildiz DD, Vardin AY, Yorulmaz A. The influence of microwave roasting on bioactive components and chemical parameters of cold pressed fig seed oil. *Grasas y Aceites* 2023;74:1–9.
- [26] Jing P, Ye T, Shi H, et al. Antioxidant properties and phytochemical composition of China-grown pomegranate seeds. *Food Chem* 2012;132:1457–64.
- [27] Marina AM, Che Man YB, Nazimah SAH, et al. Chemical properties of virgin coconut oil. *JAACS, J Am Oil Chem Soc* 2009;86:301–7.



HARNESSING GOLD NANORODS FOR NON-ENZYMATIC GLUCOSE SENSING

Zeliha Cansu CANBEK OZDIL * 

Department of Material Science and Nanotechnology Engineering, Faculty of Engineering, Yeditepe University, Istanbul, Turkey

ABSTRACT

This study presents a straightforward and non-enzymatic approach for glucose detection utilizing aggregated gold nanorods (GNRs) based on surface plasmon resonance (SPR). The GNRs exhibited enhanced sensitivity toward glucose concentrations of up to 10 mM. The LSPR-based glucose detection method demonstrated superior sensitivity, stability, ease of use, and a convenient readout. Moreover, the LSPR detection technique can be seamlessly integrated with various sensing platforms, offering the potential to expand the sensor's range and applicability. This study highlights the promising prospects of LSPR-based non-enzymatic glucose detection and its potential for integration into diverse sensing systems. For the 10 mM glucose solution, the addition of 5.85×10^9 GNRs caused a 136 nm shift. On the other hand, when 50 mM glucose is added, the shift amounted to 82 nm, while adding 100 mM glucose resulted in a shift of 71 nm. This implies that at lower glucose concentrations, the degree of aggregation is greater, suggesting a heightened sensitivity to smaller concentrations. TEM images depicted the formation of the gold nanorod aggregates upon the introduction of 10 mM glucose.

Keywords: Gold nanorods, Non-enzymatic glucose sensing, Nanosensor

1. INTRODUCTION

Low-cost, easy-to-use biosensors based on metal nanoparticles are proposed as new technology devices for the rapid detection of desired analytes providing high sensitivity and stability due to specific properties of metal nanoparticles called surface plasmon resonance (SPR) [1–3]. Namely, the optical response of nanoparticles, resulting from the collective oscillation of free conduction electrons in the metal surface under light irradiation at a resonance frequency, gives rise to SPR [4] in the light spectrum. The frequency of this oscillation is found generally in the visible region of UV-Vis spectra for materials like gold, silver, and copper. By changing the size of the nanoparticles, one can manipulate slightly the length of the plasmon peak to alter the optical properties of the material [5].

When isotropic nanoparticles are replaced with anisotropic analogs, optical features, and electrical and magnetic properties can be enhanced considerably with respect to previous cases due to their complex anisotropic structures. This kind of amelioration makes anisotropic nanoparticles quite desirable over isotropic ones for biosensing applications [6–8]. The single SPR splits into two different modes in the anisotropic nanoparticles; a transverse surface plasmon resonance (T-SPR), corresponding to the light absorption and scattering along the short axis of the particle, and a longitudinal surface plasmon resonance (L-SPR), corresponding to light absorption and scattering along the long axis of the particles. The L-SPR is quite dependent on the aspect ratio of the particle.

Such anisotropic nanoparticles can easily be tailored to enhance the capability of future MEMS (Micro-Electro-Mechanical Systems) devices [9], SERS (Surface Enhanced Raman Scattering) substrates [10], and state of art analyte sensing biosensors. The quality of the sensing is highly impacted by the variations in nanoparticle size, morphology, and the concentration of the nanoparticle [11]. To be able to use metal nanoparticles advantageously on any platform, we need to overcome some critical points such as:

- Repeatability of the synthesis and high reproducibility of the same results should be attained, which is challenging for nano production.
- The synthesis should allow scalability for any real-life applications.
-

It should be noted that reproducibility is challenging for any nanomaterial production, considering that the production is highly dependent on reaction parameters [12].

There have been many studies on gold nanoparticle-based glucose sensors [3,13–17]. In the fabrication of such sensing platforms, the mechanism of sensing is based on the oxidation of target glucose to gluconolactone and producing hydrogen peroxide, which is a strong oxidizing agent, in the presence of glucose oxidase. The sensing is achieved indirectly by the etching activity of H_2O_2 , released during the glucose oxidase enzymatic cycle, on the gold nanorods [13]. A schematic representation of the enzymatic glucose sensing mechanism is given in Figure 1a.

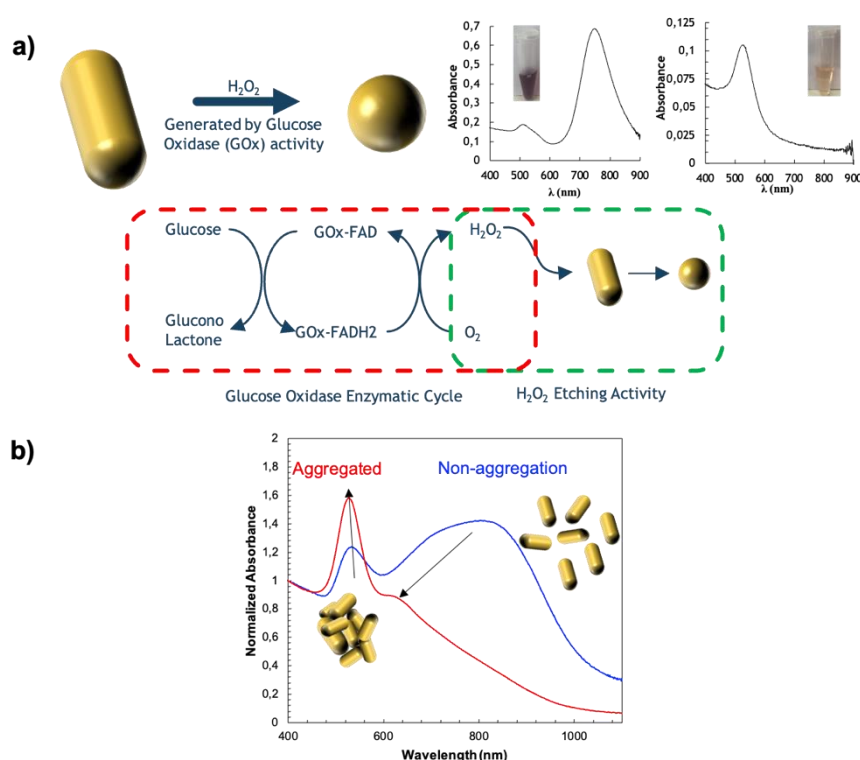


Figure 1. Schematic representation of a) enzymatic glucose sensing with GNRs based on etching via H_2O_2 activity b) non-enzymatic sensing with GNRs based on aggregation

There are limited studies unlocking the potential of gold nanorods for non-enzymatic glucose sensing since the material itself poses significant challenges [17,18]. In these works, agents like $Ag(NH_3)_2OH$, and dextran sulfate are introduced to induce aggregation to perform indirect sensing. While these tiny structures exhibit unique optical properties and demonstrate remarkable stability, their effective utilization in glucose-sensing applications demands overcoming several hurdles. One major obstacle is the need for sensitivity. Designing reliable and sensitive detection methods to translate the nanorod's optical responses into measurable signals necessitates sophisticated instrumentation and signal processing techniques.

In this work, we have provided a reproducible high-yield large-scale synthesis of gold nanorods via the chemical reduction method for non-enzymatic glucose sensing (Figure 1b). For the production of nanomaterials wet chemical synthesis method has been chosen due to the ease of the method and high reproducibility. Even though, the technique is largely affected by a number of factors (ionic strength of

water used during production, strict control of medium temperature, stirring efficiency, operator performing synthesis, etc.) [12], the fact that it does not require complex laboratory set-up and equipment brings many advantages. A schematic representation of the methodology used has been summarized in Figure 2.

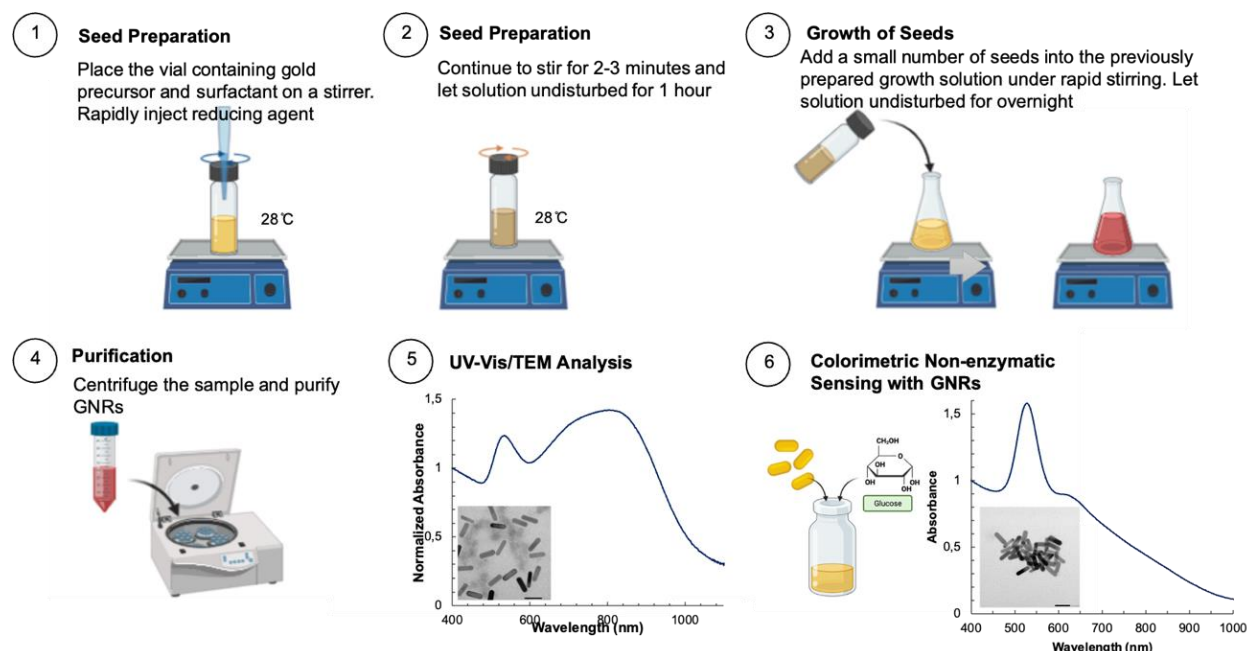


Figure 2. Schematic representation of the GNR production and characterization

2. MATERIALS and METHODS

2.1. Materials

Cetyltrimethylammonium bromide (CTAB, 99%), chloroauric acid (HAuCl_4 , extra pure), silver nitrate (AgNO_3 , extra pure), sodium borohydride (NaBH_4 , 98%), and L-ascorbic acid were obtained from Sigma without further purification. All the glassware was cleaned with aqua regia and washed with distilled water before the experiments.

2.2. Synthesis of Seeds

The preparation of the seeds followed the procedure outlined in Nikoobakht and El-Sayed's study [19]. In this process, a rapid injection of 0.1 mL of an ice-cold 0.0264 M NaBH_4 solution is carried out into a mixture containing 0.025 mL of 0.05 M HAuCl_4 solution, and 4.7 mL of 0.1 M CTAB solution, at a temperature of 28 °C. Following the injection, the resulting mixture is stirred for a duration of 2 minutes and maintained at 28 °C for a minimum of 1 hour to allow excess NaBH_4 to evaporate. The light brown color of the mixture is indicative of the size of the seeds being smaller than 5 nm [12].

2.3. Synthesis of Gold Nanorods

After the synthesis of seeds, the second step in production is their growth into final anisotropic shapes. In this stage, a reference growth solution with the following parameters has been prepared (Table 1).

Table 1 Chemical Parameters used during preparation of growth media

Stock Solution	Stock Solution Concentration	Added Quantity into Growth Solution (mL)	Final Concentration in Growth Solution [C_{final}] (mM)
HAuCl ₄ •3H ₂ O	0.1 M	1.26	0.5
CTAB	0.1 M	250	100
AgNO ₃	0.01 M	3.60	0.140
Ascorbic Acid	0.1 M	1.92	0.75
HCl	5 M	0.05	-

It should be well noted that a fresh stock solution of silver nitrate and ascorbic acid has been prepared for each synthesis for reproducibility. After the production of the growth solution, 1.5 mL of as-synthesized seed is injected rapidly into the growth media. The mixture is mixed over 20 seconds and kept at 28 °C without disturbance overnight to ensure that the growth is terminated.

2.4. Characterization of Gold Nanorods

UV-Vis spectroscopy experiments are realized by using Thermo Scientific NanoDrop 2000 Spectrophotometer. The UV-Vis spectrums of bare GNRs are recorded before any purification step. After recording, purification is performed by using a Beckman Culter Allegra centrifuge at 10000 g for 10 minutes in 3 steps. After each centrifugation, the supernatant is discarded and the sediment is washed with DI water to complete the volume to 10 mL.

Scanning electron microscopy (SEM) experiments are realized at Bogazici University Advanced Technologies R&D Centre Laboratory via Philips-FEI XL30 ESEM-FEG scanning Electron microscope at 30 kV. Transmission electron microscopy (TEM) observations are carried out by JEOL JEM 2100 Plus microscope equipped with Gatan US4000 CCD Camera operating at 200 kV. Before observation, samples are coated with plasma Au/Pd. Obtained images are analyzed via ImageJ software.

2.5. Non-enzymatic Glucose Sensing Experiments

To a series of 2 mL of freshly prepared and aerated glucose solutions, two different numbers of GNRs are added in scintillation vials. After 20 minutes waiting period, the samples are analyzed via UV-Vis spectroscopy.

3. RESULTS and DISCUSSION

The UV-Vis spectrum of GNRs, depicted in Figure 1, demonstrates two distinct peaks, one at 553 nm representing T-SPR and another at 804 nm representing L-SPR. The broad L-SPR peak can be attributed to the polydisperse nanorods. Via the UV-Vis spectrum, it is possible to characterize produced gold nanorods quantitatively. Mainly, the aspect ratio of as-produced gold nanorods can be deduced from simple relation with longitudinal surface plasmon band (λ_{L-SPR}) [20]:

$$AR = \frac{\lambda_{max} - 478}{96} \quad (1)$$

In our case, we estimated an AR of 3.39. Additionally, it is also possible to calculate the final colloidal gold concentration as 0.22 mM, converted from Au(I) into Au⁰ (C_{Au}) via the following equation;

$$A_{400\text{ nm}} = \epsilon b c_{Au} \quad (2)$$

where $A_{400\text{nm}}$ is the absorption band signal of gold at 400 nm, ϵ is the absorption coefficient ($2500\text{M}^{-1}\text{cm}^{-1}$ ref) and b is the cell path length used during measurement (1 mm). The obtained values are summarized in Table 2.

Table 2 GNR solution parametric data

Symbol	Parameter	Numeric Value
l	Average length of GNR	45.81 nm
d	Average diameter of GNR	13.26 nm
r	Average radius of GNR	6.63 nm
AR	Aspect ratio (obtained by UV)	3.39
ρ	Density of Au atom	19.32 g/cm^3
c_{Au}	Final Au(0) concentration	$2.2 \times 10^{-4} \text{ mol/L}$
V_{total}	Total volume of GNR solution	256.85 mL
Mwt_{Au}	Molecular weight of gold	196.97 g/mol

After the deduction of the final gold concentration, it is possible to do a rough estimation of the number of GNRs by calculating the volume of a single nanorod via:

$$V_{single\ nanorod} = \pi r^2 l \quad (3)$$

where r is the diameter of the nanorod with an estimation of cylindrical shape for GNRs.

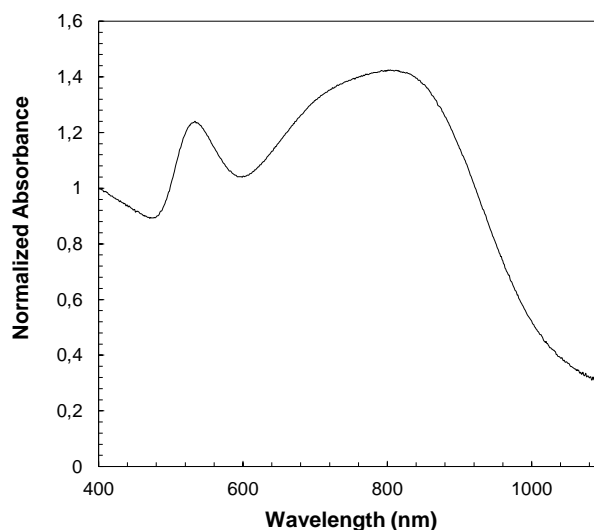


Figure 1. The UV-Vis spectrum of GNRs solution

The average radius and length of GNRs are obtained via SEM and TEM analysis. Corresponding SEM and TEM images are given in Figures 2a, b, and c. 50 particles are counted for the analysis. In microscopy images, GNRs appear more monodisperse in size and morphology. The discrepancy between the apparent polydispersity observed in the UV-Vis spectrum and the absence of such variability in microscopy images for GNRs can be attributed to the purification of the samples before microscopy observations. During the purification, by-products and excess CTAB, forming a thick organic layer around the nanorods and leading to a reduction in image resolution, are removed. This explains the difference between the UV-Vis spectrum and the microscopy images.

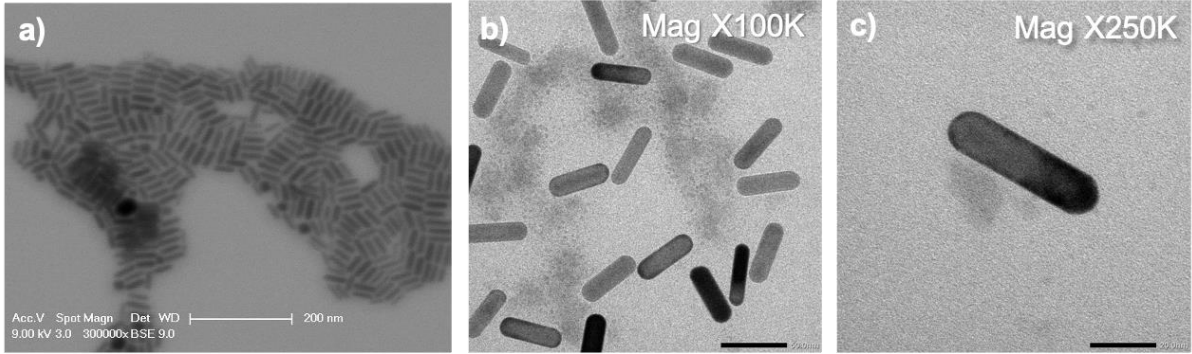


Figure 2. a) SEM micrograph of GNRs. TEM micrograph of b) GNRs and c) single GNR at higher magnification

Following that, the total mass of gold atoms in a single nanorod is calculated as 1.84×10^{15} g via:

$$m_{Au} = \rho V_{single\ nanorod} \quad (4)$$

where ρ is the density of gold. From the mass it is possible to calculate the mole of gold atoms in a single gold nanorod (n_{Au}) by using the following equation:

$$n_{Au} = m_{Au} / Mwt_{Au} \quad (5)$$

where Mwt_{Au} is the molecular weight of gold. The total number of gold atoms in all gold nanorods (N_{Au}) would be calculated by multiplying the mole number of gold atoms in a single nanorod with the Avogadro number (N_a).

$$N_{Au} = N_a \cdot n_{Au} \quad (6)$$

Finally, to calculate the total number of GNRs as 2.34×10^{11} in 1 mL solution, we have used the following equation:

$$Total\ number\ of\ Au\ nanorods = (c_{Au} \cdot V_{total}) / n_{Au} \quad (7)$$

L-SPR sensing experiments are conducted using three different concentrations of glucose (10 mM, 50 mM, and 200 mM) and two different numbers of GNRs (5.85×10^9 and 2.34×10^{10}). The number of GNRs is varied to investigate the impact of nanoparticle concentration on the L-SPR shift. With the addition of glucose, the L-SPR shows a blue shift, indicating a morphological transformation. In the case of the 10 mM glucose solution, the addition of 5.85×10^9 GNRs yielded a noticeable augmentation in the blue shift by 136 nm. Conversely, the introduction of 50 mM glucose elicited a shift of 82 nm, whereas the addition of 100 mM glucose resulted in a shift of 71 nm (Figure 3a). The observation of such a blue shift in the UV-Vis spectrum of GNRs upon the addition of glucose could be attributed to aggregation induced by polar glucose molecules. The hydroxyl groups (-OH) of glucose can interact with the positively charged CTAB molecules on the surface of the nanorods causing a blue shift in the L-SPR wavelength due to large aggregates. The aggregation after the addition of glucose is also visible in the corresponding TEM image depicted in Figure 3b.

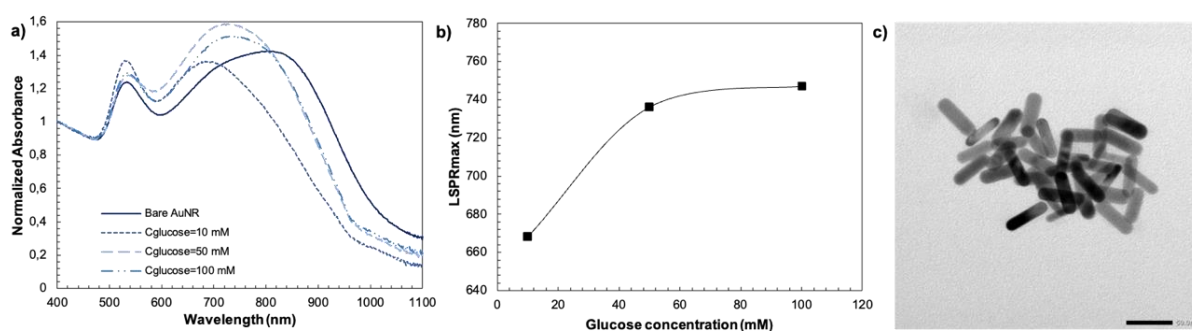


Figure 3. a) UV-Vis Spectrums of bare GNRs and Glucose-GNR mixtures with 10 mM, 50 mM, and 100 mM glucose concentrations and 5.85×10^9 number of GNRs c) Variation in L-SPR wavelength as an effect of change in glucose concentration b) Corresponding TEM image of the sample prepared with 10 mM glucose

A similar blue shift trend is observed when the number of GNRs is increased to 2.34×10^{10} . However, apart from a blue shift in L-SPR, a significant decrease in the intensity of the L-SPR leads to a disappearance, suggesting that the GNRs are undergoing morphological reshaping towards isotropic shapes (Figure 4). When the concentration of GNRs is increased while keeping the amount of glucose constant in comparison to the previous case, the nanoparticles are more likely to come into close proximity and form aggregates. Such aggregation can lead to the coupling of plasmon modes in adjacent nanorods, resulting in a broadening and eventual disappearance of distinct L-SPR peaks. The interaction between the nanorods modifies their plasmonic behaviours, leading to a loss of well-defined resonance peaks.

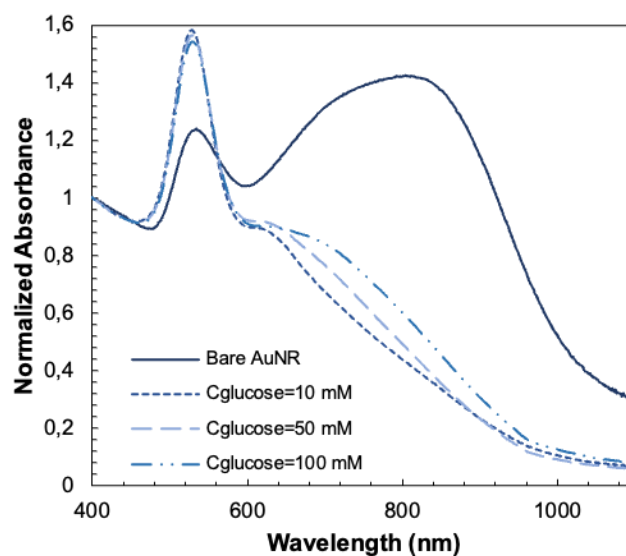


Figure 4. UV-Vis Spectrums of bare GNRs and Glucose-GNR mixtures with 10 mM, 50 mM, and 100 mM glucose concentrations and 2.34×10^{10} number of GNRs.

4. CONCLUSION

In conclusion, this study demonstrates a straightforward and non-enzymatic approach for LSPR-based glucose detection by using GNR aggregates, which exhibited heightened sensitivity towards a glucose concentration upto 10 mM. Sensitivity below 10 mM can be further improved by employing nanorods with higher aspect ratios. With its superior sensitivity, stability, ease of use, and convenient readout, LSPR detection can be combined with different types of sensing platforms to expand the sensor's range even further.

ACKNOWLEDGEMENTS

Financial support for this study was provided by Bogazici University BAP Funding under grant number 19A01P1. I would also like to express my gratitude to Elif Sumeyye Cirit for her assistance during sensing experiments.

CONFLICT OF INTEREST

The author stated that there are no conflicts of interest regarding the publication of this article.

REFERENCES

- [1] Cao J, Sun T, Kenneth T, Grattan V. Development of gold nanorod-based localized surface plasmon resonance optical fiber biosensor. 22nd International Conference on Optical Fiber Sensors, 2012; p 8421.
- [2] Saeed AA, Sánchez JLA, O'Sullivan CK, Abbas MN. DNA biosensors based on gold nanoparticles-modified graphene oxide for the detection of breast cancer biomarkers for early diagnosis. *Bioelectrochemistry*. 2017; 118, 91-99.
- [3] Xu M, Song Y, Ye Y, et al. A novel flexible electrochemical glucose sensor based on gold nanoparticles/polyaniline arrays/carbon cloth electrode. *Sensors and Actuators B: Chemical*. 2017; 252, 1187-1193.
- [4] Hu M, Chen J, Li ZY, et al. Gold nanostructures: engineering their plasmonic properties for biomedical applications. *Chem Soc Rev*. 2006; 35 (11), 1084-1094.
- [5] Kelly KL, Coronado E, Zhao LL, Schatz GC. The Optical Properties of Metal Nanoparticles: The Influence of Size, Shape, and Dielectric Environment. *J Phys Chem B*. 2002; 107 (3), 668-677.
- [6] Lohse SE, Murphy CJ. The Quest for Shape Control: A History of Gold Nanorod Synthesis. *Chem Mater*. 2013; 25(8), 1250-1261.
- [7] Huang X, Neretina S, El-Sayed MA. Gold Nanorods: From Synthesis and Properties to Biological and Biomedical Applications. *Advanced Materials*. 2009; 21 (48), 4880-4910.
- [8] Elechiguerra JL, Reyes-Gasga J, Yacaman MJ. The role of twinning in shape evolution of anisotropic noble metal nanostructures. *J Mater Chem*. 2006; 16 (40), 3906-3919.
- [9] Ramadoss R. MEMS devices for biomedical applications. *Solid State Technology*. Published online 2013. <https://electroiq.com/2013/10/mems-devices-for-biomedical-applications/>.

- [10] Scarabelli L, Coronado-Puchau M, Giner-Casares JJ, Langer J, Liz-Marzán LM. Monodisperse Gold Nanotriangles: Size Control, Large-Scale Self-Assembly, and Performance in Surface-Enhanced Raman Scattering. *ACS Nano*. 2014; 8, p 5833.
- [11] Jana NR. Nanorod Shape Separation Using Surfactant Assisted Self-Assembly. *Chem Commun*. 2003;15, p 1950.
- [12] Scarabelli L, Sánchez-Iglesias A, Pérez-Juste J, Liz-Marzán LM. A “Tips and Tricks” Practical Guide to the Synthesis of Gold Nanorods. *J Phys Chem Lett*. 2015; 6 (21), 4270-4279.
- [13] Lin Y, Zhao M, Guo Y, et al. Multicolor Colorimetric Biosensor for the Determination of Glucose based on the Etching of Gold Nanorods. *Scientific Reports*. 2016; 6 (1), p 37879.
- [14] Chen KC, Li YL, Wu CW, Chiang CC. Glucose Sensor Using U-Shaped Optical Fiber Probe with Gold Nanoparticles and Glucose Oxidase. *Sensors (Basel)*. 2018; 18 (4), p 1217.
- [15] Yin B, Zheng W, Dong M, et al. An enzyme-mediated competitive colorimetric sensor based on Au@Ag bimetallic nanoparticles for highly sensitive detection of disease biomarkers. *Analyst*. 2017; 142 (16), 2954-2960.
- [16] Tao Y, Luo F, Lin Y, Dong N, Li C, Lin Z. Quantitative gold nanorods based photothermal biosensor for glucose using a thermometer as readout. *Talanta*. 2021; 230, p 122364.
- [17] Peng CA, Pachpinde S. Longitudinal Plasmonic Detection of Glucose Using Gold Nanorods. *Nanomaterials and Nanotechnology*. 2014; 4, p 9.
- [18] Xianyu Y, Sun J, Li Y, Tian Y, Wang Z, Jiang X. An ultrasensitive, non-enzymatic glucose assay via gold nanorod-assisted generation of silver nanoparticles. *Nanoscale*. 2013; 5 (14): 6303-6306.
- [19] Nikoobakht B, El-Sayed MA. Preparation and Growth Mechanism of Gold Nanorods (NRs) Using Seed-Mediated Growth Method. *Chem Mater*. 2003; 15, p 1957.
- [20] Brioude A, Jiang XC, Pileni MP. Optical Properties of Gold Nanorods: DDA Simulations Supported by Experiments. *J Phys Chem B*. 2005; 109(27), 13138-13142.



RESEARCH ARTICLE

THE EFFECT OF GRINDING ON OPTICAL BAND GAP AND URBACH ENERGY OF
POLYPYRROLE/GRAPHENE COMPOSITES

Merve OKUTAN^{1,*} 

¹ Department of Chemical Engineering, Engineering Faculty, Hitit University, Çorum, Türkiye

ABSTRACT

The goal of this study is to better understand the effect of grinding on the E_g of polypyrrole (PPy)/commercial graphene nanoplatelets (xGnP) composites with varying amounts of xGnP. The E_g for direct transition as a function of the xGnP amount was calculated from the Tauc plot. While the average particle size of the composites decreased between 6% and 30%, there was a slight decrement in the E_g s. These values changed between 4.02 to 3.87 eV with the increasing amount of xGnP before grinding, and they reached between 3.97 to 3.88 eV after grinding. Moreover, it was determined that the E_U was inversely proportional to E_g . These findings suggest that the PPy/xGnP composites could be suitable for several applications, such as photocatalytic and optoelectronic.

Keywords: Polypyrrole, Graphene, Tauc plot, Urbach energy, UV/Vis spectroscopy

1. INTRODUCTION

Polymeric semiconductors are frequently used in application areas such as transistors [1], electrochromic materials [2], photocatalysis [3], batteries [4], supercapacitors [5], corrosion [6], and biomedical devices [7] due to their superior properties. Among them, PPy is a well-known conjugated polymer that has been the focus of many studies due to its easy synthesis, good electrical properties, biocompatibility, low oxidation potential, chemical and environmental stability, large surface area, satisfying specific capacitance, processability, strong absorption spectral range and low cost [7-10]. However, the spherical polymer particles, which are easy to agglomerate, and their relatively low mechanical strength limit PPy usage for several applications. These problems can be overcome by preparing composites/nanocomposites of PPy with various carbon-derived materials [9,11]. Moreover, electrical and optical properties can be improved owing to the fast and easy electron/ion transfer that can be obtained with the contribution of a carbon network with high carrier transport mobility such as graphene [12]. Graphene modification of the PPy main chain is expected to control the interchain interaction and make this material, which acts as an electron donor/hole transporter under UV through the delocalized π - π^* conjugated structure, more efficient for applications such as color change and photocatalysis by controlling the optical energy band gaps (E_g) [13]. It is important to monitor the electronic properties of PPy and its composites used in applications related to electronic and optical properties such as sensors, electronics, optics, and photovoltaic devices. Studies have been carried out to monitor the electronic properties with the change in optical band gap of these composites. Some of them in the literature investigating the E_g of PPy composites prepared with graphene derivatives are listed below. Bora and Dolui [9] studied a new procedure prepared for PPy/graphene via liquid-liquid interfacial polymerization and they remarked that the electrical conductivity and thermal stability of these materials were observably enhanced. The E_g of PPy and composites was determined as 2.33 eV and 2.10-1.82 eV according to increased graphene content, respectively. Liu et al. [13] reported that the graphitic carbon nitride and PPy composite, which was prepared via in-situ chemical polymerization of

pyrrole, had narrowed E_g due to the PPy, and also the addition of reduced graphene oxide (rGO) into composite led to much lower E_g between 2.4 to 2.6 eV. Sadrolhosseini et al. [14] prepared the PPy/rGO nanocomposite with had particular thickness based on deposition time via electrochemical synthesis and determined the E_g between 3.580 to 3.853 eV with decreased deposition time. Noreen et al. [15] studied about photocatalytic and antibacterial properties of PPy/graphene composites that were synthesized via in-situ chemical oxidative polymerization. While the E_g of PPy was calculated as 2.38 eV, they reported that the E_g values of composites containing 10, 30, and 50% graphene were determined as 1.85 eV, 1.69 eV, and 1.63 eV, respectively. Ahmed and Hassan [16] investigated the optical and electrical properties of PPy/graphene composites prepared via in-situ polymerization. They stated that the E_g value of PPy by direct transition, which was 2.1 eV, decreased to 1.3 eV with the contribution of 5% graphene. In all of the limited number of studies mentioned above, $FeCl_3$ was used as the oxidant, regardless of the synthesis method. It is well known that the length of the conjugated chains obtained in the synthesis of conducting polymers has a direct effect on the physical properties of the polymer and the conjugation length is related to the type and ratio of the oxidant and dopant used [17]. In addition to $FeCl_3$, several oxidizing agents such as $FeClO_4$, $AgNO_3$, H_2O_2 , and $(NH_4)_2S_2O_8$ have been used for the chemical oxidation of pyrrole [18]. When PPy was synthesized by chemical oxidative polymerization in acidic medium, it was reported that the electrical conductivity value was higher but the polymerization yield was lower than that of $(NH_4)_2S_2O_8$ when $FeCl_3$, which has low solubility in this medium, was used as oxidant [19]. Sood and co-workers used $FeCl_3$ and $(NH_4)_2S_2O_8$ as oxidants in the synthesis of PPy and compared the effect on thermal, electrical and morphological properties [18]. Dubey et al. investigated the characterization and morphological properties of PPy synthesized under ammonium per sulfate in the presence of anionic and cationic surfactants and their combinations for the energy storage capacity and its potential use in sensor applications of the prepared material [20]. Similarly, John and Jayalekshmi investigated the solubility, processability, electrical, optical and morphological properties of PPy synthesized with different dopants and ammonium per sulfate oxidant with a view to using the prepared material in potential technological applications [21]. Ravikiran et al. investigated the use of a physically prepared composite of PPy and reduced graphene oxide as a humidity sensor. Ammonium per sulfate was used as an oxidant in the synthesis of PPy [22]. Atta et al. investigated the use of PPy, synthesized in the presence of APS, and NiO conductive composites in optoelectronic devices [23]. In addition to these studies, the effect of grinding on the change in particle size was investigated to understand the optical properties of PPy and PPy/xGnP composites prepared using $(NH_4)_2S_2O_8$ as an oxidant in acidic medium. For this purpose, PPy and xGnP composites were synthesized via oxidative polymerization. Optical properties were investigated using ultraviolet-visible (UV-Vis) spectrophotometry. The E_g value was estimated via Tauc plot and Urbach tail energy (E_U) was calculated to determine defect levels based on xGnP amount for PPy based composites both before and after ball milling. In addition, while chemical and morphological properties of PPy and PPy/xGnP composites were investigated with Fourier transform infrared spectroscopy (FTIR), Raman spectroscopy, X-ray photoelectron spectroscopy (XPS), and transmission electron microscope (TEM)/scanning electron microscope (SEM) analysis; particle size of the composites was determined using a Zeta Sizer.

2. EXPERIMENTAL

2.1. Materials

Pyrrole (99.5%), hydrochloric acid (HCl, 37%) and xGnP nanoplatelets (grade C-750) were purchased from Sigma-Aldrich. Ammonium persulfate ($(NH_4)_2S_2O_8$, >98%) as an oxidizer agent was provided by Merck. Dimethyl sulfoxide (DMSO, >99%) was obtained by also Merck as a solvent for UV-Vis measurements. All chemicals were used as received.

2.2. Synthesis of PPy/xGnP Composites

PPy/xGnP composites were synthesized by oxidative polymerization of pyrrole monomer including xGnP at various loadings (1, 3, and 5 w/v) in the presence of HCl and $(\text{NH}_4)_2\text{S}_2\text{O}_8$. For this, 0.2 M pyrrole monomer and a proper amount of xGnP were mixed in 50 ml 1 M HCl. Then, 0.2 M $(\text{NH}_4)_2\text{S}_2\text{O}_8$ solution as oxidant, which was prepared in 1 M HCl, was added slowly to the monomer solution in an ice bath. The polymerization reaction was allowed at 0-5°C for 2 h under constant stirring. The obtained black product was filtrated and then washed several times with acid and ultra-pure water for purification. PPy/xGnP composite was dried at 80°C for 8 h [24]. In addition, PPy was synthesized without adding xGnP. To reveal the effect of grinding via ball milling on the Eg of composites, the prepared PPy/xGnP composites were ground in a Fritsch pulverisette 7 planetary ball mill at room temperature using a sintered alumina bowl and balls (balls to powder ratio was 10% w/w) at 500 rpm for 5 min through the forward and reverse. The samples were labelled as in Table 1.

Table 1. Abbreviations for PPy/xGnP composites according to ball milling.

	Abb.	Sample
	(PPy)i	Synthesized polypyrrole
Before ball milling (i:initial)	(PPy/xGnP1)i	Synthesized PPy/xGnP composite containing 1% (w/v) xGnP
	(PPy/xGnP3)i	Synthesized PPy/xGnP composite containing 3% (w/v) xGnP
	(PPy/xGnP5)i	Synthesized PPy/xGnP composite containing 5% (w/v) xGnP
	(PPy)bm	Ball milled polypyrrole
After ball milling (bm: ground via ball milling)	(PPy/xGnP1)bm	Ball milled PPy/xGnP composite containing 1% (w/v) xGnP
	(PPy/xGnP3)bm	Ball milled PPy/xGnP composite containing 3% (w/v) xGnP
	(PPy/xGnP5)bm	Ball milled PPy/xGnP composite containing 5% (w/v) xGnP

2.3. Characterization

The particle size distributions of the PPy, xGnP, and PPy/xGnP composites were determined using a ZetaSizer Nano ZSP laser particle analyser (Malvern). The FTIR of the PPy, xGnP, and PPy/xGnP composites was recorded by a Thermo Scientific Nicolet 6700 FTIR spectrometer equipped with an ATR (attenuated total reflectance) attachment in the wave number range from 600 to 4000 cm^{-1} . The Raman spectra of the PPy, xGnP, and PPy/xGnP composites were collected from a Renishaw Raman spectroscopy (532 nm). The optical properties of PPy, xGnP, and PPy/xGnP composites were studied using a UV-Vis spectrophotometer in the range of 200-800 nm by using Genesys 10S, Thermo USA. All samples were dispersed in DMSO at a concentration of 0.3 mg/mL using tip sonication for 15 min (Bandelin Sonopuls, type: UW 200, probe: TS113, ampl: 10%, pulse: 0.5s/1s). The TEM image of xGnP was taken from a JEOL JEM 1220 electron microscope and the morphological characterization of the (PPy/xGnP5)bm was performed with a field emission SEM (FESEM, Quanta 450 FEG model, 20-30 kV, FED).

3. RESULTS AND DISCUSSION

3.1. ZetaSizer Analysis

Particle size distribution analysis by the intensity of PPy, xGnP, and PPy/xGnP composites before and after grinding with ball milling was performed with a ZetaSizer and the results are given in Figure 1. xGnP was a commercial product with a surface area $750 \text{ m}^2 \text{ g}^{-1}$. Its average particle size was found to be around 168 nm (Figure 1a). While PPy showed an average particle size of 876 nm, the size of (PPy)bm was found 365 nm (Figures 1b and 1c). The average particle sizes of the composites containing 1, 3, and 5% of xGnP were determined to be 718, 853, and 1048 nm before ball milling (Figures 1d, 1e, and 1f). These values decreased to 674, 779, and 730 nm after grinding via ball milling (Figures 1g, 1h, and 1i), respectively. The results showed a slightly increasing trend in particle size with the ascending filler amount of composite. It is predicted that polymerization started after the adsorption of pyrrole to the electronegative oxygen atom on functional groups on the xGnP sheets [25]. Hence, PPy/xGnP composite particles were partially grown with the increment of the graphene amount in the composite due to the formation of PPy particles on the curved xGnP surface (see Figure 7b) during the synthesis [26].

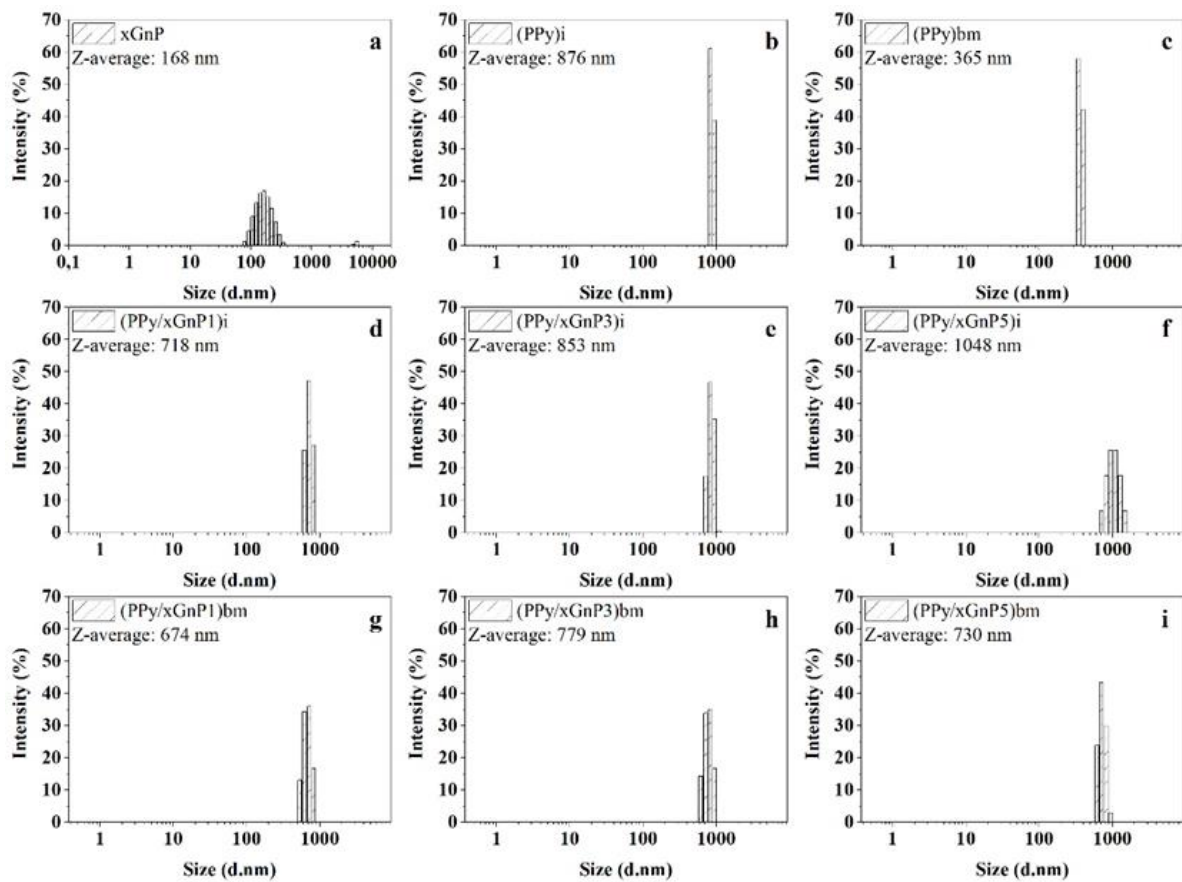


Figure 1. The particle size distribution by intensity of (a) xGnP; (b) (PPy)i, (c) (PPy)bm, (d) (PPy/xGnP1)i, (e) (PPy/xGnP3)i, (f) (PPy/xGnP5)i, (g) (PPy/xGnP1)bm, (h) (PPy/xGnP3)bm, and (i) (PPy/xGnP5)bm, respectively.

3.2. FTIR Analysis

The FTIR spectra of xGnP, PPy, and PPy/xGnP composites are given in Figure 2. The FTIR peaks of PPy at 1546 cm^{-1} , 1461 cm^{-1} , and 3433 cm^{-1} were attributed to the C-C, C-N, and N-H stretching vibrations of the ring structure in pyrrole. The peaks at 1690 cm^{-1} , 1169 cm^{-1} , and 1027 cm^{-1} can be assigned to C=N bonds, C-N in-plane vibration, and C-H band in-plane vibration for PPy, respectively. The peaks at about 2920 cm^{-1} and 2850 cm^{-1} in all spectra were associated with asymmetrical and symmetrical ring vibrations of CH_2 . The carbonyl peak ($-\text{COOH}$) at 1723 cm^{-1} , the C-O stretching vibration at 1058 cm^{-1} and the hydroxyl group ($-\text{OH}$) at 3467 cm^{-1} of xGnP showed the oxygen-containing functional groups on the graphene surface. Also for xGnP, a strong band of the stretching and deformation vibrations of CH_2 appeared at about 2332 cm^{-1} . The presence of characteristic peaks of PPy in composites spectra confirmed the existence of PPy in the composites. The shift of the C=O peak to nearly 1760 cm^{-1} was probably related to the π - π interaction of the aromatic PPy ring with oxygenated functional groups on xGnP. In short, these changes proved that the combination of graphene in the PPy matrix and the composites were successfully synthesized [9,25,27-30].

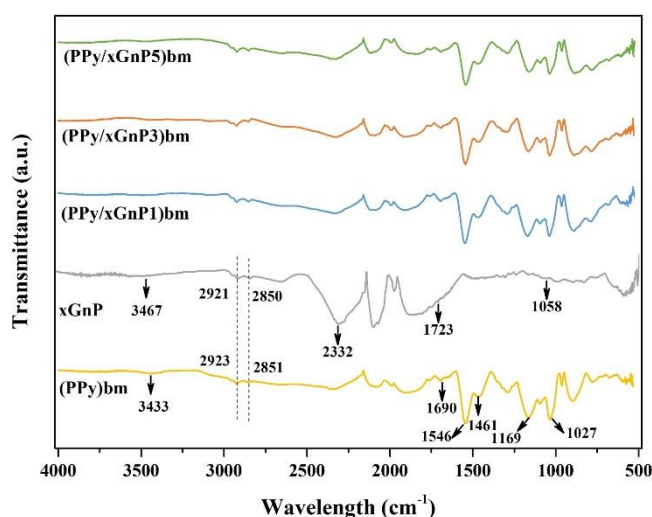


Figure 2. FTIR spectra of xGnP, (PPy)bm, (PPy/xGnP1)bm, (PPy/xGnP3)bm, and (PPy/xGnP5)bm.

3.3. Raman Analysis

The Raman spectra of xGnP, PPy, and PPy/xGnP composites are given in Figure 3. The xGnP spectrum in Figure 3a displayed three distinctive Raman bands at about 1323 cm^{-1} , 1576 cm^{-1} , and 2636 cm^{-1} , which were attributed to the D, G, and 2D bands, respectively. The characteristic Raman bands at about 1355 cm^{-1} and 1570 cm^{-1} corresponded with the C-N ring stretching and C=C backbone stretching for PPy (Figure 3a), which these Raman bands were in approximately the same position with D and G bands of graphene. The almost same bands were seen in Raman spectra of PPy/xGnP composites (Figure 3a). However, in the Raman spectra of composites, both D and G bands were shifted between 1330 - 1340 cm^{-1} and 1550 - 1570 cm^{-1} , which indicated the π - π interaction between PPy and xGnP. Furthermore, since the double bonds between the carbon atoms and other conjugated bonds lead to increase in the Raman intensities, the Raman intensities of polymer and polymer composites were higher than that of the commercial graphene as seen in Figure 3a [31-34].

In Raman spectroscopy, the D band indicates sp^3 hybridization and the amount of structural defects and edges, while the G band indicates sp^2 hybridization and a more ordered structure. In other words, the higher intensity of the D band indicates that the graphite network of the material has more defects. In addition, a more distinct G band means that the material has a more crystalline structure. The information about the structural defect can be obtained by proportioning the intensities of the D and G bands, as having similar intensities indicates the highly defective structure [31,35,36]. As seen in Figure 3b, I_D/I_G ratios for each sample were calculated by reading and proportioning the Raman band intensities at the wavelengths specified for the D and G bands in the spectrum. Although the prepared composites had a slightly ordered structure compared to xGnP, I_D/I_G ratios were almost the same. While various functionalization processes are expected to increase the defect ratio in the structure, it is predicted that there was no significant change in the size of the average sp^2 domains because of the PPy/xGnP interaction [37]. As a second opinion, it can be evaluated that the prepared composites were quite defective compared to xGnP. Because this ratio can be lower than graphene in highly defective materials where the distance between defects is less than two nm [38].

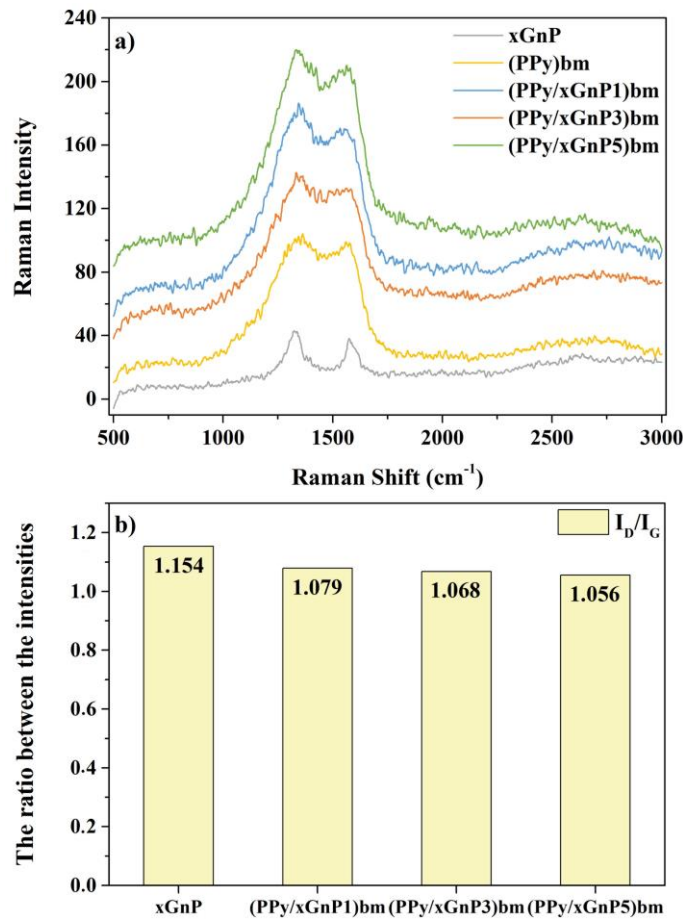


Figure 3. (a) Raman spectra and (b) I_D/I_G ratios of xGnP, (PPy)bm, (PPy/xGnP1)bm, (PPy/xGnP3)bm, and (PPy/xGnP5)bm.

3.4. XPS Analysis

XPS analysis was carried out to examine the chemical state and composition of PPy, xGnP, and PPy/xGnP composites and the spectra are shown in Figure 4. As is seen from Figure 4, the xGnP had

C1s core level peaks at 284.4 eV that could be attributed to the C-C bond, and the peak at ~288.8 eV was related to the C=O bond [39]. The N1s core level peak was absent in the xGnP, while it was seen in the PPy samples spectra, which is related to the polymerization of pyrrole [40]. In addition, Figure 4 is depicted the presence of characteristic O1s (~531 eV), C1s (~284 eV), N1s (~399 eV), and S2p (~168 eV) peaks both for the PPy and its composites with xGnP. The S2p core level peak was generated from $(\text{NH}_4)_2\text{S}_2\text{O}_8$, which was used as an oxidant for the polymerization of PPy. The change in the binding energies of PPy to higher energy levels for composites (O1s (~532 eV), C1s (~285 eV), N1s (~400 eV)) was related to the π - π interaction between the PPy and xGnP, which is in good agreement with the FTIR and Raman results. The core level peak of C-N at ~285 eV was also confirmed to be the PPy moiety in the xGnP structure. The N1s core level peaks at ~399 and ~400 eV were attributed to the -N-H group in the pyrrole ring and positively charged N of polaron (-N-H⁺). The rising energy level from 399 to 400 eV was associated with the migration of the neutral secondary amine, which also indicated a strong π - π interaction [39,41,42]. Furthermore, the Cl2p peak (~198 eV) was observed in all PPy samples due to the HCl as the dopant [43]. This confirmed the successful preparation of PPy/xGnP composites.

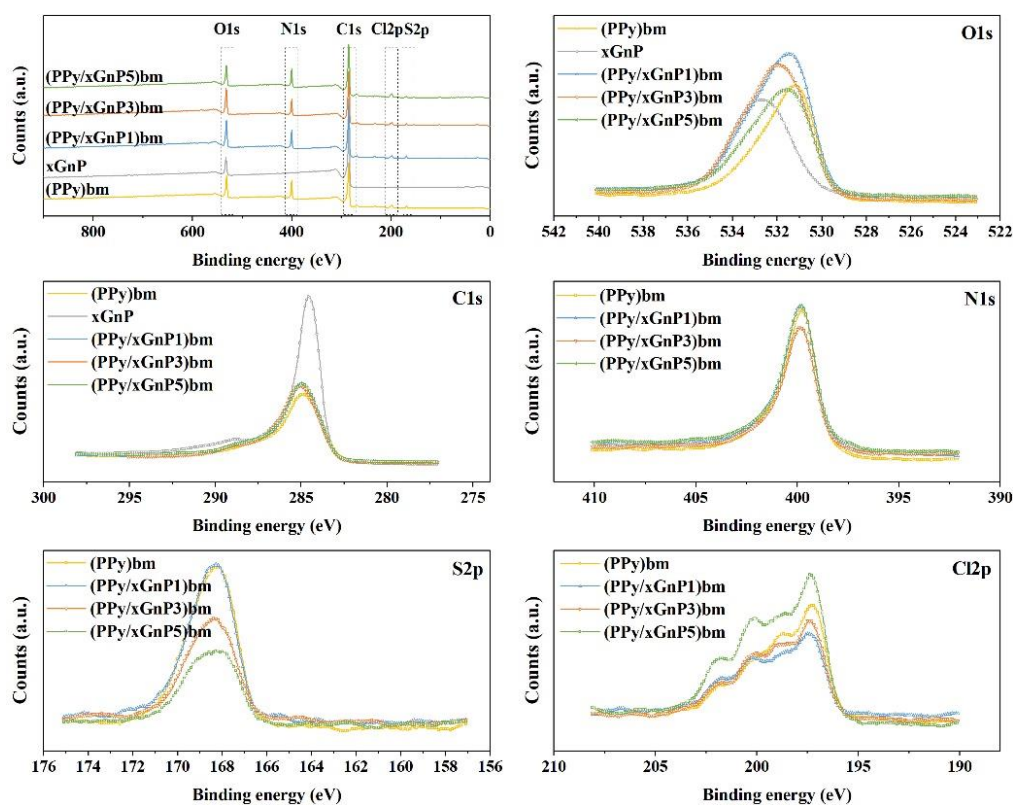


Figure 4. General and elemental (O1s, C1s, N1s, S2p, Cl2p) XPS spectra of the xGnP, (PPy)bm, (PPy/xGnP1)bm, (PPy/xGnP3)bm, and (PPy/xGnP5)bm.

3.5. UV-Vis Analysis

The UV-Vis absorption spectra of xGnP, PPy, and PPy/xGnP composites recorded in DMSO are shown in Figures 5a and 5c. xGnP showed a distinctive peak at 279 nm which, is dedicated to the π - π^* transition of the C=C bonds. For the PPy and PPy/xGnP composites, the spectra showed a characteristic band at around 275-281 nm due to the π - π^* interactions for C=C group. In addition to this peak, the spectra of synthesized composites displayed a broad absorption band between 350-400 nm related to the π - π^* transitions for the C=N group. After the ball milling, the peak that related to the sp^2 C=C bands of the

composites was slightly shifted. It was thought that this behavior could be explained by the restoration of π conjugation regions due to the change in particle size. In addition, the increase in the xGnP ratio in the composite caused an increase in the absorbance value. Similar results were observed for the UV-Vis spectra in the literature [44-48].

The E_g (eV) of xGnP, PPy, and PPy/xGnP composites was obtained with UV-Vis absorbance spectrum and the E_g values were calculated using Tauc plot as follows (Equation 1).

$$(\alpha h\nu)^{1/m} = B(h\nu - E_g) \quad (1)$$

$$\alpha(\lambda) = \left(\frac{2.303}{d}\right)A(\lambda) \quad (2)$$

where α (cm^{-1}) is the absorption coefficient which is given in Equation 2, d is sample width (cm), A is absorbance from UV-Vis analysis, h is the Planck's constant (4.14×10^{-15} eVs), ν is the frequency (s^{-1}), B is a comparative constant, and m is a constant related to the electronic transition type which is equal to $1/2$ for direct transition. The experimental method should be used to determine the most appropriate value of m . According to Equation 1, the E_g value should be directly proportional to $(\alpha h\nu)^{1/m}$. For this reason, these linear parts of the irregular graph drawn by calculating the $(\alpha h\nu)^{1/m}$ and $h\nu$ values are taken into account. The E_g value is determined as the intersection of the $h\nu$ axis by extrapolation from the linear part [49-51].

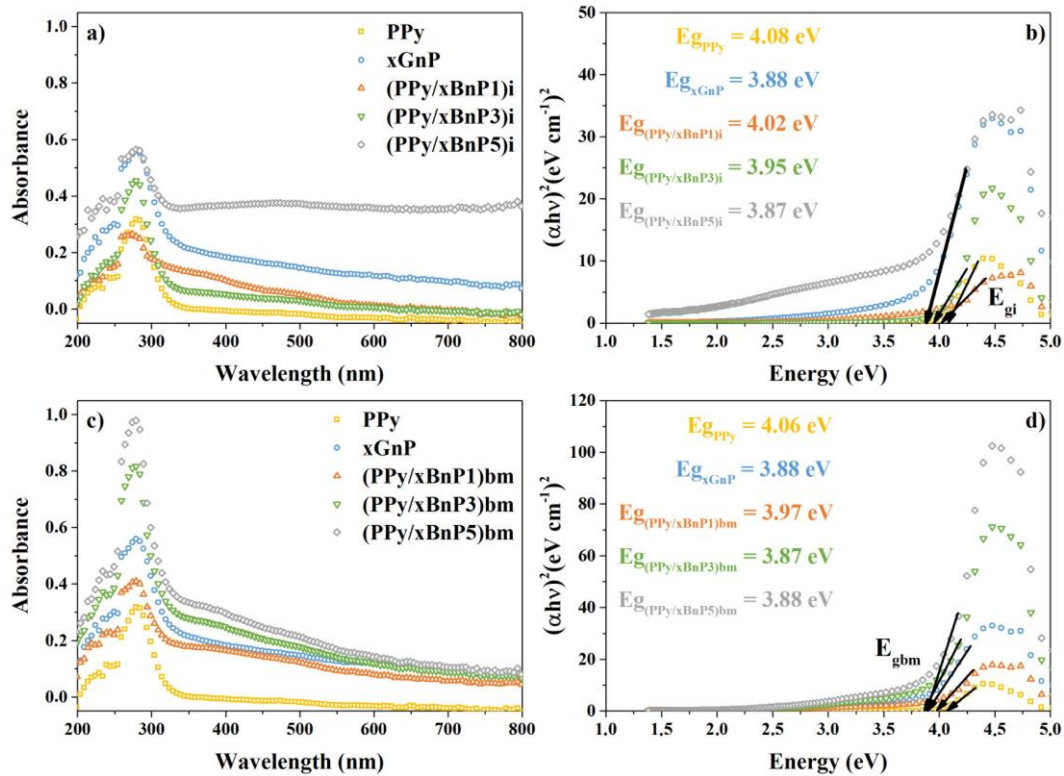


Figure 5. UV-Vis absorption spectra and Tauc plot for direct transition of xGnP, PPy, and PPy/xGnP composites (a,b) before and (c,d) after ball milling, respectively.

The Tauc plot was used to estimate the E_g for direct transition of xGnP, PPy, and PPy/xGnP composites before and after ball milling are given in Figures 5b and 5d. Based on the Tauc plot, the calculated E_g of xGnP was estimated to be ~ 3.88 eV for direct band gap transition. As can be seen from the Figures 5b and 5d, the E_g values of PPy decreased as the amount of xGnP in the composite increased, both before and after ball milling. These results showed that the number of electrons/holes in the valence and conduction bands changed due to the presence of new charge transfer complexes formed between PPy and xGnP and the disorder created in a polymer matrix [48,52,53]. In addition, there was a slight decrease in $E_{g_{bm}}$ values compared to E_{g_i} .

In semiconductors, if sub-bands form between the conduction and valence bands or there are defects, a defect tail is formed, which is known as the Urbach tail, under the conduction band and above the valence band. In this region, to estimate the defect level and the localized states in the forbidden band gap, the E_U can be calculated from Equation 3.

$$\ln(\alpha) = \ln(\alpha_0) + \left(\frac{hv}{E_U}\right) \quad (3)$$

where α_0 is a constant, hv is the energy, and the E_U is Urbach energy [48,54]. For the determination of the E_U , the first $\ln(\alpha)$ - hv graph is drawn. Then, in this region (below the E_g value), the E_U value can be calculated in the slope of the linear graph obtained from the curve of the logarithm of the absorption coefficient versus the energy. The E_U results calculated for PPy samples were given in Table 2 and the linear part of the graph of $\ln(\alpha)$ versus hv was given in Figure 6.

Table 2. E_U of xGnP, PPy, and PPy/xGnP composites.

Samples	E_U (eV)
xGnP	2.8234
PPy	0.1392
(PPy/xGnP1)i	0.9238
(PPy/xGnP3)i	1.2741
(PPy/xGnP5)i	9.8649
(PPy/xGnP1)bm	2.1852
(PPy/xGnP3)bm	2.3085
(PPy/xGnP5)bm	2.3935

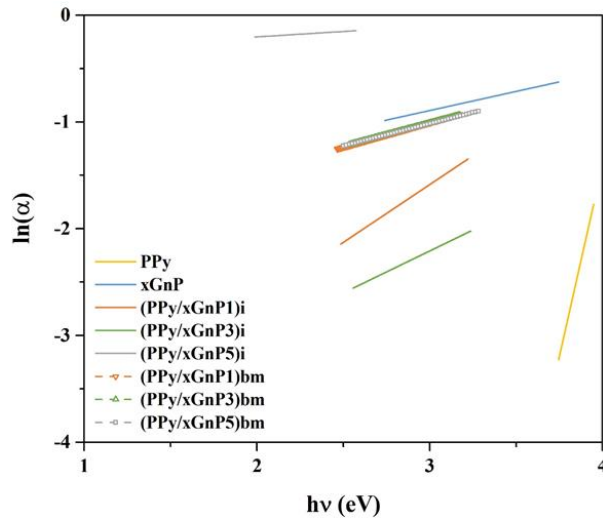


Figure 6. $\ln(\alpha)$ of xGnP, PPy, and PPy/xGnP composites versus hv .

It was determined that the E_U value of PPy was increased with the increase of xGnP in the composite both before and after ball milling. These results were inversely proportional to E_g change. Furthermore, it displayed that the xGnP led to a lower energy transition in the composites and the degree of disordering in the polymeric structure progressed due to the increasing localized states in the forbidden band gaps in the PPy structure. The results obtained are in agreement with the literature [16,48,52,53].

3.6. Surface Morphology Analysis

The structural morphology of xGnP and (PPy/xGnP5)bm composite was investigated by TEM and SEM analysis. From the TEM image of xGnP, which is given in Figure 7a, partially wrinkled and transparent graphene sheets could be clearly seen. This wrinkled sheet like morphology, seen in the literature for graphene, has been interpreted as a reduction in the angular tension between carbon bonds due to changes between sp^2 and sp^3 hybridized carbon atoms and the atomic arrangement becoming more stable by taking on a wrinkled aspect [55,56]. The SEM image for the (PPy/xGnP5)bm is given in Figure 7b. The formation of the composite can be described as the uniform absorption of the pyrrole on the xGnP surface through non-covalent interaction and polymerization and coating of PPy on the xGnP surface via in-situ polymerization [40]. From the figure, it can be seen that the almost uniform PPy particles of granular or spherical shape were embedded on the graphene sheet. Consequently, this image indicated that the pyrrole polymerization took place on the graphene sheets, and PPy was successfully anchored on the xGnP surface [9,14,57].

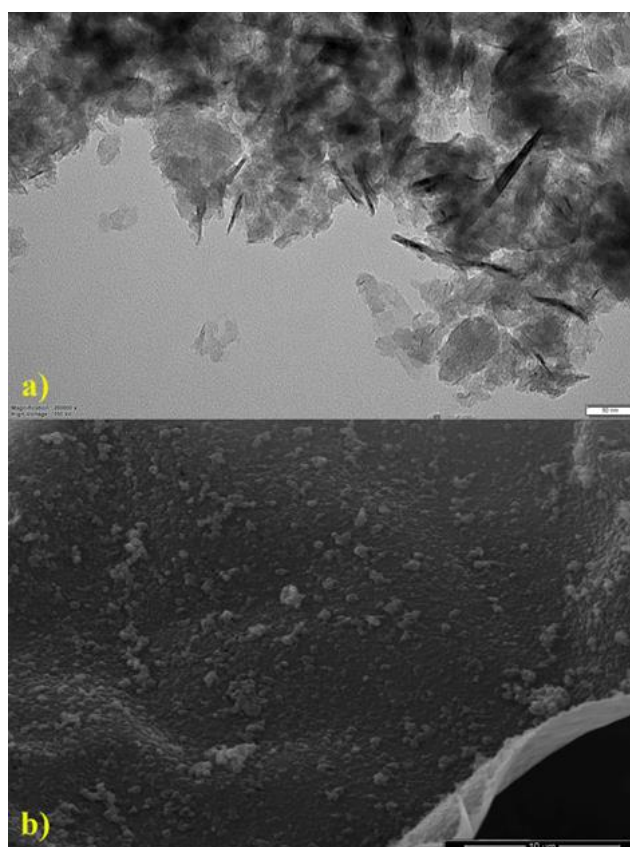


Figure 7. (a) TEM image of xGnP (scale bar 50 nm) and (b) SEM image of (PPy/xGnP5)bm (mag. 10,000 x, scale bar 10 μ m).

4. CONCLUSION

The present study describes the synthesis of PPy and PPy/xGnP composites via oxidative polymerization of pyrrole in the presence of $(\text{NH}_4)_2\text{S}_2\text{O}_8$ as an oxidant. The effect of the grinding via ball milling on the E_g and structural defects of these materials was then investigated. The E_g of the samples was calculated using UV-Vis absorption spectrophotometry. The FTIR, Raman, and XPS analysis revealed the change of the functional groups on PPy and xGnP after the composite preparation. The UV-Vis analysis confirmed the decrease in E_g calculated from the Tauc plot for the direct transition of the composites after ball milling. The decrease in band gap energy with both ball milling and increasing graphene content is attributed to the change in defect levels of the composite structure. Furthermore, the E_U value changed from 0.1392 eV for PPy to 2.3935 eV for (PPy/xGnP5)bm indicating that the defect in the polymer structure increased with the addition of xGnP to the composite. These results indicate that the optical properties improved slightly after grinding. It is expected that these findings will be helpful for several applications such as electronic, optic, and sensing.

CONFLICT OF INTEREST

The author stated that there are no conflicts of interest regarding the publication of this article.

REFERENCES

- [1] Wang Y, Qing X, Zhou Q, Zhang Y, Liu Q, Liu K, Wang W, Li M, Lu Z, Chen Y et al. The woven fiber organic electrochemical transistors based on polypyrrole nanowires/reduced graphene oxide composites for glucose sensing. *Biosens Bioelectron.* 2017; 95: 138-145.
- [2] Bezgin Carbas B, Ergin NM, Yildiz HB, Kivrak A, Demet AE. Electrochromic properties of a polydithienylpyrrole derivative with n-phenyl pyrrole subunit. *Mater Chem Phys.* 2023; 293: 126916.
- [3] Ahmad N, Sultana S, Sabir S, Khan MZ. Exploring the visible light driven photocatalysis by reduced graphene oxide supported PPy/CdS nanocomposites for the degradation of organic pollutants. *J Photochem Photobiol A Chem.* 2020; 386: 112129.
- [4] Folorunso O, Hamam Y, Sadiku R, Ray SS, Adekoya GJ. Investigation of graphene loaded polypyrrole for lithium-ion battery. *Mater Today Proc.* 2021; 38: 635-638.
- [5] Gupta A, Sardana S, Dahiya S, Punia R, Maan AS., Singh K, Tripathi R, Ohlan A. Binder-free polypyrrole/fluorinated graphene nanocomposite hydrogel as a novel electrode material for highly efficient supercapacitors. *Appl Surf Sci Adv.* 2022; 11: 100297.
- [6] Qiu S, Li W, Zheng W, Zhao H, Wang L. Synergistic effect of polypyrrole-intercalated graphene for enhanced corrosion protection of aqueous coating in 3.5% NaCl solution. *ACS Appl Mater Interfaces.* 2017; 9: 34294-34304.
- [7] Zare EN, Agarwal T, Zarepour A, Pinelli F, Zarrabi A, Rossi F, Ashrafizadeh M, Maleki A, Shahbazi MA, Maiti TK et al. Electroconductive multi-functional polypyrrole composites for biomedical applications. *Appl Mater Today.* 2021; 24: 101117.

- [8] Hao L, Yu D. Progress of conductive polypyrrole nanocomposites. *Synth Met.* 2022; 290: 117138.
- [9] Bora C, Dolui SK. Interfacial synthesis of polypyrrole/graphene composites and investigation of their optical, electrical and electrochemical properties. *Polym Int.* 2014; 63: 1439-1446.
- [10] Krishnaswamy S, Ragupathi V, Raman S, Panigrahi P, Nagarajan GS. Optical properties of p-type polypyrrole thin film synthesized by pulse laser deposition technique: Hole transport layer in electroluminescence devices. *Optik (Stuttg).* 2019; 194: 163034.
- [11] Wilczewska P, Breczko J, Bobrowska DM, Wysocka-Żołopa M, Goclon J, Basa A, Winkler K. Enhancement of polypyrrole electrochemical performance with graphene quantum dots in polypyrrole nanoparticle/graphene quantum dot composites. *J Electroanal Chem.* 2022; 923: 116767.
- [12] Velasco-Soto MA, Pérez-García SA, Alvarez-Quintana J, Cao Y, Nyborg L, Licea-Jiménez L. Selective band gap manipulation of graphene oxide by its reduction with mild reagents. *Carbon N Y.* 2015; 93: 967-973.
- [13] Liu S, Jiang X, Waterhouse GIN, Zhang ZM, Yu L. Protonated graphitic carbon nitride/polypyrrole/reduced graphene oxide composites as efficient visible light driven photocatalysts for dye degradation and E. coli disinfection. *J Alloys Compd.* 2021; 873: 159750.
- [14] Sadrolhosseini AR, Abdul Rashid S, Noor ASM, Kharazmi A, Lim HN, Mahdi MA. Optical band gap and thermal diffusivity of polypyrrole-nanoparticles decorated reduced graphene oxide nanocomposite layer. *J Nanomater.* 2016; 2016(Article ID 1949042): 1-8.
- [15] Noreen H, Iqbal J, Arshad A, Faryal R, Ata-ur-Rahman, Khattak R. Sunlight induced catalytic degradation of bromophenol blue and antibacterial performance of graphene nanoplatelets/polypyrrole nanocomposites. *J Solid State Chem.* 2019; 275: 141-148.
- [16] Ahmed, F.M., Hassan, S.M. Optical and A.C. electrical properties for polypyrrole and polypyrrole/graphene (ppy/gn) nanocomposites. *Iraqi J Phys.* 2021; 19: 72-78.
- [17] Dey S, Kumar KA. Morphological and optical properties of polypyrrole nanoparticles synthesized by variation of monomer to oxidant ratio. *Mater Today Proc.* 2019; 18: 1072-1076.
- [18] Sood Y, Mudila H, Katoch A, Lokhande PE, Kumar D, Sharma A, Kumar A. Eminence of oxidants on structural–electrical property of polypyrrole. *J Mater Sci Mater Electron.* 2023; 34: 1401.
- [19] Li XG, Li A, Huang MR, Liao Y, Lu YG. Efficient and Scalable Synthesis of Pure Polypyrrole Nanoparticles Applicable for Advanced Nanocomposites and Carbon Nanoparticles. *J Phys Chem C.* 2010; 114: 19244-19255.
- [20] Dubey N. A study on surfactant modified polypyrrole nanostructures and its applications in supercapacitors. *Int J Polym Anal Charact.* 2023; 28: 625-646.
- [21] John J, Jayalekshmi S. Polypyrrole with appreciable solubility, crystalline order and electrical conductivity synthesized using various dopants appropriate for device applications. *Polym Bull.* 2023; 80: 6099-6116.

- [22] Ravikiran YT, Chethan B, Prasad V, Raj Prakash HG, Prashantkumar M, Tiwari SK, Thomas S. Polypyrrole/reduced graphene oxide composite as a low-cost novel sensing material for fast-response humidity sensor. *Mater Chem Phys*. 2023; 303: 127800.
- [23] Atta A, Abdeltwab E, Negm H, Al-Harbi N, Rabia M, Abdelhamied MM. Characterization and linear/non-linear optical properties of polypyrrole/NiO for optoelectronic devices. *Inorg Chem Commun*. 2023; 152: 110726.
- [24] Deligöz H, Tieke B. Conducting composites of polyurethane resin and polypyrrole: solvent-free preparation, electrical, and mechanical properties. *Macromol Mater Eng*. 2006; 291: 793-801.
- [25] Manivel P, Kanagaraj S, Balamurugan A, Ponpandian N, Mangalaraj D, Viswanathan C. Rheological behavior-electrical and thermal properties of polypyrrole/graphene oxide nanocomposites. *J Appl Polym Sci*. 2014; 131: 40642(1-10).
- [26] Li S, Wu D, Cheng C, Wang J, Zhang F, Su Y, Feng X. Polyaniline-coupled multifunctional 2D metal oxide/hydroxide graphene nanohybrids. *Angew Chemie Int*. 2013; 52: 12105-12109.
- [27] Bose S, Kim NH, Kuila T, Lau K, Lee JH. Electrochemical performance of a graphene-polypyrrole nanocomposite as a supercapacitor electrode. *Nanotechnology*. 2011; 22: 295202.
- [28] Fan X, Yang Z, He N. Hierarchical nanostructured polypyrrole/graphene composites as supercapacitor electrode. *RSC Adv*. 2015; 5: 15096-15102.
- [29] Basavaraja C, Kim WJ, Thinh PX, Huh DS. Electrical conductivity studies on water-soluble polypyrrole-graphene oxide composites. *Polym Compos*. 2011; 32: 2076-2083.
- [30] Iam SN, Kumar L, Sharma N. Development of Cu-exfoliated graphite nanoplatelets (xGnP) metal matrix composite by powder metallurgy route. *Graphene*. 2015; 04: 91-111.
- [31] Bora C, Dolui SK. Fabrication of polypyrrole/graphene oxide nanocomposites by liquid/liquid interfacial polymerization and evaluation of their optical, electrical and electrochemical properties. *Polymer (Guildf)*. 2012; 53: 923-932.
- [32] Alves APP, Koizumi R, Samanta A, Machado LD, Singh AK, Galvao DS, Silva GG, Tiwary CS, Ajayan PM. One-step electrodeposited 3D-ternary composite of zirconia nanoparticles, rGO and polypyrrole with enhanced supercapacitor performance. *Nano Energy*. 2017; 31: 225-232.
- [33] Liu A, Li C, Bai H, Shi G. Electrochemical deposition of polypyrrole/sulfonated graphene composite films. *J Phys Chem C*. 2010; 114: 22783-22789.
- [34] Rosas-Laverde NM, Pruna AI, Busquets-Mataix D. Graphene oxide-polypyrrole coating for functional ceramics. *Nanomaterials*. 2020; 10: 1188.
- [35] Ferrari AC. Raman spectroscopy of graphene and graphite: disorder, electron-phonon coupling, doping and nonadiabatic effects. *Solid State Commun*. 2010; 143: 47-57.
- [36] Okutan M. Electrochemical determination of ascorbic acid with thermally reduced graphene oxide. *Gazi Üniversitesi Mühendislik-Mimarlık Fakültesi Derg*. 2020; 35: 1589-1601.

- [37] Khademeh Molavi F, Ghasemi I, Messori M, Esfandeh M. Nanocomposites based on poly(L-lactide)/poly(ϵ -caprolactone) blends with triple-shape memory behavior: effect of the incorporation of graphene nanoplatelets (GNPs). *Compos Sci Technol.* 2017; 151: 219-227.
- [38] Kovtun A, Treossi E, Mirotta N, Scidà A, Liscio A, Christian M, Valorosi F, Boschi A, Young RJ, Galiotis C et al. Benchmarking of graphene-based materials: real commercial products versus ideal graphene. *2D Mater.* 2019; 6: 25006.
- [39] Purkait T, Singh G, Kamboj N, Das M, Dey RS. All-porous heterostructure of reduced graphene oxide–polypyrrole–nanoporous gold for a planar flexible supercapacitor showing outstanding volumetric capacitance and energy density. *J Mater Chem A.* 2018; 6: 22858-22869.
- [40] Tran XT, Park SS, Song S, Haider MS, Imran SM, Hussain M, Kim HT. Electroconductive performance of polypyrrole/reduced graphene oxide/carbon nanotube composites synthesized via in situ oxidative polymerization. *J Mater Sci.* 2019; 54: 3156-3173.
- [41] Šetka M, Calavia R, Vojkúvka L, Llobet E, Drbohlavová J, Vallejos S. Raman and XPS studies of ammonia sensitive polypyrrole nanorods and nanoparticles. *Sci Rep.* 2019; 9: 8465.
- [42] Wang J, Fu D, Ren B, Yu P, Zhang X, Zhang W, Kan K. Design and fabrication of polypyrrole/expanded graphite 3D interlayer nanohybrids towards high capacitive performance. *RSC Adv.* 2019; 9: 23109-23118.
- [43] Cao J, Wang Y, Chen J, Li X, Walsh FC, Ouyang JH, Jia D, Zhou Y. Three-dimensional graphene oxide/polypyrrole composite electrodes fabricated by one-step electrodeposition for high performance supercapacitors. *J Mater Chem A.* 2015; 3: 14445-14457.
- [44] Johra FT, Lee JW, Jung WG. Facile and safe graphene preparation on solution based platform. *J Ind Eng Chem.* 2014; 20: 2883-2887.
- [45] Chaudhary K, Aadil M, Zulfiqar S, Ullah S, Haider S, Agboola PO, Warsi MF, Shakir I. Graphene oxide and reduced graphene oxide supported ZnO nanochips for removal of basic dyes from the industrial effluents. *fullerenes, Nanotub Carbon Nanostructures.* 2021; 29: 915-928.
- [46] Yaçınkaya S, Çakmak D. Electrochemical synthesis of poly(pyrrole-co-[Cu(salabza)]): its electrocatalytic activity towards the oxidation of catechol. *Hacettepe J Biol Chem.* 2016; 44: 425-434.
- [47] Nayak J, Mahadeva SK, Kim J. Characteristics of flexible electrode made on cellulose by soluble polypyrrole coating. *Proc Inst Mech Eng Part C J Mech Eng Sci.* 2012; 226: 2605-2609.
- [48] Al-Harbi LM, Alsulami QA, Farea MO, Rajeh A. Tuning optical, dielectric, and electrical properties of polyethylene oxide/carboxymethyl cellulose doped with mixed metal oxide nanoparticles for flexible electronic devices. *J Mol Struct.* 2023; 1272: 134244.
- [49] Johannes AZ, Pingak RK, Bukit M. Tauc plot software: calculating energy gap values of organic materials based on ultraviolet-visible absorbance spectrum. *IOP Conf Ser Mater Sci Eng.* 2020; 823: 012030.
- [50] Tauc J. Optical properties and electronic structure of amorphous Ge and Si. *Mater Res Bull.* 1968; 3: 37-46.

- [51] Guimarães ML, da Silva FAG, da Costa MM, de Oliveira HP. Coating of conducting polymer-silver nanoparticles for antibacterial protection of Nile tilapia skin xenografts. *Synth Met.* 2022; 287: 117055.
- [52] Alzahrani HS, Al-Sulami AI, Alsulami QA, Rajeh A. A systematic study of structural, conductivity, linear, and nonlinear optical properties of PEO/PVA-MWCNTs/ZnO nanocomposites films for optoelectronic applications. *Opt Mater (Amst).* 2022; 133: 112900.
- [53] Ali HE, Khairy Y, Sayed MA, Algarni H, Shkir M, Maged FA. A tailoring the linear/nonlinear optical and visible shielding performance of PVP/PVOH incorporated with NiO nanoparticles for optical devices. *Optik (Stuttg).* 2022; 251: 168373.
- [54] Sharma N, Prabakar K, Ilango S, Dash S, Tyagi AK. Optical band-gap and associated Urbach energy tails in defected ZnO thin films grown by ion beam sputter deposition: Effect of Assisted Ion Energy. *Adv Mater Proc.* 2021; 2: 342-346.
- [55] Boran F, Çetinkaya Gürer S. The effect of starting material types on the structure of graphene oxide and graphene. *Turkish J Chem.* 2019; 43: 1322-1335.
- [56] Oliveira AEF, Braga GB, Tarley CRT, Pereira AC. Thermally reduced graphene oxide: synthesis, studies and characterization. *J Mater Sci.* 2018; 53: 12005-12015.
- [57] Boran F, Çetinkaya S, Anaklı D, Karakışla M, Saçak M. Synthesis and characterization of Poly (o-toluidine)/Na-Feldspar conductive composites with improved electrical conductivity. *Mühendislik Derg.* 2017; 8: 901-910.



RESEARCH ARTICLE

ON THE MAXIMUM CIRCULAR INVERSES OF MAXIMUM CIRCLES

Süheyla EKMEKÇİ^{1,*} 

¹ Department of Mathematics and Computer Science, Faculty of Science, Eskişehir Osmangazi University, Eskişehir, Turkey

ABSTRACT

In this study, the inverses of maximum circles under the maximum circular inversion are examined. The maximum circular inversion is observed to transform maximum circles to curves consisting of parabolic arcs, line segments, and sometimes rays. It is seen that the image curve occurs in different shapes depending on the relative positions of the inversion circle and the maximum circle. While the images of maximum circles not passing through the inversion center are closed curves, the images of those passing through the inversion center are not closed. Inverse curves have been studied by considering the radii of the maximum circles and the positions of the lines joining their centers and the center of maximum inversion. Classifications of the inverses of maximum circles are presented.

Keywords: Maximum metric, Inversion in maximum circle, Maximum circular inversion, Inverse of maximum circle

1. INTRODUCTION

Inversion defined on a circle is a geometric transformation such that it maps a point to another point in analytical plane. Apollonius of Perga initially presented the concept of inversion with respect to circle in his treatise titled “Plane Loci”. Later, during the 1830s, Steiner researched on the inversion with respect to circle. Since then, inversions with respect to circles have been studied and developed. Also, inversions in some curves and surfaces different from circles are defined and studied, [7, 8, 12, 15, 19-20].

In geometry, the measurement of distances between points in analytical plane can be achieved through various distance functions, each offering a lot of insights. The notable ones among these distance functions are Euclidean, taxicab, maximum, Chinese checker and iso-taxicab distances. When distance functions different from Euclidean distance measures are integrated into analytical plane, various non-Euclidean geometries are formed. There are studies that enrich the literature of these geometries, [1-6, 9-11, 13-14, 16-18, 22-23]. The inversions in circles and spheres obtained by using the taxicab distance, the Chinese Checker distance, the maximum distance are defined and developed, [5, 9-11, 15-19, 21, 23].

The maximum distance between two points $A_1 = (x_1, y_1)$ and $A_2 = (x_2, y_2)$ is defined by $d_M(A_1, A_2) = \max\{|x_1 - y_1|, |x_2 - y_2|\}$. This elementary mathematical formulation coupled with its instinctively coherent explication endow it with utility of significance in the realm of computer science and engineering implementations. The maximum plane is the analytical plane endowed with the maximum distance and symbolized by \mathbb{R}_M^2 . It is almost the same as the Euclidean plane except the distance function.

In this article, the inverses of maximum circles under the maximum circular inversion have been examined. The maximum circular inversion is observed to transform maximum circles to curves

consisting of parabolic arcs, line segments, and sometimes rays. It is seen that the image curve occurs in different shapes depending on the relative positions of the inversion circle and the maximum circle. While the images of maximum circles not passing through the inversion center are closed curves, the images of those passing through the inversion center are not closed. Inverse curves have been studied by considering the radii of the maximum circles and the positions of the lines joining their centers and the center of maximum inversion. Classifications of the images are presented.

This study is organized as follows: In section 2, some concepts used in this work are mentioned. In section 3, the inversion map defined in the maximum circle and its some properties are given. In section 4, the images of the maximum circles under the inversion with respect to maximum circle are examined and the results are presented.

2. PRELIMINARIES

It is clear from the distance d_M that the maximum distance between two points $A_1 = (x_1, y_1)$ and $A_2 = (x_2, y_2)$ is equal to the greatest of the Euclidean lengths of the line segments parallel to the coordinates axes in the right triangle with the hypotenuse A_1A_2 .

Krause in [14] gave the classification of lines according to their slopes as follows: Let m be the slope of the line ℓ in plane. The line ℓ is called the steep line, the gradual line and the separator line in the cases of $|m| > 1$, $|m| < 1$ and $|m| = 1$, respectively. In the special cases that the line ℓ is parallel to x -axis or y -axis, ℓ is named as the horizontal line or the vertical line, respectively. This classification is also valid in \mathbb{R}_M^2 .

The maximum circle centered at $M = (m_1, m_2)$ with the radius r is the set of points (x, y) satisfying the equation

$$\max \{|x - m_1|, |y - m_2|\} = r.$$

Every Euclidean translation preserves the maximum distance. So, it is an isometry in the maximum plane. Reflections in the coordinate axes and the separator lines through the origin and rotations about the origin by integer multiples of $\frac{\pi}{2}$ are isometries in maximum plane, [22].

Maximum distance from the point $A = (x_1, y_1)$ to the line ℓ with the equation $ax + by + c = 0$ is

$$d_M(A, \ell) = \frac{|ax_1 + by_1 + c|}{|a| + |b|},$$

[22].

3. THE INVERSION MAP IN THE MAXIMUM CIRCLE

The inversion in the maximum circle can be defined as an analog of the inversion in the Euclidean circle. While the inversion leaves the points on the inversion circle fixed, it maps points close to the center of the inversion circle to points far from the center of the inversion circle and conversely. However, under the inversion transformation, the center of the inversion circle has no image, and no point is mapped to the center of the inversion circle. Thus, by adding only one point O_∞ called the "ideal point" or "point at infinity" to the maximum plane, the inversion is defined at the center of the inversion circle and becomes a one-to-one map. According to this:

Consider the maximum circle, denoted by \mathcal{C} , with the center O and the radius r in \mathbb{R}_M^2 . The inversion in the maximum circle \mathcal{C} is the mapping $I_{\mathcal{C}}$ of $\mathbb{R}_M^2 \cup \{O_\infty\}$ defined by $I_{\mathcal{C}}(O) = O_\infty$, $I_{\mathcal{C}}(O_\infty) = O$ and $I_{\mathcal{C}}(X) = X'$ for any point X different from O and O_∞ , where the point X' lies on the ray OX and $d_M(O, X) \cdot d_M(O, X') = r^2$. \mathcal{C} is termed the circle of the maximum circle inversion; O denotes the center of the maximum circle inversion; r signifies the radius of the maximum circle inversion; and

the point X' is called the maximum circle inverse, briefly the inverse or the image of the point X under the map I_C . Also, the maximum circle inversion has the property $I_C^2(X) = X$.

Theorem 3.1. Any point (except the inversion center) inside of inversion circle is transformed to a point outside of it under the maximum circular inversion, and conversely, [9, 23].

Theorem 3.2. Let C be the maximum circle centered at the point $O = (0,0)$ with the radius r . If the points $P = (x, y)$ and $P' = (x', y')$ are inverses of each other with respect to the maximum circular inversion I_C , then the following equality between the coordinates of P and P' holds

$$(x', y') = \frac{r^2}{(\max\{|x|, |y|\})^2} (x, y),$$

[9, 23].

Corollary 3.3. Let C be the maximum circle centered at the point $O = (a, b)$ with the radius r . If the points $P = (x, y)$ and $P' = (x', y')$ are inverses of each other with respect to the maximum circular inversion I_C where $P \neq O$, then the following equalities between the coordinates of P and P' are valid

$$x' = a + \frac{r^2(x - a)}{(\max\{|x - a|, |y - b|\})^2}$$

$$y' = b + \frac{r^2(y - b)}{(\max\{|x - a|, |y - b|\})^2},$$

[9, 23].

4. IMAGES OF MAXIMUM CIRCLES UNDER THE MAXIMUM CIRCULAR INVERSION

It is well known that the inversion in Euclidean circle inverts circles not passing through the center of inversion to circles. Also, if these circles are completely inside of inversion circle, inverse images of them are outside of inversion circle and vice-versa. Besides, under the inversion in Euclidean circle, the images of circles passing through the inversion center are lines not passing through the inversion center. Additionally, if a circle is orthogonal to the inversion circle, then it is invariant under the inversion in Euclidean circle. In this section, inverses of the maximum circles under maximum circular inversion are studied and outcomes are given.

It is clear from the definition of maximum circular inversion that it leaves the inversion circle fixed. Images of other maximum circles are examined by considering the radii of the maximum circles and the positions of the lines joining their centers and the center of inversion. Firstly, the images of circles with the same center as the inversion circle are examined. And the following theorem shows that maximum circular inversion maps these to other maximum circles with the inversion center.

Since translations are isometries in maximum plane, no generality is lost to take the center of maximum circular inversion at the origin. Therefore, throughout this study, the center O is the origin unless otherwise stated.

Theorem 4.1. The maximum circular inversion transforms the concentric maximum circles centered on the inversion center to another concentric maximum circle.

Proof. Suppose that I_C is the inversion in the maximum circle C with the center O and the radius r . Let \mathcal{K} denote a maximum circle with the center O and the radius r' . The image of \mathcal{K} under I_C satisfies the equality

$$\max\{|x'|, |y'|\} = \frac{r^2}{r'}.$$

This means the maximum circle centered at O with radius $\frac{r^2}{r}$, (Figure 1).

Moreover, if \mathcal{K} is completely inside \mathcal{C} , then the maximum distance from the inversion center to the point X on \mathcal{K} is less than r . From the definition of inversion, the maximum distance from the inversion center to the maximum circular inverse of the point X is greater than r . So, it is achieved that if the maximum circles sharing the same center with the inversion circle are completely inside the inversion circle, their maximum circular inverses are completely outside the inversion circle and vice-versa.

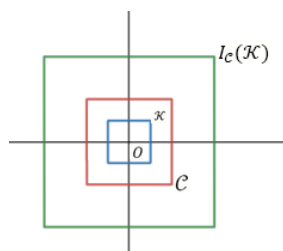


Figure 1. Maximum circular inverse of the concentric maximum circle centered on the inversion center

It is observed in the following theorems that the images of all other maximum circles are the curves other than the maximum circles and lines. Notice also that the images have different shapes and properties according to the positions of the maximum circles.

Theorem 4.2. The inversion in the maximum circle centered at the origin maps the maximum circle with the center on the coordinate axis to the curve having one of the following properties:

i) If the radius of the maximum circle is less than or equal to the maximum distance from its center to the separator lines passing through the inversion center, the image is a four-part closed curve such that two parts of the image are parallel line segments and the other two parts are parabolic arcs symmetrical about the coordinate axis, (Figure 2.a).

ii) If the radius of the maximum circle is greater than the maximum distance from its center to the separator lines passing through the inversion center, the image is an eight-part closed curve such that four parts of the image are four line segments parallel two by two and the others are four parabolic arcs symmetrical two by two about the coordinate axis, (Figure 2.b).

iii) If the radius of the maximum circle is equal to the maximum distance between its center and the inversion center, the image is the curve consisting of two rays, three line segments and two parabolic arcs, (Figure 2.c).

Proof. Suppose that I_C is the inversion in the maximum circle \mathcal{C} with the center $O = (0,0)$ and the radius r . Let \mathcal{K} and \mathcal{K}' denote a maximum circle centered at M with the radius r' and its maximum inverse curve with respect to I_C , respectively. Assume, without loss of generality, that the center M of \mathcal{K} is on x -axis and its abscissa is x_0 , where $x_0 > 0$. The maximum distance from the center M to the separator lines passing through O is $\frac{x_0}{2}$. And the maximum distance between the points M and O is equal to x_0 . The maximum circle \mathcal{K} is the set of points satisfying the equality

$$\max\{|x - x_0|, |y|\} = r'.$$

By applying the inversion map I_C to \mathcal{K} , the points on \mathcal{K}' hold the equality

$$\max\left\{\left|x' - \frac{x_0}{r^2} (\max\{|x'|, |y'|\})^2\right|, |y'|\right\} = \frac{r'}{r^2} (\max\{|x'|, |y'|\})^2.$$

Firstly, in the case that $|x'| > |y'|$ and $\left|x' - \frac{x_0}{r^2}(x')^2\right| > |y'|$, one gets immediately the equality $\left|x' - \frac{x_0}{r^2}(x')^2\right| = \frac{r'}{r^2}(x')^2$. In the case $x' < 0$, $x' = \frac{r^2}{x_0 - r'}$. When r' is greater than the maximum distance between O and M , the line segment $x' = \frac{r^2}{x_0 - r'}$, $\frac{r^2}{x_0 - r'} \leq y' \leq -\frac{r^2}{x_0 - r'}$ is on K' . If $0 \leq x' < \frac{r^2}{x_0}$, the line segment $x' = \frac{r^2}{x_0 + r'}$, $-\left(\frac{r}{x_0 + r'}\right)^2 r' \leq y' \leq \left(\frac{r}{x_0 + r'}\right)^2 r'$ is on the image. In the case $x' \geq \frac{r^2}{x_0}$, the line segment $x' = \frac{r^2}{x_0 - r'}$, $-\left(\frac{r}{x_0 - r'}\right)^2 r' \leq y' \leq \left(\frac{r}{x_0 - r'}\right)^2 r'$ where $r' \leq \frac{x_0}{2}$ or the line segment $x' = \frac{r^2}{x_0 - r'}$, $-\frac{r^2}{x_0 - r'} \leq y' \leq \frac{r^2}{x_0 - r'}$ where $\frac{x_0}{2} < r' < x_0$ is on K' . In the case that $|x'| > |y'|$ and $\left|x' - \frac{x_0}{r^2}(x')^2\right| \leq |y'|$, the parabola arcs $|y'| = \frac{r'}{r^2}(x')^2$, $\frac{r^2}{x_0 + r'} \leq x' \leq \frac{r^2}{r'}$ for $r' > \frac{x_0}{2}$ and $|y'| = \frac{r'}{r^2}(x')^2$, $\frac{r^2}{x_0 + r'} \leq x' \leq \frac{r^2}{x_0 - r'}$ for $r' \leq \frac{x_0}{2}$ are in the solution region. If both $|x'| \leq |y'|$ and $\left|x' - \frac{x_0}{r^2}(x')^2\right| > |y'|$, then $\left|x' - \frac{x_0}{r^2}(x')^2\right| = \frac{r'}{r^2}(x')^2$. For the case $x' > \frac{x_0}{r^2}(y')^2$, the parabola arc $x' = \frac{x_0 + r'}{r^2}(y')^2$, $0 \leq x' \leq \frac{r^2}{x_0 + r'}$ is not in the region determined by the inequality $\left|x' - \frac{x_0}{r^2}(x')^2\right| > |y'|$. For the other case, the equation $x' = \frac{x_0 - r'}{r^2}(y')^2$ is obtained. In special case of $r' = x_0$, the rays $x = 0$, $|y'| \geq \frac{r^2}{x_0}$ occur. If $r' < \frac{x_0}{2}$, then there is no solution. When $r' \geq \frac{x_0}{2}$, the parabola arc $x' = \frac{x_0 - r'}{r^2}(y')^2$, $(x_0 - r')\left(\frac{r}{r'}\right)^2 \leq x' \leq \frac{r^2}{x_0 - r'}$ is on the image. In the last case that $|x'| \leq |y'|$ and $\left|x' - \frac{x_0}{r^2}(x')^2\right| \leq |y'|$, then $|y'| = \frac{r'}{r^2}(y')^2$. When $r' \geq \frac{x_0}{2}$, the line segments $y' = \pm \frac{r^2}{r'}$, $(x_0 - r')\left(\frac{r}{r'}\right)^2 \leq x' \leq \frac{r^2}{r'}$ are on the image. By using the isometric reflections in the lines passing through the inversion center, It is immediately obtained similar results as the above analysis when $x_0 < 0$ or M on the y -axis.

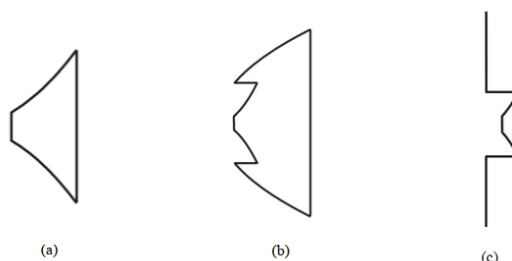


Figure 2. The image of the maximum circle whose the center is on the coordinate axis through the inversion center

Also, the images of line segments were examined according to the fact that their endpoints lie in regions determined by the separator lines passing through the inversion center as detailed in [11]. In the case that the radius of the maximum circle is less than or equal to the maximum distance from its center to the separator lines passing through the inversion center, all vertices and sides of maximum circle are in in the same region. Since the inverse images of two sides perpendicular to the coordinate axis in the region are two line segments parallel to them and the inverse images of the other two are parabola arc, the maximum circular inversion maps the maximum circle to a four-part closed curve, (Figure 2.a). In the case of ii, the vertices on one side of the maximum circle are in the alternate regions and the image of that side is a three-part curve consisting of a line segment parallel to it and two parabolic arcs. The vertices on two sides are in neighboring regions and the images of these sides are two-part curves comprising a line segment and a parabola arc. The vertices on last side are in same region and its image is a line segment parallel to it. Therefore, the maximum circular inversion maps the maximum circles in case (ii) to the eight-part closed curves as shown in Figure 2.b. If the radius of

the maximum circle is equal to the maximum distance between its center and the inversion center, the side whose vertices are in alterne regions passes through the inversion center. Then, its image consists of two rays. The properties of the other sides are the same. So, in this case the image of maximum circle under the maximum circular inversion is a seven-part open curve, (Figure 2.c).

The following corollary is a result of theorem 4.2 for the case that the inversion center is not the origin:

Corollary 4.3. The maximum circular inversion maps the maximum circle with the center on the horizontal line or the vertical line passing through the inversion center to the curve having one of the following properties:

i) If the radius of the maximum circle is less than or equal to the maximum distance from its center to the separator lines passing through the inversion center, its image is a four-part closed curve such that two parts of the image are parallel line segments and the other two parts are the symmetric parabolic arcs about the line through centers,

ii) If the radius of the maximum circle is greater than the maximum distance from its center to the separator lines passing through the inversion center, the image is a eight-part closed curve such that four parts of the image are four line segments parallel two by two and the others are four parabolic arcs symmetrical two by two about the line through centers,

iii) If the radius of the maximum circle is equal to the maximum distance between its center and the inversion center, the image curve consists of two rays, three line segments and two parabolic arcs, (Figure 3).

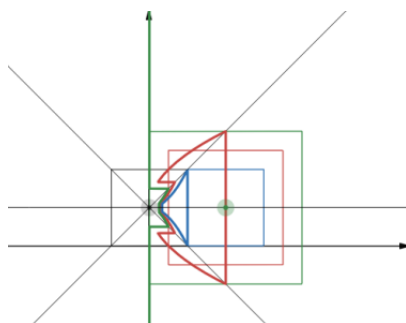


Figure 3. The images of the maximum circles with the centers on the horizontal line through the inversion center

Theorem 4.4. The maximum circular inversion maps the maximum circle with the center on the separator line passing through the inversion center to the curve having one of the following properties:

i) If the radius of the maximum circle is equal to the maximum distance between its center and the inversion center, then the image is a four-part open curve consisting of two rays and two line segments,

ii) If the radius of the maximum circle is less than the maximum distance between its center and the inversion center, then the image is a four-part close curve consisting of two parabola arcs and two line segments,

iii) If the radius of the maximum circle is greater than the maximum distance between its center and the inversion center, then the image is a six-part close curve consisting of two parabola arcs and four line segments.

Proof. Suppose that I_C is the inversion in the maximum circle C with the center $O = (0,0)$ and the radius r . Let K and K' denote a maximum circle centered at M with the radius r' and its maximum inverse with respect to I_C , respectively. Assume, without loss of generality, that the center M of K is on the separator line $y = x$ and its abscissa is x_0 , where $x_0 > 0$. The maximum distance from the center M to the other separator line passing through O and the maximum distance between the points M and O are equal to x_0 . I_C maps the points on K to the points satisfying the equality

$$\max\left\{\left|x' - \frac{x_0}{r^2}(\max\{|x'|, |y'|\})^2\right|, \left|y' - \frac{x_0}{r^2}(\max\{|x'|, |y'|\})^2\right|\right\} = \frac{r'}{r^2}(\max\{|x'|, |y'|\})^2.$$

In the case that $|x'| > |y'|$ and $\left|x' - \frac{x_0}{r^2}(x')^2\right| > \left|y' - \frac{x_0}{r^2}(x')^2\right|$, the equality $|r^2x' - x_0(x')^2| = r'(x')^2$ is obtained. For $x' < 0$, the line segment $x' = \frac{r^2}{x_0 - r'}$, $\frac{r^2}{x_0 - r'} \leq y \leq -\frac{r^2}{x_0 - r'}$ where $x_0 < r'$ lies on the locus given by the above equation. For $0 \leq x' < \frac{r^2}{x_0}$, the line segment $x' = \frac{r^2}{x_0 + r'}$, $(x_0 - r')\left(\frac{r}{x_0 + r'}\right)^2 \leq y' \leq \frac{r^2}{x_0 + r'}$ is on the image. And the solution is not sought for the case $x' \geq \frac{r^2}{x_0}$. Considering the case that $|x'| > |y'|$ and $\left|x' - \frac{x_0}{r^2}(x')^2\right| \leq \left|y' - \frac{x_0}{r^2}(x')^2\right|$, the parabola arc $y' = \frac{x_0 - r'}{r^2}(x')^2$, $\frac{r^2}{x_0 + r'} \leq x' \leq \frac{r^2}{|x_0 - r'|}$, where $x_0 \neq r'$ or the ray $y' = 0$, $\frac{r^2}{2x_0} \leq x'$, where $x_0 = r'$ is obtained. If both $|x'| \leq |y'|$ and $\left|x' - \frac{x_0}{r^2}(y')^2\right| > \left|y' - \frac{x_0}{r^2}(y')^2\right|$, then $|r^2x' - x_0(y')^2| = r'(y')^2$. For $x' < \frac{x_0}{r^2}(y')^2$, one gets that the parabola arc $x' = \frac{x_0 - r'}{r^2}(y')^2$, $\frac{r^2}{x_0 + r'} \leq y' \leq \frac{r^2}{|x_0 - r'|}$ where $x_0 \neq r'$ and the ray $x' = 0$, $\frac{r^2}{2x_0} \leq y'$, where $x_0 = r'$. Considering the case that $|x'| \leq |y'|$ and $\left|x' - \frac{x_0}{r^2}(y')^2\right| \leq \left|y' - \frac{x_0}{r^2}(y')^2\right|$, then $|r^2y' - x_0(y')^2| = r'(y')^2$. This equality signifies the line segments corresponding to $y' = \frac{r^2}{x_0 - r'}$, $\frac{r^2}{x_0 - r'} \leq x' \leq -\frac{r^2}{x_0 - r'}$ where $x_0 < r$ in the case of $y' < 0$ and $y' = \frac{r^2}{x_0 + r'}$, $(x_0 - r')\left(\frac{r}{x_0 + r'}\right)^2 \leq x' \leq \frac{r^2}{x_0 + r'}$ in the case of $0 \leq y' < \frac{r^2}{x_0}$. The case of $x_0 < 0$ or M on the separator line $y = -x$ is similar to the above analysis.

In the case that the radius of the maximum circle is less than the maximum distance between its center and the inversion center, two sides of the maximum circle are in the same region while the other two sides are in neighboring region. The image of the side perpendicular to the coordinate axis in the region is a line segment, while the image of the side parallel to the coordinate axis is a parabolic arc. Thus, the image of the maximum circle consists of the line segments $x' = \frac{r^2}{x_0 + r'}$, $(x_0 - r')\left(\frac{r}{x_0 + r'}\right)^2 \leq y' \leq \frac{r^2}{x_0 + r'}$; $y' = \frac{r^2}{x_0 + r'}$, $(x_0 - r')\left(\frac{r}{x_0 + r'}\right)^2 \leq x' \leq \frac{r^2}{x_0 + r'}$, and the parabolic arcs $y' = \frac{x_0 - r'}{r^2}(x')^2$, $\frac{r^2}{x_0 + r'} \leq x' \leq \frac{r^2}{|x_0 - r'|}$, $x' = \frac{x_0 - r'}{r^2}(y')^2$, $\frac{r^2}{x_0 + r'} \leq y' \leq \frac{r^2}{|x_0 - r'|}$, as shown in Figure 4.a.

In the case that the radius of the maximum circle is equal to the maximum distance between its center and the inversion center, two sides of the maximum circle pass through the inversion center. The images of these sides are two rays $x' = 0$, $\frac{r^2}{2x_0} \leq y'$ and $y' = 0$, $\frac{r^2}{2x_0} \leq x'$. The images of the other sides are the line segments $x' = \frac{r^2}{x_0 + r'}$, $(x_0 - r')\left(\frac{r}{x_0 + r'}\right)^2 \leq y' \leq \frac{r^2}{x_0 + r'}$; $y' = \frac{r^2}{x_0 + r'}$, $(x_0 - r')\left(\frac{r}{x_0 + r'}\right)^2 \leq x' \leq \frac{r^2}{x_0 + r'}$, as shown in Figure 4.c.

When the radius of the maximum circle is greater than the maximum distance between its center and the inversion center, the vertices on the two sides of the maximum circle are in the neighboring regions, so the image of each of these sides consists of a line segment and a parabolic arc. Each of the other two sides transforms to a line segment parallel to itself under inversion. Thus, the image of the maximum circle consists of the line segments $x' = \frac{r^2}{x_0-r'}$, $\frac{r^2}{x_0-r'} \leq y' \leq -\frac{r^2}{x_0-r'}$, $x' = \frac{r^2}{x_0+r'}$, $(x_0 - r') \left(\frac{r}{x_0+r'}\right)^2 \leq y' \leq \frac{r^2}{x_0+r'}$; $y' = \frac{r^2}{x_0-r'}$, $\frac{r^2}{x_0-r'} \leq x' \leq -\frac{r^2}{x_0-r'}$ and $y' = \frac{r^2}{x_0+r'}$, $(x_0 - r') \left(\frac{r}{x_0+r'}\right)^2 \leq x' \leq \frac{r^2}{x_0+r'}$, and the parabolic arcs $y' = \frac{x_0-r'}{r^2}(x')^2$, $\frac{r^2}{x_0+r'} \leq x' \leq \frac{r^2}{|x_0-r'|}$, $x' = \frac{x_0-r'}{r^2}(y')^2$, $\frac{r^2}{x_0+r'} \leq y' \leq \frac{r^2}{|x_0-r'|}$, as shown in Figure 4.b.

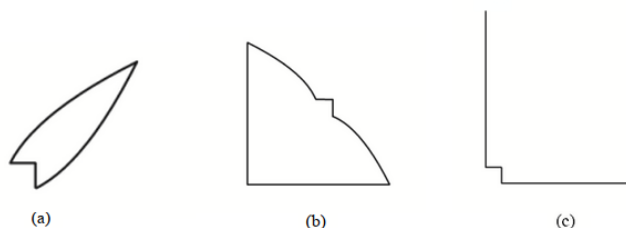


Figure 4. The image of the maximum circle with the center on the separator line through the inversion center

Theorem 4.5. The inversion in maximum circle maps the maximum circle with the center on a gradual line passing through the inversion center to the curve having one of the following properties:

- i) If the radius of the maximum circle is less than the maximum distances from its center to the separator lines passing through the inversion center, then the image is a four-part closed curve such that two parts of the image are parallel line segments and the others are parabola arcs, (Figure 5.a),
- ii) If the radius of the maximum circle is a value between the maximum distances from its center to the separator lines passing through the inversion center, then the image is a six-part closed curve consisting of three line segments and three parabola arcs, (Figure 5.b),
- iii) If the radius of the maximum circle is greater than the maximum distances from its center to the separator lines passing through the inversion center, then the image is a eight-part closed curve consisting of four line segments and four parabola arcs, (Figure 5.c),
- iv) If the radius of the maximum circle is equal to the maximum distance between its center and the inversion center, then the image is a seven-part curve consisting of two rays, three line segments and two parabola arcs, (Figure 5.d).

Proof. Suppose that I_c is the inversion in the maximum circle C with the center $O = (0,0)$ and the radius r . Let K and K' denote a maximum circle centered at M with the radius r' and its maximum inverse with respect to I_c , respectively. Assume, without loss of generality, that the coordinate of the center M is (x_0, y_0) , where $0 < y_0 < x_0$. The maximum distances from the center M to the separator lines passing through the inversion center are $\frac{x_0-y_0}{2}$ and $\frac{x_0+y_0}{2}$. And the maximum distance between the center M and the inversion center is x_0 . The points on K' satisfy the equality

$$\max\{|r^2x' - x_0(\max\{|x'|, |y'|\})^2|, |r^2y - y_0(\max\{|x'|, |y'|\})^2|\} = r'(\max\{|x'|, |y'|\})^2.$$

Considering the case that $|x'| > |y'|$ and $\left|x' - \frac{x_0}{r^2}(x')^2\right| > \left|y' - \frac{y_0}{r^2}(x')^2\right|$, it is obtained the equality

$$|r^2x' - x_0(x')^2| = r'(x')^2.$$

Firstly, suppose that $x' < 0$, then the line segment with the equation $x' = \frac{r^2}{x_0-r'}, \frac{r^2}{x_0-r'} \leq y' \leq -\frac{r^2}{x_0-r'}$ where $x_0 < r'$ yields the above equality. If $0 \leq x' < \frac{r^2}{x_0}$, then it is obtained that the line segment $x' = \frac{r^2}{x_0+r'}, (y_0 - r') \left(\frac{r}{x_0+r'}\right)^2 \leq y' \leq (y_0 + r') \left(\frac{r}{x_0+r'}\right)^2$ is on the image. When $x' \geq \frac{r^2}{x_0}$, the line segment $x' = \frac{r^2}{x_0-r'}$ where $x_0 > r'$ forms the part of K' . Depending on the values taken by the radius r' of the maximum circle K , the coordinates of the endpoints of the line segment change. If r' is a value between $\frac{x_0+y_0}{2}$ and x_0 , then the endpoints of the line segment lie on the separator lines passing through the inversion center and the line segment is $x' = \frac{r^2}{x_0-r'}, -\frac{r^2}{x_0-r'} \leq y' \leq \frac{r^2}{x_0-r'}$. If r' is a value between $\frac{x_0-y_0}{2}$ and $\frac{x_0+y_0}{2}$, the endpoints of the line segment lie on the parabola and the separator line passing through the inversion center and the line segment is $x' = \frac{r^2}{x_0-r'}, \frac{r^2(y_0-r')}{(x_0-r')^2} \leq y' \leq \frac{r^2}{x_0-r'}$. If r' is less than the value $\frac{x_0-y_0}{2}$, then the endpoints of the line segment lie on parabolas passing through the inversion center and the line segment is $x' = \frac{r^2}{x_0-r'}, \frac{r^2(y_0-r')}{(x_0-r')^2} \leq y' \leq \frac{r^2(y_0+r')}{(x_0-r')^2}$.

If both $|x'| > |y'|$ and $\left|x' - \frac{x_0}{r^2}(x')^2\right| \leq \left|y' - \frac{y_0}{r^2}(x')^2\right|$, then $|r^2y' - y_0(x')^2| = r'(x')^2$.

Suppose that $y' < \frac{y_0}{r^2}(x')^2$, one gets that the parabola arc $y' = \frac{(y_0-r')}{r^2}(x')^2, \frac{r^2}{x_0+r'} \leq x' \leq \frac{r^2}{x_0-r'}$ where $r' \leq \frac{x_0+y_0}{2}$ or $\frac{r^2}{x_0+r'} \leq x' \leq -\frac{r^2}{y_0-r'}$ where $r' > \frac{x_0+y_0}{2}$ on the image. In the case of $y' \geq \frac{y_0}{r^2}(x')^2$, the equality $y' = \frac{(y_0+r')}{r^2}(x')^2$ is obtained. If r' is less than the value $\frac{x_0-y_0}{2}$, then the endpoints of the parabola arc with the equation $y' = \frac{(y_0+r')}{r^2}(x')^2$ lie on the parabolas passing through the inversion center such that this arc on K' is $y' = \frac{(y_0+r')}{r^2}(x')^2, \frac{r^2}{x_0+r'} \leq x' \leq \frac{r^2}{x_0-r'}$. If r' is greater than the value $\frac{x_0-y_0}{2}$, then the endpoints of the parabola arc lie on the parabola and the separator line passing through the inversion center such that it is $y' = \frac{(y_0+r')}{r^2}(x')^2, \frac{r^2}{x_0+r'} \leq x' \leq \frac{r^2}{y_0+r'}$.

Considering the inequalities $|x'| \leq |y'|$ and $\left|x' - \frac{x_0}{r^2}(y')^2\right| > \left|y' - \frac{y_0}{r^2}(y')^2\right|$, then the point (x', y') on K' holds the equality $|r^2x' - x_0(y')^2| = r'(y')^2$. When $x' < \frac{x_0}{r^2}y'^2$, it is seen that the parabola arcs $x' = \frac{x_0-r'}{r^2}y'^2, \frac{r^2}{x_0-r'} \leq y' \leq \frac{r^2}{y_0-r'}$ and $x' = \frac{x_0-r'}{r^2}y'^2, \frac{r^2}{y_0+r'} \leq y' \leq \frac{-r^2}{x_0-r'}$ lie on K' where $x_0 < r'$. When the radius r' is less than x_0 , all possible cases for r' have to be considered, as above. If r' is a value between $\frac{x_0+y_0}{2}$ and x_0 , then the two parabola arcs determined by the equation $x' = \frac{x_0-r'}{r^2}y'^2$ are on K' such that their endpoints are on the separator line and the parabola passing through the inversion center: $x' = \frac{x_0-r'}{r^2}y'^2, \frac{-r^2}{x_0-r'} \leq y' \leq \frac{r^2}{y_0-r'}$ and $x' = \frac{x_0-r'}{r^2}y'^2, \frac{r^2}{y_0+r'} \leq y' \leq \frac{r^2}{x_0-r'}$. If r' is a value between $\frac{x_0-y_0}{2}$ and $\frac{x_0+y_0}{2}$, then only one parabolic arc, determined by the same equation, lies on K' such that its endpoints are on the separator line and the parabola: $x' = \frac{x_0-r'}{r^2}y'^2, \frac{r^2}{y_0+r'} \leq y' \leq \frac{r^2}{x_0-r'}$. If r' is less than the value $\frac{x_0-y_0}{2}$, then there is no solution. In the particular case of $x_0 = r'$, the rays $x' = 0, \frac{r^2}{y_0+r'} \leq y'$ and $x' = 0, y' \leq \frac{r^2}{y_0-r'}$ are on K' . When $x' \geq \frac{x_0}{r^2}y'^2$, no solution is sought.

The point (x', y') on K' satisfying the conditions $|x'| \leq |y'|$ and $\left| x' - \frac{x_0}{r^2}(y')^2 \right| \leq \left| y' - \frac{y_0}{r^2}(y')^2 \right|$ yields the equation $|r^2y' - x_0(y')^2| = r'(y')^2$. When the possible cases related to this equality are examined, the differences are observed according to the radius r' . If r' is greater than the value $\frac{x_0+y_0}{2}$, the intersection of the line $y = \frac{r^2}{y_0-r'}$ and the region $\{(x', y'): x' > y' + \frac{x_0-y_0}{r^2}y'^2, |x'| \leq |y'|\}$ is the line segment $y = \frac{r^2}{y_0-r'}, \frac{(x_0-r')r^2}{(y_0-r')^2} \leq x' \leq -\frac{r^2}{y_0-r'}$. If r' is less than $\frac{x_0+y_0}{2}$, there is no solution. If r' is greater than the value $\frac{x_0-y_0}{2}$, the intersection of the line $y = \frac{r^2}{y_0+r'}$ and the region $\{(x', y'): x' > -y' + \frac{x_0+y_0}{r^2}y'^2, |x'| \leq |y'|\}$ is the line segment $y = \frac{r^2}{y_0+r'}, \frac{(x_0-r')r^2}{(y_0+r')^2} \leq x' \leq \frac{r^2}{y_0+r'}$. If r' is less than $\frac{x_0-y_0}{2}$, there is no solution. Thus, when r' is greater than $\frac{x_0+y_0}{2}$, both of these line segments lie on K' . When r' is between the values $\frac{x_0-y_0}{2}$ and $\frac{x_0+y_0}{2}$, only one of them lies on K' . When r' is smaller than $\frac{x_0-y_0}{2}$, none of them lies on K' .

It is similar to the above when considering all possible placements of x_0 and y_0 . In the case of (i), all vertices of the maximum circle are in the same region. Since the images of two sides perpendicular to the coordinate axis in the region are two line segments $x' = \frac{r^2}{x_0+r'}, (y_0-r')\left(\frac{r}{x_0+r'}\right)^2 \leq y' \leq (y_0+r')\left(\frac{r}{x_0+r'}\right)^2$, $x' = \frac{r^2}{x_0-r'}, \frac{r^2(y_0-r')}{(x_0-r')^2} \leq y' \leq \frac{r^2(y_0+r')}{(x_0-r')^2}$ and the images of others are two parabola arcs $y' = \frac{(y_0-r')}{r^2}(x')^2, \frac{r^2}{x_0+r'} \leq x' \leq \frac{r^2}{x_0-r'}$, $y' = \frac{(y_0+r')}{r^2}(x')^2, \frac{r^2}{x_0+r'} \leq x' \leq \frac{r^2}{x_0-r'}$, the maximum circular inversion maps the maximum circle to a four-part closed curve, as shown in Figure 5.a.

Considering situation (ii), the vertices on the two sides of the maximum circle are in the neighboring regions, so the images of these sides consist of line segments and parabolic arcs. Since the images of the other two sides are a line segment and a parabola arc, the maximum circular inversion maps the maximum circle to a six-part closed curve such that the line segments are $x' = \frac{r^2}{x_0+r'}, (y_0-r')\left(\frac{r}{x_0+r'}\right)^2 \leq y' \leq (y_0+r')\left(\frac{r}{x_0+r'}\right)^2$, $x' = \frac{r^2}{x_0-r'}, \frac{r^2(y_0-r')}{(x_0-r')^2} \leq y' \leq \frac{r^2}{x_0-r'}$, $y = \frac{r^2}{y_0+r'}, \frac{(x_0-r')r^2}{(y_0+r')^2} \leq x' \leq \frac{r^2}{y_0+r'}$ and the parabola arcs are $y' = \frac{(y_0-r')}{r^2}(x')^2, \frac{r^2}{x_0+r'} \leq x' \leq \frac{r^2}{x_0-r'}$, $y' = \frac{(y_0+r')}{r^2}(x')^2, \frac{r^2}{x_0+r'} \leq x' \leq \frac{r^2}{x_0-r'}$, $x' = \frac{x_0-r'}{r^2}y'^2, \frac{r^2}{y_0+r'} \leq y' \leq \frac{r^2}{x_0-r'}$, as shown in Figure 5.b.

When it comes to situation (iii), the image of the side with the vertices in alternate regions is a three-part curve consisting of a line segment parallel to it and two parabolic arcs. The images of two sides with the vertices in neighboring regions are two-part curves comprising a line segment and a parabola arc. The image of last side with the vertices in same region is a line segment. So, image of the maximum circle in case (iii) under the maximum circular inversion is eight-part closed curve such that the line segments are $x' = \frac{r^2}{x_0+r'}, (y_0-r')\left(\frac{r}{x_0+r'}\right)^2 \leq y' \leq (y_0+r')\left(\frac{r}{x_0+r'}\right)^2$, $x' = \frac{r^2}{x_0-r'}, -\frac{r^2}{x_0-r'} \leq y' \leq \frac{r^2}{x_0-r'}$, $y = \frac{r^2}{y_0-r'}, \frac{(x_0-r')r^2}{(y_0-r')^2} \leq x' \leq -\frac{r^2}{y_0-r'}$, $y = \frac{r^2}{y_0+r'}, \frac{(x_0-r')r^2}{(y_0+r')^2} \leq x' \leq \frac{r^2}{y_0+r'}$ and the parabola arcs are $y' = \frac{(y_0-r')}{r^2}(x')^2, \frac{r^2}{x_0+r'} \leq x' \leq -\frac{r^2}{y_0-r'}$, $y' = \frac{(y_0+r')}{r^2}(x')^2, \frac{r^2}{x_0+r'} \leq x' \leq \frac{r^2}{y_0+r'}$, $x' = \frac{x_0-r'}{r^2}y'^2, \frac{-r^2}{x_0-r'} \leq y' \leq \frac{r^2}{y_0+r'}$, $x' = \frac{x_0-r'}{r^2}y'^2, \frac{r^2}{y_0+r'} \leq y' \leq \frac{r^2}{x_0-r'}$, as shown in Figure 5.c.

When the case (iv) occurs, since the side with the vertices in alternate regions passes through the inversion center, its image consists of two rays $x' = 0, \frac{r^2}{y_0+r'} \leq y', x' = 0, y' \leq \frac{r^2}{y_0-r'}$. The rest of the sides are the same as in case iii. And so, the image of the maximum circle in case (iv) under the maximum

circular inversion is a seven-part curve such that the line segments are $x' = \frac{r^2}{x_0+r'}$, $(y_0 - r') \left(\frac{r}{x_0+r'}\right)^2 \leq y' \leq (y_0 + r') \left(\frac{r}{x_0+r'}\right)^2$, $y = \frac{r^2}{y_0-r'}$, $\frac{(x_0-r')r^2}{(y_0-r')^2} \leq x' \leq -\frac{r^2}{y_0-r'}$, $y = \frac{r^2}{y_0+r'}$, $\frac{(x_0-r')r^2}{(y_0+r')^2} \leq x' \leq \frac{r^2}{y_0+r'}$, the parabola arcs are $y' = \frac{(y_0-r')}{r^2}(x')^2$, $\frac{r^2}{x_0+r'} \leq x' \leq -\frac{r^2}{y_0-r'}$, $y' = \frac{(y_0+r')}{r^2}(x')^2$, $\frac{r^2}{x_0+r'} \leq x' \leq \frac{r^2}{y_0+r'}$ and the two rays mentioned above, as shown in Figure 5.c.

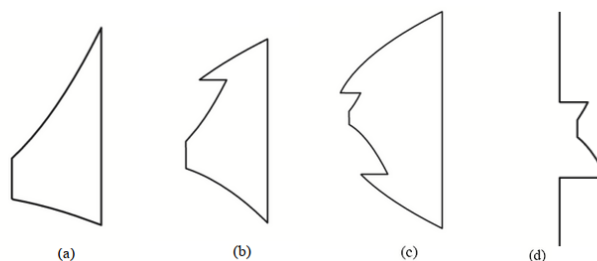


Figure 5. The image of the maximum circle with the center on the gradual line through the inversion center

It should be noted that Theorem 4.5 can be stated for the maximum circles with the centers on steep lines considering the isometric reflections in the separator lines passing through the inversion center.

5 CONCLUSION

In this study, the focus was on the examining of the images of maximum circles under the inversion in a maximum circle. Through a detailed analytical analysis, several observations were made. The study also introduced various properties related to the images of maximum circles under the maximum circle inversion. It was found that if the centers of maximum circles are different from the inversion center, their images do not form a maximum circle or a line but instead become curves comprising parabolic arcs, line segments, and rays. It was observed that if the maximum circle passes through the inversion center, the image is not closed curve. The resulting images were found to depend on the relative positions of the inversion circle and the maximum circle, leading to a classification of their images.. These findings provide to our understanding of how maximum circles are affected by maximum circular inversion. Consequently, it is thought that the results obtained in this study contribute to the literature including the subject of inversion in non-Euclidean geometry.

REFERENCES

- [1] Akça Z, Kaya R. On the taxicab trigonometry. *Journal of Inst. Math. Comput. Sci. Math. Ser.*, 1997;10(3): 151–159.
- [2] Akça Z, Kaya R. On the distance formulae in three dimensional taxicab space. *Hadronic Journal*, 2004; 27(5): 521–532.
- [3] Akça Z, Nazlı S. On the versions in the plane $\mathbb{R}_{\pi^3}^2$ of some Euclidean theorems. *New Trends in Mathematical Sciences*, 2022; 10(1): 20–27.
- [4] Akça Z, Çalış C. On the voronoi diagram and taxicab plane. *Erzincan Üiversity Journal of Science and Technology*, 2021; 14(1): 175–181.
- [5] Bayar A, Ekmekçi S. On circular inversions in taxicab plane. *Journal of Advanced Research in Pure Mathematics*, 2014; 6(4): 33-39.

- [6] Bayar A, Ekmekçi S, Öztürk İ. On complex numbers and taxicab plane. *Mathematical Sciences and Applications E-Notes*, 2015; 3(1): 58–64.
- [7] Blair DE. *Inversion Theory and Conformal Mapping*. USA, American Math. Society, 2000.
- [8] Childress N. Inversion with respect to the central conics. *Mathematics Magazine*, 1965; 38(3): 147-149.
- [9] Cırık Y. The inversions in the plane and in the space donated with the maximum metric. MSc, Eskişehir Osmangazi University, Eskişehir, Turkey, 2022.
- [10] Cırık Y, Ekmekçi S. On the maksimum spherical inversions. *Erzincan University, Journal of Science and Technology*, 2022; 15(1): 360-371.
- [11] Ekmekçi S. A note on the maximum circle inverses of lines in the maximum plane. *Ikonion Journal of Mathematics*, 2023; 5(2): 1-9.
- [12] Gdawiec K. Star-shaped set inversion fractals. *Fractals*, 2014; 22(4): 1450009-1-1450009-17.
- [13] Kaya R, Akça Z, Özcan M, Günaltılı İ. General equation for taxicab conics and their classification. *Mitt. Math. Ges. Hamburg*, 2000; 19(0): 135–148.
- [14] Krause EF. *Taxicab Geometry*. Menlo Park, California, USA, Addison –Wesley Publishing Company, 1975.
- [15] Nickel JA. A budget of inversion. *Math. Comput. Modelling*, 1995; 21(6): 87-93.
- [16] Pekzorlu A, Bayar A. On the Chinese checkers spherical inversions in three dimensional Chinese checker space. *Communications Faculty of Sciences University of Ankara Series A1: Mathematics and Statistics*, 2020; 69(2): 1498-1507.
- [17] Pekzorlu A, Bayar A. Taxicab spherical inversions in taxicab space. *Journal of Mahani Mathematical Research Center*, 2020; 9(1): 45-54.
- [18] Pekzorlu A, Bayar A. On the Chinese checkers circular inversions in the Chinese checkers plane. *Hagia Sophia Journal of Geometry*, 2022; 4(2): 28–34.
- [19] Ramirez JL. Inversions in an ellipse. *Forum Geometricorum*, 2014; 14: 107–115.
- [20] Ramirez JL, Rubiano GN. A geometrical construction of inverse points with respect to an ellipse. *International Journal of Mathematical Education in Science and Technology*, 2014; 45(8): 1254-1259.
- [21] Ramirez JL, Rubiano GN, Zlobec BJ. A generating fractal patterns by using p-circle inversion. *Fractals*, 2015; 23(4):1550047-1-1550047-13.
- [22] Salihova S. On the geometry of maximum metric. Ph.D, Eskişehir Osmangazi University, Eskişehir, Turkey, 2006.
- [23] Yüca G, Can Z. On the circular inversion in maximum plane. *Ikonion Journal of Mathematics*, 2020; 2(2): 26-34.